PONTIFICIA UNIVERSIDAD CATOLICA DE CHILE

SCHOOL OF ENGINEERING

GUIDELINES FOR NUMERICAL SEISMIC ANALYSIS OF REINFORCED CONCRETE AXIAL-FLEXURAL ELEMENTS

JUAN DIEGO POZO OCAMPO

Thesis submitted to the Office of Graduate Studies in partial fulfillment of the requirements for the Degree of Doctor in Engineering Sciences

Advisors:

MATÍAS HUBE

YAHYA KURAMA

Santiago de Chile, May, 2021

PONTIFICIA UNIVERSIDAD CATOLICA DE CHILE

SCHOOL OF ENGINEERING

GUIDELINES FOR NUMERICAL SEISMIC ANALYSIS OF REINFORCED CONCRETE AXIAL-FLEXURAL ELEMENTS

JUAN DIEGO POZO OCAMPO

Members of the Committee:

MATÍAS HUBE

YAHYA KURAMA

HERNÁN SANTA MARÍA

KAPIL KHANDELWAL

STEVEN BARBACHYN

DIEGO LÓPEZ-GARCÍA

Thesis submitted to the Office of Graduate Studies in partial fulfillment of the requirements for the Degree Doctor in Engineering Sciences

Santiago de Chile, May, 2021

ACKNOWLEDGMENTS

I would like to express my sincere gratitude to my advisors Matías Hube and Yahya Kurama for their guidance, knowledge, and for always looking out for my personal and professional wellbeing. Thank you also to the faculty, staff, and fellow students of the Pontificia Universidad Católica de Chile and the University of Notre Dame; your support has been vital during this dual Ph.D. program.

I want to thank my father Diego, my mother María del Carmen, my sister Daniela, my brother Sebastián, and my girlfriend Yadira for their unconditional support. Thank you all for encouraging me to follow my dreams, even when those dreams took me far away from home. In particular, I am incredibly grateful to you Sebastián, for our insightful conversations and your advice and help during the completion of my degree; and to you, Yadira, for your love and patience, especially while we were far apart.

Finally, I would like to thank the financial support of ANID Doctorado Nacional 2017 Folio 21171563, ANID/FONDAP/15110017 (Research Center for Integrated Disaster Risk Management, CIGIDEN), ANID / FONDECYT 1171062, and the Department of Civil and Environmental Engineering and Earth Sciences of the University of Notre Dame

GUIDELINES FOR NUMERICAL SEISMIC ANALYSIS OF REINFORCED CONCRETE AXIAL-FLEXURAL ELEMENTS

Abstract

by

Juan Diego Pozo Ocampo

In this dissertation, the capability of different distributed plasticity numerical models to simulate the seismic behavior of reinforced concrete (RC) axial-flexural elements, namely planar walls and square columns, is evaluated based on previous experimental results of isolated wall and column test specimens as a well as a 7-story wall building subassembly. Greater emphasis is placed on slender (flexure-dominant) structures with softening post-peak behavior (due to concrete crushing with or without rebar buckling) since this type of behavior has been commonly observed during experimental tests and after earthquakes and its prediction can be highly sensitive to the mesh size used in numerical modeling.

Results obtained in this dissertation include: 1) modeling recommendations to simulate the cyclic global lateral force-displacement (F-D) behavior of slender and squat RC walls, including a consistent mesh-sensitivity investigation; 2) a new metric to quantitatively evaluate simulated hysteretic F-D curves as compared with measured curves; 3) plastic hinge integration models that use material regularization (i.e., regularized plastic

hinge models) to accurately simulate and obtain objective (i.e., mesh-independent) global and local (i.e., material strains and section curvatures) behaviors of slender planar RC walls and square columns; 4) a new confined concrete crushing energy equation for regularized constitutive models to simulate RC columns through failure; and 5) quantification of variability in simulated dynamic seismic performance of RC wall structures from different distributed plasticity models.

The results of this investigation are intended to improve current numerical modeling guidelines for practitioners conducting nonlinear analysis of axial-flexural RC walls and columns as part of performance-based seismic design. The results are also aimed for researchers conducting detailed analysis to predict global and local wall and column behaviors under seismic loading.

CONTENTS

FIGURES

TABLES

CHAPTER 1:

INTRODUCTION

1.1 Motivation

Reinforced concrete (RC) axial-flexural elements (i.e., walls and columns) are often used in building structures to resist seismic loads due to their high lateral strength and deformation capacity. Current seismic design practices for these structures use linear models and capacity principles following prescriptive building codes. However, this traditional design approach cannot adequately predict the seismic performance and the amount of damage of the structure. Examples of recent damage in RC buildings were observed after the 2010 Chile, the 2011 New Zealand, and the 2017 Mexico earthquakes (Jara et al., 2020; R. Jünemann et al., 2015; Kam et al., 2011; Wallace et al., 2012). As a result, the performance-based seismic design (PBSD) procedure is desirable to explicitly evaluate the structural performance of buildings and obtain safer designs (Bozorgnia & Bertero, 2004).

To implement PBSD for a building, accurate, effective, and robust nonlinear numerical models are needed to simulate the cyclic seismic behavior of its structural components. Because it is not simple to simulate the seismic behavior of a RC structure, several documents with nonlinear modeling recommendations (ACI 318, 2014; ASCE 41, 2017; LATBSDC, 2017; NIST, 2017c; PEER/ATC, 2010; TBI, 2017) for use in PBSD

have been published. These recommendations are available mainly for lumped plasticity models (Figure 1.1a), even though the nonlinear behavior of RC elements can also be simulated with other numerical models, as presented in Figure 1.1.

Lumped plasticity models (LPMs) concentrate the nonlinear behavior of an element at its ends (i.e., at concentrated plastic hinges), while the remaining (inner) portion of the element is considered to remain elastic. LPMs employ predefined nonlinear response (e.g., moment-rotation) relationships at the element ends, calibrated to simulate the overall element behavior. LPMs are computationally efficient, robust, and relatively simple to implement, however, these models cannot account for the effect of variations in axial load during the analysis and there is no standardized guidance for its behavior under cyclic loading (ASCE 41, 2017).

Finite length plasticity models (FLPMs), presented in Figure 1.1b, concentrate the nonlinear axial-flexural behavior in a finite length of the element at its ends, while the remaining (inner) portion of the element is considered to remain linear-elastic. The nonlinear behavior is based on fiber sections that use uniaxial material stress-strain relationships. Therefore, axial-flexural interaction due to variations in axial load can be captured during the analysis, and the cyclic behavior is simulated through material cyclic stress-strain relationships. However, the inner portion of the element cannot account for changes in stiffness due to cracking, and the shear behavior is uncoupled from the axial-flexural interaction in this model.

Distributed plasticity models (DPMs) are also based on fiber sections, but these models allow the nonlinear axial-flexural behavior to develop along the entire length of the

element, as presented in Figure 1.1c. Therefore, simulation of cyclic axial-flexural interaction as well as cracking along the entire element is considered during the analysis. Additionally, depending on the element formulation, the shear behavior can be coupled or uncoupled with axial-flexural interaction.

Finally, finite element models (FEMs), presented in Figure 1.1d, can represent the nonlinear behavior of a structure by simulating its response at the continuum level. These models can account for nonlinear, coupled axial-shear-flexural interaction, including multiaxial stress-strain relationships. However, FEMs are generally impractical for PBSD due to their high computational cost and complexities involved in building and running the models, and interpreting the results.

Among the different available nonlinear models, the use of distributed plasticity models (Figure 1.1c) has become more common among researchers to evaluate the seismic behavior of RC structures due to their stability, accuracy, and modest computational cost (Jiang & Kurama, 2010; Kristijan Kolozvari, Orakcal, et al., 2015a; Yuan Lu et al., 2016; Orakcal et al., 2004; Pugh et al., 2015; Jorge A. Vásquez et al., 2016; Wu et al., 2017). However, the ultimate (i.e., failure) displacement is highly mesh sensitive when simulating RC elements with softening post-peak behavior (due to concrete crushing with or without rebar buckling) (Coleman & Spacone, 2001; L. Lowes et al., 2016; Pugh et al., 2015; Jorge A. Vásquez et al., 2016). Furthermore, different distributed plasticity models are available for simulating the nonlinear behavior of RC elements (Jiang & Kurama, 2010; Kristijan Kolozvari, Orakcal, et al., 2015a; Yuan Lu et al., 2016; Orakcal et al., 2004; Pugh et al.,

2015; Jorge A. Vásquez et al., 2016; Wu et al., 2017), with different assumptions involved in their formulations.

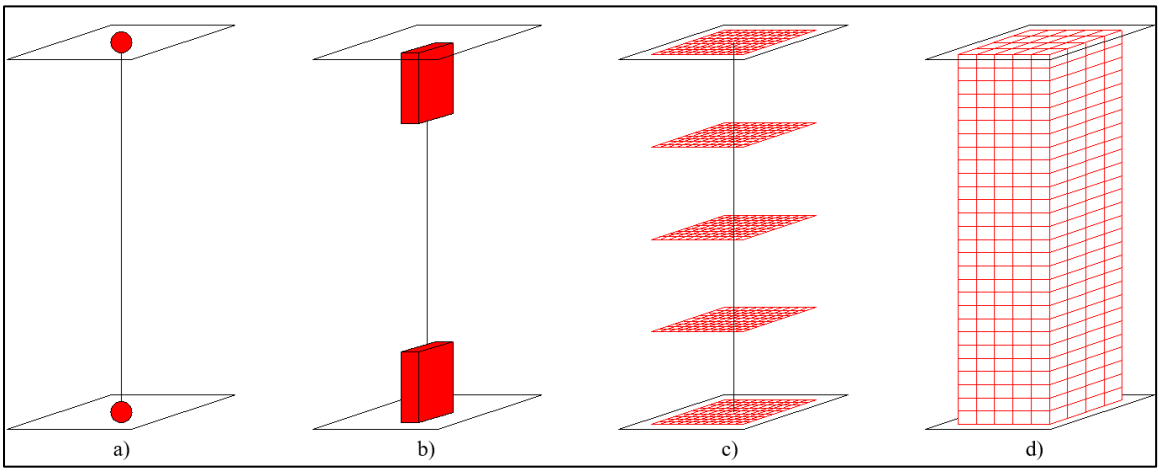

Figure 1.1: Types of nonlinear models: a) Lumped plasticity model (LPM); b) finite length plasticity model (FLPM); c) distributed plasticity model (DPM); d) finite element model (FEM). Based on NIST (2017b).

1.2 Objectives

Motivated by the recent increase in performance-based seismic design and by the current limitations of distributed plasticity models, it behooves to elucidate the following issues: Is it possible to provide reliable modeling guidelines for distributed plasticity models to simulate the cyclic behavior of RC elements? Is it possible to extrapolate these guidelines to simulate RC buildings? Is the seismic performance obtained with different models equivalent? To answer these questions, the primary objective of this research is to evaluate and provide guidelines for the nonlinear seismic analysis of axial-flexural RC elements using distributed plasticity models. To this end, the specific research objectives are to:

1. Evaluate existing nonlinear modeling approaches for isolated planar RC walls and provide modeling recommendations to accurately predict their global cyclic lateral force-displacement behavior based on previously tested wall specimens.
2. Develop a regularized plastic hinge modeling approach to simulate both the global and local cyclic behaviors of slender isolated RC walls and columns.
3. Evaluate wall modeling approaches based on comparisons with previous shake-table test measurements of a 7-story wall building subassembly.
4. Quantify the variability in the predicted dynamic seismic performance of RC wall buildings obtained by different nonlinear models.

The results of this investigation are intended to improve current modeling guidelines for practitioners conducting nonlinear analysis of axial-flexural RC walls and columns as part of performance-based seismic design. The results are also aimed for researchers conducting detailed analysis to predict global and local wall and column behaviors under seismic loading.

1.3 Scope

Among the different geometrical configurations and failure mode of RC walls and columns, the scope of this investigation is as follows:

- The focus of the research is mainly on slender planar isolated RC walls with shear span-to-depth ratios, $M/(VL_w) \geq 2.0$ and with axial-flexural compression-controlled failure modes. However, four planar squat walls are also studied in Chapter 2 to evaluate the benefits of axial-shear-flexural coupled models to simulate shear-dominant failure modes.

- The experimental columns used in this investigation are slender (shear span-to-depth ratio, $M/(VH) \geq 2.0$) and have square cross-sections.
- The investigation on regularized plastic hinge models is focused on elements with softening post-peak behavior due to concrete crushing with or without bar buckling.
- The research is limited to in-plane lateral loads combined with gravity loads.

More details about the geometry, materials, reinforcement ratios, and axial loads used in the investigation can be found in each chapter of this document.

1.4 Outline

This document is written in the format of four independent journal articles, where each chapter is a self-contained paper that has been published or is currently in the process of being peer-reviewed. As such, the remaining chapters of this document are organized as follows:

Chapter 2 aims to evaluate existing nonlinear modeling approaches and provide modeling recommendations to accurately simulate the global cyclic lateral force-displacement (F-D) behavior of slender and squat isolated planar RC walls, which is the first specific objective of this research. To this end, the capabilities of four different distributed plasticity macro-models to predict the global F-D behaviors of four slender and four squat, previously tested, planar wall specimens are quantitatively evaluated. This chapter includes detailed information on all the material and modeling parameters required by the different models, and an evaluation of the sensitivity of the F-D curves to different wall model discretizations applied consistently among the models. Additionally, a new

quantitative approach is proposed to assess the hysteretic F-D behaviors predicted by the numerical models.

Chapter 3 focuses on the development and evaluation of a regularized plastic hinge modeling approach to simulate the global and local behaviors of slender planar RC walls, which is part of the second specific objective of this research. Material regularization has been used to obtain objective global F-D responses of RC elements, however, subsequent normalization of the section curvatures based on an assumed plastic hinge length is required to obtain objective local responses, resulting in a two-step analysis process. Therefore, in this chapter, combination of the plastic hinge modeling concept with the material regularization concept is proposed and evaluated to result in a one-step analysis procedure. The proposed model allows the ability to obtain accurate and objective global and local responses, with no need for a separate curvature normalization step. Analysis results from plastic hinge models considering several regularized and unregularized concrete stress-strain relationships are shown. Additionally, it is demonstrated that the proposed regularized plastic hinge model increases the accuracy of the predicted ultimate displacement, with significant reduction in mesh-sensitivity, when simulating slender planar RC walls.

Chapter 4 addresses the part of the second specific objective of this research pertaining to slender columns. The accuracy of simulating the global and local behaviors of slender square RC columns is evaluated using plastic hinge models with unregularized and regularized concrete stress-strain relationships. A new confined concrete crushing energy equation for the regularization of the post-peak stress-strain relationship is proposed

to reduce model mesh-sensitivity in predicting the ultimate displacement of RC columns, showing accurate results when compared with available test data.

Chapter 5 aims to (1) evaluate wall modeling approaches based on comparisons with available measurements from shake-table tests, which is the third specific objective of this research, and (2) quantify the variability in the dynamic performance of slender reinforced concrete wall buildings simulated using different numerical modeling approaches, which is the fourth specific objective of this research. For these two objectives, fiber-based two-node line-element models (e.g., FLPM and DPM) are considered. The models use the same material constitutive relationships and other analysis inputs (e.g., damping) so that the quantified variability in the building performance is caused by the numerical modeling approach rather than user-selected parameters. First, the model results are evaluated against the measured shake-table behavior of a 7-story RC wall building tested at the University of California, San Diego. Then, nonlinear dynamic analyses of the 7-story wall test specimen and three RC wall archetype buildings of 4-, 8-, and 12-stories are conducted to quantify the variability in selected seismic performance assessment parameters. Based on the results, it is strongly recommended that the performance assessment of slender RC wall buildings be done using global response parameters rather than local response parameters, since the variability of the predicted response among the nonlinear models was significantly smaller for global response parameters.

Finally, Chapter 6 summarizes the findings and conclusions from this dissertation and outlines future work identified based on this research.

CHAPTER 2:

QUANTITATIVE ASSESSMENT OF NONLINEAR MACRO-MODELS FOR GLOBAL LATERAL LOAD BEHAVIOR AND DESIGN OF PLANAR RC WALLS

In this chapter, two shear-uncoupled and two shear-coupled distributed plasticity macro-models are evaluated to address the first specific objective of this research. The chapter presents detailed information on the modeling parameters used to simulate the cyclic global lateral force-displacement (F-D) behaviors of eight planar RC walls with flexure-dominant as well as shear-dominant behaviors. The chapter also presents a sensitivity analysis of the F-D curves to different wall model discretizations applied consistently between the models, and proposes a new quantitative approach to assess the hysteretic behaviors predicted by the models. Examples of modeling input files are presented in Appendix A.

2.1 Introduction

In Chile, US, New Zealand, Japan, Colombia, and many other countries located in high seismicity areas, reinforced concrete (RC) walls are often used in buildings to resist seismic loads due to their high lateral stiffness, strength, and deformation capacity. The majority of these buildings are designed using linear models and a capacity design procedure. However, this traditional design approach cannot predict the seismic

performance or the amount of damage of RC wall buildings adequately. Examples of recent damage in such buildings were observed after the 2010 Chile and the 2011 New Zealand earthquakes (R. Jünemann et al., 2015; Kam et al., 2011; Wallace et al., 2012). As a result, the Performance-Based Seismic Design (PBSD) procedure is desirable to explicitly evaluate the performance of buildings and obtain safer designs (Bozorgnia & Bertero, 2004).

To implement PBSD in a RC structural wall building, accurate, effective, and robust nonlinear numerical models are needed to simulate its seismic behavior. Hence, several standards with recommendations to develop nonlinear models and to evaluate the seismic performance of buildings have been published for conducting PBSD (ACI 318, 2014; ASCE 41, 2017; LATBSDC, 2017; NIST, 2017c; PEER/ATC, 2010; TBI, 2017). The recommendations for RC walls are mainly focused on lumped plasticity models. However, several alternate modeling techniques for estimating the nonlinear response of RC walls have also been developed (Feng et al., 2018; Fischinger et al., 2012; Jalali & Dashti, 2010; Jiang & Kurama, 2010; Rosita Jünemann et al., 2016; Kristijan Kolozvari, Orakcal, et al., 2015a; X. Lu et al., 2015; Yuan Lu et al., 2016; Massone et al., 2009; Orakcal et al., 2004; Rojas et al., 2016; Jorge A. Vásquez et al., 2016).

Numerical modeling approaches for the nonlinear cyclic response of RC walls can be divided into two groups: 1) micro-modeling approaches; and 2) macro-modeling approaches. Micro-modeling approaches are based on finite elements and can estimate detailed responses of RC walls. However, due to their high computational cost and complexities involved in the interpretation of the results, micro-models are generally

impractical for PBSD (Almeida et al., 2016; Jalali & Dashti, 2010; Wu et al., 2017). In comparison, macro-models are more computationally efficient and can still accurately predict the hysteretic response of RC walls. These latter models can be further classified into two groups: i) shear-uncoupled models, with axial-flexural interaction and independent shear behavior; and ii) shear-coupled models, with axial-shear-flexural interaction. Because macro-models are faster and simpler to implement than micro-models, macro-models are more appealing for predicting the seismic response of structural walls in engineering practice.

Although macro-models are attractive for PBSD, their assumptions and modeling parameters should be understood to select an appropriate model. Additionally, the predicted responses are sensitive to the input parameters, thus generating confusion and difficulties for practical applications. Several researchers have investigated the performance of different macro-models by simulating the behavior of experimentally tested RC walls. A brief overview of some of these investigations is provided below.

Orakcal et al. (2006) modified the shear-uncoupled Multiple-Vertical-Line-Element-Model (MVLEM) proposed by Vulcano et al. (1988) by implementing refined constitutive relations for the concrete and reinforcing steel materials. The model was validated by simulating the cyclic response of slender walls, where material stress-strain relationships were calibrated to represent the experimentally measured properties. Additionally, the sensitivity of the model response to the material and model parameters was studied.

Kolozvari et al. (2015) improved the MVLEM model to include shear and flexure coupled behavior of RC walls. The proposed model, called Shear-Flexure Interaction MVLEM (SFI-MVLEM), was validated against experimental results from RC walls with shear span-to-depth ratios $M/(VL_w)$ of 1.5 and 2.0. The results were found to be sensitive to modeling parameters, which needed to be calibrated for reliable prediction of nonlinear wall behaviors.

Pugh et al. (2015) investigated force-based fiber-element models to capture the behavior of slender walls and their failure mechanism. The concrete material parameters were based on the compressive strength, while parameters to define the steel material model were taken from experimentally-reported material properties. The study concluded that regularization of the post-peak concrete compressive behavior is needed to obtain accurate and mesh-objective simulations of slender RC walls. For this purpose, equations to obtain the concrete crushing energy to regularize confined and unconfined concrete models in compression were recommended. These equations were adopted by the Applied Technology Council (NIST, 2017c).

Lowes et al. (2016) studied the shear wall model available in PERFORM 3D software to analyze slender RC walls. Recommendations of modeling parameters for unconfined concrete, confined concrete, and reinforcing steel were provided, as well as regularization recommendations to define the post-peak compressive stress-strain behavior of concrete.

Lu et al. (2016) modified the Beam Truss Model (BMT) (Yuan Lu & Panagiotou, 2014; Panagiotou et al., 2012) and simulated the response of tested walls that experienced

both shear dominated and flexure dominated failures. The effects of different model parameters were evaluated and recommendations were developed about the angle of the diagonal elements, in-plane flexural rigidity of the vertical elements, and tensile strength of concrete in the horizontal elements. The material properties used in the models were based on the reported material properties for the simulated walls.

Kolozvari et al. (2018) provided a state-of-the-art review of five RC wall macro-models. Although the study provided extensive descriptions and simulation capabilities of the numerical models for the global and local responses of tested walls with different characteristics, a detailed description of the modeling parameters required to generate each model was not presented.

2.2 Scope, Objectives, and Original Contributions

Overall, previous investigations have shown the capabilities of a variety of macro-models to simulate the nonlinear response of RC walls. The scope of this chapter is a further contribution on this topic by targeting and addressing the following gaps from previous research:

1. Mesh-sensitivity analyses have been performed using few walls and few mesh discretizations that are not consistently applied among the different models.
2. Effectiveness of the numerical simulations has been quantitatively evaluated based on the effective stiffness, maximum strength, and ultimate displacement. However, these parameters are based on the envelope of F-D curves and do not evaluate the hysteretic behavior (i.e., pinching, reloading and unloading stiffness, cyclic energy dissipation).

The hysteretic behavior has often been evaluated qualitatively by visual comparison of the predicted and experimental cyclic F-D curves.

In accordance with these gaps, and considering that global quantities related to the F-D behavior, such as the effective drift and story drift, are used as engineering demand parameters (EDPs) to assess the performance of slender and squat RC walls, respectively, according to FEMA P-58 (2018 edition) (FEMA, 2018), this study focuses on the nonlinear modeling of the global F-D behavior of planar RC walls with the following specific objectives: 1) provide detailed information on the modeling parameters used to simulate the cyclic global F-D behaviors of a set of planar RC walls with flexure-dominant as well as shear-dominant responses, 2) evaluate the sensitivity of the F-D curves to different wall model discretizations applied consistently between the different models, and 3) propose, validate, and use a new quantitative approach to assess the hysteretic behaviors predicted by the numerical models.

Two shear-uncoupled macro-models and two shear-coupled macro-models are used to simulate the measured behaviors of eight previously-tested planar walls with different shear span-to-depth ratios $M/(VL_w)$, axial loads (N), and amount of reinforcement. All of the modeling parameters are defined using only the concrete compression strength (f_c'), reinforcing steel yield strength (f_y), geometry of the wall, and reinforcement layout. This information is commonly available or can be estimated during PBSD. Importantly, the models do not include any calibration of the material stress-strain curves to measured behaviors.

In order to provide quantitative evaluations of the predicted hysteretic F-D behaviors, the Modified Nash-Sutcliffe Efficiency (NSE_m) metric is developed, validated, and used. Additionally, the predicted results from the consistently varied model discretizations are evaluated based on the effective stiffness (K_e), maximum strength (V_{max}), and ultimate displacement (δ_u). Finally, a comparison of the computing times using the different models is presented, as well as comparisons of the local behavior of a flexure-dominated wall. Results from this investigation are expected to be used in engineering practice for conducting PBSD of RC wall buildings.

2.3 Experimental Walls

An experimental data set of eight previously tested planar RC walls were used to evaluate the numerical models. The selection of these specimens was based on the following criteria:

- Rectangular wall cross-section shape subjected to in-plane loads.
- Available data on concrete compressive strength, reinforcing steel yield strength, specimen geometry, reinforcement layout, axial load applied to the wall, and boundary conditions in the laboratory.
- Available data on the global force-displacement response and the observed failure mechanism of each wall to evaluate the simulation results.
- The data set is presented in Table 2.1, including the following information:
- $L_w =$ wall length.
- $L_w/t_w =$ cross-sectional aspect ratio, where t_w is the wall thickness.

- $M/(VL_w) =$ shear span-to-depth ratio, where M and V are the moment and shear developed at the base of the wall, respectively. For the selected wall specimens, the shear span-to-depth ratio is equal to the vertical aspect ratio from the base of the wall to the point of load application (H/L_w).
- $N/(A_g f_c') =$ axial load ratio, where N is the axial load applied to the wall, A_g is the gross cross-section area of the wall, and f_c' is the concrete compressive strength.
- $f_c' =$ concrete compressive strength.
- $f_{y_{be}} =$ yield strength of longitudinal reinforcement in boundary regions.
- $\rho_{be} =$ longitudinal reinforcement ratio at the wall boundary regions, computed using a length that includes concrete cover on each side of the boundary bars (ACI 318, 2014).
- $\rho_v =$ distributed vertical web reinforcement ratio calculated based on the remaining wall length and reinforcement.
- $\rho_h =$ distributed horizontal web reinforcement ratio.
- $V_n =$ nominal shear strength of the wall determined using ACI 318 (2014).
- $M_n =$ nominal moment strength of the wall determined using ACI 318 (2014).
- $(V@M_n)/V_n =$ ratio of the lateral load corresponding to the nominal moment strength ($V@M_n$) over the nominal shear strength of the wall.
- Failure mode indicating the mechanism causing loss of lateral load carrying capacity as follows: concrete crushing and buckling of longitudinal steel (CB), diagonal compression failure (DC), diagonal tension failure (DT), and sliding shear failure (SS).

The database contains walls with different shear span-to-depth ratios, axial load ratios, reinforcement ratios, and failure modes. The eight considered walls were cyclically

tested as cantilever structures with a lateral load applied at the top of each wall. All walls were tested until failure, apart from wall M1, which was tested up to a target drift ratio of 2% (Amón, 2018). Walls RW1, RW2, M1, and WSH6 with shear span-to-depth ratios greater than 2.0 exhibited flexural dominated behaviors, whereas walls S78, WSL5, LSW1 and LSW2 with shear span-to-depth ratios less than 2.0 showed shear dominated behaviors. All walls, except for wall WSL5, had $(V@M_n)/V_n$ ratios less than one, implying that the maximum strength should be controlled by flexural behavior. More information about the walls can be found in the references listed in Table 2.1. Note that M_n and V_n in Table 2.1 correspond to the calculated nominal moment and shear strength, respectively, and not to experimental values.

Table 2.1: Experimental data set

Wall ID	Reference	L_w (mm)	$\frac{L_w}{t_w}$	$\frac{M}{VL_w}$	$\frac{N}{A_g f_c'}$ (%)	f_c' (MPa)	$f_{y_{be}}$ (MPa)	ρ_{be} (%)	ρ_v (%)	ρ_h (%)	V_n (kN)	M_n (kN-m)	$\frac{V@M_n}{V_n}$	Failure Mode
RW1	(Thomsen & Wallace, 1995)	1219	12.0	3.13	10.0	31.6	434.5	2.95	0.30	0.33	300	515	0.45	CB
RW2	(Thomsen & Wallace, 1995)	1219	12.0	3.13	7.0	42.8	434.5	2.95	0.30	0.33	319	521	0.43	CB
M1	(Amón, 2018)	900	6.0	2.50	10.0	23.3	482.5	2.15[2]	0.32	0.25	274	330	0.54	-
WSH6	(Dazio et al., 2009)	2000	13.3	2.26	10.8	45.6	576.0	1.74	0.50	0.25	736	2366	0.71	CB
S78[1]	(Tran & Wallace, 2012)	1219	8.0	1.50	6.4	55.8	475.0	6.04	0.70	0.74	953	1475	0.85	DC
WSL5	(Hube et al., 2017)	1600	16.0	1.09	0.0	28.9	446.0	9.28	0.23	0.20	359	895	1.43	DT
LSW1	(Salonikios et al., 1999)	1200	12.0	1.00	0.0	22.2	585.0	1.68	0.55	0.52	514	351	0.57	SS
LSW2	(Salonikios et al., 1999)	1200	12.0	1.00	0.0	21.6	585.0	1.26	0.27	0.28	342	246	0.60	SS

[1] Refers to wall RW-A15-P10-S78

[2] Wall M1 did not include transverse reinforcement at boundary regions

2.4 Description of Numerical Models

The wall test specimens described above were modeled using the uncoupled macro-model shear wall element in PERFORM 3D (CSI, 2018), and three macro-models available in OpenSees (McKenna et al., 2000), namely the uncoupled Multiple-Vertical-Line-Element-Model (MVLEM) (Kristijan Kolozvari et al., 2018; Orakcal et al., 2004, 2006; Orakcal & Wallace, 2006), the coupled Shear-Flexure Interaction MVLEM (SFI-MVLEM) (Kristijan Kolozvari, 2013; Kristijan Kolozvari et al., 2018; Kristijan Kolozvari, Orakcal, et al., 2015a, 2015b; Kristijan Kolozvari, Tran, et al., 2015), and the coupled Beam Truss Model (BTM) (Yuan Lu et al., 2016; Yuan Lu & Panagiotou, 2014; Panagiotou et al., 2012). These models, shown in Figure 2.1, are summarized in this section.

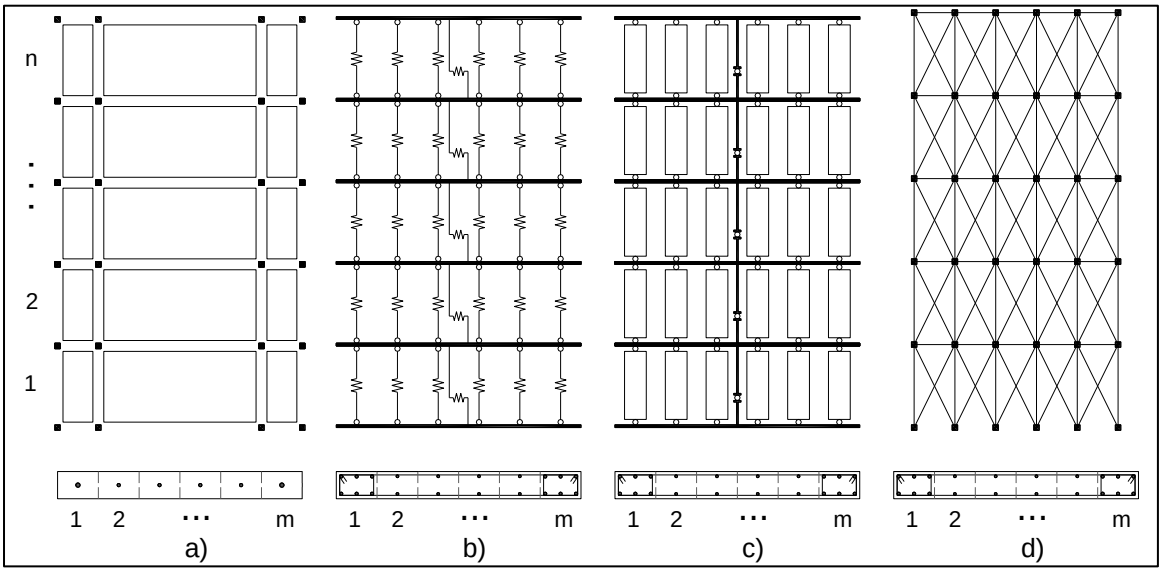

Figure 2.1: Numerical models using: a) PERFORM 3D; b) MVLEM; c) SFI-MVLEM; d) BTM.

2.4.1 PERFORM 3D

The shear wall element in PERFORM 3D is a fiber-based element with four nodes and six degrees of freedom at each node. This is an uncoupled element in which shear behavior can be added with a force-deformation rule. The longitudinal (vertical) in-plane behavior of the shear wall element is governed by a nonlinear fiber section, while the shear behaviors is assumed to be linear-elastic. In this study, a total of m pairs of fibers (each pair consisting of one concrete fiber and one reinforcing steel fiber) were used along the wall length to model a RC wall as shown in Figure 2.1a. The horizontal length of the boundary region at each end of the wall was modeled with one shear wall element with a single pair of fibers. The central region of the wall was modeled with a central shear wall element with equally distributed $m - 2$ pairs of fibers. The shear wall element assumes constant axial strain, shear strain, and curvature along its length (i.e., wall height direction). Therefore, n sets of three shear wall elements were stacked over the wall height to capture the nonlinear behavior of the wall.

2.4.2 Multiple Vertical Line Element Model (MVLEM)

As shown in Figure 2.1b, the MVLEM model of each RC wall consisted of n two-node MVLEM elements over the height. MVLEM is a fiber-based element with three degrees of freedom at each node. Each MVLEM element had m pairs (one for concrete and one for reinforcing steel) of uniaxial springs to represent the axial-flexural behavior of the wall, and one horizontal spring located at a height ch from the bottom node to simulate the shear behavior. The uniaxial and shear springs were rigidly constrained together at each end of the MVLEM element. The uniaxial springs were governed by the uniaxial nonlinear

strain-stress relationships for concrete and steel, while the uncoupled shear behavior was defined by a force-deformation rule for the shear spring.

2.4.3 Shear-Flexure Interaction Model (SFI-MVLEM)

The SFI-MVLEM model is based on the MVLEM formulation, but each pair of uniaxial springs is replaced with a RC panel subjected to membrane action (Figure 2.1c) to achieve coupled nonlinear axial-flexure-shear interaction. The behavior of the panel is described using a 2D constitutive RC formulation based on the fixed-strut-angle-model (FSAM) to relate the imposed strain field ($\varepsilon_x, \varepsilon_y, \gamma_{xy}$) to the resulting stress field ($\sigma_x, \sigma_y, \tau_{xy}$) (Ulegtekin, 2010). This formulation couples the axial and shear responses at the panel level, while the coupling of flexural and shear responses is accounted for at the element level. Shear aggregate interlock across cracks is modeled using a parameter η, which is a concrete friction coefficient to define a bilinear constitutive law for aggregate interlock. Additionally, the stiffness parameter α is used to define a linear-elastic model with stiffness αE_s (where, E_s is the Young's modulus of steel) to simulate the dowel action in the reinforcing bars. The compression softening of concrete according to Vecchio and Collins (1986) and the biaxial damage on concrete according to Mansour and Hsu (2005) are considered in the concrete material behavior.

2.4.4 Beam Truss Model (BTM)

Different from the three models presented above, the Beam-Truss-Model (BTM) is based on the strut-and-tie approach, where the RC wall is discretized using force-based beam-column elements and diagonal nonlinear truss elements (Figure 2.1d). The diagonal

truss elements use a biaxial material model for the concrete, which accounts for compression softening and captures shear resistance and axial-shear-flexure coupling (Yuan Lu et al., 2016). In this study, the vertical elements at the ends of each wall were modeled using force-based beam-column elements with two Gauss-Lobatto integration points, while the diagonal elements were modeled using nonlinear four-node truss elements (termed as *truss2* in OpenSees). The interior vertical and horizontal elements each consisted of two nonlinear two-node truss elements in parallel to account for the concrete and steel behavior.

The Beam-Truss-Model is sensitive to the angle of the diagonal elements; and thus, equations have been proposed to calculate a recommended angle (Yuan Lu et al., 2016; Moharrami et al., 2014). Defining the lengths of the horizontal and vertical elements as L_h and L_v, respectively, for a given discretization of n and m (refer to Figure 2.1d), the resulting angle of the diagonal elements is $\theta_d = \tan^{-1}(L_v/L_h)$. The discretization n and m of a wall in height and length can be selected to satisfy the recommended angle of the diagonal elements; however, a constant value over the height is not always possible because of wall geometry constraints (e.g., $H = \sum L_v$). In such cases, at least one vertical element will have a different length in order for the model height to match the wall height, resulting in a different angle for the diagonal elements in that row. Alternatively, the values of n and m could be selected to result in a constant angle as close as possible to (but not exactly the same as) the recommended angle, while also satisfying the wall geometry constraints. In this study, this constant angle approach was used as it is more appealing for practical purposes.

2.5 Modeling Parameters

For assessing the seismic behavior of RC walls when conducting PBSD, detailed information about materials or the wall behavior is not commonly available. Therefore, this section provides specific information to define the modeling parameters of the four aforementioned models based only on the wall geometry, reinforcement layout, concrete compression strength, and steel yield strength. Table 2.2 presents the stress-strain models used for the concrete and reinforcing steel materials in the different numerical models. As described in further detail in the following sub-sections, the material stress-strain relationships in PERFORM 3D are piecewise linear, while the relationships in the other models use curved envelopes. Importantly, the concrete and reinforcing steel stress-strain behaviors used for the wall models in this chapter were not calibrated with experimental test results so as to generate modeling guidelines suitable for the design of RC walls. The modeling parameters used for wall WSH6 discretizations in Figure 2.10 a4-d4 are summarized in Table 2.3 for the four models. The procedures to obtain these values, described in the following sub-sections, were also used to determine the modeling parameters for the other walls and discretizations analyzed. The MVLEM, SFI-MVLEM, and BTM OpenSees input files for wall WSH6 are presented in Appendix A.

Table 2.2: Material stress-strain relationship

Material model	Stress-strain relationship		Reference
Inelastic Concrete 1D	Piecewise linear defined using the "YULRX" model		(CSI, 2018)
ConcreteCM	$y(x) = \frac{nx}{1 + \left(n - \frac{r_c}{r_c - 1}\right)x + \frac{x^{r_c}}{r_c - 1}}$	$x \le x_{cr}^{-}$	(Kristijan Kolozvari et al., 2018)
	$y(x) = y(x_{cr}^{-}) + \frac{dy}{dx}(x_{cr}^{-})(x - x_{cr}^{-}) \ge 0$	$x > x_{cr}^{-}$	
ConcretewBeta	$f_c(\varepsilon) = E_c\varepsilon + \frac{f_c' - E_c\varepsilon_c}{\varepsilon_c^2}\varepsilon^2$	$\varepsilon \le \varepsilon_c$	(Yuan Lu & Panagiotou, 2014)
	$f_c(\varepsilon) = \frac{f_c' - f_{cc}'}{(\varepsilon_c - \varepsilon_{cc})^3}(\varepsilon - \varepsilon_{cc})^3 + f_{cc}'$	$\varepsilon_c < \varepsilon \le \varepsilon_{cc}$	
	$f_c(\varepsilon) = f_{cc}' + E_{des}(\varepsilon - \varepsilon_{cc}) \ge 0$	$\varepsilon > \varepsilon_{cc}$	
Inelastic Steel Material Non-Buckling	Piecewise linear defined using the "YULRX" model		(CSI, 2018)
SteelMPF	$f_s^*(\varepsilon^*) = b\varepsilon^* + \frac{(1-b)\varepsilon^*}{\left(1 + \varepsilon^{*R}\right)^{1/R}}$		(Kristijan Kolozvari et al., 2018)
Steel02	$f_s^*(\varepsilon^*) = b\varepsilon^* + \frac{(1-b)\varepsilon^*}{\left(1 + \varepsilon^{*R}\right)^{1/R}}$		(Filippou et al., 1983)

Table 2.3: Modeling parameters for wall WSH6

Steel Parameters

PERFORM 3D[a] m=4, n=20					MVLEM[a,b] m=4, n=11		SFI-MVLEM[b,c] m=4, n=6		BTM m=8, n=11	
Inelastic Steel Material, Non-Buckling					*SteelMPF*		*SteelMPF*		*Steel02*	
	Tension		Compression							
	D	F (MPa)	D	F (MPa)						
Y	0.00288	576	0.00288	576	$f_{y_{be}}$[d] (MPa)	576	$f_{y_{be}}$[d] (MPa)	576	$f_{y_{be}}$ (MPa)	576
U	0.07776	876	0.03162	691	E_s (MPa)	200000	E_s (MPa)	200000	E_s (MPa)	200000
L	0.08064	876	0.03450	691	b[d]	0.02	b[d]	0.02	b	0.02
R	0.08352	0.88	0.08352	0.7	R_0	20	R_0	20	R_0	20
X	0.12528	0.88	0.12528	0.7	cR_1	0.925	cR_1	0.925	cR_1	0.925
FR/FU		0.001		0.001	cR_2	0.15	cR_2	0.15	cR_2	0.15
E_s(MPa)	200000		200000							

Concrete Parameters

Inelastic 1D Concrete Material					*ConcreteCM*		*ConcreteCM*		*ConcretewBeta*				
	Unconfined		Confined		Unconfined		Unconfined			Diagonal[e]	Horizontal[e]	Vertical	Confined
	D	F (MPa)	D	F (MPa)	f_c' (MPa)	45.6	f_c' (MPa)	45.6	f_c' (MPa)	45.6	45.6	45.6	45.6
Y	0.00108	34.2	0.00137	43.6	ε_c	0.00226	ε_c	0.00226	ε_c	0.00200	0.00200	0.00200	0.00200
U	0.00200	45.6	0.00400	58.1	E_c (MPa)	34350	E_c (MPa)	34350	$f_{c_{int}}$ (MPa)	22.8	22.8	22.8	29.1
L	0.00202	45.6	0.00404	58.1	r_c	6.87	r_c	6.87	$\varepsilon_{c_{int}}$	0.00439	0.00555	0.00383	0.00949
R	0.01826	0.05	0.03162	0.06	x_{cr}^-	1.065	x_{cr}^-	1.143	f_u (MPa)	0.001	0.001	0.001	0.001
X	0.02739	0.05	0.04743	0.06	f_t (MPa)	2.09	f_t (MPa)	2.09	ε_u	0.00677	0.00911	0.00566	0.01423
FR/FU		0.001		0.001	ε_t	0.00008	ε_t	0.00008	f_t (MPa)	0.001	0.001	2.23	2.23
E_c (MPa)	31738		31738		r_t	1.20	r_t	1.20	$f_{t_{int}}$ (MPa)	0.001	0.001	0.001[h]	0.001[h]
					x_{cr}^+	10000	x_{cr}^+	10000	$\varepsilon_{t_{int}}$	0.00040	0.00040	0.00040[h]	0.00040[h]
					GapClose[f]		GapClose[f]		$f_{t_{res}}$ (MPa)	0.001	0.001	0.001[h]	0.001[h]
					Confined[g]		**Confined[g]**		$\varepsilon_{t_{res}}$	0.00080	0.00080	0.00080[h]	0.00080[h]
					f_{cc}' (MPa)	58.1	f_{cc}' (MPa)	58.1	α[f]	161.4	161.4	0.5	0.5
					ε_{cc}	0.00536	ε_{cc}	0.00536	β_{int}[f]	0.4	-	-	-
					r_c	9.28	r_c	9.28	$\varepsilon_{n_{int}}$[f]	0.01767	-	-	-
					x_{cr}^-	1.106	x_{cr}^-	1.216	β_{res}[f]	0.1	-	-	-
									$\varepsilon_{n_{res}}$[f]	0.07068	-	-	-
									M[f]	-	-	0.0467	0.10875
									E_c[f] (MPa)	33764	33764	33764	33764
									f_{cc}'[f] (MPa)	-	-	-	58.1
									ε_{cc}[f]	-	-	-	0.00475

[a] Also requires a material for shear behavior, which was assumed linear-elastic with effective stiffness $G_c = \left(\frac{1}{10}\right) 0.4E_c$ in this study

[b] Requires additional element parameter c, taken as 0.4 in this study

[c] Requires additional *FSAM* material parameters η and α, taken as 1.0 and 0.002, respectively, in this study

[d] Values for tension and compression

[e] Tension behavior neglected in this study

[f] Optional parameters defined in this study

[g] Same values as for unconfined concrete except for parameters listed below

[h] Dummy values when parameter M is defined

2.5.1 PERFORM 3D

Concrete and reinforcing steel stress-strain envelopes were modeled using the "YULRX" cyclic degradation model with strength loss. The YULRX model is based on values corresponding to the yield strength (Y), ultimate strength (U), strength loss (L), residual strength (R), and maximum deformation (X) (CSI, 2018) of each material. Unconfined and confined concrete were modeled with the *Inelastic Concrete 1D* material without tension strength, which has been found to have minor effect on the global cyclic behavior of a RC wall (K Kolozvari et al., 2017). The modulus of elasticity (Young's modulus) was defined as $E_c = 4700\sqrt{f_c'}$ MPa (ACI 318, 2014), and the concrete compression envelope parameters ($FY, FU, FR/FU, DU, DL$ and DR) were defined based on the recommendations of Lowes et al. (2016). Note that in these parameters, F refers to stresses and D refers to strains. The peak strength of confined concrete was taken as $f_{cc}' = Kf_c'$, where K is the strength increase factor according to Mander et al. (1988). Zero residual strength was considered to be consistent with the confined concrete materials of the other two concrete models used in this study. Strain at residual strength of the concrete was obtained based on a crushing energy approach to reduce mesh-sensitivity of the F-D results (Coleman & Spacone, 2001; Nakamura & Higai, 2001; Pugh et al., 2015). Based on previous studies of RC walls, the crushing energy for unconfined concrete was taken as $G_{fc} = 2f_c'$ in MPa (Pugh et al., 2015) and the crushing energy for confined concrete was taken as $G_{fcc}/G_{fc} = 5(K - 0.85)$, including a lower limit of 1.0 and an upper limit of 2.5 (L. Lowes et al., 2016).

Reinforcing steel was modeled using the *Inelastic Steel Material Non-Buckling*, with the incorporation of a simple buckling model where the steel compression envelope drops after the surrounding concrete exceeds the strain corresponding to residual strength (L. Lowes et al., 2016; Pugh et al., 2015). The point of ultimate strength (DU, FU) on the steel stress-strain envelope was obtained considering a post-yield stiffness factor of $b = 0.02$ as adopted by Menegotto and Pinto (1973) and an ultimate-to-yield ratio (FU/FY) of 1.52 for A615 grade 60 steel according to Bournonville et al. (2004) (which is similar to the mean measured FU/FY ratio of 1.45 for the considered walls). An energy dissipation factor of 0.75 and a stiffness factor of 0.5 were used to capture the cyclic degradation of the steel stress-strain relationship as recommended by Lowes et al. (2016).

The shear force-deformation relationship can have a significant effect on the computed responses of RC walls (Kristijan Kolozvari & Wallace, 2016). A typical value for the uncracked shear stiffness of concrete is $G_c = 0.4E_c$ based on the assumption that the Poisson's ratio of concrete is approximately 0.2. However, the post-cracked shear stiffness is substantially less than the uncracked stiffness, and an effective value of $G_c = \frac{1}{10}0.4E_c$ was used in this study as recommended for nonlinear models in previous research (Pugh et al., 2015) and modeling guideline documents (NIST, 2017c; PEER/ATC, 2010).

2.5.2 MVLEM

Concrete response was defined using a modified Chang and Mander (1994) model, which is implemented in OpenSees as *ConcreteCM* (Kristijan Kolozvari, Orakcal, et al., 2015b). The parameters needed to define the stress-strain relationship for unconfined concrete in compression ($E_c,\ \varepsilon_c,\ r_c$) were calculated using the recommended equations by

Chang and Mander (1994) as: $E_c = 8200{f_c'}^{3/8}$, $\varepsilon_c = {f_c'}^{1/4}/1150$, and $r_c = f_c'/5.2 - 1.9$, where f_c' is in MPa. The required parameters to define the tensile behavior of concrete $(f_t, \varepsilon_t, r_t, x_{cr}^{+})$ were obtained following the recommendations of Orakcal et al. (2006) to model the tension stiffening effect, which are based on Belarbi and Hsu (1994): $f_t = 0.31\sqrt{f_c'}$ MPa, $\varepsilon_t = 0.00008$, $r_t = 1.2$, and $x_{cr}^{+} = 10000$. The peak strength of confined concrete was calculated as $f_{cc}' = Kf_c'$, at a corresponding strain of $\varepsilon_{cc} = \varepsilon_c[1 + 5(K - 1)]$ (Karthik & Mander, 2011), where K is the strength increase factor according to Mander et al. (1988). The shape parameter of the compression stress-strain relationship for confined concrete was calculated as $r_c = f_{cc}'/5.2 - 1.9$, where f_{cc}' is in MPa. The residual stress in *ConcreteCM* is zero, and its corresponding strain is indirectly obtained through the parameter x_{cr}^{-}. This parameter is used to define where the envelope curve starts following a straight line (Kristijan Kolozvari et al., 2018) (see Table 2.2). Therefore, the values of x_{cr}^{-} for confined and unconfined concrete were iterated to regularize the post-peak stress-strain concrete envelopes with the same crushing energies used in the PERFORM 3D models. As an example, values of x_{cr}^{-} of 1.106 and 1.065 were obtained for confined and unconfined concrete, respectively, using n = 11 elements in height to simulate wall WSH6. Additionally, a more gradual gap closure was used in this study by defining the $GapClose$ parameter in *ConcreteCM* as 1.

The reinforcing steel was modeled using the uniaxial *SteelMPF* (Kristijan Kolozvari, Orakcal, et al., 2015b) material in OpenSees, which is based on the Menegotto and Pinto (1973). model A strain hardening ratio of $b = 0.02$ and parameters used to define the cyclic degradation of the curvature coefficient and the Bauschinger effect of $R_0 = 20$,

$cR_1 = 0.925$, and $cR_2 = 0.15$ were adopted from Menegotto and Pinto (1973). No isotropic hardening (Filippou et al., 1983) was accounted for, and symmetric tension and compression behaviors were considered.

The MVLEM simulations used the same linear-elastic shear force-deformation relationship as detailed in the previous section for the PERFORM 3D models. The value of c required to define the height of the center of rotation and the location of the shear spring from the base of each MVLEM element was taken as 0.4 (Massone & Wallace, 2004; Orakcal et al., 2006).

2.5.3 SFI-MVLEM

Since the SFI-MVLEM model is based on the MVLEM model, the same value of c, and the same parameters to define the unconfined concrete, confined concrete, and reinforcing steel behaviors were used. However, in the SFI-MVLEM model, the shear behavior is coupled using the *FSAM* material in OpenSees, which incorporates compression softening and biaxial damage of concrete. To define the *FSAM* material, the parameters η and α, as well as the vertical and horizontal reinforcing steel ratios, are required. A value of $\eta = 1.0$ was used, noting that Kolozvari (2013) found this parameter to have a minor effect on the global behavior of a wall. The parameter α was found to affect the wall behavior and a recommended value was not identified in the literature. Therefore, a parametric investigation was conducted to calibrate the value of α which is the only parameter that was calibrated in this study based on the experimental walls presented in Table 2.1.

To determine α, several models of each of the eight considered RC walls were analyzed with constant values of $m = 5$ and $n = 10$ but with different values of α. The resulting lateral F-D curves from these analytical models were compared against the respective experimental F-D curves in terms of NSE_m (defined in Section 2.6.2), as shown in Figure 2.2a. These results show that squat shear-controlled walls are more sensitive to the value of α as the NSE_m of walls S78, WSL5, LSW1 and LSW2 varied significantly with the selected α values. Note that points corresponding to the largest values of α for walls S78 and WLS5 are not shown in Figure 2.2a because they are below the y-axis range.

Figure 2.2b presents the number of walls for each value of α that resulted in a value of NSE_m larger than $\max(NSE_m) - 0.01$, where $\max(NSE_m)$ is the maximum NSE_m value predicted for each wall within the considered α values. This small range for NSE_m was selected because higher values of NSE_m indicate better model predictions, as described later in Section 2.6.2. Figure 2.2b shows that the slender walls RW2, M1, and WSH6 can be simulated with any of the considered α values, while a value of $\alpha \leq 0.01$ should be used to simulate wall RW1. Figure 2.2b also shows that squat walls (WSL5, LSW1, and LSW2) need lower α values to obtain NSE_m values larger than $\max(NSE_m) - 0.01$, except for wall S78, where lower NSE_m values result from α values above or below 0.002. From these findings, values of α between 0.0001 and 0.005 were found to result in better predictions for the majority of the walls, and a value of $\alpha = 0.002$ was chosen to model all slender and squat walls in the current study. Note that even though the selected value of α was determined based on a parametric investigation using models with constant

$m = 5$ and $n = 10$, the same value of $\alpha = 0.002$ was used in all the simulations with varying model discretizations as presented later.

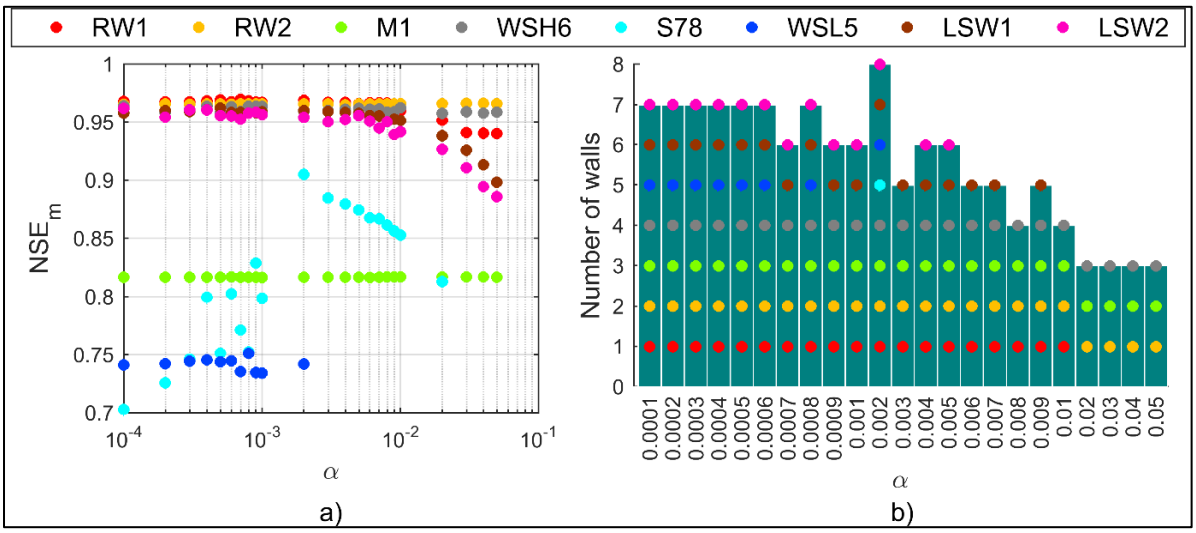

Figure 2.2: Evaluation of SFI-MVLEM models based on: a) effect of α parameter on NSE_m; b) number of walls with $NSE_m \geq max(NSE_m) - 0.01$.

2.5.4 BTM

The concrete behavior in the BTM models was defined using the constitutive model described by Lu and Panagiotou (2014), which is available as *ConcretewBeta* in OpenSees. The strain at peak stress of unconfined concrete and the modulus of elasticity were defined as $\varepsilon_c = 0.002$ and $E_c = 5000\sqrt{f_c'}$ MPa, respectively (Yuan Lu & Panagiotou, 2014). The peak strength point $(\varepsilon_{cc}, f_{cc}')$ of confined concrete was calculated in the same manner as in the MVLEM and SFI-MVLEM models based on Mander et al. (1988). The compressive stress-strain envelopes of unconfined and confined concrete were assumed linear between the peak strength point and the residual stress point (ε_u, f_u) with zero stress at corresponding strains of ε_u and ε_{cu} for unconfined and confined concrete, respectively.

Therefore, values for the intermediate stress-stress point for the compression post-peak envelope ($\varepsilon_{c_{int}}, f_{c_{int}}$) were calculated as the average values between the peak strength point and the residual stress point. Values of ε_u and ε_{cu} were calculated accounting for mesh-size effects (Yuan Lu & Panagiotou, 2014). The trilinear $\beta - \varepsilon_n$ relationship passing through the (β, ε_n) points of $(1, 0)$, $(0.4,\ 0.01\ L_R/L_d)$, and $(0.1, 0.04\ L_R/L_d)$ was used to model biaxial effects according to Vecchio & Collins (1986) and to account for axial-shear-flexure interaction in the diagonal elements (Yuan Lu et al., 2016), where L_d is the length of the diagonal elements. The reference length (L_R) used to regularize the concrete stress-strain relationships for the vertical and horizontal elements was 600 mm, while the value for diagonal elements was $600\sqrt{2}$ mm (Vecchio & Collins, 1986) .

A tensile strength of $f_t = 0.33\sqrt{f_c'}$ MPa (Yuan Lu & Panagiotou, 2014) was assumed for the vertical elements, and the post-cracking tension stress-strain relationship considered effects of tension stiffening through the parameter M according to Stevens et al. (1991). Additionally, a value of $\alpha = 0.5$ (Yuan Lu & Panagiotou, 2014) was used to control the path of unloading from tensile strain. The tension behavior of concrete in the horizontal and diagonal elements was neglected based on Lu et al. (2016). Therefore, the post-cracking stress-strain behavior given by the points [$(\varepsilon_{t_{int}}, f_{t_{int}})$, $(\varepsilon_{t_{res}}, f_{t_{res}})$] was defined with near zero stress values; however, a value of $\alpha = 23.9\sqrt{f_c'}$ (where f_c' is in MPa) was used for walls with boundary regions to control the pinching behavior during unloading from tensile strain.

The reinforcing steel was modeled using the uniaxial *Steel02* material in OpenSees, which is also based on the Menegotto and Pinto model (Filippou et al., 1983; Menegotto

& Pinto, 1973). A strain hardening ratio of $b = 0.02$ and parameters required to define the cyclic degradation and the Bauschinger effect of $R_0 = 20$, $cR_1 = 0.925$ and $cR_2 = 0.15$ were considered as recommended by Menegotto and Pinto (1973).

2.6 Evaluation of Numerical Simulations

This section presents the criteria used to evaluate the numerical simulations obtained with the four models based on the effective stiffness, maximum strength, hysteretic behavior, ultimate displacement, and computing time.

The evaluations of the considered models were made for simulations with varying discretization of each wall in length (m) and height (n) to assess how the discretization affects the predicted response of the walls. The discretization schemes adopted for each wall are presented in Table 2.4. A minimum value of m = 4 (required to represent the axial stiffness of the wall (Orakcal et al., 2006)) was used in all models, where the outer elements at each end simulated the boundary regions, and the two inner elements simulated the central region of the wall. The value of m was increased up to a maximum of 8 to have a finer discretization of the central region. A maximum value of n = 20 was used for all models to simulate a refined mesh along the wall height, while a minimum value of n = 4 was considered to adequately capture the nonlinear behavior. Different minimum values of n were used for the MVLEM and SFI-MVLEM models (Table 2.4) to result in an element length such that it was possible to regularize the confined and unconfined concrete modeled with *ConcreteCM* as described in Section 2.5.2. Matlab scripts were developed to generate the OpenSees models considering increments of 1 in m and n, while n was incremented

by 2 in the PERFORM 3D simulations because each model had to be created manually through a time-consuming process. Examples of wall discretization using m=6 elements in length and n=5 elements in height for the four models can be seen in Figure 1.1.

Table 2.4: Discretization schemes

Wall ID	PERFORM 3D				MVLEM				SFI-MVLEM				BTM				Number of simulations
	m		n		m		n		m		n		m		n		
	min	max	min	max	min	max	min	max	min	max	min	max	min	max	min	max	
RW1	4	8	4	20	4	8	6	20	4	8	6	20	4	8	4	20	280
RW2	4	8	4	20	4	8	5	20	4	8	5	20	4	8	4	20	290
M1	4	8	4	20	4	8	5	20	4	8	5	20	4	8	4	20	290
WSH6	4	8	4	20	4	8	5	20	4	8	5	20	4	8	4	20	290
S78	4	8	4	20	4	8	5	20	4	8	5	20	4	8	4	20	290
WSL5	4	8	4	20	4	8	5	20	4	8	5	20	4	8	4	20	290
LSW1	4	8	4	20	4	8	6	20	4	8	6	20	4	8	4	20	280
SLW2	4	8	4	20	4	8	5	20	4	8	5	20	4	8	4	20	290

2.6.1 Effective Stiffness and Maximum Strength

Numerical models of RC wall structures have been typically evaluated quantitatively based on specific information of the backbone force-displacement curves (Jiang & Kurama, 2010; Yuan Lu & Panagiotou, 2014; Orakcal et al., 2006; Pugh et al., 2015). In this study, these evaluations were done based on the numerical-to-experimental effective stiffness ratio (RK_e) and maximum strength ratio (RV_{max}), where K_e and V_{max} were calculated from the mean positive and negative backbone curves, and K_e was calculated as the slope between the origin and the point on the mean backbone curve at 70% of the maximum strength (i.e., $0.7V_{max}$) (Ghannoum & Matamoros, 2014).

2.6.2 Hysteretic Behavior

For PBSD, it is necessary that the numerical models accurately represent the cyclic response of RC walls, though this has often been done qualitatively by visual comparison of the predicted and experimental cyclic F-D curves. The models have to properly account for cyclic deterioration mechanisms like strength deterioration, pinching, and unloading and reloading stiffness degradation. Evaluation of the accuracy of numerical simulations based on backbone F-D curves does not take into account these cyclic properties. Therefore, a hysteretic evaluation method is needed for the numerical simulations of RC walls under cyclic loads.

To evaluate the hysteretic behavior of the numerical simulations in this study, the Nash-Sutcliffe Efficiency (NSE) (Nash & Sutcliffe, 1970) and the energy error (E_e) were used. The NSE is a standardized statistical measure that determines the relative magnitude

of the residual variance compared to the variance of the measured data. This metric, which is computed using Eq. (2-1), has been commonly used to evaluate simulated responses of different watershed models (ASCE Task Committee, 1993; Moriasi et al., 2007).

$$NSE = 1 - \frac{\sum_{i=1}^{n}\left(Y_i^{exp} - Y_i^{num}\right)^2}{\sum_{i=1}^{n}\left(Y_i^{exp} - \bar{Y}^{exp}\right)^2} \tag{2-1}$$

In the calculation of NSE, Y_i^{exp} is the ith value of the experimental data, Y_i^{num} is the ith value of the numerically simulated data, $\bar{Y}^{exp}$ is the mean of the experimental data, and n is the total number of data points. NSE ranges between $-\infty$ and 1.0, where a value of 1.0 indicates perfect agreement between the experimental and simulated data. Considering that the numerically simulated nonlinear F-D curve of a RC wall is obtained through a displacement-controlled cyclic pushover analysis, and if the measured displacement data from a wall test is used as input for this cyclic pushover analysis, then, the only difference between the experimental and simulated F-D curves is the vector of forces. Therefore, Y in Eq. (2-1) represents the vector of forces. It is important to note that NSE may vary with the number of data points, however, for the common number of points collected in a cyclic experimental test, the variation of NSE is negligible.

The cumulative area of the force-displacement curve, which represents the amount of dissipated energy through structural damage, has been used to compare the experimental and numerical hysteretic responses of structural elements (Kristijan Kolozvari, 2013; Pang et al., 2007). Therefore, an energy error (E_e) can be calculated by Eq. (2-2), where E_{exp} and E_{num} are the cumulative dissipated energy from the experimental test and numerical

simulation of a RC wall, respectively. In this expression, a value of $E_e = 0$ indicates perfect agreement between the observed and simulated data.

$$E_e = \left| \frac{E_{exp} - E_{num}}{E_{exp}} \right| \tag{2-2}$$

Figure 2.3 presents three comparisons of F-D curves for wall M1 (Table 2.1) modeled by BTM models with m = 7 and varying n (refer to Figure 1.1d). The calculated NSE and E_e for each simulation are presented in each graph. The quantitative evaluation of the NSE and E_e values presents a relation with the qualitative evaluation of the F-D curves, showing that better simulations are achieved when NSE and E_e approach 1.0 and 0.0, respectively. In Figure 2.3, better simulations are observed when n increases from 4 to 8. The hysteretic behavior of the simulation with n = 4 (Figure 2.3a) shows significant strength degradation during the first cycles to drift ratios of approximately 1.5 and 2%. Despite the lower forces predicted in these cycles, the wide hysteretic loops result in similar energy dissipation as the one predicted with n = 6 (Figure 2.3b). Therefore, the values of E_e are similar and the values of NSE are different when comparing simulations with n = 4 and n = 6. The opposite is true for the simulations with n = 6 (Figure 2.3b) and n = 8 (Figure 2.3c), showing similar values of NSE and different values of E_e because the width of the cycles do not change substantially while the cycles obtained with n = 8 predict higher strength, resulting in higher dissipated energy. These results show that the different levels of accuracy of the three simulated responses cannot be distinguished adequately using either NSE or E_e alone.

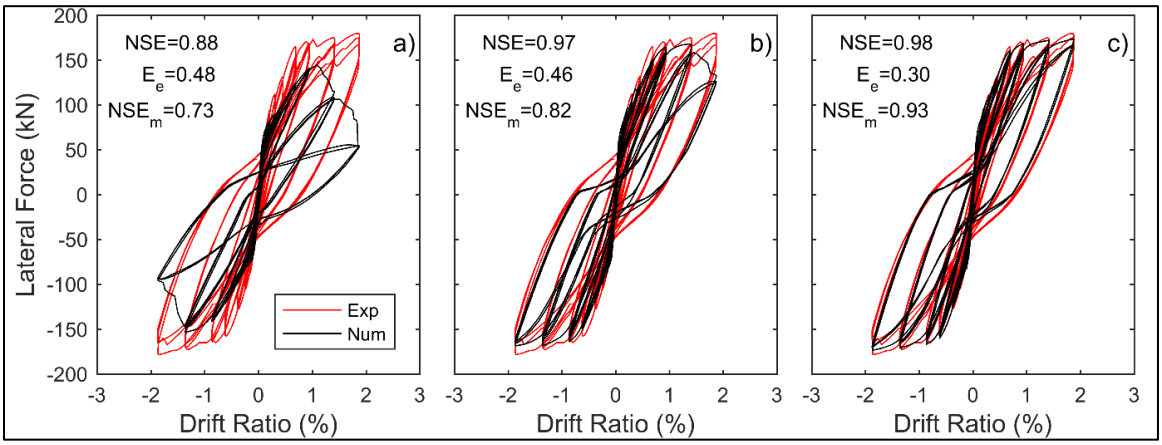

Figure 2.3: Wall M1 simulated by BTM, m=7 a) n=4; b) n=6; c) n=8.

To overcome this limitation of using NSE or E_e alone as a quantitative comparison metric, a Modified Nash-Sutcliffe Efficiency (NSE_m), presented in Eq. (2-3), is proposed. In this new metric, the original NSE value is reduced by an energy error factor (E_{e_f}), calculated by Eq. (2-4) that was derived based on qualitative evaluations of the F-D curves obtained by the four models. The E_{ef} increases exponentially until an energy error (E_e) of approximately 0.395, and is capped at a maximum value of E_{ef} = 0.15 (see Figure 2.4). The values of NSE_m calculated for wall M1 for the three models are also presented in Figure 2.3. These values exhibit a better quantifiable metric than those of NSE and E_e individually to classify the numerical simulations, and they agree with a qualitative evaluation of the curves and distinguish different levels of accuracy (i.e., the values increase for improved simulations from left to right). Therefore, the NSE_m metric was used to evaluate the cyclic predictions from the numerical models in this study.

$$NSE_m = NSE - E_{ef} \tag{2-3}$$

$$E_{ef} = min\left(0.15,\ \ 65e^{-10(1-E_e)} - 0.00295\right) \quad (2\text{-}4)$$

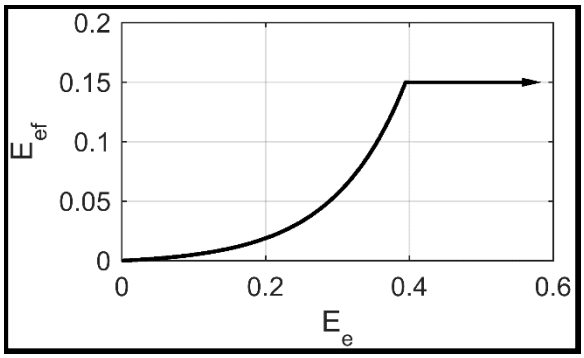

Figure 2.4: Energy error factor.

2.6.3 Ultimate Displacement

The ultimate displacement was evaluated based on the ratio of numerical-to-experimental values of the drift capacity $(R\delta_u)$. The drift capacity was calculated as the drift corresponding to a strength loss of 20% from the maximum strength, and was obtained from the mean of the positive and negative backbones of the F-D curve. When the backbone of the simulated response did not present a strength loss of 20% within the displacement protocol of the experimental test, larger displacements were applied in the numerical simulation until this condition was achieved.

2.6.4 Computing Time

Displacement increments of 1.0, 0.5, 0.1 and 0.05 mm were used in the displacement-controlled protocol of the cyclic pushover analyses to evaluate the computing time of the studied models. All analyses were performed on a desktop computer with an Intel® Core™ i7-4790 processor, CPU of 3.60 GHz, and 8.00 GB RAM on Windows 7, using PERFORM 3D Version 7.0.0 and OpenSees version 2.5.0 32-bit.

2.6.5 Local Behavior

Even though global quantities, such as the effective drift, are used as engineering demand parameters (EDPs) to assess the performance of slender RC walls according to FEMA P-58 (2018), ASCE 41 (2017) uses plastic hinge rotation, while PEER TBI (2017) uses strains. Therefore, local quantities (i.e., strains and curvatures) are needed to evaluate the performance of a slender RC wall when using these documents.

It has been shown that the local behavior from a flexural wall simulation is highly sensitive to the vertical discretization of the model because the nonlinear deformations localize in the critical elements with the highest moment (Coleman & Spacone, 2001; Pugh et al., 2015). In a cantilever wall model, this localization occurs in the lowest row of elements over a height of H/n (where H is the wall height and n is the number vertical elements; see Figure 1.1). Therefore, postprocessing of the simulation results is needed to convert the local deformations obtained with any vertical discretization to local deformations over an assumed plastic hinge length, L_p. Coleman and Spacone (2001) presented a procedure that can be applied to postprocess curvatures based on the curvature of the first element. Alternatively, postprocessing can be conducted based on the curvatures of the elements within the plastic hinge length. In this process, the plastic hinge rotation (θ_p) can be estimated using Eq. (2-5a) or Eq. (2-5b) as

$$\theta_p = \phi_1 L_p \qquad \text{for } H/n \geq L_p \qquad \text{(2-5a)}$$

$$\theta_p = (H/n)\sum_{i=1}^{j-1}\phi_i + \big(L_p - (j-1)(H/n)\big)\phi_j \qquad \text{for } H/n < L_p \leq jH/n \qquad \text{(2-5b)}$$

where, ϕ_i is the curvature in the ith vertical element (see Figure 2.1) and j is the number of vertical elements within the assumed plastic hinge length (i.e., $jH/n \geq L_p$).

The second term in Eq. (2-5b) is the rotation of the part of the jth vertical element within the plastic hinge length.

The postprocessed θ_p obtained from Eq. (2-5) is assumed to be uniform over L_p, and thus, the associated plastic hinge curvature, ϕ_p, can be calculated as $\phi_p = \theta_p / L_p$. Moreover, the average neutral axis depth, c_p over the plastic hinge length can be calculated using Eq. (2-6), where c_i is the neutral axis depth in the ith vertical element (see Figure 2.1).

$$c_p = c_1 \qquad \text{for } H/n \geq L_p \qquad \text{(2-6a)}$$

$$c_p = \left[(H/n)\sum_{i=1}^{j-1} c_i + \left(L_p - (j-1)(H/n)\right)c_j\right]/L_p \qquad \text{for } H/n < L_p \leq jH/n \qquad \text{(2-6b)}$$

Then, the maximum compression and tension strains of the wall can be calculated as $\varepsilon_c = \phi_p c_p$ and $\varepsilon_t = \phi_p\left(L_w - c_p\right)$, respectively. Note that if $H/n \geq L_p$ (i.e., Eq. (2-5a) and Eq. (2-6a) apply), no curvature and strain postprocessing is needed since $\phi_p = \phi_1$ and $c_p = c_1$.

2.7 Results

This section presents the results and evaluations for the simulations conducted with the four models. The effective stiffness ratio (RK_e), maximum strength ratio (RV_{max}), and Modified Nash-Sutcliffe Efficiency (NSE_m) are presented for the eight walls. The drift capacity ratio ($R_{\delta u}$) is presented only for walls RW1, WSH6, and S78 because for these walls a strength loss of 20% from the maximum strength can be identified in the experimental data. Comparisons of computing time are also presented for these three walls.

2.7.1 Effective Stiffness and Maximum Strength

The RK_e and RV_{max} values for each analysis with a different wall discretization (Table 2.4) are presented as boxplots in Figure 2.5. Overall, the variability of RV_{max} was small when using different wall discretizations in the PERFORM 3D, MVLEM, and SFI-MVLEM simulations (Figure 2.5a-c), while RK_e showed more variability for these models. The variability in the BTM simulations (Figure 2.5d) was generally higher than the variability in the other models because the wall discretization affected the angle of the diagonal elements. The influence of the angle of the diagonal elements in BTM models is presented elsewhere (Yuan Lu et al., 2016; Yuan Lu & Panagiotou, 2014; Moharrami et al., 2014; Panagiotou et al., 2012).

The maximum strength of the flexure-dominated walls RW1, RW2, M1, and WSH6 were accurately simulated by PERFORM 3D. The RV_{max} values indicated mostly small overestimations, with a highest value of 1.19 for wall RW1. Median and mean values of RV_{max} indicated that the model predictions were within $\pm$10% of the values from the experiments, except for wall RW1, which had a mean error in the order of +18%. The effective stiffness was underestimated for walls RW1, M1, and WSH6, with values of RK_e as low as 0.55 for wall WSH6, while it was overestimated for wall RW2, with a highest ratio of 1.17. In comparison, for the shear-dominated walls S78, WSL5, LSW1, and LSW2 (Figure 2.5a), RV_{max} was overestimated while RK_e was underestimated using the PERFORM 3D model. Values of RV_{max} as high as 2.22 resulted for wall WSL5, showing the inaccuracy of the PERFORM 3D model to simulate the behavior of walls in which the maximum strength was controlled by shear.

Results from MVLEM (Figure 2.5b) adequately predicted the evaluation parameters for the flexure-dominated walls RW1, RW2, M1, and WSH6. The maximum strength was predicted within a range of $\pm$10% of the experimental values; with the exception of wall RW1, which reached a maximum RV_{max} value of 1.18. Except for wall WSH6, the effective stiffness was generally overestimated, with a maximum RK_e of 1.56 for wall RW2. Evaluation parameters for the shear-dominated walls S78, WSL5, LSW1 and LSW2 indicated greater variability than for the flexure-dominated walls. The maximum strength was overestimated in these four walls, with RV_{max} values as high as 2.33 for wall WSL5. Mean values of RK_e showed overprediction for walls S78, WSL5, and LSW1, while the mean effective stiffness ratio for wall LSW2 was underestimated (RK_e=0.94).

Evaluation parameters for the flexure-dominated walls simulated by SFI-MVLEM (Figure 2.5c) were similar to the values for MVLEM, but showed more variability when considering discretizations with different m and n values. For the effective stiffness, the highest variability when using different discretizations occurred in wall WSL5, with RK_e reaching a maximum of 1.7 (without considering the outliers of the boxplot). In comparison, the results for maximum strength were much better, with interquartile ranges within $\pm$16% error of the experimental values for all walls. The SFI-MVLEM predictions of maximum strength for the shear-dominated walls were better than the values obtained with PERFORM 3D and MVLEM because of the ability to simulate coupled shear-flexure behavior.

Numerical-to-experimental ratios obtained from the BTM simulations with different m and n values varied significantly, which implies that the selected discretization in BTM is very important in predicting the global response of RC walls. Overall, prediction of the effective stiffness had the highest range of variability for the flexure-dominated walls, while the maximum strength was generally underestimated. The variability of the maximum strength predictions was greater for the shear-dominated walls, while the effective stiffness was consistently underestimated for walls WSL5, LSW1, and LSW2.

It can be concluded from Figure 2.5 that simulations obtained with models based on the fiber analysis approach (PERFORM 3D, MVLEM, and SFI-MVLEM) presented less variations when using different discretizations. Thus, a reduced number of elements in length and height could be used in these models to represent the global behavior of RC walls. Conversely, since the BTM model is based on the strut-and-tie analysis approach, wall discretization presented a large impact in the global behavior of the simulations, thus the number of elements should be carefully selected when using this model.

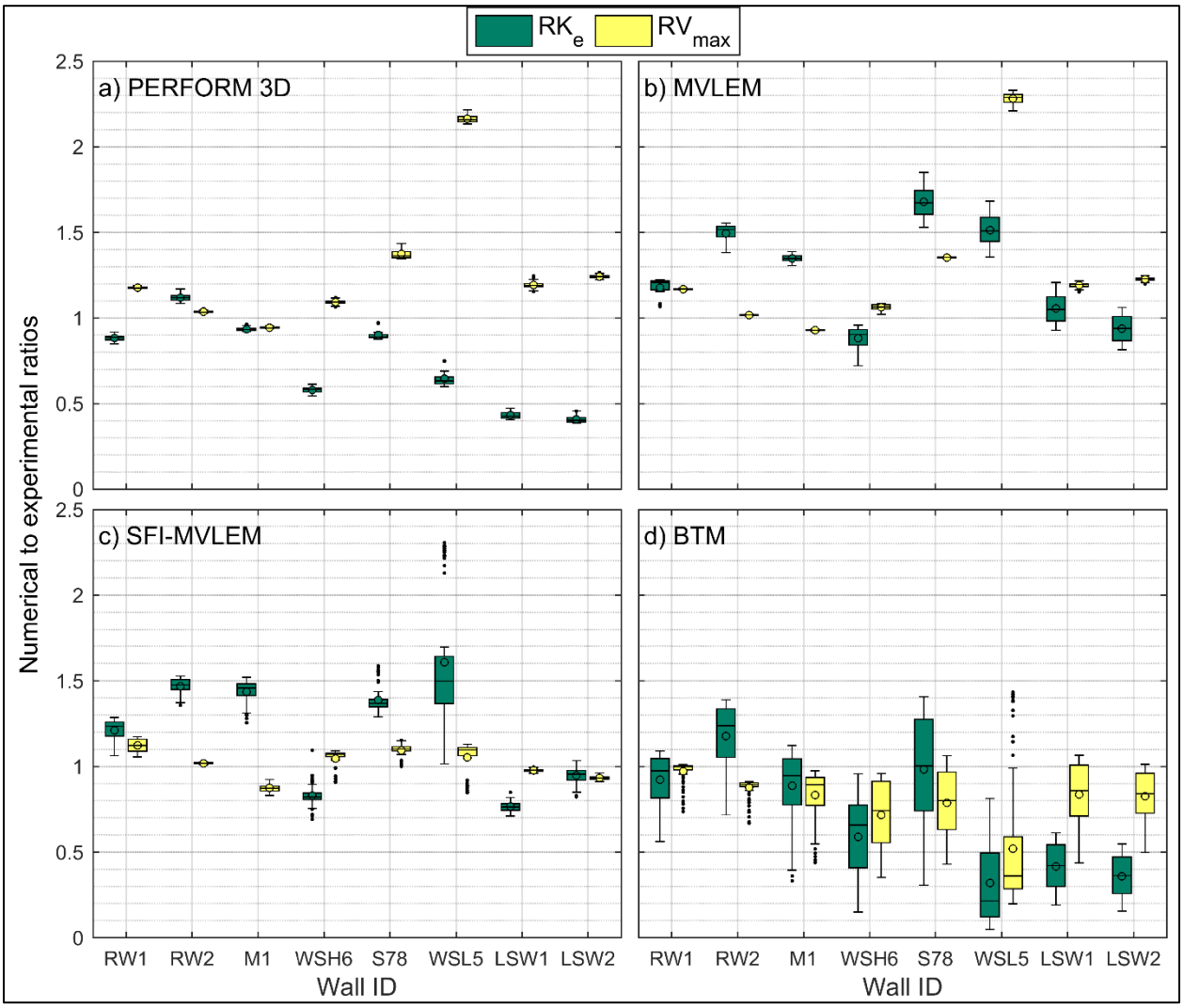

Figure 2.5: Variability in K_e and V_{max} ratios for models using: a) PERFORM 3D; b) MVLEM; c) SFI-MVLEM; d) BTM.

Lu et al. (2016) recommended that the angle of the diagonal elements θ_d in BTM should be estimated according to Eq. (2-7), where V_{max} is the maximum resisted lateral force, ρ_h is the horizontal web reinforcement ratio, t_w is the thickness of the wall, d is the distance between the outermost vertical elements (see Figure 2.1d), and H is the wall

height. In addition, an upper bound of θ_d=65° is suggested, and that θ_d should be greater than or equal to 45° for walls with a shear-to-span-ratio larger than 1.0.

$$\theta_d = \tan^{-1}\left(\frac{V_{max}}{f_y \rho_h t_w d}\right) \leq \tan^{-1}\left(\frac{H}{d}\right) \quad (2\text{-}7)$$

The numerical-to-experimental ratios of the effective stiffness and maximum strength obtained with the BTM simulations are presented in Figure 2.6 as a function of the angle of the diagonal elements. The recommended angle from Eq. (2-7) is also presented in the figure. For the flexure-dominated walls (Figure 2.6a-d), values of θ_d around the recommended value from Eq. (2-7) yielded accurate simulations of the analyzed parameters (i.e., the numerical-to-experimental ratios are reasonably close to 1.0). However, for the shear-dominated walls (especially WLS5, LSW1, and LSW2; Figure 2.6f-h), at least one of the evaluation parameters is highly underestimated or overestimated for diagonal angles around the value calculated by Eq. (2-7). Based on these results, the values of m and n that define the wall discretization for BTM simulations should be selected to obtain a θ_d value equivalent to Eq. (2-7) for flexure-controlled walls.

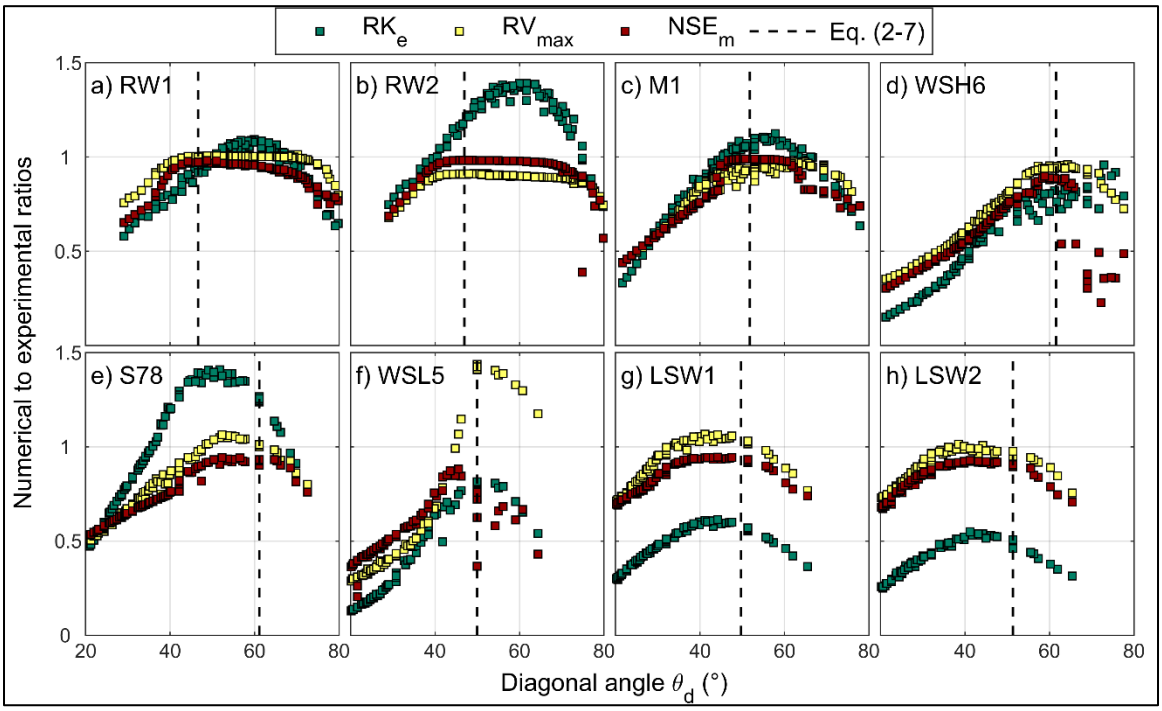

Figure 2.6: Numerical-to-experimental ratios of K_e, V_{max}, and NSE_m for BTM simulations with different diagonal angles of walls a) RW1; b) RW2; c) M1; d) WSH6; e) S78; f) WSL5; g) LSW1; h) LSW2.

2.7.2 Hysteretic Behavior

The accuracy of the analytical models, when considering discretizations with different m and n values, in predicting the hysteretic behaviors of the eight walls was evaluated based on the Modified Nash-Sutcliffe Efficiency (NSE_m), as depicted in Figure 2.7. Like the parameters evaluated before, the highest variability when using different discretizations occurred in the BTM simulations. Simulations of the flexure-dominated walls achieved maximum values of NSE_m greater than 0.90, except for the BTM simulations of wall WSH6 where a maximum value of 0.90 was obtained for a simulation with m = 8 and n = 11 elements. Excluding the BTM simulations, the minimum NSE_m

value for the flexure-dominated walls, considering all discretizations, was 0.80 for wall WSH6 simulated by PERFORM 3D. The NSE_m values for the shear-dominated walls were smaller than for the flexure-dominated walls, which implies less accurate predictions from the simulations of shear-dominated walls. Minimum NSE_m values of -6.54 and -4.74 (i.e., negative values not shown in Figure 2.7) were obtained for wall WSL5 simulated by MVLEM and PERFORM 3D, respectively. As expected, the shear-coupled models resulted in greater NSE_m for the shear-dominated walls, demonstrating the benefits of considering shear-flexure interaction to simulate squat walls.

The simulated hysteretic behavior was classified as good for NSE_m >0.95, satisfactory for values of NSE_m between 0.95 and 0.85, unsatisfactory for values between 0.85 and 0.75, and poor for NSE_m <0.75. These limits were verified through qualitative evaluations of the F-D simulations, with additional quantitative support by comparing the measured test results of two identical wall test specimens described subsequently. The large variability in NSE_m from the BTM simulations can be seen in the contours depicted in Figure 2.8 for the different wall discretizations in length and height. This figure shows that it was possible to obtain good estimations of the hysteretic behavior (i.e., NSE_m >0.95) from the BTM simulations of the flexure-dominated walls RW1, RW2, and M1 for several values of m and n. Figure 2.8 shows that all simulations for the other five walls were not able to achieve NSE_m >0.95, but satisfactory results were obtained for certain discretizations. Finally, the figure shows similar NSE_m values for combinations of m and n distributed along diagonal bands in each plot, indicating an evident relationship between the model discretization, which affects the angle of the diagonal elements, θ_d and the

accuracy in predicting the hysteretic behavior of the experimentally tested walls. Specifically, a trend is evident where larger values of n (lower L_v as presented in Section 2.4.4), resulting in lower values of θ_d, also result in lower values of NSE_m, especially for the shear-controlled walls. This trend can be seen in Figure 2.6 as well. Therefore, a larger value of m is required to increase θ_d and the accuracy of the simulated hysteretic behavior in BTM models with larger values of n. Based on these results, it is concluded that m and n pairs that result in a diagonal angle close to the value calculated with Eq. (2-7) are needed to adequately simulate the hysteretic behavior of the walls.

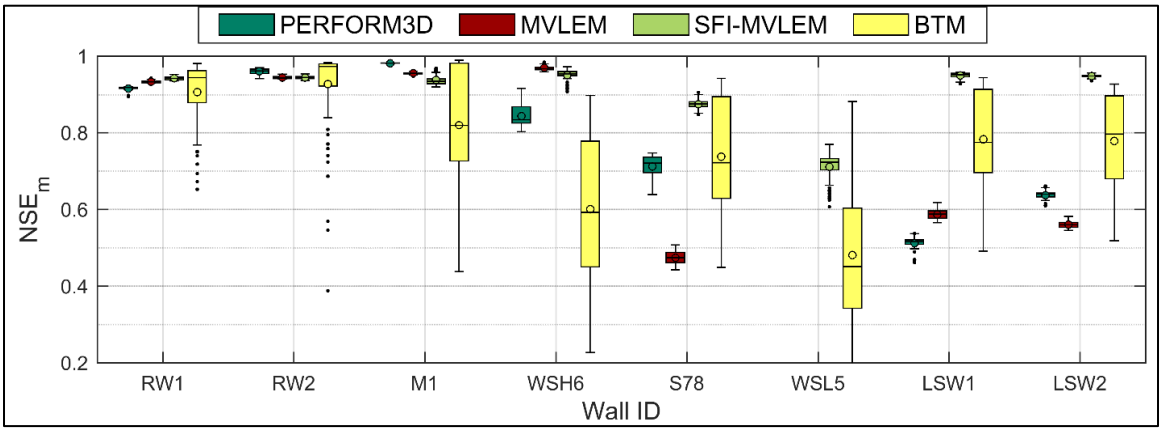

Figure 2.7: Variability in NSE_m (results of PERFORM 3D and MVLEM for WSL5 are below the plot range).

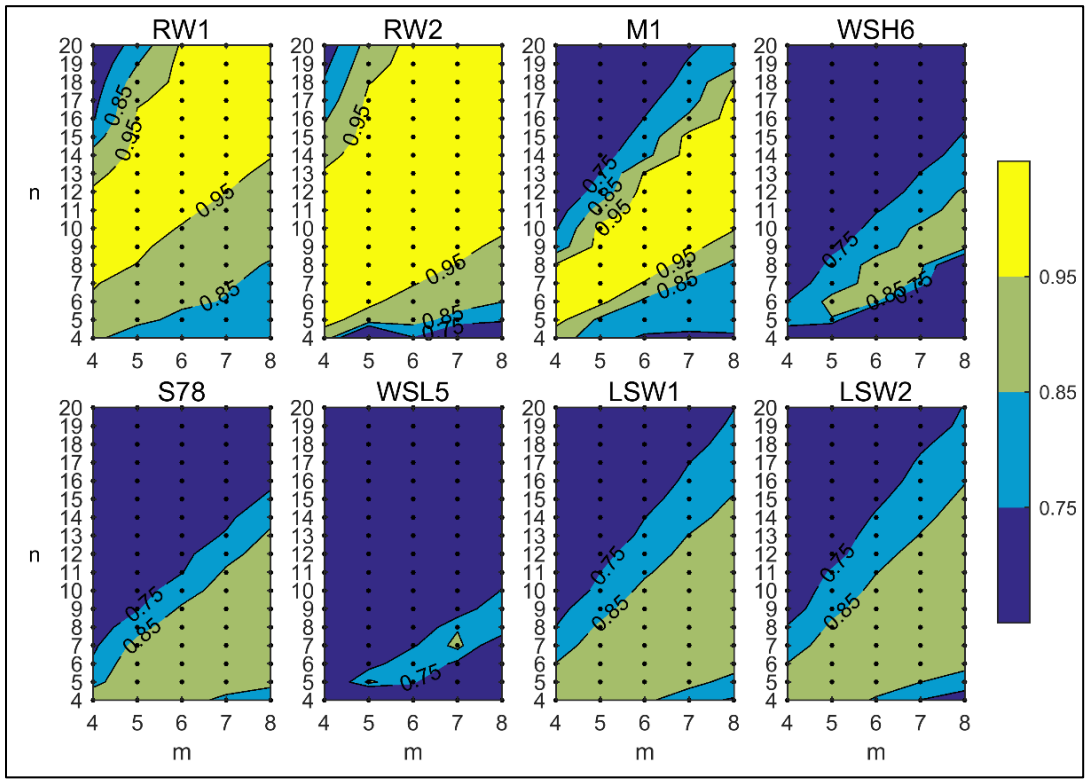

Figure 2.8: NSE_m contours for BTM models with varying m and n.

In order to obtain thresholds for the aforementioned evaluation parameters, the measured force-displacement curves of two identical RC wall specimens (M1 and M2) were compared. These walls were built at the same time, using the same material properties, and were tested under the same axial load and same lateral displacement protocol at the Laboratory of Structural Engineering of Pontificia Universidad Católica de Chile (Amón, 2018). The F-D relationships of the two walls, and the calculated $NSE_m, RK_e,$ and RV_{max} values are presented in Figure 2.9. Different peak cycle displacements are observed because they correspond to actual wall displacements and not to the actuator control displacements. Since slightly different displacement histories were

measured for the two walls, and because NSE_m requires the force at the same displacement in both walls, forces were interpolated between the peak cyclic displacements. The F-D curves of Figure 2.9 show that experimental tests of identical walls present differences, and a NSE_m value of 0.95 was obtained from this comparison [treating the measured results from M2 as "numerical" results in Eq. (2-1) and Eq. (2-2)]. Although more tests of identical walls are needed to obtain statistically meaningful results, three main observations can be stated: 1) the proposed value of NSE_m=0.95 seems reasonable to classify a simulated hysteretic behavior as good; 2) the effective stiffness presented a relatively large ratio of 1.26 between the tested walls (Figure 2.9), consistent with the large variation and inaccuracy in the numerical simulations; and 3) the difference in the maximum strength was negligible between the two walls, which suggests that models should predict the maximum strength more precisely than the effective stiffness.

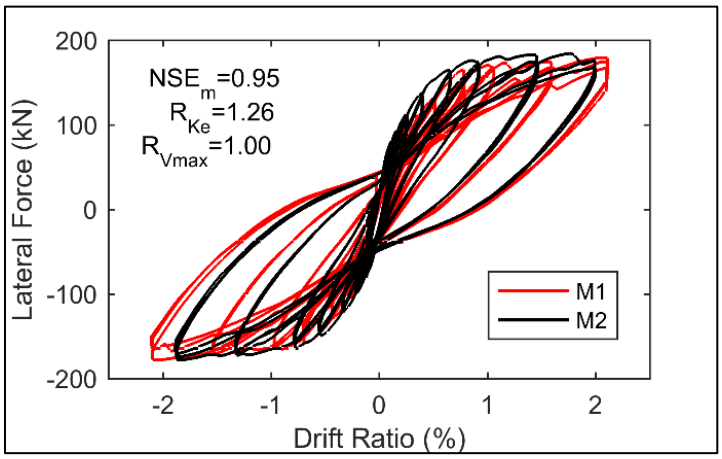

Figure 2.9: Evaluation of quantitative parameters for two experimentally tested RC walls.

The F-D responses that resulted in the maximum NSE_m for each of the different models are depicted in Figure 2.10, which also presents the m and n values for each case and the corresponding effective stiffness and maximum strength ratios. Figure 2.10 shows good correlation between the NSE_m values and a qualitative (visual) evaluation of the hysteretic results for the four models. The figure shows that the hysteretic behaviors of the flexure-dominated walls (RW1, RW2, M1, and WSH6) was accurately predicted using PERFORM 3D (Figure 2.10a1-4). The NSE_m values reflected good hysteretic simulations for walls RW2 and M1, while the values for walls RW1 and WSH6 were classified as satisfactory due to the prediction of a more pinched behavior for these walls. On the other hand, hysteretic simulations of the shear-dominated walls S78, WSL5, LSW1, and LSW2 (Figure 2.10a5-8) were classified as poor, being worst for wall WLS5, with a negative value of NSE_m (Figure 2.10a6). The low values of NSE_m for squat walls demonstrate the inability of PERFORM 3D to simulate shear-dominated hysteretic behaviors.

As shown in Figure 2.10b2-4, the hysteretic behaviors from the MVLEM simulations of the flexure-dominated walls RW2, M1, and WSH6 were classified as good. The maximum NSE_m=0.94 for wall RW1 (Figure 2.10b1) was classified as satisfactory, which is caused by the inability of the model to capture the strength degradation in the last cycle of the test. All hysteretic simulations of the shear-dominated walls (Figure 2.10b5-8) were classified as poor in terms of NSE_m, mainly because the predicted cycles dissipated more energy due to the incapability of the model to simulate the shear-flexure interaction. The MVLEM force-displacement curves were similar to those of PERFORM 3D because both models are shear-uncoupled, use the same shear force-deformation relationship,

present a fiber-based formulation with plane sections, and assume uniform curvature along the element length. However, as an important difference, the PERFORM 3D concrete and steel material models are based on linear piecewise envelopes and unloading and reloading behaviors, whereas the materials in MVLEM are characterized by curved envelopes with smoothed unloading and reloading behaviors (see Table 2.2). These differences in the material constitutive laws influenced the shapes of the force-displacement curves in the PERFORM 3D and MVLEM simulations (Figure 2.10a,b).

The SFI-MVLEM simulations of the flexure-dominated walls (Figure 2.10c1-4) resulted in similar hysteretic behaviors as those from the MVLEM simulations, with the exception that the hysteretic simulation of wall RW1 was classified as good because NSE_m reached 0.95. This parameter was large for this wall because of the ability to predict the strength reduction in the last positive cycle with SFI-MVLEM (Figure 2.10c1). The SFI-MVLEM hysteretic simulations for the shear-dominated walls (Figure 2.10c5-8) were classified as good for walls LSW1 and LSW2, satisfactory for wall S78, and unsatisfactory for wall WSL5. The greater NSE_m values using SFI-MVLEM are related to the ability of the model to predict pinching behavior more consistently with the experimental behavior.

The BTM hysteretic simulations generated satisfactory force-displacement curves for walls WSH6, S78, WSL5, LSW1, and LSW2, and good curves for walls RW1, RW2, and M1. The largest NSE_m value was for wall M1, where the estimated unloading and reloading curves followed the test results well, even though the maximum strength was underpredicted by 10% (Figure 2.10d3). It should be noted that even though all models had a fixed base; and thus, the sliding shear failure of walls LSW1 and LSW2 could not be

modeled, both SFI-MVLEM and BTM models were still able to satisfactorily capture the hysteretic behavior of these walls until failure.

The Modified Nash-Sutcliffe Efficiency (NSE_m), which was specifically developed to quantify the hysteretic behavior of the numerical simulations, should be considered together with other quantitative metrics such as the effective stiffness ratio (RK_e) and the maximum strength ratio (RV_{max}) to evaluate the simulated global behavior. As an example, Figure 2.10b7 shows the F-D response of wall LSW1 simulated with MVLEM, where the maximum strength was overestimated by 15% and the effective stiffness was underestimated by 6%. These relatively small errors could result in a potentially false sense of accuracy when clearly the model is not able to capture the cyclic behavior (i.e., especially the pinching behavior). This discrepancy in the hysteretic behavior is well captured by the low value of NSE_m, classifying the wall hysteretic behavior as poorly simulated. While it may be possible to arrive at this judgement through a qualitative visual evaluation of the hysteretic curves, the use of NSE_m allows a more objective, quantitative evaluation.

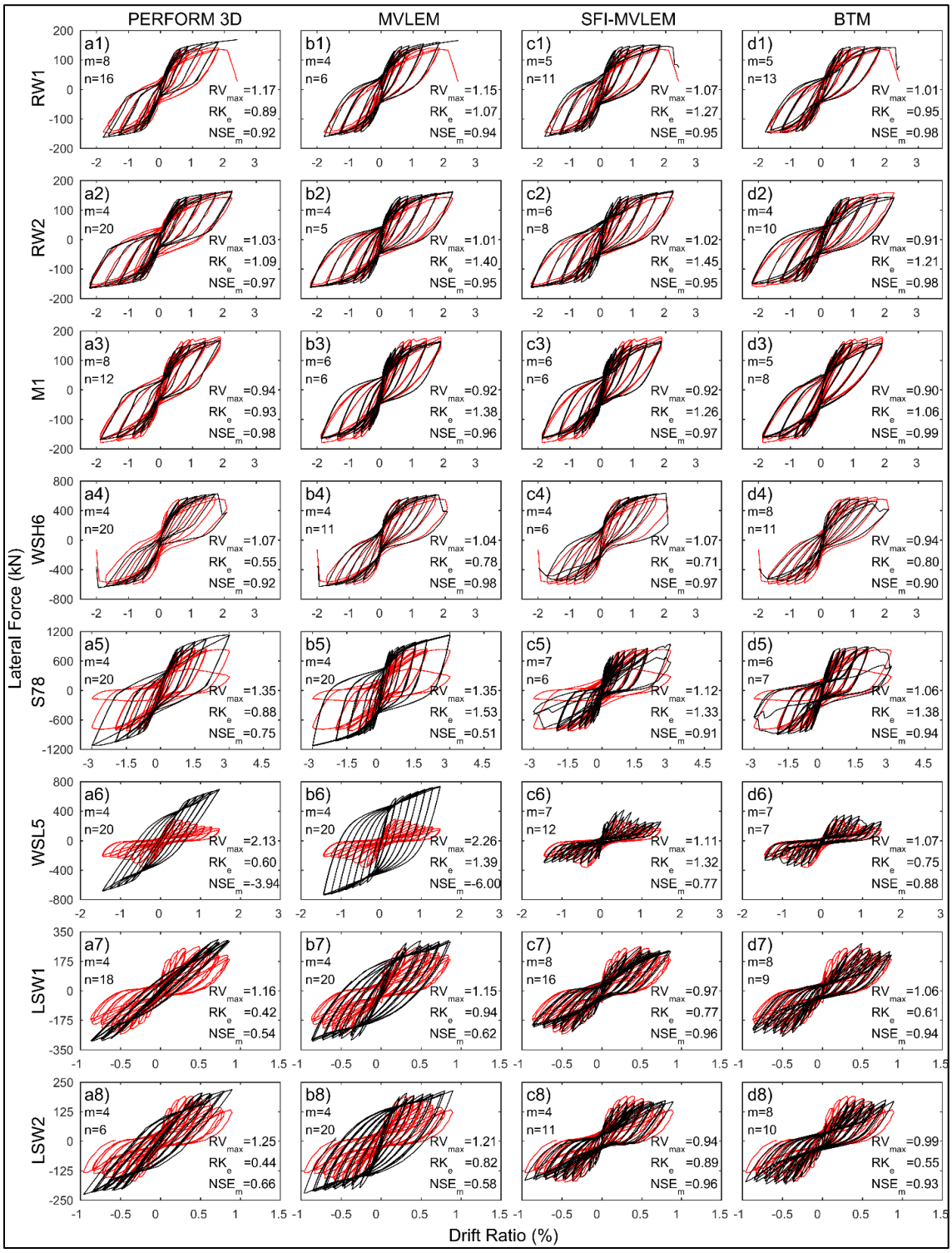

Figure 2.10: Force-displacement curves with maximum NSE_m (experimental results shown in red and numerical simulations shown in black).

2.7.3 Ultimate Displacement

Numerical-to-experimental ultimate displacement ratios obtained from the models that resulted in the maximum NSE_m for walls RW1, WSH6, and S78 are presented in Table 2.5. The maximum errors when estimating the ultimate displacement with the shear-coupled SFI-MVLEM and BTM models occurred for wall RW1, and were 8.6% and 8.0%, respectively. The PERFORM 3D and MVLEM models were considerably less accurate in predicting the ultimate displacements of the selected walls, except for wall WSH6, because these models do not incorporate shear-flexure interaction and assume linear elastic shear behavior. The largest overestimation of the ultimate displacement occurred for walls RW1 and S78, showing the inadequacy of the shear-uncoupled models to simulate the experimentally observed ultimate displacements.

Table 2.5: Experimental data set

	PERFORM 3D	MVLEM	SFI-MVLEM	BTM
RW1	2.493	1.927	1.086	1.080
WSH6	0.983	0.962	1.017	0.969
S78	1.543	1.737	1.001	0.967

2.7.4 Computing Time

Computing times for the simulations that resulted in the maximum NSE_m for walls RW1, WSH6, and S78 are presented in Table 2.6. The shear-uncoupled PERFORM 3D and MVLEM models required shorter computational times due to the reduced number of iterations needed to achieve equilibrium at different loading steps. These two models took similar computational times to finish the analyses for the three walls with displacement increments of 1.0 mm and 0.5 mm. However, for displacement increments of 0.1 mm and 0.05 mm, the MVLEM simulations required shorter computing times than those with PERFORM 3D, probably because of the smaller number of degrees of freedom. The shear-coupled SFI-MVLEM simulations required longer computing times to converge than the PERFORM 3D and MVLEM models. Finally, the BTM simulations presented several convergence problems and required smaller displacement increments to obtain a solution for the entire displacement protocol. In comparison with SFI-MVLEM, the BTM simulations took similar computing times for wall RW1 and about 2.5 times for wall WSH6. Although not shown in Table 2.6 because of the reduced displacement increment, the BTM model required 140.23 seconds with a displacement increment of 0.025 mm to obtain a solution for the entire loading protocol of wall S78. Note that while there were significant differences among the numerical models, the times required to simulate walls were generally short, with the longest time little over 2 minutes.

Table 2.6: Computing time

Wall ID	Displacement Increment	PERFORM 3D	MVLEM	SFI-MVLEM	BTM
		Computing Time (sec)			
RW1	1.0 mm	2.4	2.0	8.2	-
	0.5 mm	4.4	3.0	15.1	-
	0.1 mm	16.1	11.2	52.0	45.2
	0.05 mm	34.1	21.6	84.8	81.2
WSH6	1.0 mm	2.1	2.5	4.3	-
	0.5 mm	3.4	3.2	7.0	-
	0.1 mm	20.0	9.6	23.4	57.4
	0.05 mm	37.7	18.2	39.6	100.4
S78	1.0 mm	2.9	3.3	15.4	-
	0.5 mm	4.8	4.6	23.3	-
	0.1 mm	22.0	12.0	76.9	-
	0.05 mm	52.4	21.3	131.6	-

2.7.5 Local Behavior

This section presents and evaluates the simulation results for the local behavior of the flexure-dominated wall RW2 using MVLEM. This model was chosen because the global behavior of the wall showed little variation to the element discretization (see Figure 2.5b and Figure 2.7). The numerical-to-experimental curvature ratio contours obtained from the 1st element ($R\phi_1$) at a lateral drift of 2.0%, presented in Figure 2.11a, show that: 1) the horizontal discretization of the wall (parameter m) has a negligible effect on the local behavior of the wall, 2) the local behavior is significantly influenced by the vertical discretization of the wall (parameter n), and 3) larger simulated curvatures are obtained for finer vertical discretizations. In comparison, the post-processed numerical-to-experimental curvature ratio contours ($R\phi_p$) at 2.0% drift, presented in Figure 2.11b, show that the sensitivity of the results to the vertical discretization of the wall is significantly reduced. The postprocessed curvatures were calculated by applying Eq. (2-5) to obtain plastic hinge rotations assuming a plastic hinge length equal to one half of the wall length (i.e., $L_p = L_w/2$ (Abdullah, 2019)), as described in Section 2.6.5.

Figure 2.11c and Figure 2.11d compare the unprocessed vertical strains and the postprocessed vertical strains (i.e., from the postprocessed curvatures) with the measured strains at different drift levels for coarse (n = 5) and fine (n = 20) vertical discretizations of the wall, respectively. For the coarse mesh (Figure 2.11c), the unprocessed tensile strains (i.e., positive strains) were predicted with errors less than 15%, while the compressive strains were underpredicted with errors between 49% and 74%. In this case, the post-processed strains were the same as the unprocessed strains because Eq. (2-5a) was applied

(i.e., $\phi_1 = \phi_p$). For the fine mesh (Figure 2.11d), the unprocessed tensile strains (Num_1 in Figure 2.11) were highly overestimated, with errors between 105% and 114%, while the compressive strain errors were between 29% and 63%. In comparison, the tensile strain erros from the postprocessed curvatures (Num_p in Figure 2.11) decreased significantly to between 4% and 33%, while the compressive strain errors increased slightly to between 31% and 68%.

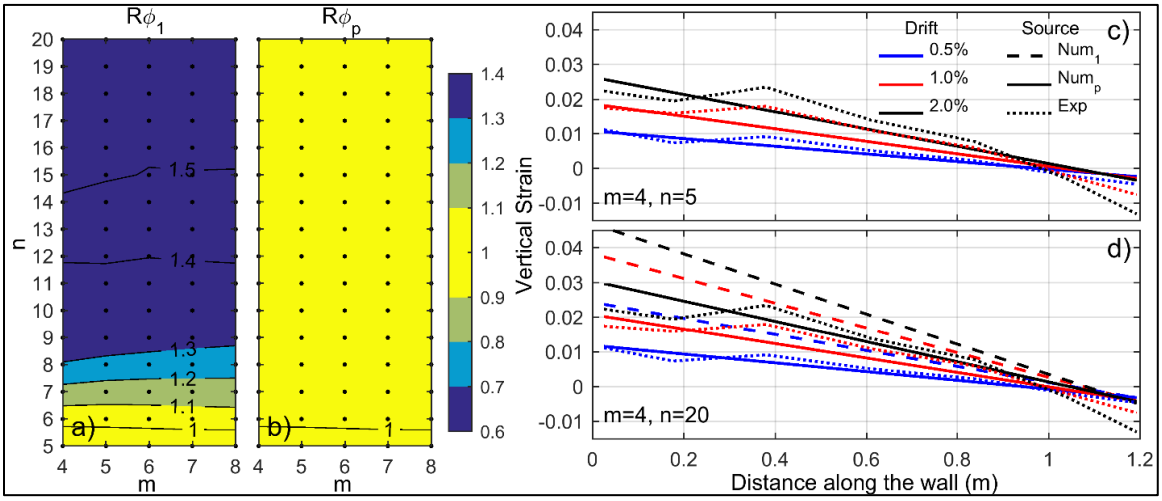

Figure 2.11: Evaluation of local behavior of wall RW2 simulated using MVLEM based on a) numerical (unprocessed)-to-experimental curvature ratio contours ($R\phi_1$) for 2.0% drift; b) numerical (post-processed)-to-experimental curvature ratio contours ($R\phi_p$) for 2.0% drift; c) vertical strain profiles for coarse vertical discretization; d) vertical strain profiles for fine vertical discretization. Note that in c) and d), colors and line styles are associated with drift and strain source, respectively.

2.8 Summary and Conclusions

In this study, shear-uncoupled macro-models PERFORM 3D and MVLEM, and shear-coupled macro-models SFI-MVLEM and BTM, were studied to simulate the nonlinear hysteretic global lateral force-displacement behavior of eight experimentally tested planar RC walls. A detailed definition of all modeling parameters was presented based only on the wall geometry, reinforcement layout, concrete compression strength, and steel yield strength, which would all be known during the design stage of a wall in practice. Concrete and reinforcing steel material stress-strain relationships were not calibrated with the experimental test results so as to generate modeling guidelines for the Performance-Based Seismic Design (PBSD) of RC walls. A total of 2,300 analyses with different model discretizations were performed for the eight walls. The predicted force-displacement curve from each analysis was evaluated based on numerical-to-experimental ratios for the effective stiffness, maximum strength, and ultimate displacement (RK_e, RV_{max}, and $R\delta_u$, respectively). Additionally, the hysteretic response of the numerical simulations was assessed by the proposed Modified Nash-Sutcliffe Efficiency (NSE_m) metric, and the computing time of the simulations was compared considering four different displacement control analysis increments. The main conclusions based on the comparisons between the numerical and experimental results are listed below. Note that these conclusions are mainly focused on the nonlinear hysteretic global lateral force-displacement behavior of planar walls. Further studies are needed to investigate the applicability of these findings to the local behavior (e.g., strains and curvatures), behavior of non-planar or coupled walls, and behavior under dynamic loading of RC walls.

1. The modeling parameters presented in this study for the PERFORM 3D and MVLEM models were adequate to simulate the global cyclic behavior of slender RC walls. In addition, the modeling parameters for the SFI-MVLEM and BTM models were found suitable to simulate the global cyclic behavior of both slender and squat walls. Therefore, the proposed parameters may be used in PBSD to estimate the cyclic lateral force-displacement behavior of planar RC walls.
2. Simulations from PERFORM 3D, MVLEM, and SFI-MVLEM presented small variations in RK_e, RV_{max}, and NSE_m when varying the discretization of the walls. Consequently, the responses from these models did not substantially improve when using finer meshes, and a coarse mesh can be used to simulate the global cyclic behavior of RC walls with these three models. In comparison, wall discretization had a large effect on the BTM simulations, and thus, the number of elements in length and height should be carefully selected when using this model. Values of m and n that result in a diagonal angle, θ_d close to the value calculated with Eq. (2-7) are needed to adequately simulate the hysteretic behavior of the walls.
3. The effective stiffness from the numerical simulations presented large variations and inaccuracy when compared with the experimental test results. The effective stiffness was in general highly overestimated by the MVLEM and SFI-MVLEM simulations, while it was mostly underestimated by PERFORM 3D and BTM. The large variability in effective stiffness was also observed from the experimental results of two identical RC walls, corroborating the comparatively large unpredictability of this evaluation metric.

4. The proposed Modified Nash-Sutcliffe Efficiency (NSE_m) was shown to be an appropriate metric to quantify the ability of the models to simulate the hysteretic behavior of RC walls, as it was able to accurately evaluate complex cyclic behaviors including strength and stiffness deterioration, and pinching. Additionally, limit values of NSE_m were defined to classify the hysteretic simulations, which agreed with qualitative evaluations of the predicted force-displacement curves. Based on these classifications, shear-uncoupled PERFORM 3D and MVLEM models provided good and satisfactory simulations of the hysteretic behavior for the studied slender walls, but provided poor simulations of the hysteretic behavior for the squat walls, because of the lack of shear-flexure interaction. In comparison, shear-coupled models SFI-MVLEM and BTM resulted in NSE_m factors of more than 0.90 (classified as satisfactory) for seven of the eight walls investigated.
5. The ultimate displacements predicted by the shear-coupled SFI-MVLEM and BTM models were within 8.6% error, showing the ability of these models to capture the reduction in lateral strength of three walls with different shear span-to-depth ratios.
6. Significant differences in computing time were found between the shear-coupled and shear-uncoupled models, where the latter ones were faster. Although the computing times required to simulate the considered rectangular RC walls were short (with the longest time over 2 minutes), the comparisons presented in the chapter are helpful in evaluating the numerical efficiency of the RC wall models.
7. Comparisons of the local behavior (i.e., base curvatures and strains) for the flexure-dominated wall RW2 simulated by MVLEM showed that the horizontal discretization

parameter, m has a negligible effect on the results. However, the local results were significantly influenced by the vertical discretization of the wall (parameter n), with larger numerical curvatures resulting from finer vertical discretizations. Significant improvements in curvature and tension strain accuracy and reduced sensitivity to the vertical discretization of the wall were obtained when using curvatures postprocessed according to Section 2.6.5.

CHAPTER 3:

REGULARIZED PLASTIC HINGE MODEL FOR NONLINEAR CYCLIC LATERAL LOAD ANALYSIS OF SLENDER RC WALLS

This chapter focuses on the development and evaluation of a regularized plastic hinge modeling approach to simulate the global and local behaviors of slender planar RC walls, as part of the second specific objective of this research. Previous research has shown that one of the biggest limitations of conventional (i.e., without material regularization) plastic hinge models is that the predicted ultimate (failure) displacement is extremely sensitive to the assumed plastic hinge length. Based on the analysis of eight previously tested walls, this chapter shows that the mesh-sensitivity of the analysis results can be significantly reduced by using regularized material models within the assumed plastic hinge length. As an important advantage over other regularized models, the proposed plastic hinge model can accurately predict both the global and local wall behaviors with no need for a separate normalization step for the curvatures. A sample regularized plastic hinge wall model is presented in Appendix A.5.

3.1 Introduction

Reinforced concrete (RC) walls are commonly used in buildings to resist seismic loads due to their large lateral stiffness, strength, and deformation capacity. The design

philosophy for slender RC walls is aimed to generate a ductile failure mechanism characterized by flexural yielding of the longitudinal reinforcement at the base. Despite this design philosophy, walls with non-ductile behavior have been observed after recent strong earthquakes (Rosita Jünemann et al., 2016; Kam et al., 2011; Sritharan et al., 2014; Wallace et al., 2012). Common failure modes have included crushing of the concrete, buckling of the longitudinal reinforcement, fracture of the longitudinal reinforcement, and lateral instability of the walls. Moreover, experimental testing has shown that slender RC walls with shear span-to-depth ratios greater than 2.0 are often governed by flexural failure modes characterized by concrete crushing and bar buckling (Alarcon et al., 2014; Birely, 2012) or bar fracture (Blandon et al., 2018; Yiqiu Lu et al., 2017).

Since the use of nonlinear numerical models is becoming common in earthquake engineering design practice, it is essential to develop effective modeling techniques that can accurately predict the global behavior as well as the local behavior of RC walls through failure (e.g., peak strength, ultimate displacement, concrete and reinforcement strains). It is also important that the modeling techniques present low computational demand (as compared to continuum finite element models) and that their modeling parameters require minimum calibration, so that they can be used to analyze a wide range of structures in design. Previous research towards these modeling goals for flexural RC walls have focused on compression-controlled (L. Lowes et al., 2016; Pugh et al., 2015) and tension-controlled (Yiqiu Lu & Henry, 2017, 2018) failure modes. These latter failure modes are common in lightly reinforced walls.

Developing efficient and practical modeling approaches that perform equally well independent of mesh size and number of integration points, referred to as mesh-objective models, has been an important research topic in recent years. Specifically, it is well known that in force-based beam-column elements, the ultimate displacement of a RC wall with compression-controlled failure is highly sensitive to the critical length (i.e., length of the critical integration point) over which the nonlinear behavior and failure of the element are concentrated after softening (Pugh et al., 2015). For this purpose, researchers have proposed regularized (i.e., modified) constitutive stress-strain models for confined concrete, unconfined concrete, and reinforcing steel based on experimentally-calibrated failure energy equations for these materials (Pugh et al., 2015; Jorge A. Vásquez et al., 2016). These previous studies have focused on minimizing the model mesh sensitivity in predicting the ultimate displacement of flexural walls under compression-controlled failure modes. However, one major drawback of mesh-objective models with regularized materials is that the curvature and local material strain response are still very sensitive to the mesh size, limiting the ability of these models to accurately capture the wall behavior at the section level (Coleman & Spacone, 2001; Pugh et al., 2015). To overcome this drawback, Coleman and Spacone (2001) proposed equations to normalize the curvatures in a postprocessing step based on an assumed plastic hinge length. This normalization is required because the length of the critical integration point in a mesh-objective model is not necessarily equal to the assumed plastic hinge length. The normalized section curvatures can then be used to obtain accurate predictions of the concrete and steel strains. The resulting analysis is a two-step process, involving: 1) regularization of the constitutive

stress-strain models to determine the global displacements from a mesh-objective structural analysis; and 2) postprocessing of the section curvatures to determine the material strains based on normalization equations and an assumed plastic hinge length.

The two-step process makes the structural analysis less practical to implement. Furthermore, the curvature normalization equations are approximate, are dependent on the structural configuration, and can be challenging to implement for cyclic behavior. Importantly, the need for the normalization of section curvatures has been lost or not emphasized in recent studies on regularized beam-column element models (Pugh et al., 2015; Jorge A. Vásquez et al., 2016), possibly giving users of these models a potentially false sense of accuracy in terms of curvatures and material strains.

Alternatively, beam-column elements with a plastic hinge integration method (M. H. Scott & Hamutçuoğlu, 2008; Michael H. Scott & Fenves, 2006; Michael H. Scott & Ryan, 2013) do not require curvature normalization because the length of the critical integration point can be matched to the assumed plastic hinge length. However, the ultimate displacement of a RC wall is highly sensitive to the assumed plastic hinge length (Almeida et al., 2016).

In accordance with the described limitations, the current chapter evaluates the effectiveness of material regularization (Coleman & Spacone, 2001; L. Lowes et al., 2016; Pugh et al., 2015) in force-based beam-column elements utilizing plastic hinge integration (M. H. Scott & Hamutçuoğlu, 2008; Michael H. Scott & Fenves, 2006; Michael H. Scott & Ryan, 2013) to simulate slender planar RC walls with softening responses. The focus is particularly on walls with compression-controlled failure modes for which the simulated

behavior is often highly mesh-sensitive (Coleman & Spacone, 2001). The advantages of combining material regularization with plastic hinge integration are: 1) sensitivity of the estimated global wall displacements (including the ultimate displacement) to the assumed plastic hinge length is significantly reduced; and 2) local curvatures and material strains can be estimated with no need for a subsequent postprocessing step. The proposed approach is described below and then critically evaluated using the measured results from eight previously-tested slender planar RC wall specimens. The results are also compared against conventional analyses without regularization of the material stress-strain curves.

3.2 Background

Line-element models are commonly used to simulate the nonlinear behavior of slender RC walls because of their simplicity and balance between accuracy and computational efficiency. The simplest approach involves lumped-plasticity models, where an elastic beam-column element is connected in series with nonlinear springs simulating plastic hinge regions with a predefined moment-rotation relationship. Moment-rotation backbone curves can be obtained from standard reference documents (e.g., ASCE 2017 (ASCE 41, 2017)), and are based on the wall geometry, axial force, shear force, and concrete confinement. However, major drawbacks of the lumped-plasticity modeling approach are: 1) it does not take into account variations in axial and shear forces during the analysis; 2) there is no standardized guidance for cyclic moment-rotation relationships (NIST, 2017c), and 3) spurious damping forces that lead to inaccurate results are generated in nonlinear time history analysis when Rayleigh damping is used (Chopra & McKenna, 2016).

In comparison with lumped-plasticity models, distributed-plasticity beam-column models with fiber sections (K. Kolozvari et al., 2018; Pozo et al., 2020; Pugh et al., 2015) provide a more accurate approach to simulate RC walls because they can capture the variation of axial force in the axial-flexural interaction. Additionally, the cyclic response of distributed-plasticity elements is simulated through cyclic uniaxial concrete and steel material constitutive stress-strain relationships, and no spurious damping forces are generated when Rayleigh damping is used (Chopra & McKenna, 2016). Distributed-plasticity models can be implemented using: 1) the displacement-based (DB) formulation, which assumes a linear curvature variation and a constant average axial deformation along the length of the element (Hellesland & Scordelis, 1981); and 2) the force-based (FB) formulation, which assumes a linear moment variation and a constant axial force along the length of the element (Spacone et al., 1996). The FB formulation is used in this study because equilibrium is strictly satisfied, as opposite to the DB formulation where equilibrium is satisfied in an average sense within an element.

Two disadvantages of distributed-plasticity models are: 1) shear deformations are uncoupled from axial-flexure interaction; and 2) highly mesh-sensitive softening responses can develop due to deformation localization from concrete crushing or rebar buckling in compression-controlled RC walls (Pugh et al., 2015). Nevertheless, shear deformations are relatively small in slender RC walls (Segura & Wallace, 2018a), and regularization techniques based on material failure energy criteria have been proposed to obtain objective global force-deformation responses using FB beam-column elements with the Gauss-Lobatto integration method (Pugh et al., 2015; Jorge A. Vásquez et al., 2016). Some of the

important concepts and developments for the nonlinear modeling of flexural RC walls are discussed below.

3.2.1 Plastic Hinge Length for RC Walls

Previous researchers have proposed different equations for the plastic hinge length, L_p of RC walls (Bohl & Adebar, 2011; Hoult et al., 2018; Hube et al., 2014; Kazaz, 2013; Massone & Alfaro, 2016; Paulay & Priestley, 1993; Takahashi et al., 2013; Wallace & Orakcal, 2002). These equations have been proposed to accurately simulate the ultimate displacement of RC walls, and not necessarily to match the actual length where deformations and damage concentrate, as has been reported in some experimental studies (Arteta et al., 2014; Hube et al., 2014; Segura & Wallace, 2018b). Among the available plastic hinge length equations for RC walls, Eq. (3-1) (Paulay & Priestley, 1993), Eq. (3-2) (Bohl & Adebar, 2011), and Eq.(3-3) (Kazaz, 2013) were selected to calculate a mean plastic hinge length, $L_{p,mean}$ in this study. Importantly, acknowledging that several L_p equations are available in the literature, a sensitivity analysis considering a range between 0.75 and 1.25$L_{p,mean}$ was performed. In Eq. (3-1) to Eq. (3-3), L_w is the length of the wall, M/V is the ratio between the moment and shear at the expected plastic hinge region and is equal to the effective wall height, H_{eff}, $P/(f_c' A_g)$ is the axial load ratio, ρ_{sh} is the horizontal web reinforcement ratio, f_y is the steel yield strength, and f_c' is the unconfined concrete compression strength.

$$L_p = 0.2L_w + 0.044(M/V) \quad (3\text{-}1)$$

$$L_p = (0.2L_w + 0.05(M/V))\left(1 - 1.5\frac{P}{f_c' A_g}\right) \leq 0.8L_w \quad (3\text{-}2)$$

$$L_p = 0.27L_w\left(1 - \frac{P}{f_c' A_g}\right)\left(1 - \frac{f_y \rho_{sh}}{f_c'}\right)\left(\frac{M/V}{L_w}\right)^{0.45} \quad (3\text{-}3)$$

3.2.2 Regularization of Materials Stress-Strain Relationship

The concept of constant fracture energy has been widely used in continuum finite-element models to regularize the mesh-dependent behavior of concrete in tension. The same concept was also applied by Coleman and Spacone (2001) to regularize the concrete strain-stress behavior in compression, and recently by Pugh et al. (2015) and Vasquez et al. (2016), who also proposed to regularize the post yielding slope of the reinforcing steel stress-strain curve. Most recently, the concrete and reinforcing steel regularization approaches proposed by Pugh et al. (2015) have been adopted by NIST (2017c) as described below. More details about regularized materials can be found elsewhere (Pugh et al., 2015).

The need to regularize the concrete compressive stress-strain constitutive behavior to reduce model mesh-sensitivity when material softening occurs can be explained by considering unconfined concrete cylinders subjected to uniform compression through failure. Experimental observations have shown that the stress versus displacement responses of cylinders with different lengths are similar because damage concentrates in a localized region. However, the stress versus strain response is dependent on the gage length used to measure the strains. Therefore, the average post-peak stress-strain curves obtained by dividing the total axial displacement with the cylinder length depend on the length of the tested specimen (Jansen & Shah, 2002; Nakamura & Higai, 2001). Such studies (Jansen

& Shah, 2002; Nakamura & Higai, 2001) have demonstrated that the unconfined concrete crushing energy, Gf_c is a material property. Therefore, regularization of concrete response in a force-based beam-column element can be accomplished by defining the strain at residual stress, ε_u as a function of a critical length, L_{cr} and the concrete crushing energy (refer to Figure 3.1a). However, it is important to note that: 1) appropriate values of Gf_c and Gf_{cc} (crushing energy for confined concrete) should be calibrated from experimental results; and 2) even though the post-peak global force-displacement responses from regularized models that are meshed differently (i.e., with different L_{cr}) may be objective, the local material strains will still be different (i.e., non-objective local behaviors) (Coleman & Spacone, 2001; Jorge A. Vásquez et al., 2016).

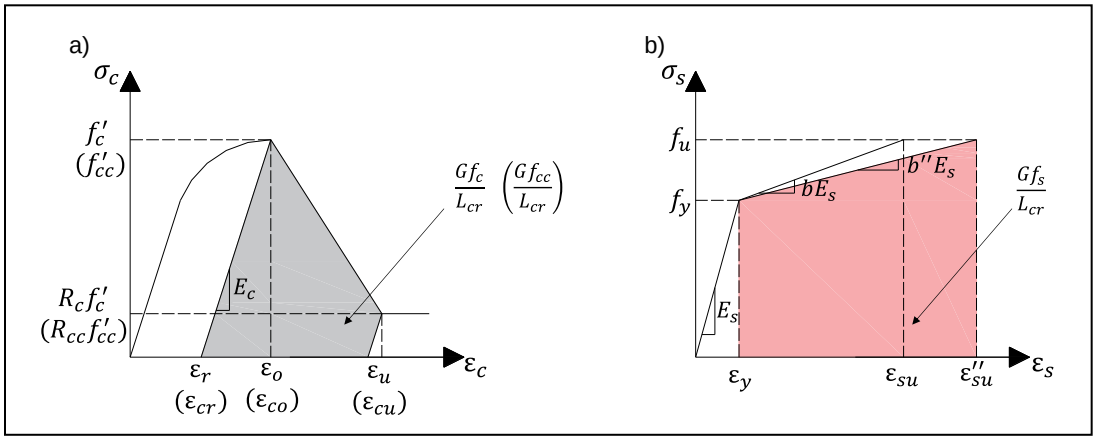

Figure 3.1: Regularization of material stress-strain relationships. a) Unconfined and confined concrete (terms in parentheses correspond to confined concrete); b) reinforcing steel. Based on NIST (2017c).

If a linear post-peak concrete stress-strain relationship and an elastic unloading response are assumed (Figure 3.1a), the regularized ultimate strain for unconfined concrete ε_u, at residual stress $R_c f_c'$, can be calculated using Eq. (3-4) to obtain a constant concrete crushing energy Gf_c. This equation was derived by equating the shaded area of Figure 3.1a to Gf_c/L_{cr}, and reveals that a larger value of ε_u is required in a model with a smaller L_{cr}. A similar equation for confined concrete can be obtained by replacing the corresponding terms in parentheses in Figure 3.1a.

$$\varepsilon_u = \frac{1}{1+R_c} \cdot \left[\frac{2Gf_c}{f_c' L_{cr}} - \frac{f_c'}{E_c} + (1+R_c)\varepsilon_o + R_c^2 \frac{f_c'}{E_c} \right] \tag{3-4}$$

Note that in a force-based beam-column element, the critical length, L_{cr} corresponds to the length (or weight) of the integration point where the nonlinear deformations concentrate. In a cantilever wall with uniform reinforcement along its height, L_{cr} is the length of the bottommost integration point, where the moments are largest (Coleman & Spacone, 2001).

Pugh et al. (2015) proposed Eq. (3-5) and Eq. (3-6) for the crushing energy of unconfined and confined concrete, Gf_c and Gf_{cc}, respectively, based on comparisons between numerical and measured ultimate displacements of slender planar RC walls. They utilized FB beam-column elements with the Gauss-Lobatto integration method. Eq. (3-5) was proposed based on the results of two walls without confinement, where f_c' is in MPa, whereas Eq. (3-6) was proposed based on the results of eight walls with confined boundary regions. These concrete crushing energy equations were adopted by NIST (2017c).

$$Gf_c = 2f_c' \tag{3-5}$$

$$Gf_{cc} = 1.70\ Gf_c \tag{3-6}$$

The form of Eq. (3-6) implies that the confined concrete crushing energy only depends on the unconfined concrete strength, f_c' and not on the amount of confining steel. Recognizing this limitation, Lowes et al. (2016) proposed Eq. (3-7) for the confined concrete crushing energy based on the results of five walls simulated with the *Shear Wall* element available in Perform 3D. Eq. (3-7) considers the effect of confinement by using the confined concrete strength ratio, $K = f_{cc}'/f_c'$ according to Mander et al. (1988) and has a lower limit of Gf_c. It should be noted that the *Shear Wall* element in Perform 3D is a four-node element that uses a displacement-based formulation, and Eq. (3-7) has not been evaluated in a force-based beam-column element, which is the element used in this study.

$$Gf_{cc} = Gf_c \ \leq 5(K - 0.85)\ Gf_c \leq 2.5\ Gf_c \tag{3-7}$$

The tensile stress-strain relationship of reinforcing steel presents hardening behavior after yielding and before the ultimate stress, f_u. Since larger strains are accompanied by larger stresses in this hardening range, localization of damage is not expected before reaching the ultimate stress, resulting in a spread of yielding. Despite this distribution of yielding, Pugh et al. (2015) demonstrated that when concrete in compression softens and deformations localize, reinforcing steel has to be also regularized to improve model objectivity for the global behavior of RC walls. Pugh et al. proposed the post-yield ultimate strain and slope of the steel stress-strain relationship to be regularized using Eq. (3-8) and Eq. (3-9), respectively (Figure 3.1b). Eq. (3-8) requires a critical length, L_{cr} and an assumed gage length of L_{gage} = 200 mm. This steel regularization was adopted by NIST (2017c).

$$\varepsilon''_{su} = \varepsilon_y + \left(\frac{L_{gage}}{L_{cr}}\right)\left(\varepsilon_{su} - \varepsilon_y\right) \tag{3-8}$$

$$b'' = \frac{f_u - f_y}{E_s\left(\varepsilon''_{su} - \varepsilon_y\right)} = b\,\frac{\left(\varepsilon_{su} - \varepsilon_y\right)}{\left(\varepsilon''_{su} - \varepsilon_y\right)} \tag{3-9}$$

3.2.3 Normalization of Section Curvatures

To obtain objective local section curvatures (and strains) from force-based beam-column elements with regularized materials, Coleman and Spacone (2001) developed a curvature normalization (postprocessing) method. This normalization step is required because the critical length, L_{cr} of a mesh-objective model does not necessarily match the assumed plastic hinge length, L_p where damage concentrates. The curvature normalization approach is based on the assumption that the total curvature (ϕ) has an elastic (ϕ_e) and an inelastic (ϕ_i) component, where the latter is concentrated in the model over L_{cr}. For a cantilever wall with uniform reinforcement along its height, L_{cr} is the length (or weight) corresponding to the first integration point above the base. Coleman and Spacone (2001) proposed to estimate the normalized curvatures using Eq. (3-10), where the inelastic curvatures are scaled by the factor sf given in Eq. (3-11). In this latter equation, H_{eff} is the height of the wall from the base to the point of zero moment, and L_p is the assumed plastic hinge length of the wall.

$$\phi = \phi_e + sf\ \phi_i \tag{3-10}$$

$$sf = \frac{L_{cr}\left(2H_{eff} - L_{cr}\right)}{L_p\left(2H_{eff} - L_p\right)} \tag{3-11}$$

3.3 Experimental Walls

Eight previously-tested RC walls, presented in Table 3.1, were used to evaluate the numerical simulations in this chapter. All of these walls are planar and slender, with shear span-to-depth ratios $[M/(VL_w)]$ equal to or greater than 2.0. Walls that did not have lap splices near the base, failed through a compression-controlled mode (concrete crushing and/or bar buckling), and showed a lateral strength reduction of at least 20% of the maximum strength were selected. Therefore, the ultimate failure displacement of the selected walls was reached after a range of softening behavior. In Table 3.1, $K = f'_{cc}/f'_c$ is the confined concrete strength ratio calculated according to Mander et al. (1988), and δ_u is the ultimate lateral displacement of the wall at 20% strength reduction from the maximum strength. For wall WP1, the ultimate displacement was taken at 15% strength reduction during positive loading because bar buckling and significant crushing were reported at this displacement level (Segura, 2017). Note that walls WP1, WP2, and WP3 had nonsymmetrical confined toe regions at the two ends.

Values of plastic hinge length (L_p) calculated for the eight walls using Eq. (3-1) to Eq. (3-3) are presented in Table 3.2, as well as the mean of the calculated values for each wall.

Table 3.1: Experimental walls

Wall ID	Reference	t [mm]	L_w [mm]	[a]H_{eff} [mm]	$\frac{M}{VL_w}$	$\frac{P}{f_c' A_g}$	f_c' [MPa]	f_y [MPa]	K	δ_u [mm]	Scaling Factor	[d]Failure Mode
WSH4	(Dazio et al., 2009)	150	2000	4560	2.3	0.057	40.9	576	1.00	73.0	0.50	CS
WSH6	(Dazio et al., 2009)	150	2000	4520	2.3	0.108	45.6	576	1.27	92.9	0.50	CS
RW1	(Thomsen & Wallace, 2004)	102	1219	3810	3.1	0.102	31.6	434	1.18	82.2	0.25	S
WP1	(Segura & Wallace, 2018b)	152	2286	8560	3.7	0.096	35.80	506	1.30 ([b]1.31)	34.9	0.50	CS
WP2	(Segura & Wallace, 2018b)	152	2286	8560	3.7	0.083	41.7	506	1.49 ([b]1.50)	43.7	0.50	CS
WP3	(Segura & Wallace, 2018b)	152	2286	8560	3.7	0.081	42.4	506	1.28 ([b]1.39)	37.6	0.50	CS
WR10	(Oh et al., 2002)	200	1500	3000	2.0	0.076	36.2	449	1.19	86.1	[c]NR	CS
HPCW03	(Deng et al., 2008)	100	1000	2100	2.1	0.175	57.2	433	1.30	52.8	[c]NR	C

[a] Effective height, H_{eff} = height between the base of the wall to the point of zero moment

[b] Values in parentheses correspond to the west boundary region (Segura & Wallace, 2018b)

[c] NR= Not reported

[d] CS = concrete crushing and steel buckling; C = concrete crushing; S = steel buckling

Table 3.2: Plastic hinge length of the analyzed walls

Wall ID	L_p (mm)			
	Eq. (3-1)	Eq. (3-2)	Eq. (3-3)	$L_{p,mean}$
WSH4	601	575	523	566
WSH6	599	525	494	539
RW1	411	368	430	403
WP1	834	757	645	745
WP2	834	775	662	757
WP3	834	777	664	758
WR10	432	399	414	415
HPCW03	292	225	306	274

3.4 Element and Material Models

The force-based (FB) beam-column element in OpenSees (McKenna et al., 2000) was used to model the eight experimental walls. This is a two-node line-element where fiber cross sections are assigned at different integration points (IP) along the length, and plane-section deformations are assumed at each IP. The locations and weights of the IPs depend on the integration method (e.g., Gauss-Lobatto, Gauss-Legendre, Gauss-Radau, modified Gauss-Radau). Each fiber cross section simulates the axial-flexural behavior of

the wall, and is divided into a number of fibers, where nonlinear concrete and steel uniaxial stress-strain material relationships are assigned (see Figure 3.2).

In this study, unconfined and confined concrete fibers were simulated with the *Concrete02* (Yassin, 1994) material in OpenSees. The pre-peak compressive stress-strain relationship in *Concrete02* is defined by the Hognestad parabola (see Table 3.3). The strain at peak strength was calculated as $\varepsilon_o = 2f_c'/E_c$ (or $\varepsilon_{co} = 2f_{cc}'/E_c$ for confined concrete) to achieve a Young's modulus of $E_c = 4700\sqrt{f_c'}$ (in MPa units) according to ACI 318 (2019). The post-peak stress-strain relationship is linear to a residual compressive stress of $R_c f_c'$ (or $R_{cc} f_{cc}'$ for confined concrete). The tensile response is bilinear, where the tensile strength was defined as $0.33\sqrt{f_c'}$ (in MPa units) as in Pugh et al. (2015), and the post-cracking behavior considers zero residual tensile stress.

Steel reinforcement was simulated with the Menegotto and Pinto (1973) model, which is available in OpenSees as the *Steel02* material. The parameters of the *Steel02* model are defined elsewhere (Filippou et al., 1983; Menegotto & Pinto, 1973). The *MinMax* material (parameter β in Table 3.3) was used in combination with *Steel02* to simulate complete loss of the steel compressive stress, as a simple model to represent the effect of rebar buckling, when the ultimate strain of confined concrete fiber immediately adjacent to the steel fiber was exceeded (Pugh et al., 2015). Other models that realistically simulate the process of rebar buckling can be found in (Dhakal & Maekawa, 2002; Kim & Koutromanos, 2016; Massone & Moroder, 2009).

The constitutive relationships of the materials used to simulate the axial-flexural behavior of the walls in this study are presented in Table 3.3. The reported test-day material

properties for concrete (e.g., f_c') and for steel (e.g., f_y, f_u, and ε_{su}) were used to define these constitutive models. The shear behavior was simulated using a linear-elastic material with an effective shear modulus of $G_{eff} = 0.04E_c$, as recommended elsewhere (PEER/ATC, 2010; Pugh et al., 2015).

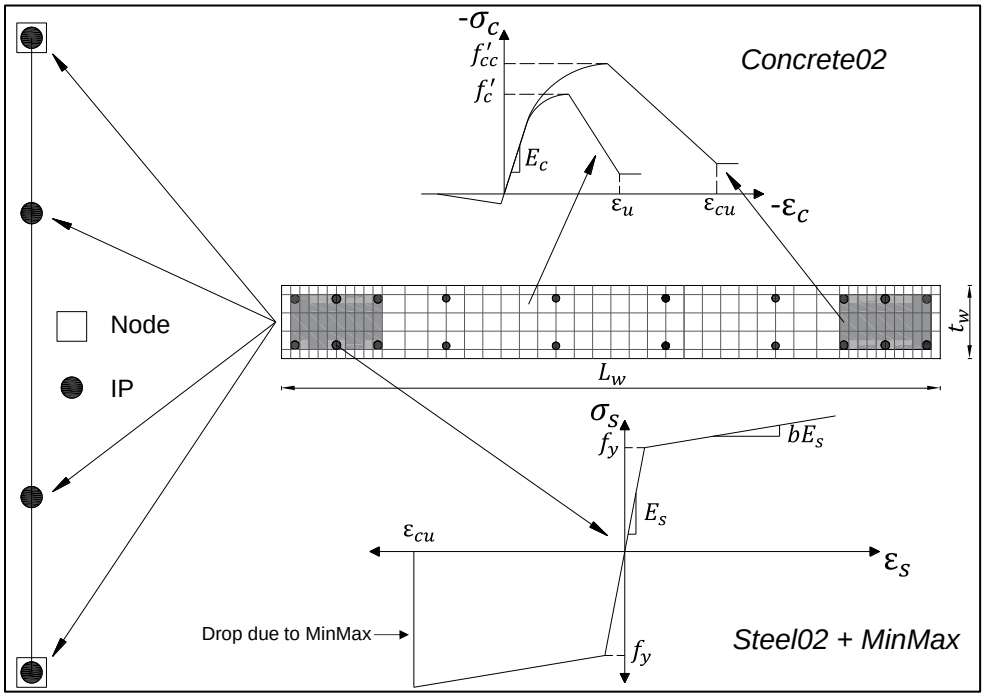

Figure 3.2: Fiber section and material constitutive models.

Table 3.3: Material constitutive relationships. Note that concrete compression stress-strain relationship simulated with *Concrete02* is presented here using positive values.

Material	Constitutive relationship	
Concrete02	$\sigma_c(\varepsilon_c) = f_c' \left[\frac{2\varepsilon_c}{\varepsilon_o} - \left(\frac{\varepsilon_c}{\varepsilon_o}\right)^2\right]$	$0 \le \varepsilon_c \le \varepsilon_o$
	$\sigma_c(\varepsilon_c) = f_c' + \frac{f_c' - R_c f_c'}{\varepsilon_o - \varepsilon_u}(\varepsilon_c - \varepsilon_o)$	$\varepsilon_o < \varepsilon_c \le \varepsilon_u$
	$\sigma_c(\varepsilon_c) = R_c f_c'$	$\varepsilon_c > \varepsilon_u$
Steel02 + *MinMax*	$\sigma_s^*(\varepsilon^*) = \beta\left[b\varepsilon^* + \frac{(1-b)\varepsilon^*}{\left(1+\varepsilon^{*R}\right)^{1/R}}\right]$	
	$\beta = 1; once\ \varepsilon_s < \varepsilon_{cu}, \beta = 0$	

3.5 Effect of Material Regularization in Gauss-Lobatto Integration Method

The FB beam-column element with Gauss-Lobatto integration method has been commonly used to model isolated RC walls (Coleman & Spacone, 2001; Pugh et al., 2015; Jorge A. Vásquez et al., 2016) because it includes integration points located at the ends of the element, where the maximum moments occur. Furthermore, all of the previous work on material regularization for FB beam-column elements has used the Gauss-Lobatto integration method. A schematic representation of a cantilever wall with different number

of Gauss-Lobatto integration points (NIP) is presented in Figure 3.3. The location and weight of each IP are tabulated in the same figure. Since the maximum moment in a cantilever wall occurs at the base, the critical integration point is the bottommost one, with its corresponding critical length, L_{cr} highlighted in the figure. It can be seen that the critical length is shorter for models with a greater number of IPs.

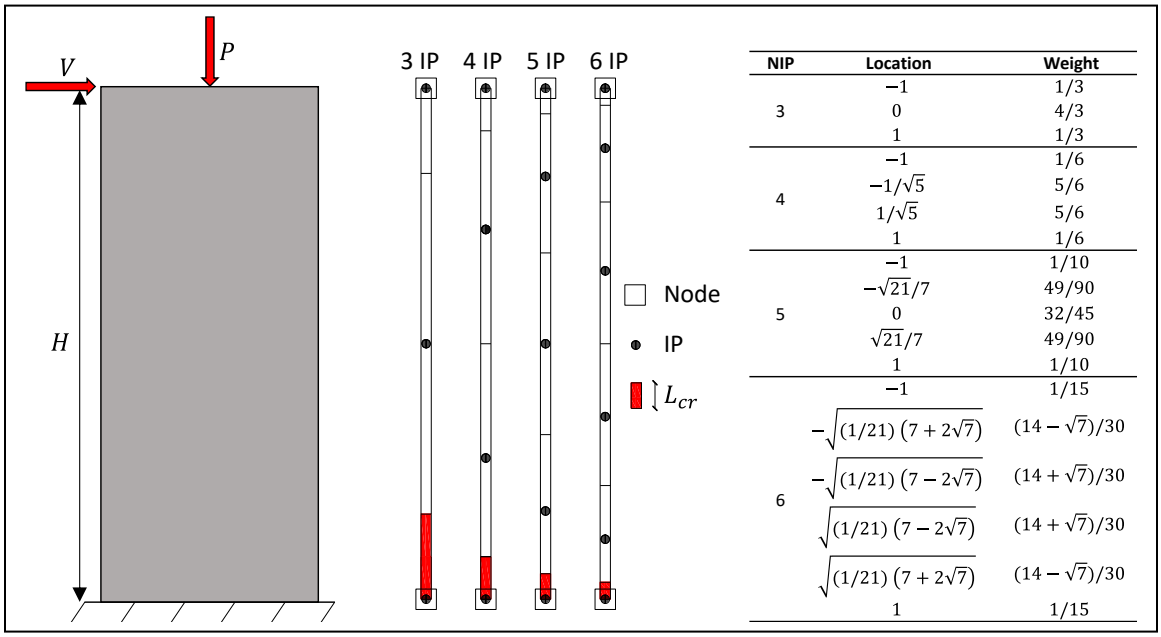

NIP	Location	Weight
3	-1	$1/3$
	0	$4/3$
	1	$1/3$
4	-1	$1/6$
	$-1/\sqrt{5}$	$5/6$
	$1/\sqrt{5}$	$5/6$
	1	$1/6$
5	-1	$1/10$
	$-\sqrt{21}/7$	$49/90$
	0	$32/45$
	$\sqrt{21}/7$	$49/90$
	1	$1/10$
6	-1	$1/15$
	$-\sqrt{(1/21)\,(7+2\sqrt{7})}$	$(14-\sqrt{7})/30$
	$-\sqrt{(1/21)\,(7-2\sqrt{7})}$	$(14+\sqrt{7})/30$
	$\sqrt{(1/21)\,(7-2\sqrt{7})}$	$(14+\sqrt{7})/30$
	$\sqrt{(1/21)\,(7+2\sqrt{7})}$	$(14-\sqrt{7})/30$
	1	$1/15$

Figure 3.3: Schematic representation of a cantilever wall with different number of Gauss-Lobatto IPs.

Figure 3.4 shows the monotonic pushover analysis results of wall WSH4 (Dazio et al., 2009). Four different models of the wall were developed; each with a single element but using three, four, five, and six Gauss-Lobatto integration points (refer to Figure 3.3). The legend of the figure shows the resulting critical length, L_{cr} at the base of each model. Materials without regularization (WO), with only concrete regularization (C), and with

both concrete and steel regularization (CS) were considered in the analyses. The regularization of concrete and steel materials are shown in Figure 3.1.

The monotonic pushover analyses were conducted using displacement-control loading protocol until a reduction of 20% in lateral load (V) was reached. It can be seen from Figure 3.4 that when the same material stress-strain relationships without regularization (WO) were used for the four models with the different L_{cr}, the global lateral load, V versus displacement, δ response (Figure 3.4 a1) was nonobjective, i.e., the models with different L_{cr} predicted different responses. However, the local moment-curvature response at the critical IP for the models without material regularization (Figure 3.4 b1) was objective. This difference is because the sectional behavior depends on the material stress-strain relationships, the axial force, and the moment at the location of the IP, which are the same for the critical IP regardless of the total number of IPs. However, the global response depends not only on the sectional behavior but also the integration length, which depends on the number of IPs, as shown in Figure 3.3.

Once the concrete was regularized, the global behavior in Figure 3.4 a2 became objective, with further (albeit considerably smaller) improvements when steel was also regularized (Figure 3.4 a3). However, when regularized material models were used, the local moment-curvature behavior was nonobjective (Figure 3.4 b2, b3), limiting the performance evaluation of the wall based on section curvature and material strains.

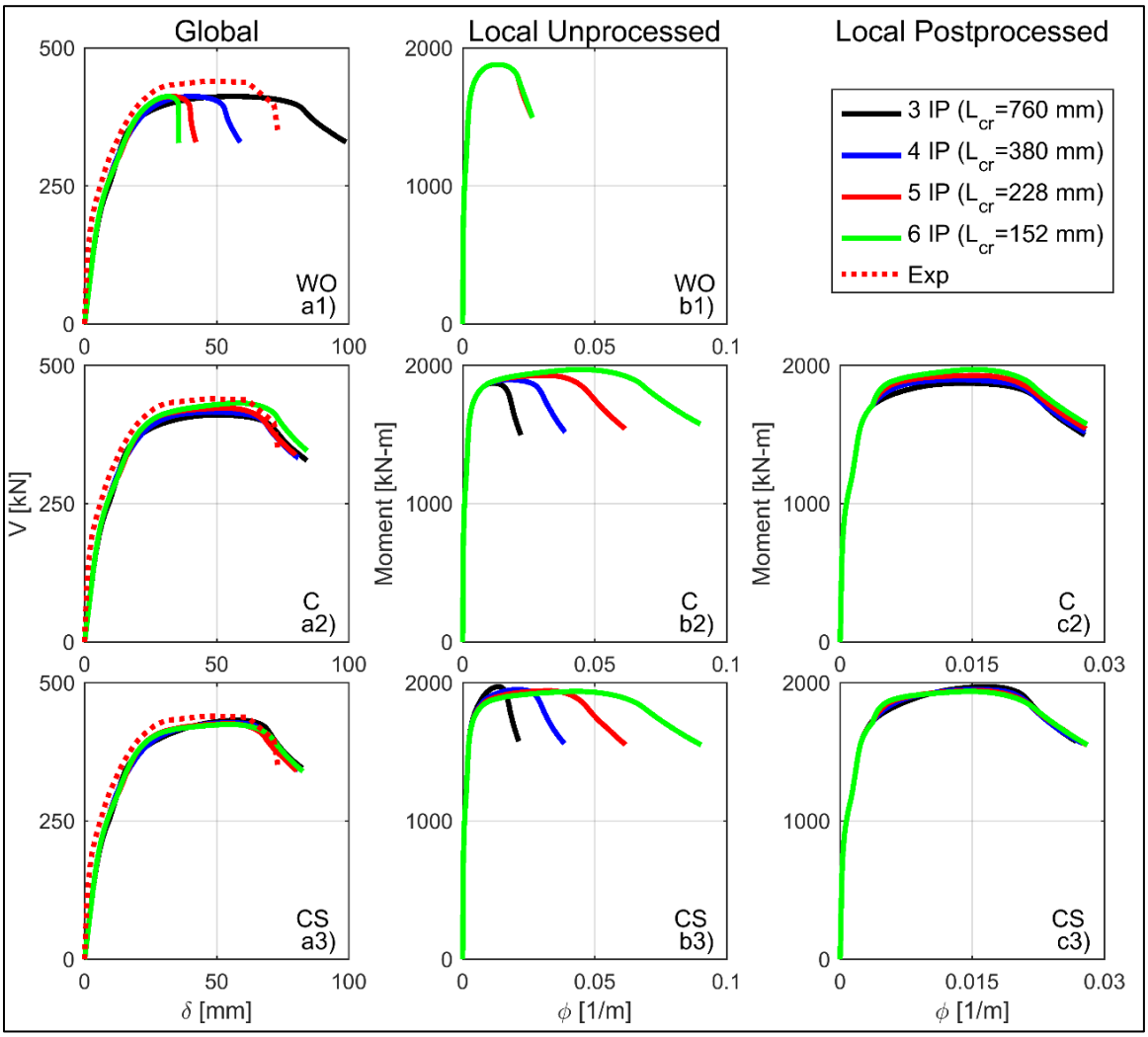

Figure 3.4: Effect of material regularization on the Gauss-Lobatto integration method (WO: without regularization, C: with concrete regularization, CS: with concrete and steel regularization): a) Global response; b) Local unprocessed response at critical IP; c) Local postprocessed (normalized) response at critical IP.

Using Eq. (3-10) and Eq. (3-11) with the mean plastic hinge length ($L_{p,mean} = 566$ mm) from Table 3.2, the normalized local moment-curvature responses from the regularized models of wall WSH4 are presented in Figure 3.4 c2 and c3. It can be seen that the normalized moment-curvature results of the monotonic pushover analyses were

objective. However, it may be challenging to implement Eq. (3-10) and Eq. (3-11) for cyclic analysis. Furthermore, the assumptions involved in Eq. (3-11) may not be appropriate for walls interacting with other elements (e.g., coupled walls) since the displacement contribution due to the flexibility of the other elements is not considered in the equation. These limitations can be overcome by combining material regularization with plastic hinge integration, as described below.

3.6 Effect on Material regularization in Plastic Hinge Integration Method

If the critical length, L_{cr} in a model matches the plastic hinge length, L_p, over which damage is assumed to concentrate, then such a model will result in objective global as well as local responses without requiring normalization of the curvatures because the scale factor presented in Eq. (3-11) will be 1.0. However, different equations for L_p are available in the literature [e.g., Eq. (3-1) to Eq. (3-3)], and the analysis results can vary greatly based on the selected L_p. This sensitivity of the nonlinear analysis results to L_p can be significantly reduced by using regularized materials and the plastic hinge integration method. The accuracy and advantages of the proposed approach are presented below by comparing analysis results of the eight walls listed in Table 3.1 with results from conventional (i.e., unregularized) materials.

The Gauss-Radau integration method has been used in recent studies to simulate the nonlinear lateral load behavior of RC walls (Parra et al., 2019). In order to ensure that the critical length exactly matches the desired plastic hinge length, the FB beam-column element with the modified Gauss-Radau plastic hinge integration method (M. H. Scott &

Hamutçuoğlu, 2008; Michael H. Scott & Fenves, 2006; Michael H. Scott & Ryan, 2013) was used with both regularized and unregularized materials. The modified Gauss-Radau integration method uses one element with six integration points along its length (M. H. Scott & Hamutçuoğlu, 2008), as follows: 1) two Gauss-Radau points with weights scaled by four at each end of the element, and 2) two Gauss-Legendre points in the interior part of the element. The locations and weights of the six integration points in the modified Gauss-Radau method are presented in Eq. (3-12) and are schematically presented in Figure 3.5.

$$\begin{aligned} x = &\quad \{\ 0; \quad \frac{8L_{pI}}{3}; \quad 4L_{pI} + \frac{L_{int}\left(3-\sqrt{3}\right)}{6}; \quad 4L_{pI} + \frac{L_{int}\left(3+\sqrt{3}\right)}{6}; \quad L - \frac{8L_{pJ}}{3}; \quad L\} \\ w = &\quad \{L_{pI}; \quad 3L_{pI}; \quad 0.5L_{int}; \quad 0.5L_{int}; \quad 3L_{pJ}; \quad L_{pJ}\} \end{aligned} \tag{3-12}$$

Where, H is the total length of the element, L_{pI} and L_{pJ} are the plastic hinge lengths specified by the user at the two ends, and the interior length of the element is determined as $L_{int} = H - 4L_{pI} - 4L_{pJ}$. An important advantage of the modified Gauss-Radau method is that it includes integration points at the element ends (i.e., x_1 and x_6 in Figure 3.5), thus accurately modeling the maximum moment at the base of a cantilever wall. Note that $L_{pJ} = 0$ was used in this study because a cantilever wall has zero moment at the top. This also ensured that L_{int} remained positive for all of the plastic hinge lengths (i.e., L_{pI}) investigated in this chapter.

The following sections present the results of using the modified Gauss-Radau plastic hinge integration method with unregularized and regularized concrete and steel materials. As stated previously, the experimentally reported test-day material properties for

concrete (e.g., f_c') and steel (e.g., f_y, f_u, and ε_{su}) were used to define the unregularized and regularized stress-strain constitutive relationships.

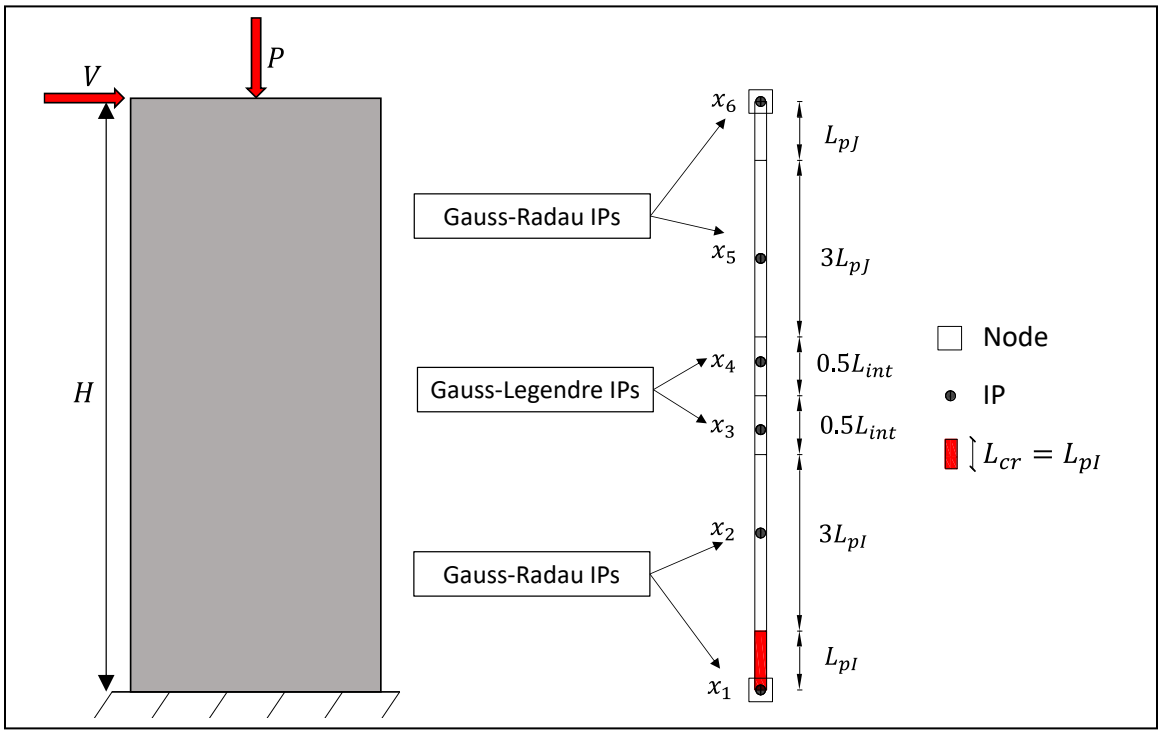

Figure 3.5: Locations and integration weights for the modified Gauss-Radau integration method.

3.6.1 Unregularized Materials

Cyclic pushover analyses of the eight walls from Table 3.1 were conducted using the FB beam-column element with the described plastic hinge integration method with unregularized concrete and steel materials. Assumed plastic hinge lengths equal to $L_{p,mean}$ (Table 3.2) were used to define the location and weights of the integration points (see Figure 3.5) of each wall. The peak confined concrete strength, f_{cc}' as well as the ultimate compression strains ε_u and ε_{cu} (for unconfined and confined concrete, respectively) were

determined using three models: Priestley et al. (1996), Saatcioglu and Razvi (1992), and Scott et al. (1982). The stress-strain relationships from the three models, for unconfined and confined concrete of wall WP1, are shown in Figure 3.6. The ultimate concrete compression strain, ε_u or ε_{cu}, was assumed to occur at a residual stress of 20% (i.e., $R_c = R_{cc} = 0.2$) of the respective peak stress (i.e., $0.2f_c'$ and $0.2f_{cc}'$) for unconfined and confined concrete, respectively. Note that this assumption is not consistent with Priestley et al. (1996), where a greater confined concrete stress at ultimate strain is assumed following the Popovics equation. Furthermore, the strain corresponding to the peak strength was calculated as $\varepsilon_o = 2f_c'/E_c$ and $\varepsilon_{co} = 2f_{cc}'/E_c$ to obtain a predetermined value of E_c when using the *Concrete02* material in OpenSees. The modulus of elasticity for the three models and for both unconfined and confined concrete was calculated as $E_c = 4700\sqrt{f_c'}$ (in MPa units) according to ACI 318 (2019).

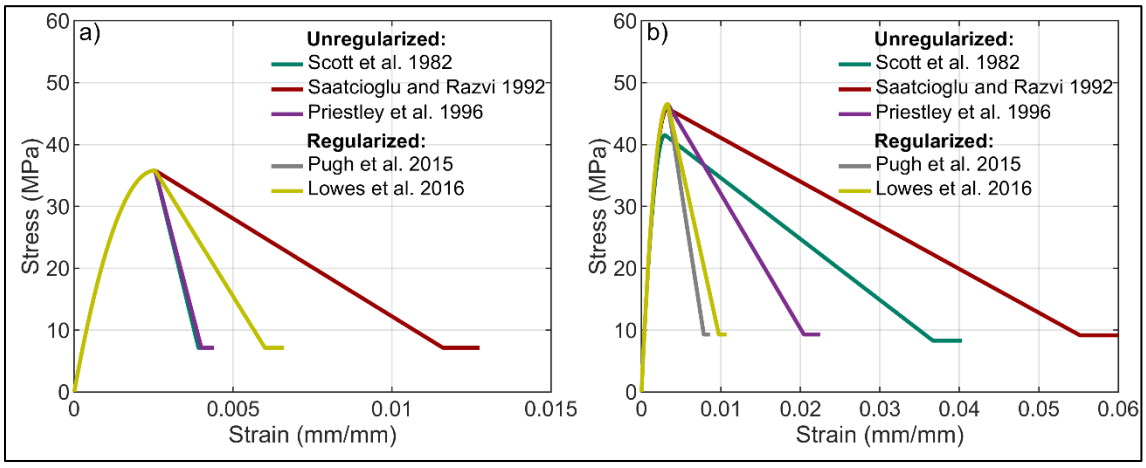

Figure 3.6: Concrete material constitutive models for wall WP1 (east boundary region). a) Unconfined concrete, b) confined concrete.

The numerical-to-experimental ultimate displacement ratios, $R\delta_u = \delta_{u,num}/\delta_{u,exp}$ for the eight walls using unregularized materials and $L_{p,mean}$ from Table 3.2 are presented in Table 3.4. The models with f'_{cc}, ε_u, and ε_{cu} from Saatcioglu and Razvi (1992) resulted in highly unconservative overpredictions of the measured ultimate displacement for all walls, while the models with f'_{cc}, ε_u, and ε_{cu} from Scott et al. (1982) and Priestley et al. (1996) resulted in unconservative overpredictions for all but two of the walls (WSH4 and HPCW03). On average, the best results were obtained using f'_{cc}, ε_u, and ε_{cu} from Priestley et al. (1996), which assumes an ultimate strain of ε_u=0.004 for unconfined concrete and Eq. (3-13) for confined concrete, where, ρ_s is the total volumetric ratio of confining steel and ε_{su} is the confining steel strain at maximum tensile stress, which was taken as 9%.

$$\varepsilon_{cu} = 0.004 + \frac{1.4\rho_s f_y \varepsilon_{su}}{f'_{cc}} \tag{3-13}$$

Figure 3.7 presents the hysteretic lateral force versus displacement behaviors of the eight walls, where the numerical results (black lines) were obtained using the unregularized concrete materials with f'_{cc}, ε_u, and ε_{cu} from Priestley et al. (1996). The predicted hysteretic behaviors of the walls prior to substantial strength loss were similar to the measured behaviors (red lines). However, the predicted ultimate displacement at failure was substantially different and unconservative for the majority of the walls. From Table 3.4 and Figure 3.7, it is clear that unregularized plastic hinge models are not adequate to predict the ultimate displacement of the considered slender planar RC walls.

Table 3.4: Numerical-to-experimental ultimate displacement ratios, $R\delta_u = \delta_{u,num}/\delta_{u,exp}$ obtained with simulations using $L_{p,mean}$.

Wall ID	Unregularized Materials			Regularized Materials	
	Scott et al. (1982)	Saatcioglu and Razvi (1992)	Priestley et al. (1996)	Pugh et al. (2015)	Lowes et al. (2016)
WSH4	0.63	1.68	0.68	1.10	1.10
WSH6	1.47	2.19	1.36	0.86	0.98
RW1	1.26	2.23	1.40	1.15	1.13
WP1	2.56	4.16	1.93	0.86	0.98
WP2	3.27	5.47	2.46	0.80	1.03
WP3	2.55	4.39	2.74	0.92	1.06
WR10	2.21	3.33	1.86	1.00	1.00
HPCW03	0.88	1.99	0.86	0.87	1.04
Mean	1.85	3.18	1.66	0.94	1.04
St. Dev.	0.93	1.38	0.73	0.13	0.05

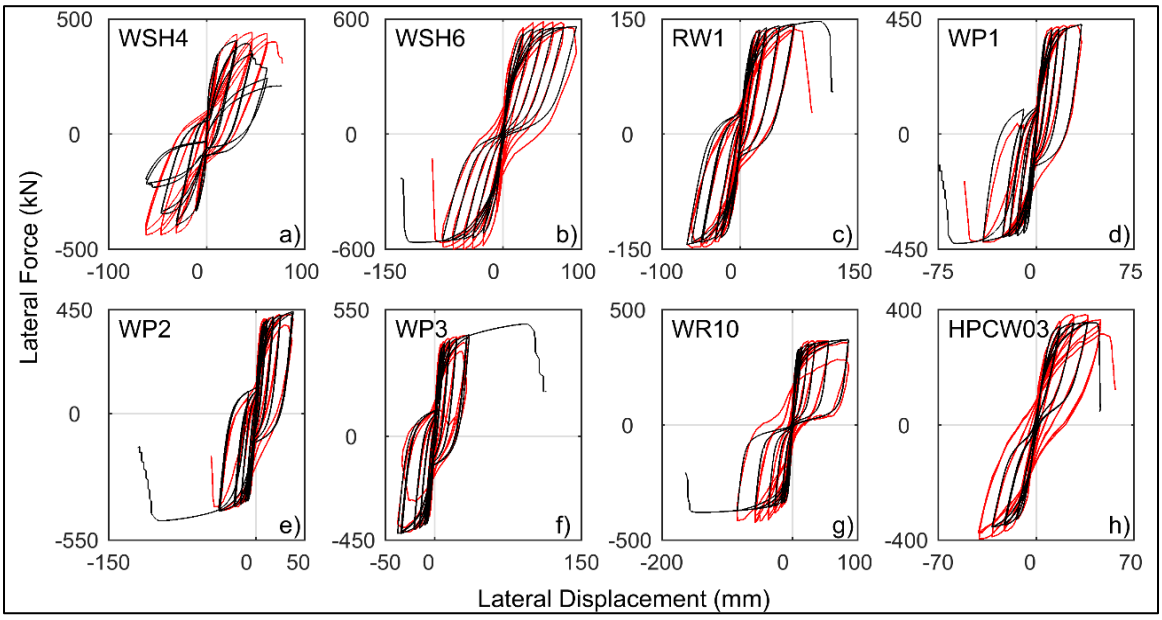

Figure 3.7: Lateral force-displacement behaviors using plastic hinge integration method and unregularized materials based on Priestley et al. (1996) (Measured results in red and numerical results in black).

3.6.2 Regularized Materials

This section presents the analysis results of the eight walls using the same FB beam-column element with the modified Gauss-Radau plastic hinge integration method described above, but with regularized concrete and steel materials. Since regularization only affects the post-peak behavior of concrete, the unconfined concrete stress-strain relationships up to the peak point were the same as those in the unregularized plastic hinge models. Similarly, the regularized confined concrete stress-strain relationships up to the peak point were the same as the unregularized confined concrete relationship with f'_{cc} based on Priestley et al. (1996), which uses the confined strength ratio, $K = f'_{cc}/f'_c$ according to Mander et al. (1988). For the post-peak strain-stress behavior, regularization was done

using a constant concrete crushing energy for both unconfined and confined concrete. The unconfined concrete crushing energy in Eq. (3-5) was used in combination with two values of confined concrete crushing energy per Pugh et al. (2015) [Eq. (3-6)] and Lowes et al. (2016) [Eq. (3-7)]. Based on these Gf_c and Gf_{cc} values, the ultimate strains of unconfined and confined concrete were calculated using Eq. (3-4). The ultimate concrete compression strain, ε_u or ε_{cu}, was assumed to occur at a residual stress of 20% (i.e., $R_c = R_{cc} = 0.2$) of the respective peak stress (i.e., $0.2f_c'$ and $0.2f_{cc}'$) for unconfined and confined concrete, respectively. As an example, the regularized unconfined and confined concrete stress-strain models for wall WP1 (using $L_{cr} = L_{p,mean}$ =745 mm) are shown in Figure 3.6. The only difference between the two regularized confined concrete models is the ultimate strain based on the different Gf_{cc} values from Eq. (3-6) and Eq. (3-7). Steel regularization was also considered in the regularized plastic hinge models by using Eq. (3-8) and Eq. (3-9) with a gage length of L_{gage} = 200 mm.

The numerical-to-experimental ultimate displacement ratios, $R\delta_u$ for the eight walls using the regularized materials and $L_{p,mean}$ from Table 3.2 are presented in Table 3.4. Regularized materials consistently provided better predictions of the measured ultimate displacements (i.e., the $R\delta_u$ values were closer to 1.0) than simulations with unregularized materials. The best predictions were obtained using Eq. (3-7) (L. Lowes et al., 2016) for the confined concrete crushing energy, Gf_{cc} resulting in $R\delta_u$ ratios within $\pm$13% error. The lateral force-displacement curves from these analyses are presented in Figure 3.8, showing accurate simulations of the cyclic behavior of the eight walls up through the ultimate displacement. This is an important finding because it shows the

benefits of combining regularized materials with the plastic hinge integration method, as compared with unregularized materials.

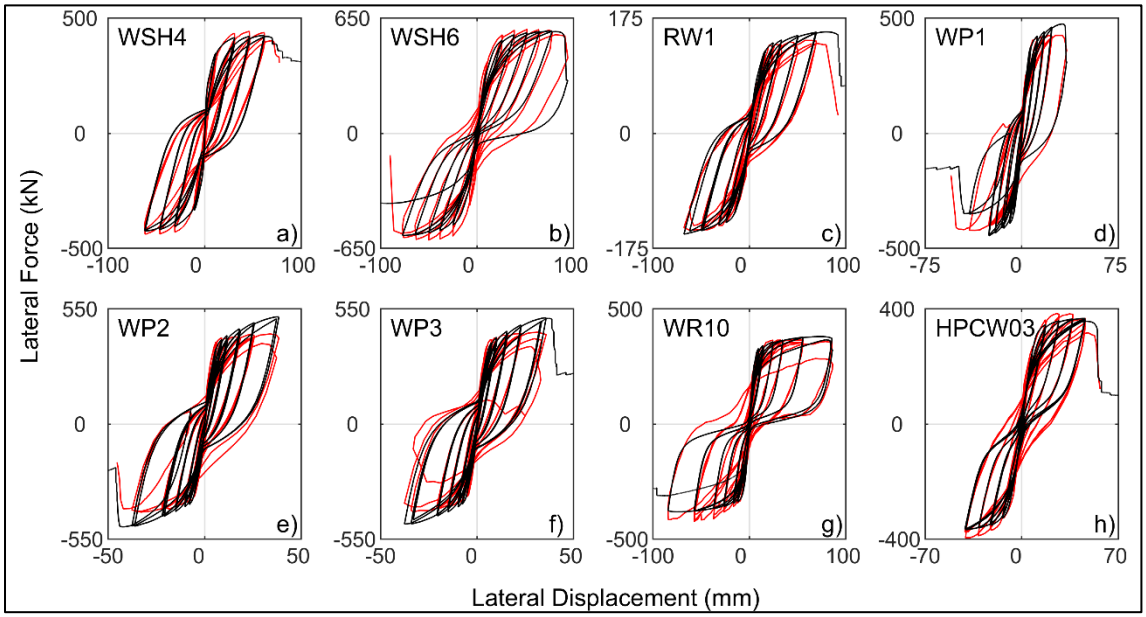

Figure 3.8: Lateral force-displacement behaviors using plastic hinge integration method and regularized materials with concrete crushing energy according to Eq. (3-5) and Eq. (3-7) (Measured results in red and numerical results in black).

It should be noted that the numerical lateral force-displacement behaviors for walls WSH6, WR10, and HPCW03 in Figure 3.7 and Figure 3.8 generally underestimated the measured residual displacements of the walls upon unloading (i.e., displacement at each zero force crossing). This discrepancy in the residual displacement was likely due to a combination of the following two factors. First, the *Concrete02* (Yassin, 1994) material in OpenSees was not able to accurately simulate the gradual crack closure behavior of concrete as compared to other concrete material models e.g., Chang & Mander, (1994); Waugh et al. (2008). Second, all of these slender walls had a relatively low shear-to-depth

ratio (close to 2.0), resulting in increased contribution of shear to the wall lateral displacement. Specifically, nonlinear shear deformations in slender RC walls are generally associated with non-zero residual displacements (Massone & Wallace, 2004), but this behavior was not captured in the models since a linear-elastic material was used to simulate the shear deformations of the walls.

3.7 Sensitivity of Ultimate Displacement to Assumed Plastic Hinge Length

The analysis results presented in the previous section were obtained using the modified Gauss-Radau plastic hinge integration method with the mean plastic hinge length ($L_{p,mean}$) from Table 3.2. To study the sensitivity of the numerical predictions of the ultimate displacement to the assumed plastic hinge length, parametric analyses were conducted considering L_p values ranging between 0.75 and 1.25$L_{p,mean}$. This range is greater than the mean $\pm$ one standard deviation, and is also greater than the range between the minimum and maximum L_p values in Table 3.2. This wide range was considered in order to include L_p values that can result from equations other than Eq. (3-1) – Eq. (3-3). The numerical-to-experimental ultimate displacement ratios ($R\delta_u$) using the unregularized and regularized material models are presented in Figure 3.9 (note that $R\delta_u$ values greater than 4.0 are not presented in the figure because of the selected plot range). In general, the ultimate displacements from the unregularized material models (Figure 3.9a-c) were very sensitive to the assumed plastic hinge length, with the greatest variations when using the Saatcioglu and Razvi (1992) concrete parameters. In comparison, the ultimate displacements from the regularized material models (Figure 3.9 d,e) were much less

sensitive to the assumed plastic hinge length. This reduced sensitivity of the results to the assumed plastic hinge length, which is a major benefit of using regularized materials, was because of the regularized post-peak stress-strain behaviors of the unconfined and confined concrete [Eq. (3-4)] based on the critical length (i.e., $L_{cr} = L_p$).

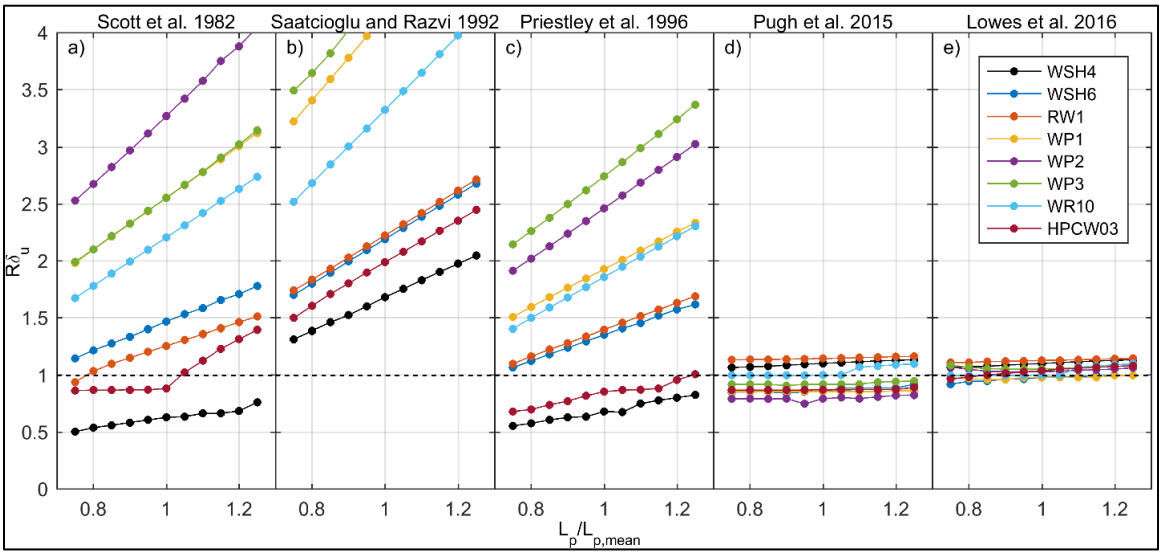

Figure 3.9: Sensitivity of the predicted ultimate displacement to the assumed plastic hinge length. Unregularized (conventional) material models (a-c), regularized material models (d,e).

3.8 Comparisons of Local Wall Response

The ability to predict local wall response is very important for accurate assessment of the performance at the section level (curvature and material strain demands). Comparisons between the numerically simulated axial-flexural (i.e., vertical) strains and the average experimentally measured strains along the length of walls WP1 and WP3, at various rotation levels, are shown in Figure 3.10 and Figure 3.11 for models with unregularized and regularized materials, respectively. The simulations were conducted

using the plastic hinge integration method with the mean plastic hinge length. Ratios of numerical-to-experimental extreme compression (C) and tension (T) vertical strains of the walls are listed in Table 3.5.

The experimental strains were measured at five locations along the length of each wall, and are average strains over a total gage height of 1118 mm (44 in.) (Segura, 2017; Segura & Wallace, 2018b). The corresponding simulations with unregularized and regularized materials were based on f'_{cc}, ε_u, and ε_{cu} from Priestley et al. (1996), and Gf_c and Gf_{cc} from Eq. (3-5) and Eq. (3-7), respectively. Each model included two elements, where the bottommost element had a total height of 1118 mm (to match the experimental measurement height for the strains) with a critical length, L_{cr} matching $L_{p,mean}$ (745 mm and 758 mm for walls WP1 and WP3, respectively from Table 3.2). To be consistent with the measured strains, the predicted strains in Figure 3.10 and Figure 3.11 were calculated as average strains from all of the IPs in the bottom element, thus covering the full experimental gage height of 1118 mm. Note that because walls WP1 and WP3 had unsymmetrical confined regions at the ends, the vertical strain comparisons are presented for both positive and negative rotations (Figure 3.10 and Figure 3.11, top and bottom rows, respectively). Note also that it was not possible to obtain reliable curvature or strain predictions from models with regularized materials but other integration methods (e.g., Figure 3.3) because it was not practical to implement the curvature normalization in Eq. (3-10) and Eq. (3-11) to the cyclic analysis results. As stated previously, this is a major limitation of the curvature normalization approach.

The numerical-to-experimental ratios of strains in Table 3.5 show that both unregularized and regularized material models resulted in underpredictions (i.e., ratios smaller than 1.0) of the compressive strains for positive rotations of wall WP1, and mostly overpredictions for negative rotations. The tension strains were overpredicted by both models. The largest differences between the numerical and experimental results were for the compression strains at +1.5% rotation, reaching errors of 49% and 35% for the unregularized and regularized material models, respectively. The mean errors in compressive strains considering both directions of loading were 12% and 5% for the unregularized and regularized material models, respectively, showing better accuracy when using material regularization. The tension strains were also generally considerably better predicted by the model with regularized materials at both positive and negative rotations, with mean error of 1% as compared with 12%.

The extreme compression strains for wall WP3 were mostly underestimated by both models with unregularized and regularized materials, while the extreme tension strains were generally overpredicted. The largest differences were in the tension strains at the third cycle (3/3) to +1.5% rotation, with 65% and 51% error in models with unregularized and regularized materials, respectively. The mean errors from the two models were 15% and 12% for the compressive strains, and 17% and 11% for the tension strains, respectively, again, showing the increased accuracy from the material regularization. Even though the improvement in the strain predictions were smaller for wall WP3 than for wall WP1, models with regularized materials were also able to capture the ultimate displacement as reported in Table 3.4. The larger differences in the local response predictions of the walls

as compared to the global predictions can be attributed to the modeling assumption of plane-section deformations, which can be inaccurate, especially at large lateral displacements (K. Kolozvari et al., 2018). While recent studies have shown better predictions of compression and tension strains of slender planar RC walls using continuum finite element models (which do not assume plane-section deformations), the ultimate failure displacement predictions from these models present considerable variations (Kristijan Kolozvari et al., 2019). As such, the simplicity, efficiency, and improved global as well as local accuracy of FB beam-column element models with plastic hinge integration and material regularization provide significant benefits for the nonlinear analysis of flexural RC walls.

It should also be mentioned that measured strains can be greatly sensitive to the location and gauge length of the potentiometers used in the experiments. Therefore, the numerical-to-experimental ratios presented in Table 3.5 may have been significantly different if the potentiometers were placed differently in each test. Because the sensitivity of the ultimate displacement to the assumed L_p is effectively reduced by using regularized materials (Figure 3.9d,e), future development of new L_p equations calibrated based on measured local (rather than global) behaviors can ultimately result in models that predict the local behavior of RC walls with higher accuracy.

Table 3.5: Ratios of numerical-to-experimental vertical strains; extreme compression (C) and extreme tension (T).

WP1					WP3				
Rotation	Unregularized		Regularized		Rotation	Unregularized		Regularized	
(%)	C	T	C	T	(%)	C	T	C	T
+ 0.75	0.75	1.01	0.77	0.96	+ 0.75	1.00	1.09	1.02	1.07
+ 1.0	0.72	1.07	0.75	1.01	+ 1.0	1.01	1.23	1.02	1.19
+ 1.5	0.51	1.22	0.65	1.08	+ 1.5 (1/3)	0.85	1.37	0.92	1.29
					+ 1.5 (3/3)	0.57	1.65	0.60	1.51
- 0.75	1.09	1.14	1.13	1.10	- 0.75	0.96	0.88	0.98	0.87
- 1.0	1.10	1.07	1.14	1.02	- 1.0	0.82	0.88	0.83	0.86
- 1.5	1.08	1.24	1.28	0.91	- 1.5 (1/3)	0.93	1.09	0.97	1.03
					- 1.5 (2/3)	0.67	1.15	0.70	1.06
mean	0.88	1.12	0.95	1.01	mean	0.85	1.17	0.88	1.11
COV	0.29	0.08	0.27	0.07	COV	0.19	0.22	0.18	0.20

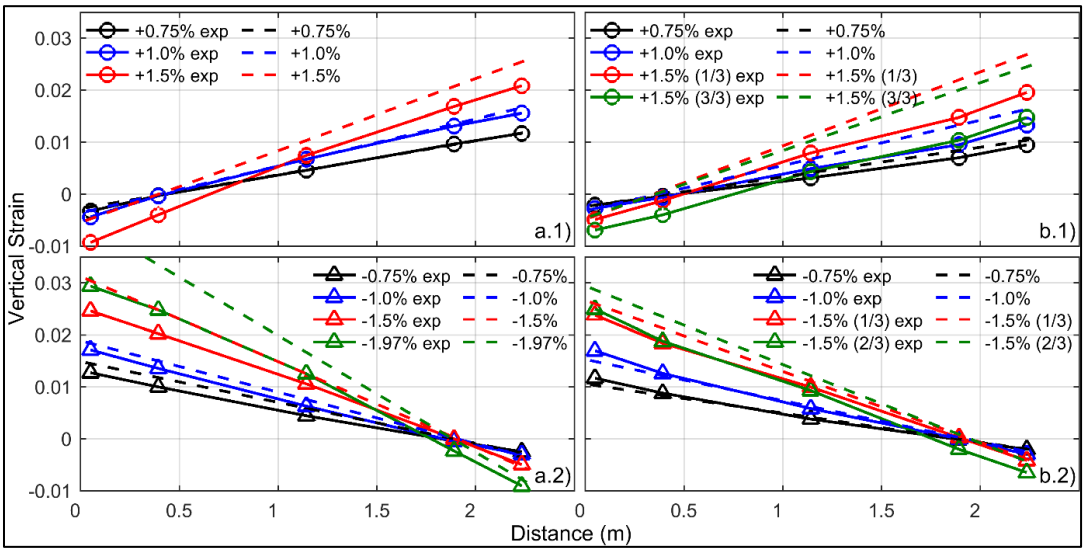

Figure 3.10: Vertical strain profiles at various rotation levels using unregularized materials. a.1) Wall WP1, positive rotation; a.2) wall WP1, negative rotation; b.1) wall WP3, positive rotation; b.2) wall WP3, negative rotation.

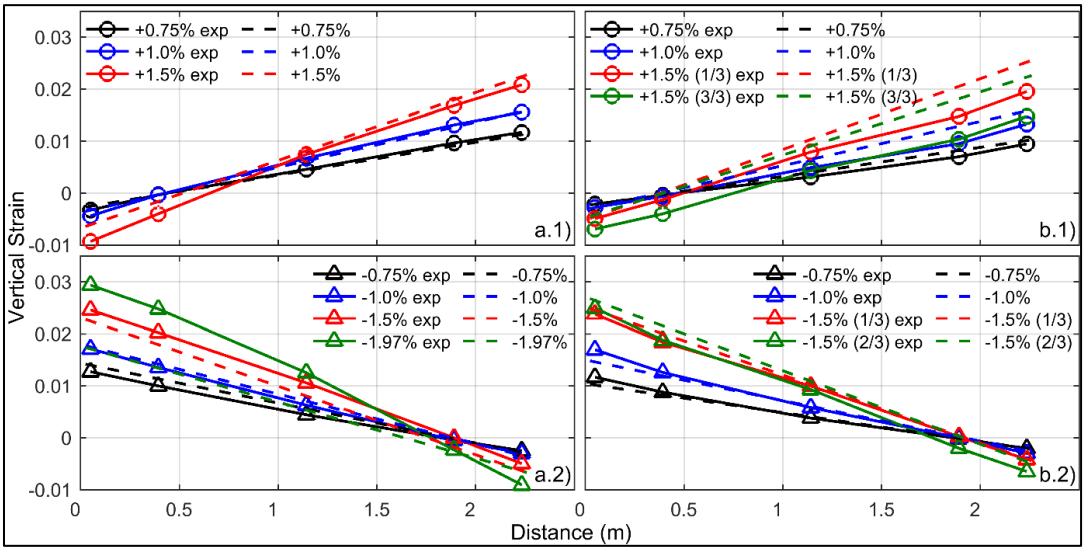

Figure 3.11: Vertical strain profiles at various rotation levels using regularized materials. a.1) Wall WP1, positive rotation; a.2) wall WP1, negative rotation; b.1) wall WP3, positive rotation; b.2) wall WP3, negative rotation.

3.9 Summary and Conclusions

This chapter discusses and critically evaluates the effect of material regularization in force-based beam column elements with plastic hinge integration to simulate the global and local responses (including the ultimate failure displacement, section curvatures, and material strains) of slender planar RC walls under cyclic lateral loading. The study extends the plastic hinge integration method by incorporating material models that regularize the post-peak stress-strain relationships of concrete and steel based on available failure energy approaches. The important findings and conclusions from this research are as follows:

1. The use of material regularization with the Gauss-Lobatto integration method results in mesh-objective predictions of the global behavior of slender RC walls. However, the local section curvature and material strains from these models are still extremely sensitive to the mesh size. Normalization of the curvatures based on an assumed plastic hinge length has been proposed in the literature, showing significant reductions of this sensitivity. As an important limitation, the equations needed for curvature normalization have not been generalized. Furthermore, the need to normalize the curvatures in a second step after the nonlinear analysis has been lost or not emphasized in some of the recent literature on nonlinear RC wall modeling.
2. In comparison, the use of unregularized materials with the Gauss-Lobatto integration method results in objective section curvatures and material strains. However, the predicted ultimate displacement at failure is extremely sensitive to the length of the critical integration point.

3. The modified Gauss-Radau plastic hinge integration method allows the user to match the critical length to an assumed plastic hinge length. As a major benefit demonstrated in this chapter, the sensitivity of the model results to the assumed plastic hinge length is significantly reduced when regularized rather than unregularized materials are used.
4. As an additional benefit, curvature and strain predictions using the modified Gauss-Radau plastic hinge integration method with regularized materials do not require an additional normalization step. As such, this approach is suitable for a wider range of nonlinear modeling applications.
5. Regularization of the concrete stress-strain relationship has a more significant effect on the analysis results than regularization of the steel stress-strain relationship.

Future research is needed to investigate the modified Gauss-Radau plastic hinge integration method with regularized materials for: 1) nonplanar RC walls; 2) nonlinear dynamic analysis; and 3) improved predictions of local wall behavior.

CHAPTER 4:
REGULARIZED PLASTIC HINGE MODEL FOR NONLINEAR CYCLIC LATERAL LOAD ANALYSIS OF SLENDER RC COLUMNS

Due to the demonstrated benefits of regularized plastic hinge models to simulate the global and local behaviors of RC walls presented in Chapter 3, this chapter investigates the use of regularized plastic hinge models for slender RC columns as part of the second specific objective of this research. Unregularized concrete stress-strain relationships, as well as regularized material stress-strain relationships developed for RC walls are studied. A new confined concrete regularization equation is proposed to reduce model mesh sensitivity in cyclic analysis of RC columns, showing accurate results when compared with available test data. A sample regularized plastic hinge column model is presented in Appendix A.6.

4.1 Introduction

The use of nonlinear numerical analysis is becoming increasingly common in earthquake engineering design practice of reinforced concrete (RC) structures. As such, it is essential to develop effective modeling techniques that can accurately predict the cyclic axial-flexural behavior of RC columns and walls through failure (e.g., peak lateral strength, ultimate displacement). Previous research towards this goal for RC columns has investigated lumped plasticity models using semi-empirical equations to define the

moment-rotation backbone parameters (Ghannoum & Matamoros, 2014; Haselton et al., 2016). Although lumped plasticity models are numerically robust and simple to implement, they present two major drawbacks: 1) variations in axial load cannot be accounted for during the analysis; and 2) there is no standardized guidance for cyclic hysteretic moment-rotation relationships (ASCE 41, 2017).

In comparison, distributed plasticity models with fiber cross sections can predict the nonlinear response of RC columns more accurately than lumped plasticity models because: 1) the variation of axial load in the axial-flexural interaction can be captured; and 2) the hysteretic behavior of the element is simulated through cyclic uniaxial concrete and steel material constitutive stress-strain relationships. However, as a major disadvantage of distributed plasticity models, the ultimate displacement (i.e., failure displacement) of a RC element with softening post-peak behavior (e.g., due to concrete crushing or rebar buckling) is highly sensitive to the length of the critical integration point (IP) over which the nonlinear behavior and failure of the element are concentrated (Coleman & Spacone, 2001; Pugh et al., 2015; Michael H. Scott & Fenves, 2006; Jorge A. Vásquez et al., 2016). To reduce this variability, researchers have proposed two families of numerical analysis techniques: 1) plastic hinge integration methods in which the length of the critical IP is matched to an experimentally-calibrated plastic hinge length, L_p (Michael H. Scott & Fenves, 2006); and 2) regularized concrete stress-strain relationships based on an experimentally-calibrated post-yield crushing energy (Coleman & Spacone, 2001). Each of these techniques have limitations as follows.

In the case of the plastic hinge integration method, the simulated ultimate displacement of the element can be highly sensitive to the assumed plastic hinge length and material stress-strain relationships (Almeida et al., 2016; Sideris & Salehi, 2016; Zendaoui et al., 2016). Importantly, since several plastic hinge length equations (Bae & Bayrak, 2008; M. P. Berry et al., 2008; Corley, 1966; Mattock, 1967; Paulay & Priestley, 1992; Priestley & Park, 1987) and concrete stress-strain relationships (Priestley et al., 1996; Saatcioglu & Razvi, 1992; B. D. Scott et al., 1982) are available in the literature, different results could be obtained when using different parameters. In the case of regularized material constitutive relationships, the local response of the element (e.g., section curvatures and material strains) can be highly inaccurate if the length of the critical IP is significantly different than the plastic hinge length (Coleman & Spacone, 2001; Pozo et al., 2020; Pugh et al., 2015).

It may be possible to mitigate the aforementioned limitations by combining the plastic hinge integration concept with regularized material stress-strain relationships. Accordingly, the objective of this chapter is to evaluate the accuracy and sensitivity of the simulated global and local behaviors of RC columns to the plastic hinge length and material stress-strain regularization. For this purpose, a force-based (FB) beam-column element with plastic hinge integration method is used to analyze a set of twenty-eight previously-tested RC columns. The evaluation of the FB beam-column element is conducted using: 1) unregularized (conventional) material stress-strain relationships; and 2) regularized material stress-strain relationships.

Previous researchers have recommended material regularization equations for the cyclic simulation of RC walls (NIST, 2017c; Pugh et al., 2015). The plastic hinge analysis results of the 28 previously-tested columns are used to evaluate the applicability of these equations to columns. Additionally, to the best of the authors' knowledge, no concrete stress-strain regularization recommendations are available specifically for the cyclic modeling of RC columns. Therefore, a new regularization equation for the compressive crushing energy of confined concrete is proposed based on calibration and validation of the analysis results to the measured data from the 28 columns.

4.2 Experimental Dataset

A dataset of twenty-eight previously tested square RC columns, as listed in Table 4.1, was used to evaluate the numerical models. These specimens constitute a subset of the database developed by Berry et al. (2004), focusing on columns that failed due to concrete crushing (with or without rebar buckling), and therefore, evidenced softening post-peak behavior of the lateral load versus displacement relationship. The dataset contains only slender columns with a shear span-to-depth ratio $M/(VH) \geq 2.9$, including a wide range of material properties, axial load ratios, and reinforcement ratios. The following information is presented for each column in the dataset:

- H = column cross section height (same as width).
- f_c' = compressive strength of unconfined concrete.
- f_y = yield strength of longitudinal steel.

- $P/(f_c'A_g)$ = axial load ratio, where P is the axial load applied to the column and A_g is the gross cross-section area.
- $M/(VH)$ = shear span-to-depth ratio, where M and V are the moment and shear developed at the critical section of the column, respectively.
- s/d_b = transverse reinforcement spacing, s divided by the longitudinal bar diameter, d_b.
- ρ_l = longitudinal steel ratio, calculated as A_{st}/A_g, where A_{st} is the total area of longitudinal steel in the section.
- $A_{sh}/(sb_c)$ = transverse reinforcement ratio in each direction defined according to ACI 318 (2019), where A_{sh} is the transverse reinforcement area, and b_c is the cross-sectional dimension of the concrete core measured to the outside edge of the outer transverse reinforcement.
- $L_{p,mean}$ = mean plastic hinge length calculated from the plastic hinge length equations presented in Table 4.2, where d is the effective depth of the column section, z is the distance from the critical section to the point of contraflexure, P_o is the nominal axial capacity (calculated by Eq. 22.4.2.2 of the ACI 318 (2019)), and the rest of variables were previously defined.

The column specimen dataset was divided into two groups: 1) columns 1 to 17, which were used to calibrate an equation for the confined concrete crushing energy (referred to as the "calibration" columns); and 2) columns 18 to 28, which were used to validate the proposed regularization equation (referred to as the "validation" columns). This division of the full dataset of 28 columns was done considering three aspects: 1) to

use about 60% of the columns for calibration and 40% of the columns for validation of the equation; 2) to have validation columns from the same experimental programs as for the calibration columns; and 3) to have experimental parameters (as presented in Table 4.1) for the validation columns within the maximum and minimum range of the parameters for the calibration columns, so that the validation is done within the limits of the calibration.

Table 4.1: Experimental column dataset

Column ID	Column Name	Ref.	H (mm)	f_c' (MPa)	f_y (MPa)	$\frac{P}{f_c' A_g}$	$\frac{M}{VH}$	$\frac{s}{d_b}$	ρ_l	$\frac{A_{sh}}{sb_c}$	$L_{p,mean}$ (mm)
1	Unit 3	(Ang, 1981)	400	23.6	427.0	0.38	4.0	6.3	0.015	0.013	237
2	Unit 1	(Soesianawati, 1986)	400	46.5	446.0	0.10	4.0	5.3	0.015	0.005	215
3	Unit 4	(Soesianawati, 1986)	400	40.0	446.0	0.30	4.0	5.9	0.015	0.003	232
4	Unit 1	(Tanaka, 1990)	400	25.6	474.0	0.20	4.0	4.0	0.016	0.013	243
5	Unit 4	(Tanaka, 1990)	400	25.6	474.0	0.20	4.0	4.0	0.016	0.013	243
6	Unit 6	(Tanaka, 1990)	550	32.0	511.0	0.10	3.0	5.5	0.012	0.009	267
7	Unit 8	(Tanaka, 1990)	550	32.1	511.0	0.30	3.0	4.5	0.012	0.011	283
8	No. 3	(Ohno & Nishioka, 1984)	400	24.8	362.0	0.03	4.0	5.3	0.014	0.004	213
9	Specimen 6	(Atalay & Penzien, 1975)	305	31.8	429.0	0.18	5.5	5.8	0.016	0.005	230
10	Specimen 9	(Atalay & Penzien, 1975)	305	33.3	363.0	0.26	5.5	3.5	0.016	0.007	228
11	Specimen 11	(Atalay & Penzien, 1975)	305	31.0	363.0	0.28	5.5	3.5	0.016	0.007	230
12	U1	(Saatcioglu & Ozcebe, 1989)	350	43.6	430.0	0.00	2.9	6.0	0.032	0.003	209
13	U7	(Saatcioglu & Ozcebe, 1989)	350	39.0	437.0	0.13	2.9	2.6	0.032	0.010	217
14	BG-1	(Saatcioglu & Grira, 1999)	350	34.0	455.6	0.43	4.7	7.8	0.020	0.005	250
15	BG-2	(Saatcioglu & Grira, 1999)	350	34.0	455.6	0.43	4.7	3.9	0.020	0.010	250
16	BG-3	(Saatcioglu & Grira, 1999)	350	34.0	455.6	0.20	4.7	3.9	0.020	0.010	233
17	BG-4	(Saatcioglu & Grira, 1999)	350	34.0	455.6	0.46	4.7	7.8	0.029	0.006	257
18	Unit 4	(Ang, 1981)	400	25.0	427.0	0.21	4.0	5.6	0.015	0.010	224
19	Unit 2	(Soesianawati, 1986)	400	44.0	446.0	0.30	4.0	4.9	0.015	0.007	232
20	Unit 3	(Soesianawati, 1986)	400	44.0	446.0	0.30	4.0	5.7	0.015	0.005	232
21	Unit 2	(Tanaka, 1990)	400	25.6	474.0	0.20	4.0	4.0	0.016	0.013	243
22	Unit 5	(Tanaka, 1990)	550	32.0	511.0	0.10	3.0	5.5	0.012	0.009	267
23	Unit 7	(Tanaka, 1990)	550	32.1	511.0	0.30	3.0	4.5	0.012	0.011	283
24	Specimen 10	(Atalay & Penzien, 1975)	305	32.4	363.0	0.27	5.5	5.8	0.016	0.004	229
25	Specimen 12	(Atalay & Penzien, 1975)	305	31.8	363.0	0.27	5.5	5.8	0.016	0.004	230
26	U3	(Saatcioglu & Ozcebe, 1989)	350	34.8	430.0	0.14	2.9	3.0	0.032	0.007	218
27	U6	(Saatcioglu & Ozcebe, 1989)	350	37.3	437.0	0.13	2.9	2.6	0.032	0.010	218
28	BG-8	(Saatcioglu & Grira, 1999)	350	34.0	455.6	0.23	4.7	3.9	0.029	0.006	242

Table 4.2: Plastic hinge length equations

Plastic Hinge Equation	Reference
$L_p = 0.5d + 0.032z/\sqrt{d}$ (in meter units)	(Corley, 1966)
$L_p = 0.5d + 0.05z$	(Mattock, 1967)
$L_p = 0.08z + 6d_b$	(Priestley & Park, 1987)
$L_p = 0.08z + 0.022d_b f_y$ (in mm and MPa units)	(Paulay & Priestley, 1992)
$L_p = 0.05z + 0.1f_y d_b/\sqrt{f_c'}$ (in mm and MPa units)	(M. P. Berry et al., 2008)
$L_p = [0.3P/P_o + 3\rho_l - 0.1]z + 0.25H \geq 0.25H$	(Bae & Bayrak, 2008)

4.3 Force-Based Beam-Column Element with Plastic Hinge Integration Method

A single force-based (FB) beam-column element in OpenSees (McKenna et al., 2000) was used to model the nonlinear axial-flexural behavior of each column specimen. This is a two-node line-element where fiber sections are assigned at different integration points along the length, and plane section deformations are assumed at each integration point (IP). Each fiber section is divided into several concrete and steel fibers, where nonlinear concrete and steel uniaxial stress-strain material relationships are assigned. In this study, the shear force-deformation relationship of the element was assumed to be linear-elastic, with an effective shear modulus of $G_{eff} = 0.04E_c$ as recommended elsewhere (NIST, 2017c; PEER/ATC, 2010; Pugh et al., 2015), where E_c is the concrete

Young's modulus. Further information on the plastic hinge integration method and the fiber cross-sections used to model the axial-flexural behavior of the column is provided below.

4.3.1 Plastic Hinge Integration Method

The critical IPs in a column are generally located at the ends, where the moments are largest and damage is expected to concentrate. To ensure that the concentration of damage in the element exactly matches a desired, user-defined plastic hinge length in each model, the modified Gauss-Radau integration method (M. H. Scott & Hamutçuoğlu, 2008) could be used. This method utilizes six IPs to integrate the axial-flexural deformations of the FB beam-column element over the column length. The IPs are distributed as follows: 1) two Gauss-Radau points with weights scaled by four at each end of the element; and 2) two Gauss-Legendre points in the interior part of the element. The IP locations (x) and weights (w) of the six integration points in the modified Gauss-Radau method are given in Eq. (4-1), and are schematically presented for a cantilever column in Figure 4.1, where L is the total length of the element, L_{pI} and L_{pJ} are the plastic hinge lengths specified by the user at the two ends, and $L_{int} = L - 4L_{pI} - 4L_{pJ}$. Since the modified Gauss-Radau integration method includes integration points at the element ends [i.e., x_1 and x_6 in Eq. (4-1)], it accurately simulates the response under the maximum end moments of the element. Additionally, it integrates quadratic polynomials exactly, and provides the exact solution for the linear elastic behavior of the element (Michael H. Scott & Fenves, 2006).

$$\begin{matrix} x = & \{ & 0; & \frac{8L_{pI}}{3}; & 4L_{pI} + \frac{L_{int}(3-\sqrt{3})}{6}; & 4L_{pI} + \frac{L_{int}(3+\sqrt{3})}{6}; & L - \frac{8L_{pJ}}{3}; & L\} \\ w = & \{ & L_{pI}; & 3L_{pI}; & 0.5L_{int}; & 0.5L_{int}; & 3L_{pJ}; & L_{pJ}\} \end{matrix} \quad (4\text{-}1)$$

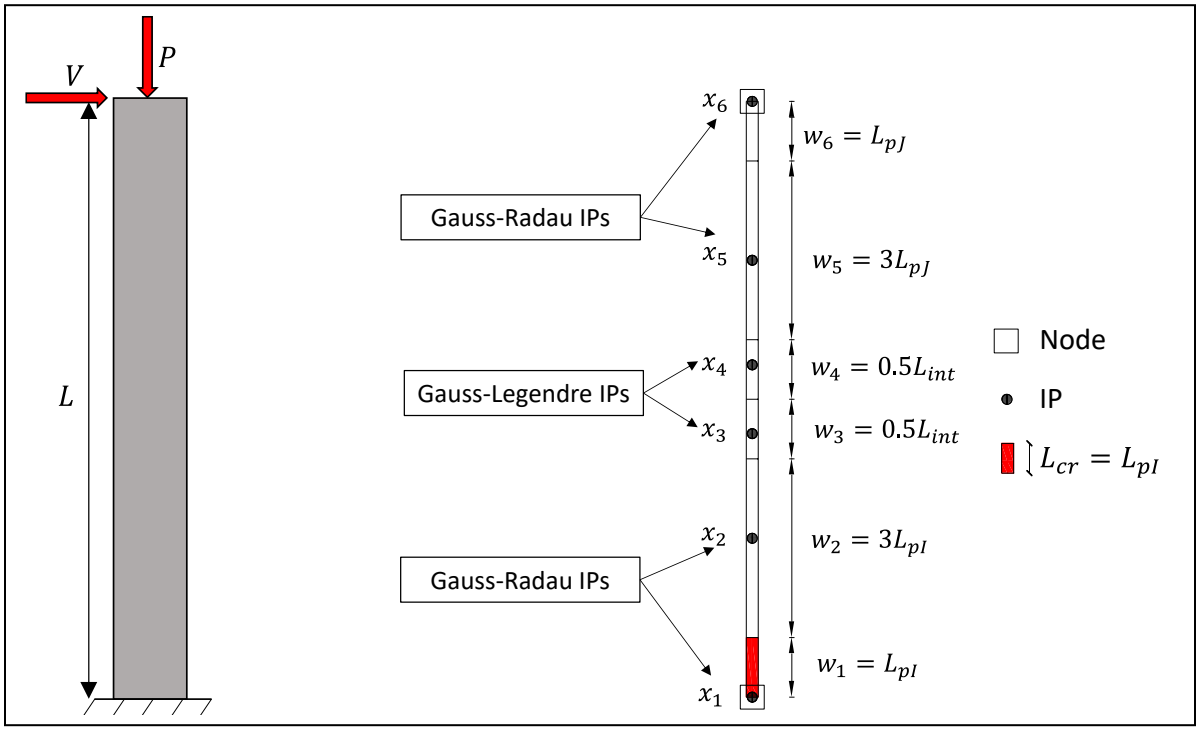

Figure 4.1: Locations and integration weights used in plastic hinge integration method.

The drawback of the modified Gauss-Radau integration method is that negative integration weights occur in the interior IPs when $L_p > 0.125L$ (with $L_p = L_{pI} = L_{pJ}$, which is common in prismatic RC columns), since L_{int} becomes negative. When negative integration weights occur, the locations of the 3rd and 4th IPs move towards the top and bottom of the element, respectively. These interior IPs with negative weights do not affect the element response because the nonlinear behavior is controlled by the IPs located at the ends of the element. However, if L_p reaches a value of $0.342L$, the locations of the 3rd and 4th IPs reach the element ends, after which the element response is not accurate. Therefore, L_p cannot be larger than $0.342L$.

For cantilever columns, the weight of the 6th IP (i.e., L_{pJ}) can be set to zero, for which the number of IPs in the modified Gauss-Radau method are reduced to four, to increase the range of L_{pI} that does not cause negative integration weights. However, this is not an appropriate approach to simulate columns in a moment resisting frame where plastic hinges can form at both ends. Alternatively, to ensure that $L_{cr} = L_p$ at both ends and to further increase the range of L_p that does not cause negative integration weights, the Endpoint integration method (Michael H. Scott & Fenves, 2006) could be used. The drawback of this method is that the elastic response is not accurate for elements with varying moment diagram (i.e., the method provides exact solutions only for constant functions), therefore, it is not acceptable for columns where the moment diagram is typically linear.

Based on the advantages and disadvantages of the different integration methods described above, the modified Gauss-Radau integration method with $L_{cr} = L_{pI} = L_{pJ} = L_p$ was used for the column analyses described in this chapter. This selection was made because this method accurately represents the elastic response of the element, and because the largest L_p used in all of the analyses conducted was $0.327L$, which is smaller than the maximum limit of $0.342L$ when negative integration weights impact the nonlinear response.

4.3.2 Fiber Cross Sections

The column cross sections were divided in three types of fibers: 1) unconfined concrete fibers to simulate the behavior of the section cover; 2) confined concrete fibers to

simulate the behavior of the concrete core (defined center-to-center of outer hoop reinforcement); and 3) steel fibers to simulate the behavior of the reinforcing bars. The section cover and concrete core were divided into 30 (on each side) and 200 fibers, respectively, while one fiber per reinforcing bar was used for the steel.

The unconfined and confined concrete fibers in each column section were simulated with the *Concrete02* material in OpenSees. The pre-peak compressive stress-strain relationship in *Concrete02* is defined by the Hognestad parabola. The strain at peak stress was calculated as $\varepsilon_o = 2f_c'/E_c$ for unconfined concrete and $\varepsilon_{co} = 2f_{cc}'/E_c$ for confined concrete (where f_{cc}' is the compressive strength of confined concrete), to obtain a material with an initial stiffness (i.e., Young's modulus) of $E_c = 4700\sqrt{f_c'}$ (in MPa units) according to ACI 318 (2019). Beyond the peak stress point, the stress-strain relationship reduces linearly to a residual compressive stress. The tensile behavior of the concrete is bilinear, reducing to zero residual stress through tension-softening behavior after cracking, which was assumed to occur at a tensile strength of $0.33\sqrt{f_c'}$ (in MPa units) according to ACI 318 (2019).

The longitudinal steel reinforcement in each column was simulated using the Menegotto and Pinto (1973) stress-strain model, which is available in OpenSees as the *Steel02* material. The *MinMax* material model was used in combination with *Steel02* to simulate complete loss of the steel compressive stress, as a simple model to represent the effect of rebar buckling, when the ultimate (i.e., crushing) strain, ε_{cu} of the confined concrete fiber immediately adjacent to the steel fiber was exceeded (Pugh et al., 2015).

As stated previously, plastic hinge models using both unregularized and regularized material stress-strain relationships were evaluated. Regularization of the concrete stress-strain relationship is typically done for compression, while steel regularization has been proposed for both compression and tension (Pugh et al. 2015). The unregularized and regularized concrete and steel material relationships utilized in this study are described below.

4.4 Unregularized Concrete and Steel Material Model Parameters

Conventional plastic hinge models use unregularized stress-strain curves to define the concrete and steel stress-strain relationships (NIST, 2017a). For the unregularized concrete models in this chapter (Figure 4.2a,b), the compressive strength of confined concrete, f'_{cc} as well as the ultimate compression strains, ε_u and ε_{cu} for unconfined and confined concrete, respectively, were determined according to the following three models: 1) Priestley et al. (1996); 2) Saatcioglu and Razvi (1992); and 3) Scott et al. (1982). For the Saatcioglu and Razvi (1992) and Scott et al. (1982) models, ε_u and ε_{cu} were assumed to be reached at a residual stress of $0.2f'_c$ and $0.2f'_{cc}$, respectively (i.e., $R_c = R_{cc} = 0.2$).

For the model by Priestley et al. (1996), the ultimate strain of unconfined concrete was taken as ε_u=0.004 at a residual stress of $0.2f'_c$. For confined concrete, the model assumes that the ultimate strain, ε_{cu} is reached at fracture of the transverse confining steel according to Eq. (4-2) from Priestley et al. (1996), where ρ_s is the volumetric ratio of the transverse steel and ε_{su} is the transverse steel strain at maximum tensile strength, which was taken as 0.09.

$$\varepsilon_{cu} = 0.004 + 1.4\rho_s f_y \varepsilon_{su} / f'_{cc} \quad (4\text{-}2)$$

The stress at ultimate strain, ε_{cu} of the confined concrete model by Priestley et al (1996) was obtained following Mander et al. (1988), which uses the Popovic's equation. Finally, the *MinMax* material model in OpenSees was used in combination with *Concrete02* to simulate the complete loss of concrete compressive stress at ε_{cu}, simulating the effect of the confining steel fracture.

For the unregularized steel materials, a bilinear stress-strain envelope with hardening post-yielding behavior, defined by a strain hardening ratio, b (i.e., post-yield stiffness bE_s) (Figure 4.2c), was modeled using the *Steel02* material in OpenSees. The steel strain hardening ratio for each column specimen was determined using the reported yield strength, f_y, the corresponding yield strain, ε_y (determined as f_y/E_s, with E_s=200 GPa), the reported maximum tensile strength, f_u, and the corresponding strain, which was taken as 0.09 per NIST (2017b) recommendations.

4.5 Regularized Concrete and Steel Material Model Parameters

Regularization of the concrete compressive stress-strain constitutive behavior can be explained by considering unconfined concrete cylinders subjected to uniform compression through failure. Laboratory observations have shown that the post-peak axial load versus total displacement behaviors of cylinders with different lengths are similar because damage concentrates in a localized region regardless of the total length. However, the average post-peak stress-strain curves obtained by dividing the total axial displacement

with the cylinder length depend on the length of the tested specimen (Jansen & Shah, 2002; Nakamura & Higai, 2001).

In a distributed-plasticity beam-column element, the critical length, L_{cr} corresponds to the length assigned to the integration point where the moment is largest and nonlinear deformations concentrate (i.e., critical integration point x_1 in Figure 4.1). However, the assumed critical length, L_{cr} in a model may not accurately represent the length over which damage concentrates in a real column, resulting in erroneous predictions in the post-peak softening range of behavior (Coleman & Spacone, 2001). Researchers (Jansen & Shah, 2002; Nakamura & Higai, 2001) have found that the concrete crushing energy, defined as Gf_c (refer to the shaded area in Figure 4.2a) is an invariant material property, regardless of the assumed L_{cr}. Similarly, the crushing energy for confined concrete can be defined as Gf_{cc} (refer to the shaded area in Figure 4.2b).

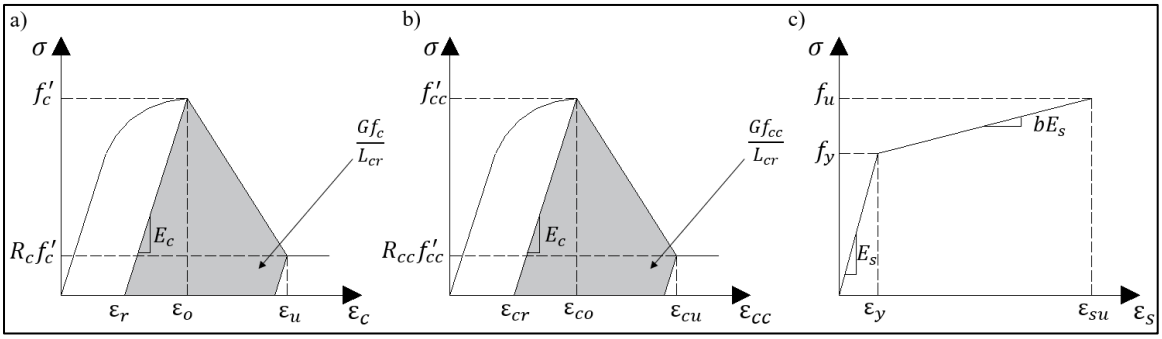

Figure 4.2: Material stress-strain curves. a) Unconfined concrete; b) confined concrete; c) reinforcing steel.

If the concrete post-peak stress-strain curve is regularized so that the concrete crushing energies for unconfined and confined concrete are equal to constant predetermined (calibrated) values of Gf_c and Gf_{cc}, respectively, then models with different

L_{cr} will result in similar (i.e., objective) global force-displacement responses (Coleman & Spacone, 2001). Considering the linear post-peak stress-strain relationship and elastic unloading response of *Concrete02* (Figure 4.2a), the regularized ultimate strain for unconfined concrete, ε_u, at a residual stress of $R_c f_c'$ can be calculated using Eq. (4-3) to obtain a constant unconfined concrete crushing energy Gf_c. This equation was derived by equating the shaded area of Figure 4.2a to Gf_c/L_{cr}. A similar equation for confined concrete can be obtained by replacing the appropriate terms, as shown in Eq. (4-4).

$$\varepsilon_u = \frac{1}{1+R_c} \cdot \left[\frac{2Gf_c}{f_c' L_{cr}} - \frac{f_c'}{E_c} + (1+R_c)\varepsilon_o + R_c^2 \frac{f_c'}{E_c} \right] \tag{4-3}$$

$$\varepsilon_{cu} = \frac{1}{1+R_{cc}} \cdot \left[\frac{2Gf_{cc}}{f_{cc}' L_{cr}} - \frac{f_{cc}'}{E_c} + (1+R_{cc})\varepsilon_{co} + R_{cc}^2 \frac{f_{cc}'}{E_c} \right] \tag{4-4}$$

In this concrete regularization approach, it is important to note that: 1) appropriate values of Gf_c and Gf_{cc} need to be calibrated from experimental results; and 2) even though the post-peak global force-displacement responses from models that have critical IPs with different locations and weights (i.e., that result in a different L_{cr}) will be similar (i.e., objective), the local material strains will be different (i.e., non-objective local behaviors) (Coleman & Spacone, 2001).

For the column models developed using the plastic hinge integration method in Section 4.3.1, L_{cr} in Eq. (4-3) and Eq. (4-4) was taken as L_p. Furthermore, similar to the unregularized concrete models, the ultimate concrete compression strains, ε_u and ε_{cu}, of the regularized unconfined and confined concrete models were assumed to occur at a residual stress of $0.2f_c'$ and $0.2f_{cc}'$ (i.e., $R_c = R_{cc} = 0.2$), respectively.

The tensile stress-strain relationship of reinforcing steel presents hardening behavior after yielding and before the ultimate stress. Since larger strains are accompanied by larger stresses in this hardening range, localization of damage is not expected before reaching the ultimate stress, resulting in a spread of yielding. However, Pugh et al. (2015) demonstrated that steel regularization is required to improve objectivity of the global behavior when simulating RC walls. In this steel regularization, the post-yield stiffness of the stress-strain relationship is regularized based on an assumed gage length of L_{gage} = 200 mm. However, its applicability has not been investigated in RC columns. More details of the steel regularization method based on Pugh et al. (2015) can also be found in NIST (2017a).

4.5.1 Available Regularized Concrete Crushing Energy Equations for Slender RC Walls

Unconfined and confined concrete crushing energy equations for modeling slender RC walls have been proposed by Pugh et al. (2015) and adopted by NIST (2017a) as:

$$Gf_c = 2.0f_c' \text{ (N/mm for } f_c' \text{ in MPa units)} \quad (4\text{-}5)$$

$$Gf_{cc} = 1.70Gf_c \text{ (N/mm for } f_c' \text{ in MPa units)} \quad (4\text{-}6)$$

As shown later in this chapter, these equations for slender RC walls do not result in accurate simulations of the ultimate displacement prediction of slender RC columns. Note that when using these equations, regularization of the steel stress-strain relationship is also required as described in Pugh et al. (2015).

4.5.2 Proposed Regularized Concrete Crushing Energy Equations for Slender RC Columns

There are currently no recommendations specifically developed of the concrete crushing energy for cyclic analyses of slender RC columns. Thus, an equation to estimate the confined concrete crushing energy, Gf_{cc} was developed based on the 17 calibration column specimens listed in Table 4.1. The proposed equation was subsequently validated using the remaining 11 specimens. The peak strength of confined concrete, f'_{cc}, was defined according to Mander et al. (1988), and regularization of the post-peak concrete stress-strain relationship was performed using Eq. (4-3) and Eq. (4-4), where the mean plastic hinge length from Table 4.1 (i.e., $L_{cr} = L_{p,mean}$) was used in each model.

Four cases were evaluated by analyzing the predicted ultimate displacements of the calibration columns. These cases differed based on the equation used for the unconfined concrete crushing energy, Gf_c, and the regularization of the steel stress-strain relationship. For Gf_c, Eq. (4-5) from Pugh et al. (2015) and Eq. (4-7) from Nakamura and Higai (2001) were used. Then, simulations with and without steel regularization (NIST, 2017c; Pugh et al., 2015) were performed with each of these two Gf_c equations and varying values of Gf_{cc}. This process considered Gf_{cc} to be represented as a function of Gf_c, as in the case of Eq. (4-6) for slender walls.

$$Gf_c = 8.8\sqrt{f'_c} \quad \text{(N/mm for } f'_c \text{ in MPa units)} \tag{4-7}$$

Out of the four cases, the best simulation results were obtained by using Eq. (7) to define Gf_c, and without steel regularization. These results are demonstrated in Figure 4.3a, which shows the simulated-to-measured ultimate displacement ratio, $R\delta_u$, for the calibration columns as a function of Gf_{cc}/Gf_c. For all columns, a positive correlation can

be seen where $R\delta_u$ increases with increasing Gf_{cc}/Gf_c. The ultimate displacement of each column, δ_u was defined as the displacement corresponding to 20% reduction in lateral resistance, based on the effective lateral load-displacement curve with P-Δ effects removed as presented in Berry et al. (2004). The removal of the P-Δ effects was necessary in order to capture strength loss due to material deterioration rather than geometric effects.

Figure 4.3b shows the value of Gf_{cc}/Gf_c required to obtain an ultimate displacement ratio of $R\delta_u$=1.0 (meaning exact match of the simulated and measured δ_u) for each calibration column plotted versus the confined concrete strength ratio, $K = f'_{cc}/f'_c$ according to Mander et al. (1988). The ID of each column is presented in the figure. Except for column ID 11, a value of Gf_{cc} larger than Gf_c was required to accurately simulate the ultimate displacement of the analyzed columns. Furthermore, Gf_{cc}/Gf_c generally increased with increasing confinement (i.e., increasing K). The linear regression that best matches the results is presented with a dashed line in the plot, obtaining an R^2=0.57.

A better linear regression fit was investigated by considering other relationship forms, while still maintaining simplicity of the equation as a goal for use in design. For the development of the final recommended equation, Figure 4.3c shows the results of Gf_{cc}/Gf_c normalized by $f_c'^2$ versus K, where an improved linear regression equation was obtained, with an R^2 value of 0.84. Based on these results, the proposed confined concrete crushing energy is given according Eq. (4-8), where Gf_{cc} is constrained to a minimum of Gf_c, following the trend in Figure 4.3.

$$Gf_{cc} = 0.008(K-1)f_c'^2 Gf_c \geq Gf_c \quad \text{(N/mm for } f_c' \text{ in MPa units)} \tag{4-8}$$

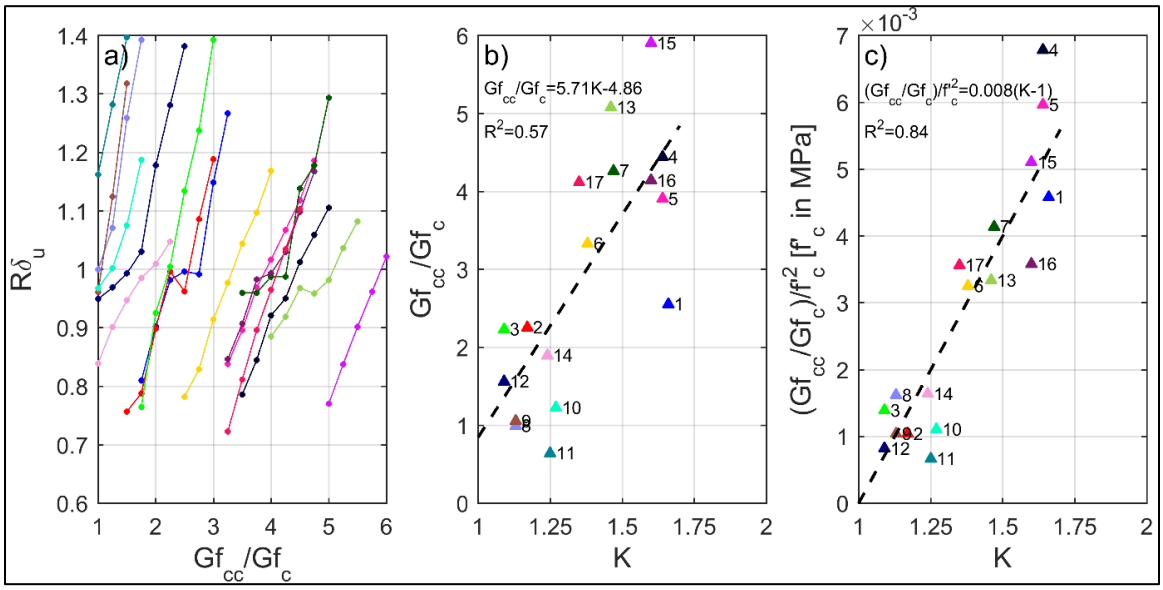

Figure 4.3: Confined concrete crushing energy calibration. a) Ultimate displacement ratio, $R\delta_u$ versus Gf_{cc}/Gf_c; b) Gf_{cc}/Gf_c versus K for $R\delta_u$=1; c) $(Gf_{cc}/Gf_c)/f_c'^2$ versus K for $R\delta_u$=1.

Note that as stated previously, Eq. (4-8) was determined using Gf_c defined with Eq. (4-7), and without steel regularization, as these selections resulted in the best match to the measured ultimate displacements of the calibration specimens. Table 4.3 shows the values of the confined concrete strength ratio, $K = f'_{cc}/f'_c$, the unconfined concrete crushing energy, Gf_c, the proposed confined concrete crushing energy, Gf_{cc}, and the simulated-to-measured ultimate displacement ratio, $R\delta_u$, for all of the 28 column specimens. The mean and coefficient of variation of $R\delta_u$ for the columns used to calibrate (ID 1-17) and to validate (ID 18-28) Eq. (4-8) are also tabulated. It can be seen that Eq. (4-7) and Eq. (4-8) resulted in reasonably accurate simulations of the ultimate displacement even for the validation columns that were not used in the calibration process.

Additionally, Figure 4.4 presents comparisons between the experimental (measured) and simulated lateral load versus displacement curves for the entire column dataset, including P-Δ effects. The experimental and simulated curves are presented beyond the ultimate displacement (as defined previously), which is marked in each plot. The cyclic behavior of each column up to the onset of failure is captured reasonably well, simulating the peak strength, ultimate displacement, and strength and stiffness degradation.

Table 4.3: Simulated-to-measured ultimate displacement ratio, $R\delta_u$, using the proposed Eq. (4-8)

Model Calibration					Model Validation				
Column ID	K	Gf_c (N/mm) [Eq. (4-7)]	Gf_{cc} (N/mm) [Eq. (4-8)]	$R\delta_u$	Column ID	K	Gf_c (N/mm) [Eq. (4-7)]	Gf_{cc} (N/mm) [Eq. (4-8)]	$R\delta_u$
1	1.66	42.75	124.83	1.11	18	1.46	44.00	101.23	1.39
2	1.17	60.01	178.97	1.17	19	1.26	58.37	232.12	0.97
3	1.09	55.66	65.85	0.70	20	1.17	58.37	151.31	1.08
4	1.64	44.52	149.93	0.76	21	1.64	44.52	149.93	0.84
5	1.64	44.52	149.93	0.87	22	1.38	49.78	155.40	1.47
6	1.38	49.78	155.40	0.94	23	1.47	49.86	194.22	0.71
7	1.47	49.86	194.22	0.96	24	1.12	50.10	51.39	0.83
8	1.13	43.82	43.82	1.00	25	1.12	49.59	49.59	0.85
9	1.13	49.62	53.73	0.97	26	1.28	51.91	142.82	0.84
10	1.25	50.76	113.97	1.12	27	1.47	53.74	283.22	1.02
11	1.25	49.02	93.56	1.36	28	1.45	51.31	214.79	0.94
12	1.09	58.11	78.27	1.02					
13	1.46	54.96	304.64	1.11					
14	1.24	51.31	115.80	1.04					
15	1.60	51.31	285.93	0.91					
16	1.60	51.31	285.93	1.38					
17	1.35	51.31	167.52	0.72					
mean				1.01					1.00
COV				0.19					0.24

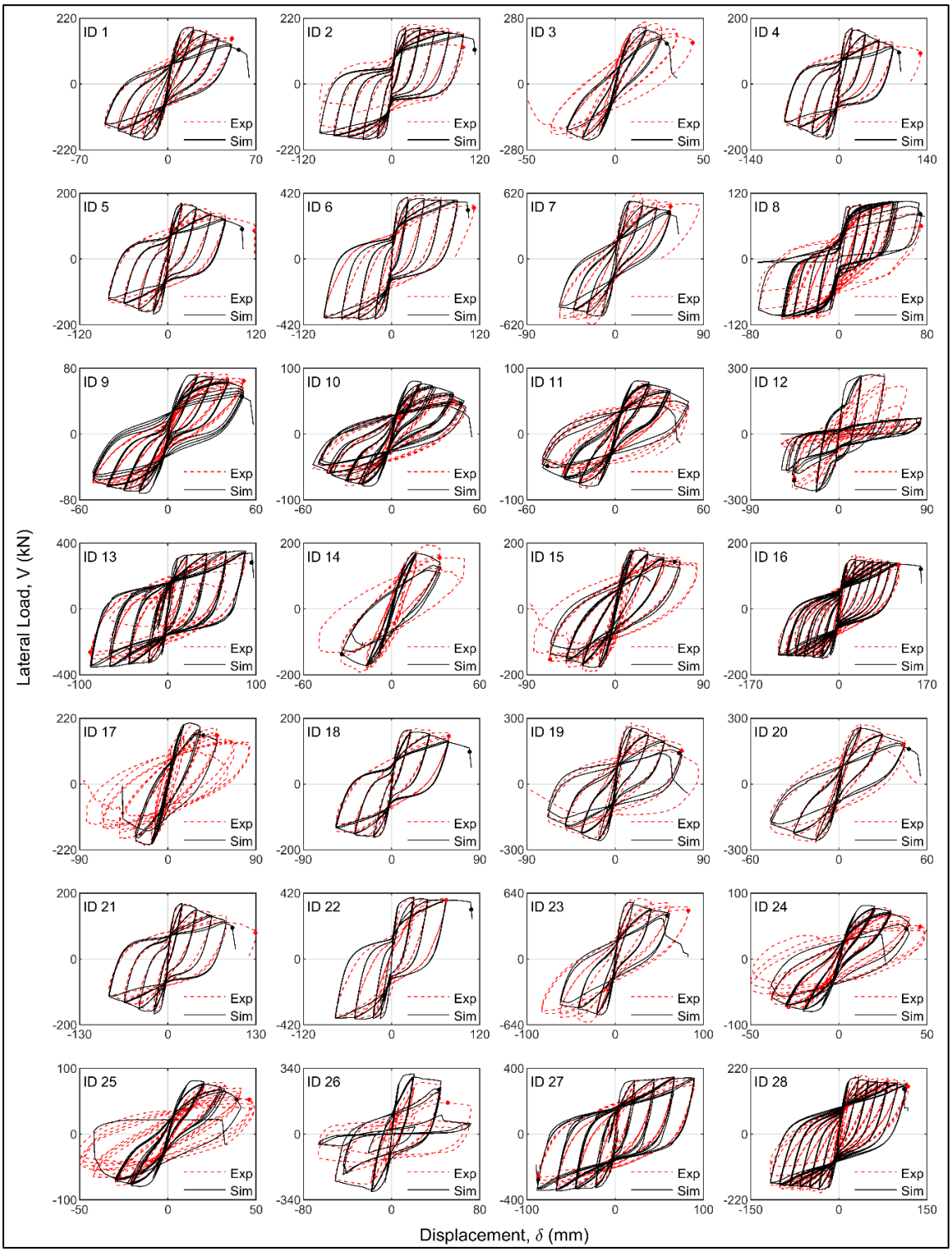

Figure 4.4: Lateral load versus displacement comparisons using proposed regularized plastic hinge model. Ultimate displacement points shown using small, filled circles.

4.6 Comparison of Plastic Hinge Model Results

This section presents comparisons of the column simulations using the proposed regularized concrete parameters in Section 4.5.2 with four other simulations using: 1) unregularized concrete parameters from Priestley et al. (1996), Saatcioglu and Razvi (1992), and Scott et al. (1982), as described in Section 4.4; and 2) regularized concrete and steel parameters developed by Pugh et al. (2015) for RC walls, as described in Section 4.5.1. For all simulations, the critical integration length of the FB beam-column element, L_{cr} was assumed to be equal to the mean plastic hinge length, $L_{p,mean}$ presented in Table 4.1.

To demonstrate the differences between the simulation models, the unregularized and regularized compressive stress-strain relationships for the five sets of unconfined concrete material parameters for column ID 13 are shown in Figure 4.5a. All five unconfined concrete stress-strain relationships are the same up to the peak point, while the post peak behaviors are different because the models reach the residual stress of $0.2f_c'$ at different values of ε_u. Note that to calculate ε_u for the regularized models, Eq. (4-5) was used for the model by Pugh et al. (2015), while Eq. (4-7) from Nakamura and Higai (2001) was used for the proposed model.

Similarly, the unregularized and regularized compressive stress-strain relationships for the confined concrete material parameters for column ID 13 are shown in Figure 4.5b. The peak point and post-peak behavior of the unregularized confined concrete stress-strain relationships are different due to the different approaches to estimate f_{cc}' and ε_{cu}. For both of the regularized models, the confined concrete stress-strain relationships up to the peak

point at f'_{cc} are the same as the unregularized relationship based on Priestley et al. (1996). Beyond the peak point, the two regularized confined concrete models reach the residual stress of $0.2f'_{cc}$ at different values of ε_{cu}, calculated based on the confined concrete crushing energy Eq. (4-6) as proposed by Pugh et al. (2015) and Eq. (4-8) as proposed herein.

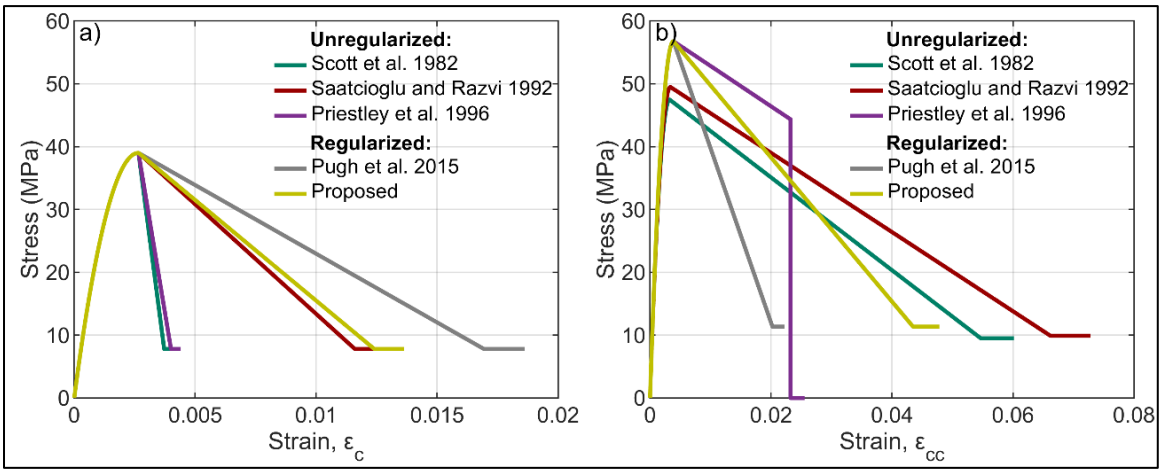

Figure 4.5: Concrete compressive stress-strain relationships for column ID 13. a) Unconfined concrete; b) confined concrete.

4.6.1 Comparison of Global Column Behaviors

This section presents comparisons of the predicted global lateral load versus displacement behaviors of the 28 column specimens using the three sets of unregularized and two sets of regularized material parameters. In addition to the ultimate displacement ratio, $R\delta_u$, defined in Section 4.5.2, the global behaviors are compared based on the simulated-to-measured ratios of the effective stiffness, RK_e, and maximum strength, RV_{max}. The effective stiffness and maximum strength were determined from the mean (considering both the positive and negative loading directions) backbone lateral load-

displacement curve for each specimen. The effective stiffness was calculated as the slope between the origin and the point on the mean backbone curve at 70% of the maximum strength.

Figure 4.6 presents the variability (as box plots) of the simulated-to-measured ratios of the effective stiffness, maximum strength, and ultimate displacement obtained using the five sets of material parameters for the 28 columns. The variabilities for the effective stiffness were similar among the different material sets. This may be expected since all of the material model parameters had the same concrete Young's modulus. The different models also resulted in similar simulations for the maximum strength, which was likely because 25 out of the 28 columns were controlled by yielding of the steel in tension, and thus, differences in the concrete compression strength had relatively small effect on their axial-flexural strength. All five material parameter sets predicted the maximum strength within $\pm$20% error, and overpredicted the effective stiffness, which is common in RC components and is typically attributed to un-simulated shrinkage cracking that may have occurred in the laboratory test specimens (L. N. Lowes et al., 2019).

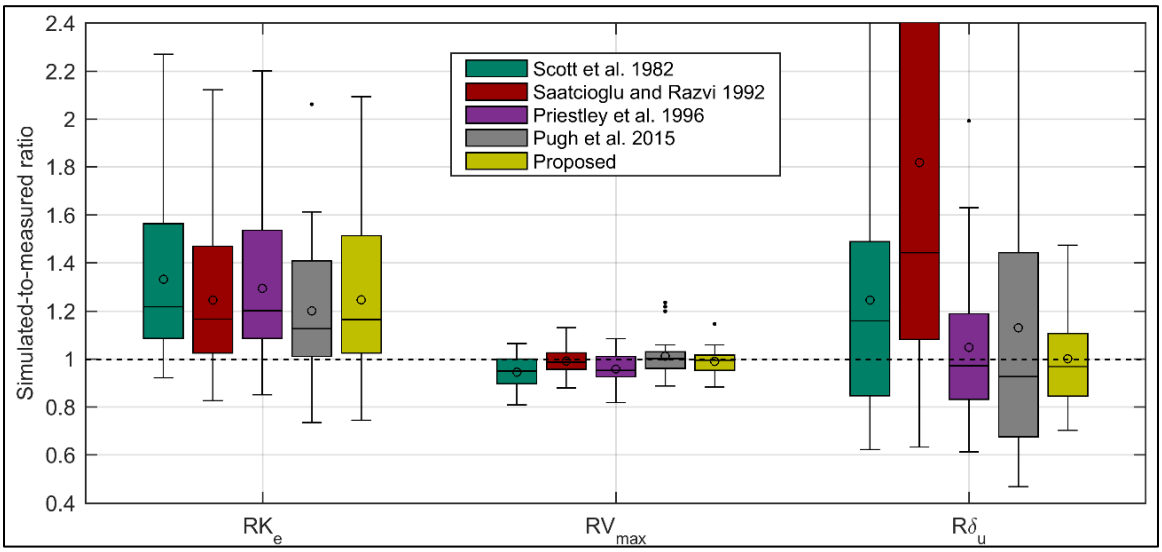

Figure 4.6: Variability in simulation of column global behaviors.

The ultimate displacement presented the largest differences among the simulations with the different material parameter sets. Table 4.4shows the simulated-to-measured ultimate displacement ratio using the unregularized and regularized sets of material parameters for all the columns in the dataset. On average, the unregularized models with f'_{cc}, ε_u, and ε_{cu} from Saatcioglu and Razvi (1992) resulted in the highest un-conservative overpredictions of the measured ultimate displacement, while the best unregularized model results were obtained using f'_{cc}, ε_u, and ε_{cu} from Priestley et al. (1996). Importantly, the regularization approach developed by Pugh et al. (2015) for slender RC walls was not adequate to simulate the ultimate displacement of the RC columns, since it presented a large variability (see Figure 4.6 and COV in Table 4.4). In comparison, there were significant improvements of the accuracy and reduced variability on the simulation of the ultimate displacement when using the proposed regularization for RC columns [i.e., Eq. (4-8), together with Eq. (4-7)] for RC columns.

Table 4.4: Simulated-to-measured ultimate displacement ratio, $R\delta_u$

Column ID	Unregularized			Regularized	
	Scott et al. 1982	Saatcioglu and Razvi 1992	Priestley et al. 1996	Pugh et al. 2015	Proposed
1	1.90	5.00	1.99	0.87	1.11
2	1.09	1.29	0.67	1.05	1.17
3	0.78	1.07	0.61	1.16	0.70
4	1.66	2.68	1.08	0.63	0.76
5	1.85	2.95	1.20	0.58	0.87
6	1.58	2.15	0.96	0.74	0.94
7	1.24	3.06	1.18	0.74	0.96
8	1.31	1.58	1.08	2.63	1.00
9	1.03	2.03	1.38	2.48	0.97
10	1.27	1.11	1.15	2.01	1.12
11	1.38	1.38	1.39	2.31	1.36
12	0.97	1.18	0.97	1.96	1.02
13	1.26	1.55	0.71	0.63	1.11
14	0.85	0.97	0.99	0.99	1.04
15	0.71	0.72	0.95	0.65	0.91
16	1.40	2.07	1.23	0.72	1.38
17	0.62	0.63	0.97	0.70	0.72
18	2.62	4.09	1.63	1.19	1.39
19	0.91	1.16	0.74	0.72	0.97
20	0.99	1.38	0.86	1.10	1.08
21	1.66	2.69	1.08	0.52	0.84
22	2.42	3.26	1.52	1.10	1.47
23	0.84	1.51	0.79	0.47	0.71
24	0.83	1.09	0.83	1.71	0.83
25	0.83	0.86	0.86	1.70	0.85
26	0.85	0.85	0.97	1.03	0.84
27	1.23	1.55	0.75	0.61	1.02
28	0.81	1.03	0.83	0.70	0.94
mean	1.25	1.82	1.05	1.13	1.00
COV	0.40	0.59	0.30	0.56	0.21

4.6.2 Comparison of Local Column Behaviors

Results for measured local behaviors (i.e., curvatures and strains) of tested RC columns are scarce in the literature. As such, this section presents simulated-to-measured comparisons for the available local behavior data for nine of the columns in Table 4.1. These simulations were conducted using the mean plastic hinge length, $L_{p,mean}$ (Table 4.1) with unregularized steel material properties and: 1) unregularized concrete material properties from Priestley et al. (1996); and 2) the proposed regularized concrete materials [i.e., using Eq. (4-7) and Eq. (4-8)]. These two sets of concrete material parameters were selected because they provided the best ultimate displacement results out of the three unregularized and two regularized sets of material parameters, respectively, as described previously.

Figure 4.7a-b presents the measured and simulated results of local curvatures for two columns (ID 1 and 18) tested by Ang (1981), plotted against the lateral displacement ductility, $\mu_\delta = \delta/\delta_y$ (where δ_y is the experimentally reported yield displacement). The measured curvatures are averages of the two reported values closest to the critical sections above and below the center block [where the lateral load was applied as described in Ang (1981)], while the simulated curvatures correspond to the values obtained from the critical integration point in each model. It can be seen that both sets of material parameters presented similar curvature estimations that generally underestimated the experimental values; with better predictions at greater μ_δ. The higher underestimation at lower μ_δ is likely because of the stiffness overestimation shown in the previous section.

Figure 4.7c-i compares the extreme confined concrete compressive strains for seven columns tested by Tanaka (1990). The experimental strains correspond to the values measured from potentiometers closest to the critical section, over gauge lengths of 160 mm for column ID 4, 5, and 21, and 180 mm for column ID 6, 7, 22, and 23. The simulation results underestimated the extreme confined concrete compressive strains for all seven columns, except for $\mu_\delta < 2$ in column ID 23. These underestimations can be explained by the values of $L_{p,mean}$ used in the models (Table 4.1), which were larger than the length of the potentiometers, thus modeling average strains over a greater column length. Generally, both sets of material parameters presented similar strain estimations, but at larger μ_δ, the strains from the simulations using the proposed concrete regularization were more accurate than those from the unregularized simulations. At the last measured data point of the seven columns (i.e., closest reported point to failure), the strains from the proposed regularized model varied between -63% to -7% of the measured values. When excluding column ID 5 and 21 for which the simulations had the greatest underestimation of strain, the simulated strains for the last available data point were within -29% to -7% of the measured values.

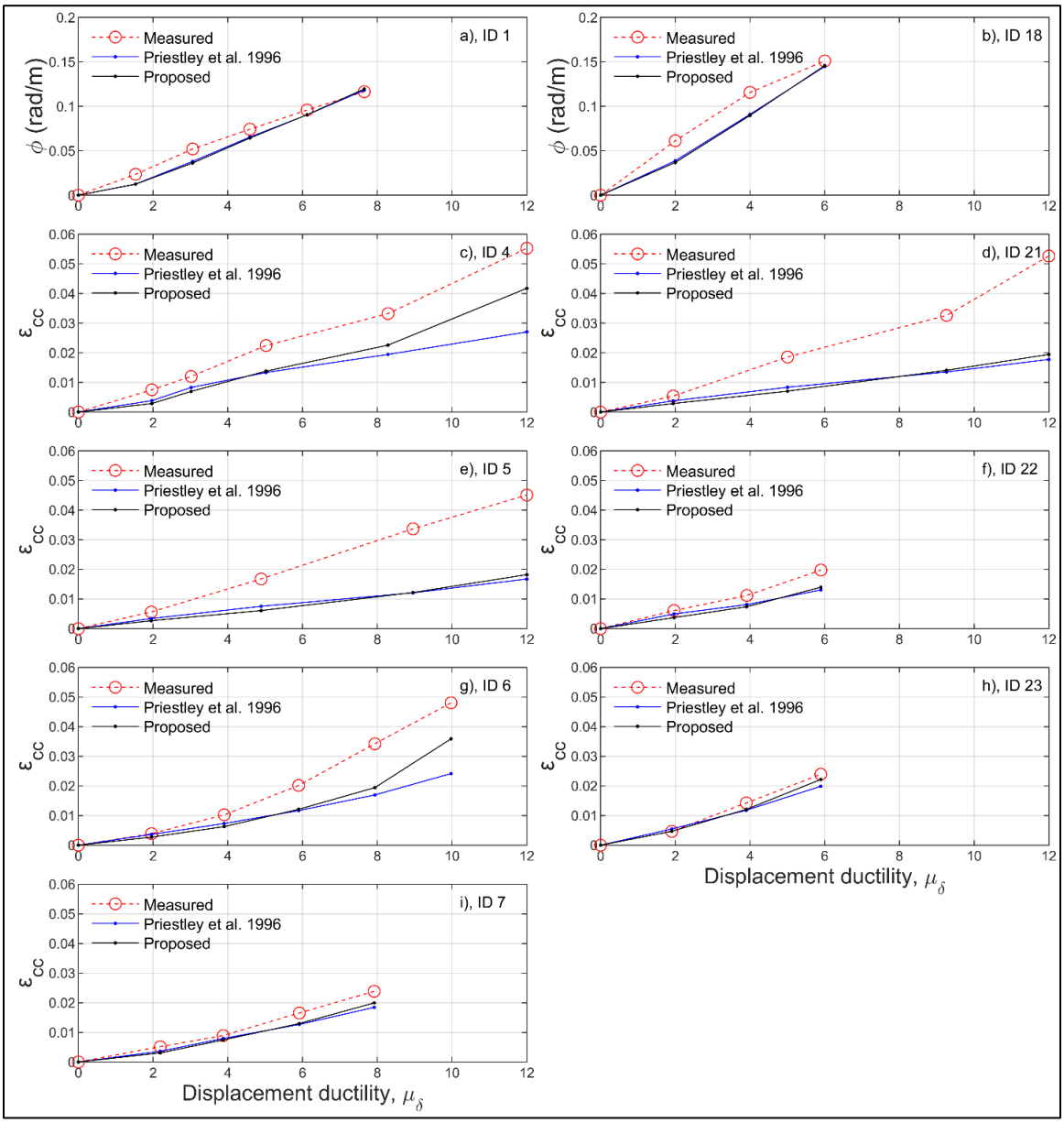

Figure 4.7: Comparison of local results at critical IP. Curvature (a-b); extreme confined concrete compression strain (c-i).

4.7 Sensitivity Analysis

The analysis results presented in the previous section were obtained using models with L_{cr} equal to the mean plastic hinge length, $L_{p,mean}$ from Table 4.1. Since many plastic hinge length equations for RC columns are available in the literature (see Table 4.2), the sensitivity of the simulated global and local column behaviors to the assumed plastic hinge length is studied herein based on parametric analyses using $L_{cr} = L_p$ values ranging between $0.5L_{p,mean}$ and $1.5L_{p,mean}$. It is important to note that none of these models reached the limit of $L_p = 0.342L$, and thus, negative integration weights did not affect the element response as discussed in Section 4.3.1.

4.7.1 Sensitivity Analysis of Global Results

Since the concentration of damage in a RC column occurs in the post-peak softening range of the lateral load versus displacement behavior, the assumed plastic hinge length has a small effect on the effective stiffness and maximum strength (Pugh et al., 2015). As such, only the sensitivity of the ultimate displacement prediction to the assumed value of L_p is presented in this section.

The simulated-to-measured ultimate displacement ratios from the three unregularized and two regularized sets of material parameters are depicted in Figure 4.8 for the 28 columns (note that $R\delta_u$ values greater than 5.0 are not presented in the figure because of the plot range selected for clarity). In general, the predicted ultimate displacement increased as the assumed plastic hinge length increased. The ultimate displacements predicted by the unregularized models (Figure 4.8a-c) were highly sensitive to the assumed plastic hinge length, with the greatest variations when using the Saatcioglu

and Razvi (1992) concrete parameters. In comparison, the ultimate displacements predicted by the regularized models (Figure 4.8d,e) were much less sensitive to the assumed plastic hinge length.

The reduced sensitivity of the global results to the assumed plastic hinge length is the most important benefit from the regularization of the post-peak concrete stress-strain relationships [i.e., Eq. (4-3) and Eq. (4-4)]. The results in Figure 4.8e show that the proposed confined concrete regularization [using Eq. (4-8), together with Eq. (4-7)] provided much more accurate simulations of the ultimate displacement, with a small and generally constant variability for the considered range of L_p (see mean $\pm$ σ lines in Figure 4.8), as compared to the regularization equations proposed by Pugh et al. (2015) for slender RC walls (Figure 4.8d).

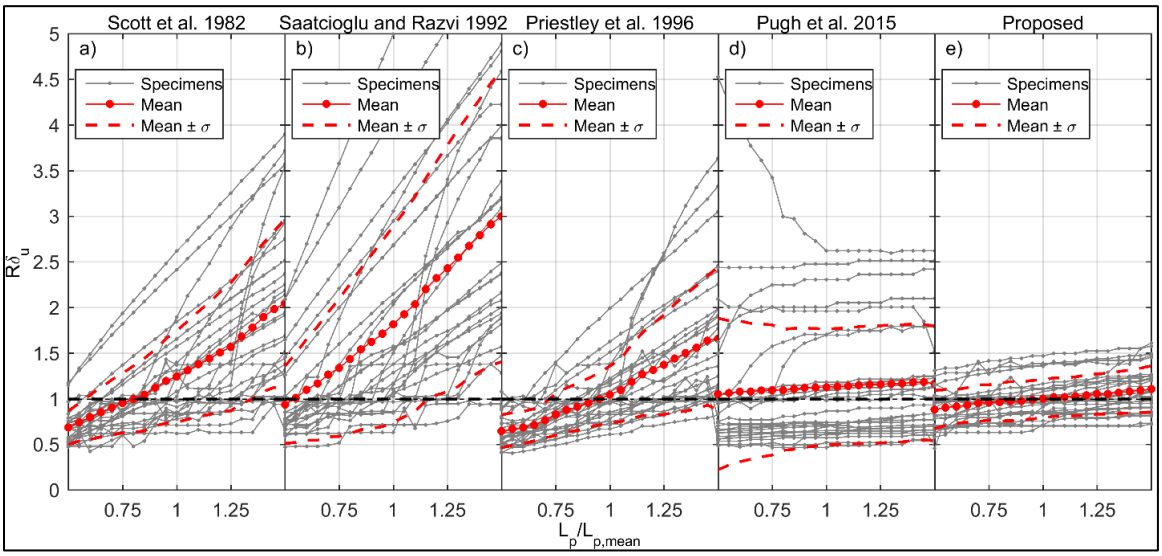

Figure 4.8: Sensitivity of predicted ultimate displacement to assumed plastic hinge length. Unregularized plastic hinge models (a-c); regularized plastic hinge models (d,e).

4.7.2 Sensitivity Analysis of Local Results

The simulated-to-measured ratio of curvatures, $R\phi$ and extreme confined concrete compressive strains, $R\varepsilon_{cc}$ corresponding to the last points plotted in Figure 4.7 (i.e., at the largest reported μ_δ in each test) are presented in Figure 4.9. Missing points (resulting in incomplete lines) in Figure 4.9 correspond to simulations that did not reach the largest measured μ_δ because of earlier predicted failure of the column when using smaller values of $L_p/L_{p,mean}$. These premature failure predictions were more common when using the unregularized concrete materials (Figure 4.9a) than when using the proposed regularized concrete materials (Figure 4.9b; where, the only missing points are for the simulations of column ID 6 with $L_p/L_{p,mean}$ ≤0.65). In general, the results show that the local column behavior is very sensitive to the assumed plastic hinge length when using either set of material parameters. As such, concrete regularization did not reduce the sensitivity of the

simulated local behavior to the assumed L_p, unlike the effectiveness of regularization in reducing the sensitivity of the simulated global behavior to L_p, as shown in Figure 4.8e.

It should be mentioned that measured local behaviors (curvatures and strains) can also be greatly sensitive to the location and gauge length of the potentiometers used in each experiment. Therefore, the simulated-to-measured curvature and strain ratios presented in Figure 4.9 may have been significantly different if the potentiometers were placed differently in each test (since the denominator of the ratios would change). To investigate this effect, the large black circle markers in Figure 4.9 represent the results that may be expected from models for which the plastic hinge length, L_p, exactly matched the gauge length of the potentiometers used in each column test. Missing circle markers in each plot indicate models outside the plotted data range or with earlier predicted failure of the column. Note that these results were not simulated, but rather interpolated between the analyzed cases (depicted by the smaller markers) in Figure 4.9. It can be seen that the predictions of local behavior would not have been accurate even if the assumed L_p values exactly matched the experimental gauge lengths.

As another important observation from Figure 4.9, different $L_p/L_{p,mean}$ ratios ranging between 0.70 and 1.05 (not considering column ID 5 and 21) would be needed to obtain accurate simulations of local behavior (i.e., $R\phi$ and $R\varepsilon_{cc}$ ratios that are close to 1.0) using the proposed regularized concrete parameters. Since the sensitivity of global column response to the assumed L_p is significantly reduced by these regularized concrete parameters (Figure 4.8e), future development of new L_p equations calibrated based on measured local (rather than global) column behavior can ultimately result in a regularized

plastic hinge model that can accurately capture both global and local behaviors of RC columns.

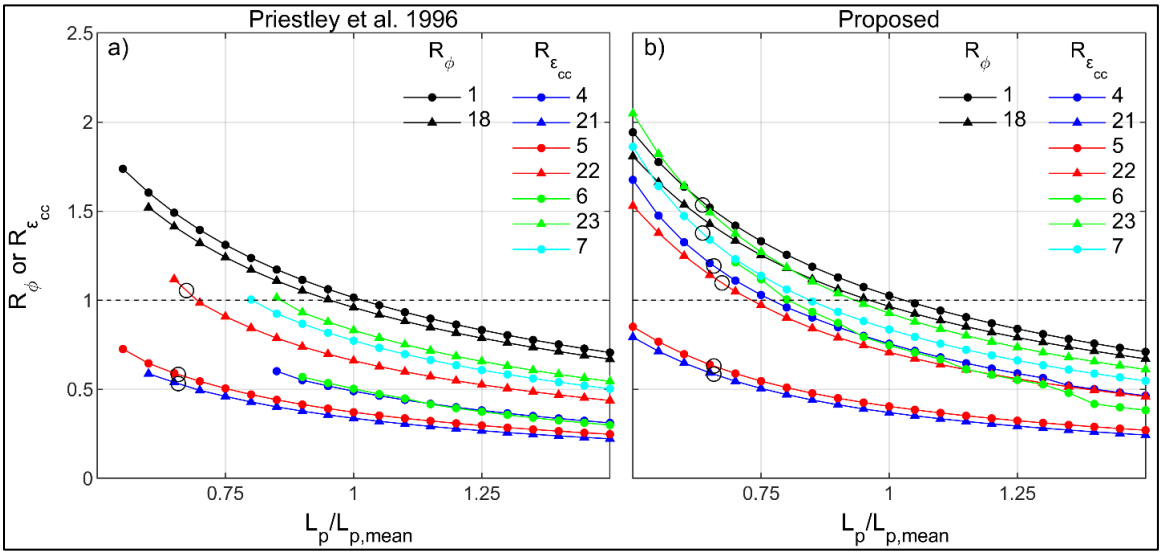

Figure 4.9: Sensitivity of predicted curvatures and strains to assumed plastic hinge length. a) Unregularized plastic hinge models with concrete materials from Priestley et al. (1996); b) proposed regularized plastic hinge models.

4.8 Summary and Conclusions

This chapter critically evaluates the accuracy and sensitivity of the simulated global and local lateral load behaviors of slender RC columns to the assumed plastic hinge length and material stress-strain relationships. The study was conducted using the force-based beam-column element in OpenSees with the modified Gauss-Radau plastic hinge integration method. A new equation for the confined concrete crushing energy was calibrated based on the measured ultimate (failure) displacement of 17 previously-tested column specimens, and validated using a set of 11 additional column specimens. The simulated global lateral load behaviors (effective stiffness, maximum strength, and

ultimate displacement) of these 28 columns using the proposed regularization equation were compared with results obtained using three sets of unregularized (conventional) concrete stress-strain models as well as a regularized concrete model available for slender RC walls. For the evaluation of local column behaviors (curvatures and strains), the results obtained from the proposed regularization equation and one set of unregularized material parameters were evaluated using available measured data from nine columns. Finally, sensitivity analyses of the simulated global and local column behaviors to the assumed plastic hinge length were conducted. The important findings and conclusions from the chapter are as follows:

1. The proposed regularization equation for the confined concrete crushing energy provided reasonably accurate simulations of the ultimate (i.e., failure) lateral displacement of the 28 column specimens, including the 11 validation columns that were not used in the calibration of the equation. The confined concrete crushing energy is given in Eq. (4-8) and is based on the unconfined concrete crushing energy using Eq. (4-7) from Nakamura and Higai (2001). Unlike available regularization procedures for slender RC walls, the proposed model for RC columns does not require regularization of the reinforcing steel stress-strain relationship.
2. The full reversed-cyclic hysteretic behaviors up to the ultimate displacement of the 28 column specimens were also generally well captured by the proposed regularized plastic hinge model, simulating cyclic strength and stiffness degradation.
3. The accuracy and variability of the effective stiffness and maximum strength from the simulation of the 28 columns were similar among the three unregularized and two

regularized sets of material parameters. The effective stiffness was generally overpredicted (as is common for the numerical modeling of RC components), while the maximum strength was predicted within $\pm$20% error.

4. The ultimate (failure) lateral displacement of the columns presented much larger variability than effective stiffness and maximum strength. The best unregularized model results were obtained using the concrete material parameters from Priestley et al. (1996). The model using the available regularization equations for slender RC walls was not adequate to consistently simulate the ultimate displacement of the column specimens with high accuracy. In comparison, the model using the proposed regularization equation presented significant improvements of accuracy in the prediction of ultimate displacement.
5. In terms of local column responses, unregularized (with concrete material parameters from Priestley et al. (1996)) and regularized (using the proposed regularization equation) plastic hinge models presented similar curvature predictions, which generally underestimated the measured values at the critical sections of two column specimens, with better predictions at greater lateral displacements.
6. The simulation results from the unregularized (with concrete material parameters from Priestley et al. (1996)) and regularized (using the proposed regularization equation) plastic hinge models mostly underestimated the available measured extreme confined concrete compression strains for seven columns. This underestimation was because the plastic hinge lengths used in these models were larger than the potentiometer lengths used for the measurements, thus modeling average strains over greater lengths. At large

column displacements, the strains from the proposed regularized plastic hinge model were better than the simulations from the unregularized model.

7. The predicted ultimate displacement was very sensitive to the assumed plastic hinge length, L_p when using unregularized models. This sensitivity was significantly reduced when using regularized models, and further improved when using the proposed regularization equation. This presents a major advantage of the proposed regularized plastic hinge model over unregularized plastic hinge models.
8. The predictions of local behavior (curvatures and strains) were very sensitive to the assumed plastic hinge length, L_p for both the unregularized and regularized models. As such, regularization of the material stress-strain relationships did not reduce the sensitivity of the simulated local behaviors to the assumed L_p, unlike the effectiveness of regularization in reducing the sensitivity of the simulated global behavior to L_p.
9. The simulations of local behavior would not have provided accurate results even if the assumed L_p values exactly matched the gauge lengths of the potentiometers used in the experimental measurements of column curvatures and concrete strains. Further, different $L_p/L_{p,mean}$ ratios would be needed to obtain accurate simulations of local behavior for the different column specimens. Since the sensitivity of global column response to the assumed L_p is significantly reduced by using the proposed regularized plastic hinge model, future development of new L_p equations calibrated based on measured local (rather than global) column behavior can ultimately result in accurate predictions of both global and local behaviors.

CHAPTER 5:

QUANTIFICATION OF VARIABILITY IN SIMULATED SEISMIC PERFORMANCE OF RC WALL BUILDINGS

In this chapter, the third and fourth specific objectives of this dissertation are studied based on five numerical models with different fiber-based two-node line-elements, namely FB-BC, DB-BC, MVLEM, FLPM-H/6, and FLPM-H/2. The models were developed using the same material constitutive relationships and other analysis inputs (e.g., damping) so that the quantified variability in the predicted building performance was caused by the numerical modeling approach rather than user-selected parameters. The models were first validated against the measured shake-table behavior of a 7-story RC wall building tested at the University of California San Diego. Then, nonlinear dynamic analyses of the 7-story wall test specimen and three RC wall archetype buildings of 4-, 8-, and 12-stories were conducted to quantify the variability in selected seismic performance assessment parameters. Additionally, damage fragility curves for the buildings were developed and compared following the FEMA P695 methodology.

The variability in the numerical model responses of the four buildings was evaluated using ground motion suites corresponding to three hazard levels with 50%, 10%, and 2% probability of exceedance in 50 years, and based on commonly-used global (interstory drift ratio and roof drift ratio) and local (plastic hinge rotation and curvature at

the critical length) response parameters. The results show that the variability in global response parameters is significantly smaller than the variability in local response parameters.

5.1 Introduction

Advances in the nonlinear numerical simulation of reinforced concrete (RC) structural walls have allowed the assessment of their inelastic behavior when conducting performance-based seismic design (PBSD). In this design approach, the structure is evaluated considering different seismic hazard levels and performance objectives based on global response parameters (e.g., interstory drifts) as well as local or element-level response parameters (e.g., plastic hinge rotations). If the wall response quantified using these performance parameters does not comply with specified acceptance criteria, it must be redesigned, involving an iterative process.

Several nonlinear modeling approaches can be used for the performance assessment of RC wall structures. Since different nonlinear models are based on different assumptions and approaches, the analysis results and the performance assessment can vary, limiting confidence in the design outcome. The effect of the modeling approach on the predicted seismic behavior of RC walls has been evaluated based on linear analyses (Chacón et al., 2017) and nonlinear analyses of pseudo-static experimental tests (K. Kolozvari et al., 2018; Kristijan Kolozvari et al., 2019; Pozo et al., 2020; Pugh et al., 2015). In comparison, evaluations of model variability based on nonlinear dynamic response are rare in the literature because of the higher computational cost as well as limited shake-table experimental data.

Several studies (Grange et al., 2009; Huy, 2008; Kelly, 2007; Martinelli & Filippou, 2009) have shown the capabilities of different nonlinear models to predict the shake-table test response of a 7-story wall building subassembly (Panagiotou et al., 2011), while other studies (Deger & Wallace, 2015; Rosita Jünemann et al., 2016; Maffei et al., 2014; J. A. Vásquez et al., 2020; Zhang et al., 2017) have used different models to simulate the observed damage in wall buildings after the 2010 Chilean earthquake. However, the results from these studies cannot be used to quantify the variability of the response predicted by the different modeling approaches since the simulations included other differences that impacted the outcomes (e.g., different material constitutive relationships, damping assumptions, element connectivity assumptions).

Marafi et al. (2019) quantified the variability in the collapse probability of RC wall archetypes when using force-based and displacement-based beam-column numerical modeling approaches. As an important limitation, many of the numerical analyses did not converge when using the force-based approach, leading to interpretations of unrealistic collapse probabilities. Moreover, the variability in the analysis results was only quantified for the collapse of the archetypes, even though other performance levels (i.e., at different seismic hazard levels) are also important for PBSD.

In accordance with the above knowledge gaps, the current study investigates and quantifies the variability obtained from stable (i.e., without convergence problems) numerical analyses of RC wall buildings in terms of 1) global and local performance assessment parameters at three seismic hazard levels, and 2) damage fragility curves. The focus is on slender walls where the axial-flexural behavior dominates the nonlinear

response. The considered numerical models, which are described next, are referred to as: FB-BC, DB-BC, MVLEM, FLPM-H/6, and FLPM-H/2. These five models are first validated against the measured seismic shake-table test behavior of a 7-story wall building subassembly. Then, nonlinear dynamic analyses of the 7-story wall test specimen and three archetype wall buildings from Marafi et al. (2019) are conducted to quantify the variability in the resulting performance assessment parameters and fragility curves. Importantly, the models investigated all used the same material constitutive relationships and other analysis inputs (e.g., damping) so that the quantified differences in the building performance are caused by the numerical modeling approach rather than user-selected parameters.

5.2 Description of Numerical Modeling Approaches

The following five nonlinear approaches for modeling RC walls are compared in the study: 1) force-based beam-column (FB-BC) element model; 2) displacement-based beam-column (DB-BC) element model; 3) multiple vertical line element model (MVLEM); and 4) two finite length plasticity models using two different plastic hinge lengths (FLPM-H/6 and FLPM-H/2). These modeling approaches were selected because they have been used quite frequently in previous research. Furthermore, these element models are available in a single computational platform (OpenSees, (McKenna et al., 2000)), and thus, the same material constitutive relationships, damping definitions, and element connectivity can be used, resulting in the modeling approach to be the only difference among the simulations.

All five modeling approaches utilize two-node line elements based on fiber sections with cyclic uniaxial concrete and steel material constitutive stress-strain relationships. The

models simulate axial-flexural interaction by assuming a linear strain distribution over the cross-section depth (i.e., plane sections remain plane assumption), while the shear behavior is uncoupled from the axial-flexural behavior. The shear behavior was considered as linear-elastic in the five models because shear deformations are relatively small in slender RC walls (Segura & Wallace, 2018a). The following paragraphs present a summary of the primary differences in the selected modeling approaches.

The force-based beam-column (FB-BC) element model (Spacone et al., 1996) assumes linear moment variation and constant axial force along the length of each line element. This model accurately represents the moment and axial force distributions over the height of a wall, therefore, one element per story with multiple integration points is enough to represent the nonlinear curvature distribution (Figure 5.1a). Equilibrium is strictly satisfied at each integration point of the FB-BC model; however, intra-element iterations are required to relate the element forces with the nodal displacements. The shear behavior can be incorporated at the section level in OpenSees per Marini and Spacone (2006).

The displacement-based beam-column (DB-BC) element model (Hellesland & Scordelis, 1981) employs linear curvature variation and constant average axial deformation along the length of each line element. Therefore, multiple elements per story are required to accurately capture the nonlinear variation of curvatures when simulating a wall (Figure 5.1b). Equilibrium is satisfied on average within an element, and not at each integration point as in the case of the FB-BC model. To simulate the shear behavior, a shear spring in

series with each DB-BC element is required, resulting in additional nodes to model the wall.

The multiple vertical line element model (MVLEM) (Orakcal, 2004) employs a series of vertical uniaxial springs (i.e., macro fibers) that represent the axial-flexural behavior of the wall, and one horizontal spring to simulate the shear behavior. The vertical uniaxial springs are rigidly constrained together at each end of the element to force the plane sections remain plane assumption. The MVLEM model assumes constant curvature variation and constant average axial deformation along the length of each element. Therefore, multiple elements per story are required to accurately capture the nonlinear variation of curvatures when simulating a wall (Figure 5.1c).

The finite length plasticity model (FLPM) (Michael H. Scott & Fenves, 2006) is similar to the FB-BC model. However, nonlinearity is concentrated over an assumed plastic hinge length located at each end of the element, while the inner length of the element is assumed to remain linear-elastic. This modeling approach has been implemented in OpenSees using the *beamWithHinges* element, where the user specifies an assumed plastic hinge length. FLPM models with two different plastic hinge lengths are considered in this study, as defined in the next section (Figure 5.1d,e). The shear behavior can be incorporated at the section level as in the case of the FB-BC model.

Note that RC elements with softening post-peak behavior (e.g., due to concrete crushing and rebar buckling) are highly sensitive to the critical length, L_{cr} over which the nonlinear behavior and failure of the element are localized. The critical length corresponds to the weight of the first integration point in the FB-BC model, it is equal to the element

length in the DB-BC and MVLEM models, and it is equal to the assumed plastic hinge length in the FLPM models (see Figure 5.1).

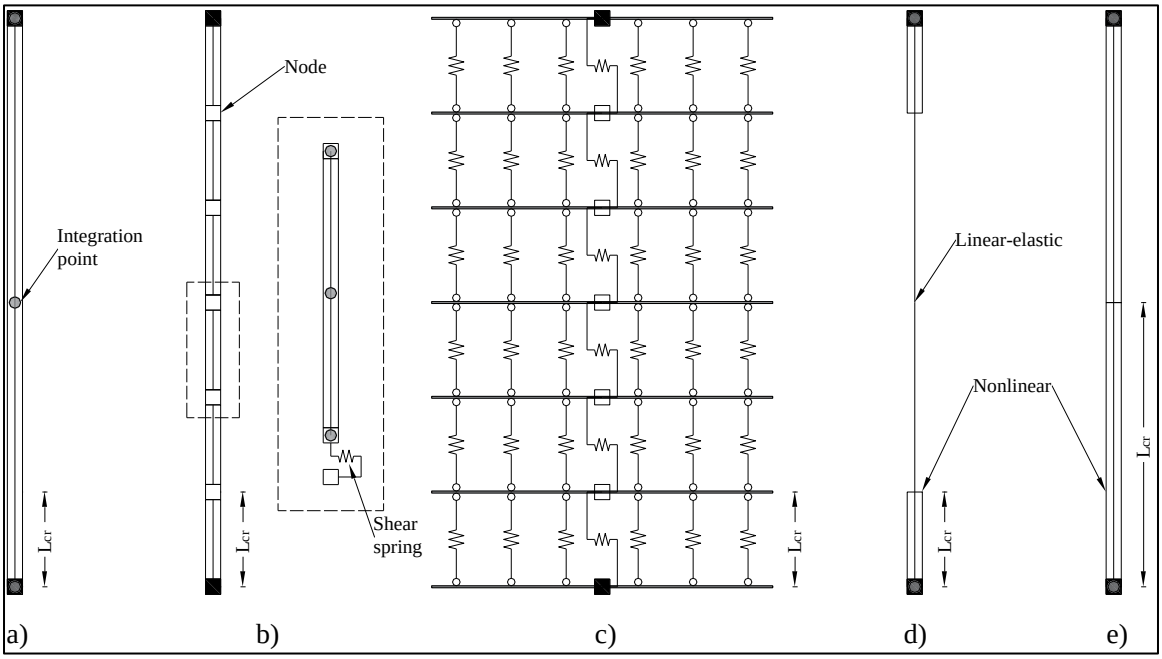

Figure 5.1: Nonlinear models to simulate each story of a RC wall. a) FB-BC; b) DB-BC; c) MVLEM; d) FLPM-H/6; and e) FLPM-H/2.

5.3 Validation of Numerical Models

The selected models were validated using the measured shake-table test response of a 7-story wall building subassembly. Only a brief description of the tested building is presented here, since more information can be found elsewhere (Panagiotou, 2008; Panagiotou et al., 2011). The building was designed for a site in Los Angeles, California and had a story height of 2.74 m, resulting in a total height of 19.2 m from the top of the foundation. The test subassembly comprised of: 1) a 3.66 m long web wall with thickness of 203 mm in the first and seventh stories, and 152 mm elsewhere; 2) a 4.88 m long flange

wall with thickness of 203 mm in the first story and 152 mm elsewhere; 3) a precast segmental wall for torsional stability; and 4) a 203 mm thick slab at each floor that was also supported on four auxiliary gravity steel columns. The web and flange walls were connected by a slotted slab connection designed to enable shear transfer with minimal moment transfer between these walls, while the web wall and the precast segmental wall were connected using a pin-pin horizontal steel truss. The structure was subjected to four ground motion records (referred to as EQ1, EQ2, EQ3, and EQ4, with sequentially increasing intensities), in addition to low amplitude white noise before and after each record for system damage identification. The records were applied in the direction of the web wall; therefore, the web wall provided the main lateral resistance while the flange wall and the precast segmental wall provided transverse and torsional stability.

Two-dimensional (2D) models of the test specimen were developed with lumped masses at each floor (Figure 5.2). As shown later in the chapter, it was adequate to model the structure in 2D since the lateral loading and primary response during the tests concentrated in the web wall direction. The models consisted of nonlinear line elements to simulate the web wall (primary focus of the current study) at its centerline, horizontal rigid links at each floor level to connect the centerline of the web wall with its edges, linear elastic line elements simulating the flange wall and the precast segmental wall, linear elastic truss elements simulating their connections to the web wall, and linear elastic line elements simulating the foundation.

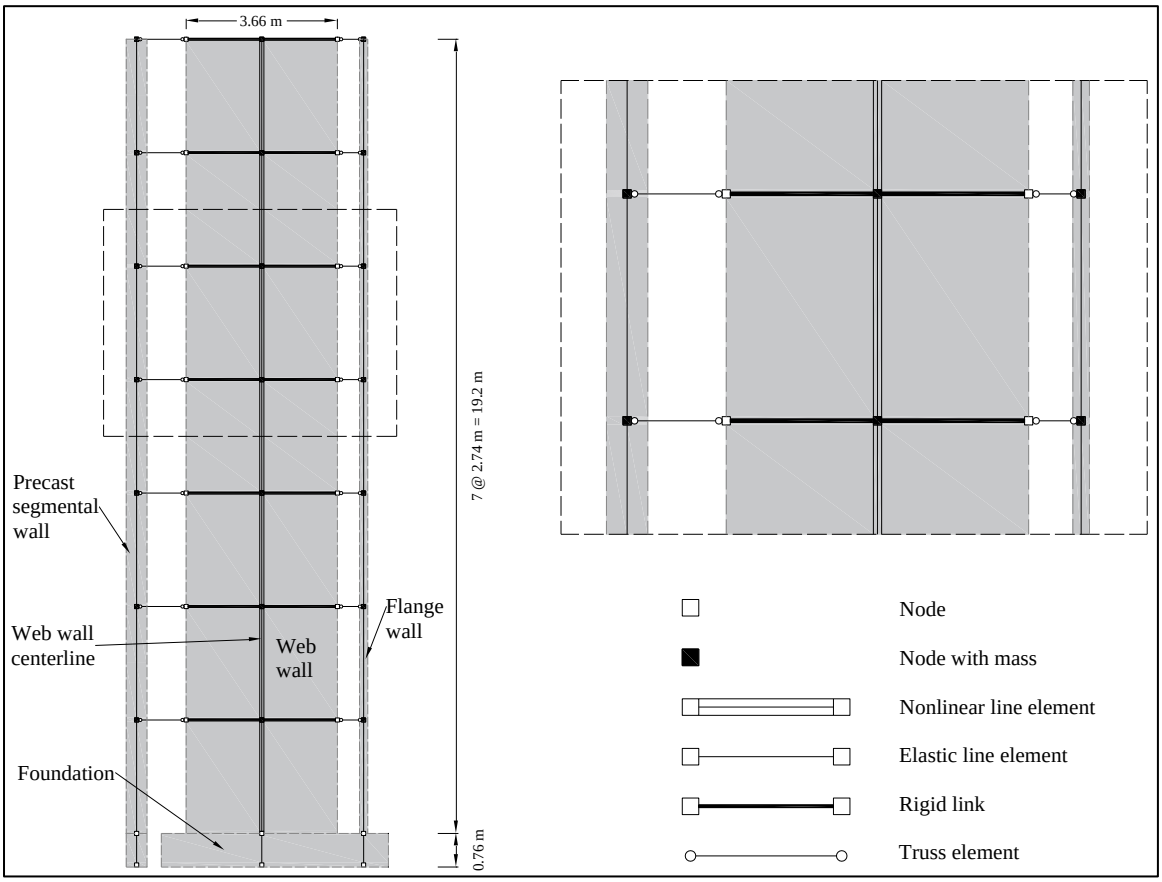

Figure 5.2: 2D numerical model geometry of the 7-story wall building.

The nonlinear axial-flexural behavior of the web wall was simulated using the five models in Figure 5.1. One element with three Gauss-Lobatto integration points (grey circles in Figure 5.1a) was used in each story of the FB-BC model. This selection for the integration points resulted in a critical length of one-sixth the story height ($L_{cr} = 457$ mm), where the nonlinear axial-flexural deformations concentrated. Six elements per story were used in the DB-BC and MVLEM models to obtain the same critical length as in the FB-BC model (see Figure 5.1b,c). One element per story, with nonlinear behavior concentrated at both ends of the element was considered in the FLPM models (Figure 5.1d,e). As stated

previously, the critical length in a FLPM element is equal to the assumed plastic hinge length specified by the user. In this study, FLPM models with two different plastic hinge lengths were considered as follows: 1) a plastic hinge length equal to one-sixth the story height (FLPM-H/6; Figure 5.1d) – to result in the same critical length as in the FB-BC, DB-BC, and MVLEM models; and 2) a plastic hinge length equal to one half the story height (FLPM-H/2; Figure 5.1e) – following the recommendations of ASCE 41 (2017).

Unconfined and confined concrete were simulated in all the models using the uniaxial *Concrete02* material in OpenSees. The pre-peak compressive stress-strain relationship in *Concrete02* is defined by the Hognestad parabola. An initial stiffness (i.e., Young's modulus) of $E_c = 4700\sqrt{f_c'}$ (in MPa units) was assumed for both unconfined and confined concrete following ACI 318 (2019), where f_c' is the compressive strength of the unconfined concrete. The peak stress point in *Concrete02* is assumed to be reached at a strain of $\varepsilon_o = 2f_c'/E_c$ for unconfined concrete and $\varepsilon_{co} = 2f_{cc}'/E_c$ for confined concrete, where f_{cc}' is the compressive strength of the confined concrete. In this study, f_{cc}' was calculated as $f_{cc}' = Kf_c'$, where K is the confined concrete strength ratio from Mander et al. (1988). Beyond the peak strength, the compressive stress-strain relationship reduces linearly to a residual stress point, which was determined by regularization (Pugh et al., 2015) based on the critical length of each model. The regularization of the post-peak stress-strain relationship was done using an unconfined concrete crushing energy of $Gf_c = 2f_c'$ (N/mm for f_c' in MPa units; (Pugh et al., 2015)) and a confined concrete crushing energy of $Gf_{cc} = 5(K - 0.85)\, Gf_c \leq 2.5\, Gf_c$, but not less than Gf_c (in N/mm units; (L. Lowes et al., 2016)).

The tensile behavior of the *Concrete02* material is bilinear, reducing to zero stress through tension-softening after cracking. The tensile strength at cracking was taken as $0.62\sqrt{f_c'}$ (in MPa units) according to ACI 318 (2019), while the tension softening stiffness was taken as $0.1E_c$.

The reinforcing steel was simulated using the Menegotto and Pinto (1973) model, which is available in OpenSees as the *Steel02* material. The *MinMax* material model was used in combination with *Steel02* to simulate: 1) complete loss of steel compressive stress, representative of buckling, when the ultimate (i.e., crushing) strain of confined concrete was exceeded (Pugh et al., 2015), and 2) steel fracture in tension. Note that when one of the *MinMax* material limits is exceeded, the steel fiber no longer contributes to the resistance of the section in either direction (i.e., compression or tension).

The gravity loads in all models were applied first, by means of a static analysis. Then, a dynamic analysis was conducted using a single continuous sequence of concatenated ground motion records from EQ1 to EQ4. Rayleigh damping proportional to the mass and initial stiffness was assumed, with a damping ratio of 1.0% in the first two vibration modes of the building (Martinelli & Filippou, 2009).

Roof displacement responses of the 7-story wall building subassembly, subjected to the four ground motions, are presented in Figure 5.3. The numerical responses predicted by the five models show good agreement with the measured response for the four ground motions. Maximum response parameters are typically used for performance assessment, and thus, experimental and numerical envelopes of maximum floor displacement, interstory drift ratio, and story shear force are presented in Figure 5.4. The numerical

models generally overpredicted the maximum floor displacements and interstory drifts, except for EQ3 (see the first two columns of plots in Figure 5.4). Furthermore, the numerical models generally underpredicted the story shear forces, except for EQ1 (see the third column in Figure 5.4). Numerical-to-experimental ratios of the maximum roof displacement, interstory drift ratio, and base shear are presented in Figure 5.5, showing that the analyses were generally able to predict the measurements within $\pm$30% error (except for the maximum interstory drift ratio for EQ2 and the maximum base shear for EQ1 using the FLPM-H/6 model).

The results in Figure 5.3, Figure 5.4, and Figure 5.5 demonstrate the capabilities of the selected models to simulate the dynamic response of a RC wall building subassembly. However, different models predict different results and thus, the performance assessment of the structure can differ from model to model. Therefore, the variability in the simulated performance assessment parameters is quantified next using three RC wall building archetypes in addition to the 7-story wall building test subassembly.

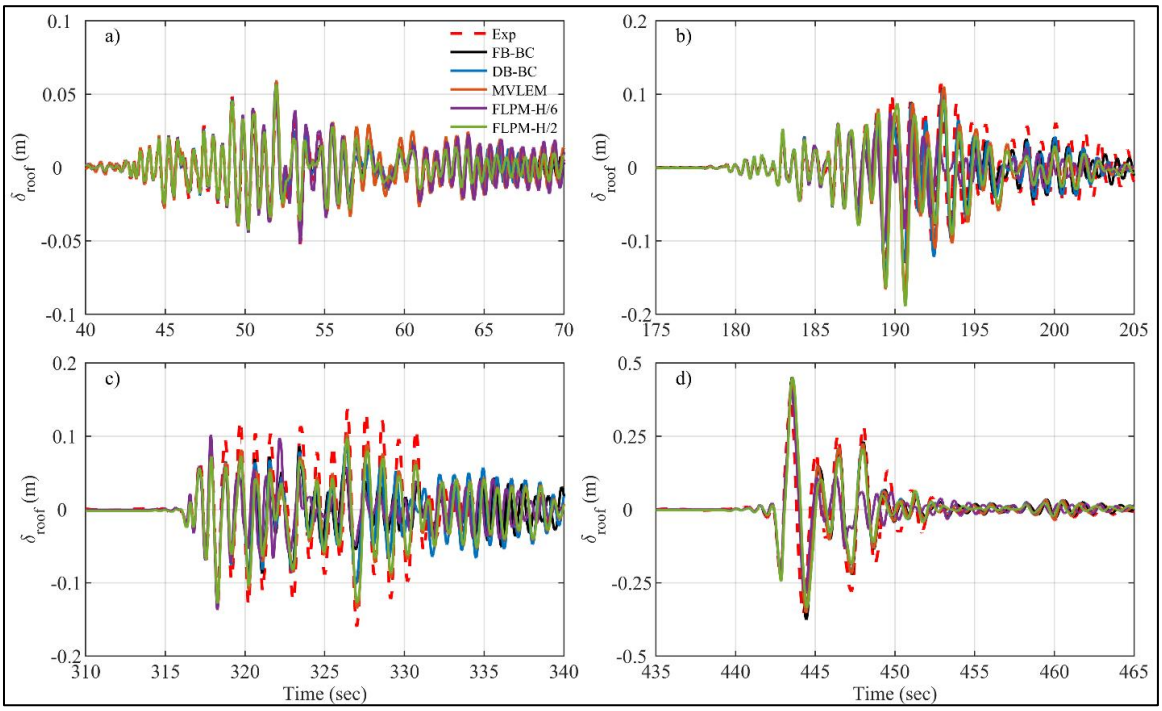

Figure 5.3: Experimental and numerical roof displacement time histories. a) EQ1; b) EQ2; c) EQ3; and d) EQ4.

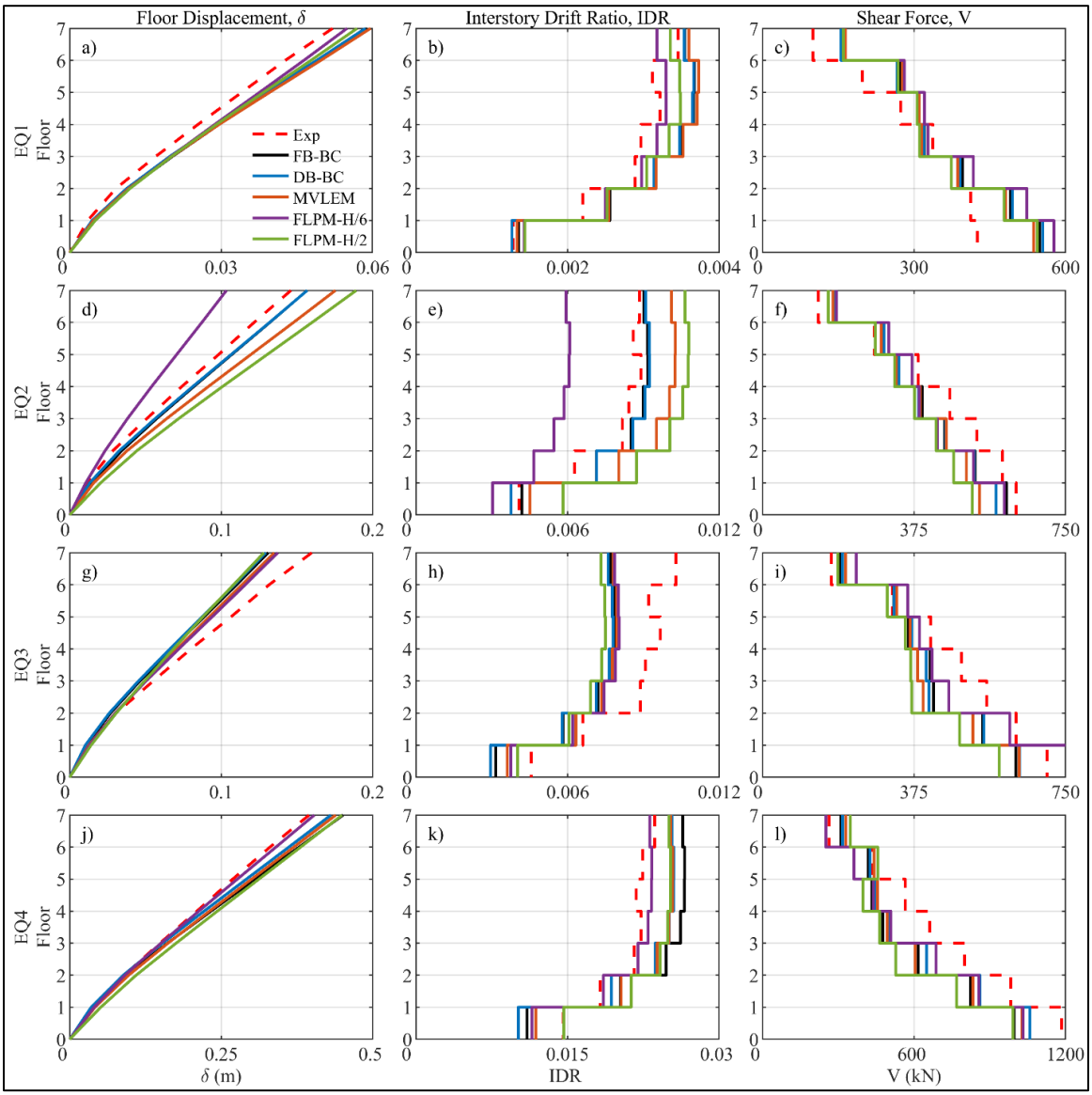

Figure 5.4: Experimental and numerical envelopes of peak floor displacement, interstory drift ratio, and story shear-force for the ground motion records (each row is for a different ground motion record).

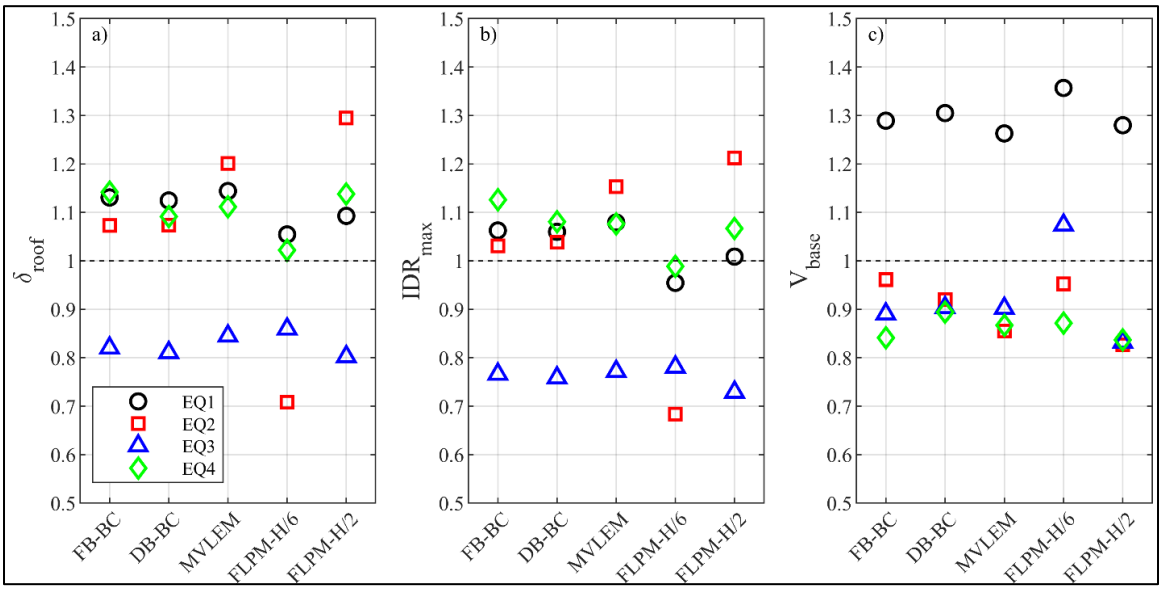

Figure 5.5: Numerical-to-experimental ratios. a) Maximum roof displacement; b) maximum interstory drift; and c) maximum base shear.

5.4 Building Archetypes and Seismic Hazard Levels

The previous section presented the validation of the numerical models to simulate the measured dynamic shake-table behavior of a 7-story wall building test subassembly. This section presents a description of three archetype wall buildings (referred to as 4-, 8-, and 12-story buildings) designed by Marafi et al. (2019) for a site in Los Angeles, California, that are used in addition to the 7-story wall building test subassembly to quantify the variability in the numerical performance assessment. The three archetypes are 36.6 m long by 36.6 m wide in plan, with four 9.15 m bays of slab-column gravity framing in each direction. The lateral resisting system consists of two solid RC walls in each direction in the 4- and 8-story buildings (Figure 5.6a), and four walls in each direction in the 12-story building (Figure 5.6b). The walls in the 4-story building are 610 mm thick by 7.32 m long, while the walls in the 8- and 12-story buildings are 610 mm thick by 9.15 m

long. The three archetypes have a first story height of 4.57 m, while the other stories are 3.96 m high, as shown for the first four stories of the buildings in Figure 5.6c.

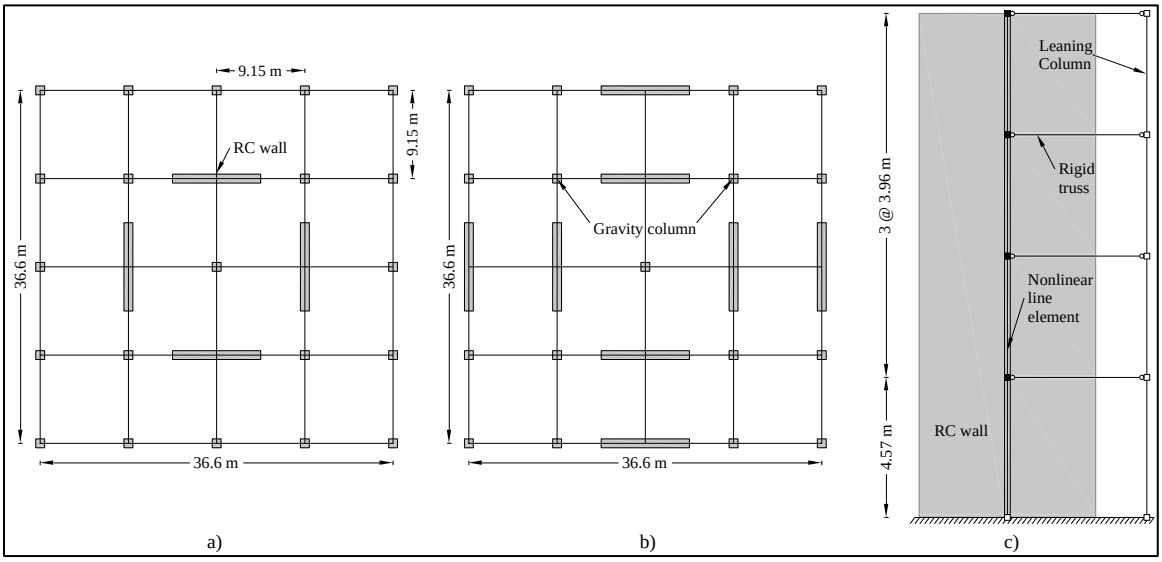

Figure 5.6: Archetype buildings. a) 4- and 8-story building floor plan; b) 12-story building floor plan; and c) elevation of the lower four stories of the buildings.

The archetypes were analyzed using 2D numerical models where only one of the RC walls was simulated because of symmetry. Therefore, one-half of the total mass was considered when simulating the 4- and 8-story buildings and one-fourth of the total mass when simulating the 12-story building. Every 2D model (Figure 5.6c) included nonlinear elements to simulate each story of the RC wall, a leaning column to simulate P-Delta effects, a horizontal rigid truss element to connect the leaning column with the wall centerline at each floor, and a lumped mass at each floor. Five different models were developed for each building, with the FB-BC, DB-BC, MVLEM, FLPM-H/6, and FLPM-H/2 elements in Figure 5.1 representing the RC wall in each story. The concrete and steel

material models presented in Section 5.3 were used in the simulations, based on the expected concrete and steel material strengths ($f_c' = 44.8$ MPa and $f_y = 484$ MPa) from Marafi et al. (2019). A Rayleigh damping ratio of 2.0% was assigned in the first two vibration modes of the archetype buildings. This value was chosen because it is less than the maximum damping ratio of 2.5% suggested by ASCE 7 (2017), and is consistent with the 2.0% damping ratio used by Marafi et al. (2019) to simulate the same archetypes.

The FB-BC, DB-BC, FLPM-H/6, and FLPM-H/2 models resulted in fundamental periods of T=0.61, 0.30, 0.74, and 1.18 sec for the 7-, 4-, 8-, and 12-story buildings, respectively. Slightly longer fundamental periods (with negligible differences) of T=0.62, 0.31, 0.76, and 1.20 sec, respectively, were obtained using the MVLEM model. The longer periods obtained with the MVLEM are attributed to the use of macro fibers to represent the wall cross section, which resulted in slightly smaller moments of inertia.

The variability in the numerical model responses was evaluated using three ground motion suites corresponding to three hazard levels: 1) ten pairs of records with a 50% probability of exceedance in 50 years (i.e., 50%/50) developed by the SAC steel project for a site in Los Angeles (Somerville et al., 1997); 2) ten pairs of records with a 10% probability of exceedance in 50 years (i.e., 10%/50) developed by the SAC steel project for a site in Los Angeles (Somerville et al., 1997); and 3) twenty-two pairs of records recommended by FEMA P695 (2009) for the maximum considered earthquake with a probability of exceedance of 2% in 50 years (i.e., 2%/50). The ground motion records in each suite were scaled such that the average 5%-damped acceleration response spectrum was not less than the target spectrum for each hazard level over a range of periods from

0.2T and 1.5T (ASCE 7, 2010), where T=0.61, 0.30, 0.74, and 1.18 sec for the 7-, 4-, 8-, and 12-story buildings, respectively.

The target spectrum for the 50%/50 hazard level was obtained following the procedure in FEMA 356 (2000), while the 10%/50 and 2%/50 target spectra corresponded to the design basis earthquake (DBE) and the maximum considered earthquake (MCE), respectively, in ASCE 7 (2010). As an example, the scaled ground motion suites for the 8-story building (with T=0.74 sec) are presented in Figure 5.7, with target spectra for the three hazard levels obtained for a site in Los Angeles.

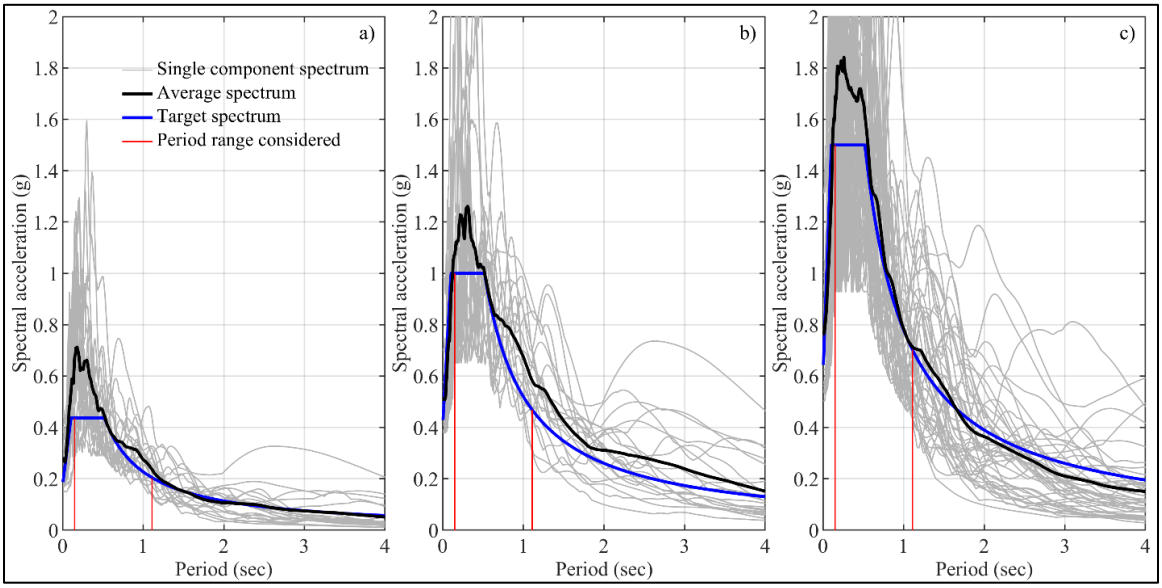

Figure 5.7: Ground motion records scaled for the 8-story building.
a) 50%/50; b)10%/50; and c) 2%/50 hazard level.

5.5 Performance Assessment Parameters

Nonlinear dynamic response analyses of the 7-story wall building subassembly, and of the 4-, 8-, and 12-story building archetypes were conducted to quantify the variability

in selected performance (i.e., damage) assessment parameters under the three hazard levels (50%/50, 10%/50, and 2%/50) as simulated by the five modeling approaches. Existing PBSD guidelines (ASCE 41, 2017; LATBSDC, 2017) specify criteria to assess the seismic performance of wall buildings based on the interstory drift ratio, IDR as a global parameter, and plastic hinge rotation, θ_p as a local or element-level parameter. As such, these parameters were included in the variability assessment. The variability in roof drift ratio, Δ_{roof} was also studied as a global performance parameter since ACI 318 (2019) requirements for special boundary elements of structural walls are based on Δ_{roof}. Finally, since strain response parameters have also been recommended for the performance assessment of walls when using fiber-based models (ACHISINA, 2017; TBI, 2017), the curvature at the critical length, ϕ_{cr} was also considered as a local parameter in the variability assessment. Note that the ϕ_{cr} results from the FLPM-H/2 model were not considered in this quantification since the L_{cr} of this model was significantly greater than the L_{cr} of the other models (see Figure 5.1), preventing consistent comparisons.

The plastic hinge rotation was calculated as the rotation over an assumed plastic hinge length, L_p of one half the story height, H according to ASCE 41 (2017). The equations used to calculate the plastic hinge rotation and the curvature at the critical length for each story are given in Table 5.1.

Table 5.1: Equations used to calculate plastic hinge rotation and curvature at the critical length for each story.

Model	Plastic hinge rotation	Curvature
FB-BC	$\theta_p = \phi_1 L_{cr} + (L_p - L_{cr})\phi_2$	$\phi_{cr} = \phi_1$
DB-BC	$\theta_p = \theta_{(H/2)} - \theta_{(0)}$	$\phi_{cr} = (\theta_{(L_{cr})} - \theta_{(0)})/L_{cr}$
MVLEM	$\theta_p = \theta_{(H/2)} - \theta_{(0)}$	$\phi_{cr} = (\theta_{(L_{cr})} - \theta_{(0)})/L_{cr}$
FLPM-H/6	$\theta_p = \phi_1 L_{cr} + \theta_e$	$\phi_{cr} = \phi_1$
FLPM-H/2	$\theta_p = \phi_1 L_{cr}$	-

ϕ_1 is the curvature of the first integration point, ϕ_2 is the curvature of the second integration point, θ_e is the rotation of the internal elastic element up to $L_p = H/2$, where H is the story height. $\theta_{(H/2)}$, $\theta_{(L_{cr})}$, and $\theta_{(0)}$ are the rotations of the nodes located at distances $L_p = H/2$, L_{cr}, and at the base of each story, respectively.

As examples of the response data generated from the dynamic analyses, the gray lines in Figure 5.8 show the peak interstory drift ratios (IDR) of the 8-story building simulated with the five models (each row of the figure) and with the seismic records of the three hazard levels (each column of the figure). Note that the peak IDR values for the different stories in a particular simulation (i.e., in each dotted line) did not necessarily occur

at the same time during the simulation. The average peak IDR values are represented using continuous lines in each plot.

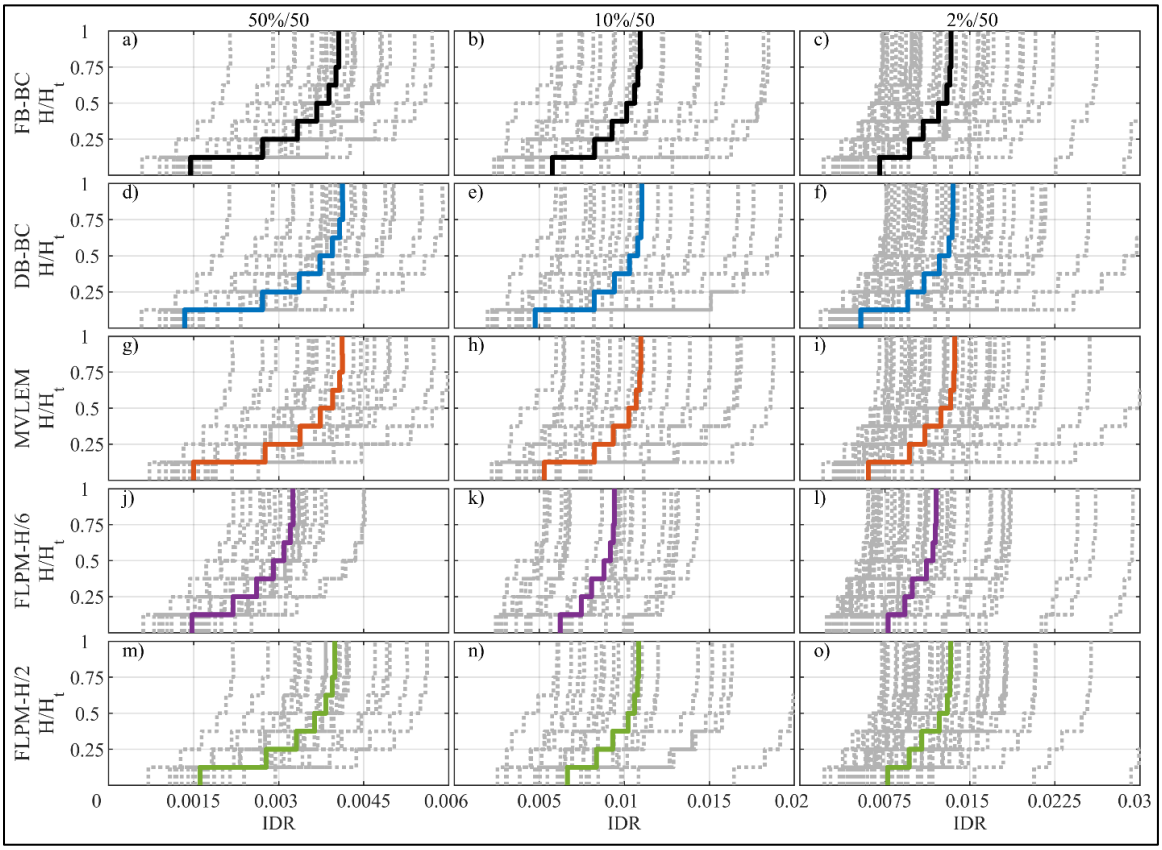

Figure 5.8: Peak interstory drift ratio for the 8-story building. Response to a single record in dotted lines and average response in continuous lines.

The average peak interstory drift ratios (IDR) predicted for all four buildings are presented in Figure 5.9 (the average results shown in Figure 5.8 for the 8-story building are the same as those in Figure 5.9g, h, and i). Similarly, the average results for the plastic hinge rotation, θ_p are presented in Figure 5.10. These average results, and those for roof drift ratio, Δ_{roof}, and curvature at the critical length, ϕ_{cr}, are used in the next section to

quantify the variability in the response parameters. As may be expected for axial-flexural response, the plastic hinge rotations, θ_p were concentrated at the base of each building (Figure 5.10), while larger IDR results were predicted in the top stories (Figure 5.9). Two different deformation components contributed most to the calculated IDR values: 1) axial-flexural deformations within the particular story, and 2) rigid body rotation of the wall due to the damage concentration (i.e., plastic hinge rotation) at the base. Since the second component due to base rotation does not correspond to damage in the top stories, the larger IDR results in the top stories do not indicate larger damage in these stories.

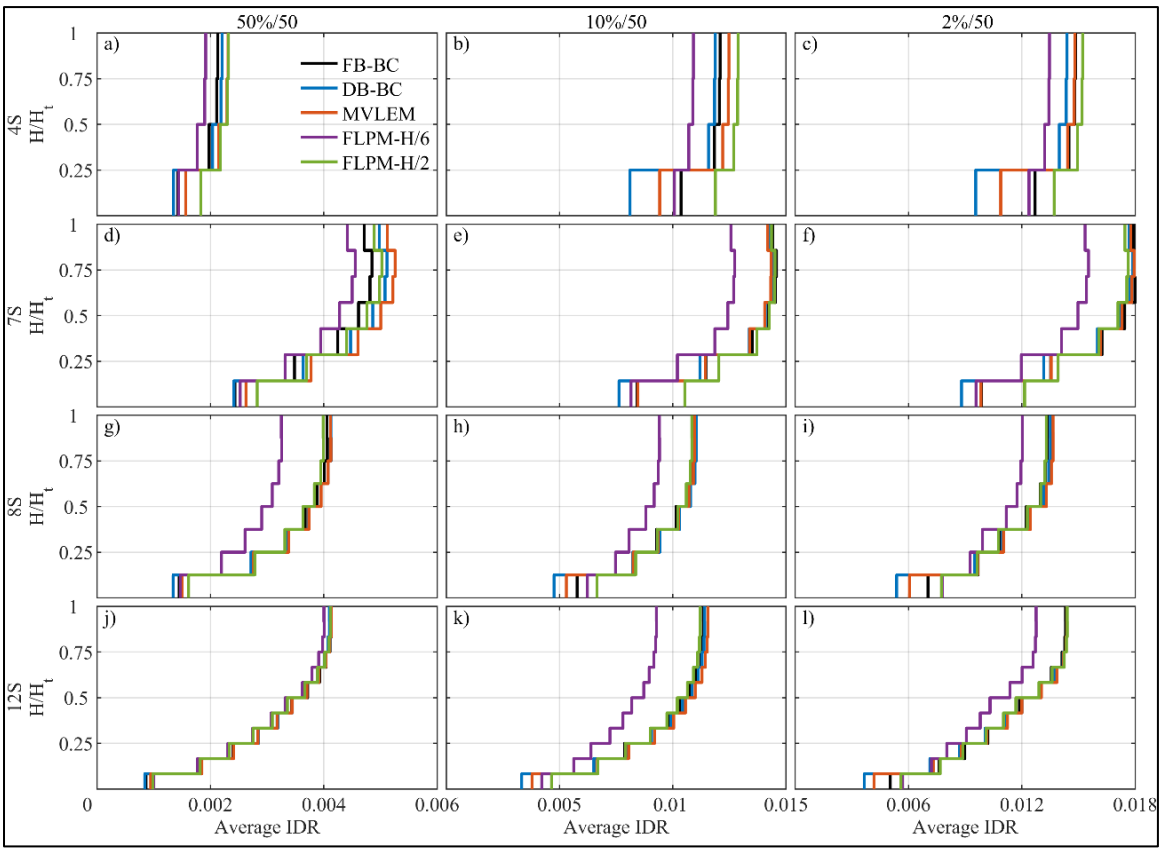

Figure 5.9: Average interstory drift ratio.

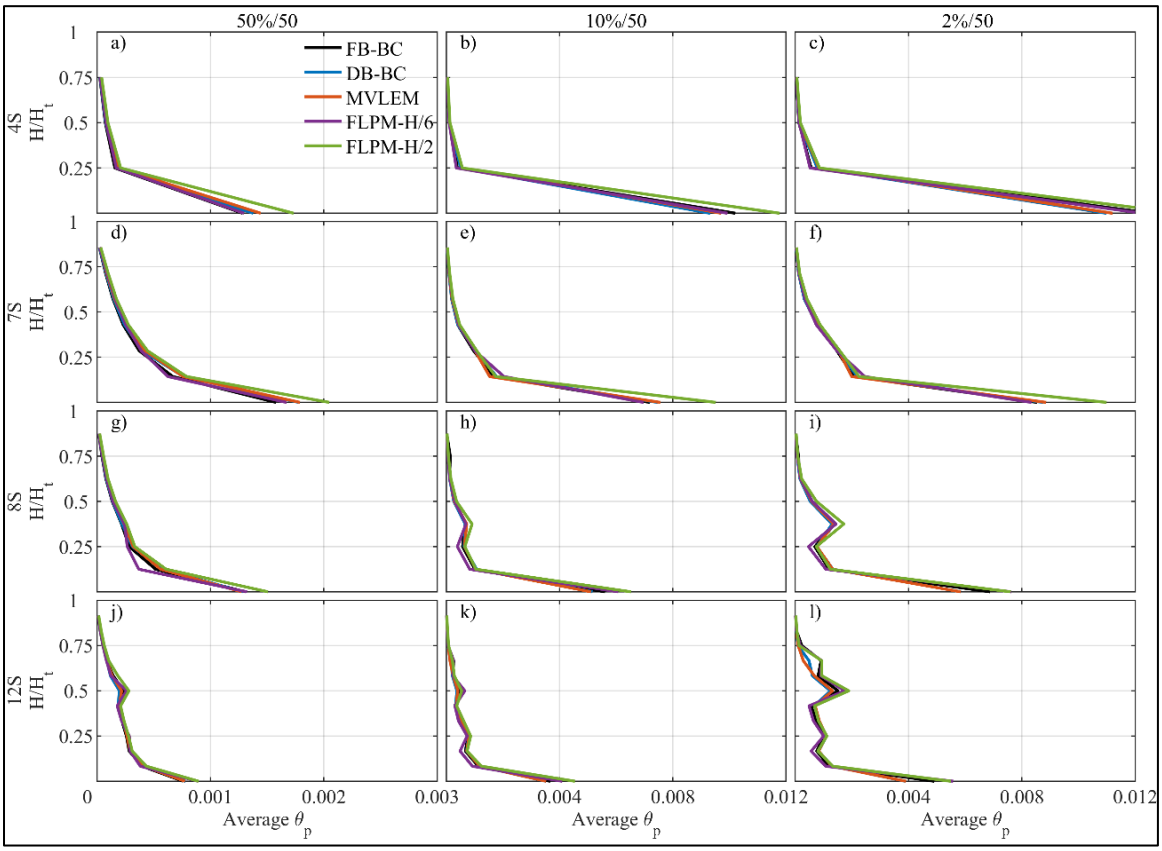

Figure 5.10: Average plastic hinge rotation.

Table 5.2 shows the number of earthquake records resulting in predicted collapse from the five considered models of each building at the 2%/50 hazard level. Building collapse was defined to occur at expected failure of the gravity resisting system at 5% interstory drift ratio, as has been recommended based on experimental results of slab-column gravity systems (Hueste et al., 2009; Matzke et al., 2015), which is the most typical gravity system used in RC wall buildings. This 5% interstory drift ratio has been previously used to define collapse in RC wall buildings by other authors (Gogus & Wallace, 2015; Marafi et al., 2019). Overall, the FLPM-H/6 model predicted the same or more number of collapses than the other models. The seismic records that produced collapse in the FB-BC,

DB-BC, MVLEM, and FLPM-H/2 models were part of the records that produced collapse in the FLPM-H/6 model. As such, the records that produced collapse when using the FLPM-H/6 model were excluded from the average results from all of the models at the 2%/50 hazard level. This exclusion was also considered when estimating the average results in Figure 5.8, Figure 5.9, and Figure 5.10. This decision was made so that the average results used in the variability quantification would not be skewed by the few extreme values from these records.

Table 5.2: Number of predicted collapses for 2%/50 hazard level.

	4S	7S	8S	12S
FB-BC	3	1	2	3
DB-BC	1	0	1	0
MVLEM	1	0	1	0
FLPM-H/6	3	2	3	3
FLPM-H/2	2	2	2	3

The generally larger number of collapses predicted by the FLPM-H/6 model may be explained by the reduced ultimate (i.e., failure) displacement capacity from this model, as illustrated by the pushover curves of the 8-story building in Figure 5.11. The FLPM-H/6 model showed strength degradation at a significantly lower displacement than the other four models, which caused larger drift demands in the nonlinear dynamic analyses. Since

the nonlinearity in the FLPM-H/6 model is concentrated over a short length of the element, this model is not capable to simulate the spread of nonlinear behavior in a RC wall, limiting the ductility capacity of the structure at failure. Ultimately, because of the significant difference in the average IDR results from the FLPM-H/6 model as compared with the other models (Figure 5.9), and also considering the larger differences from the validation results of this model for the maximum floor displacements and interstory drifts in Figure 5.4d and Figure 5.4e, it was decided to exclude the FLPM-H/6 model from the quantification of variability discussed in the next sections.

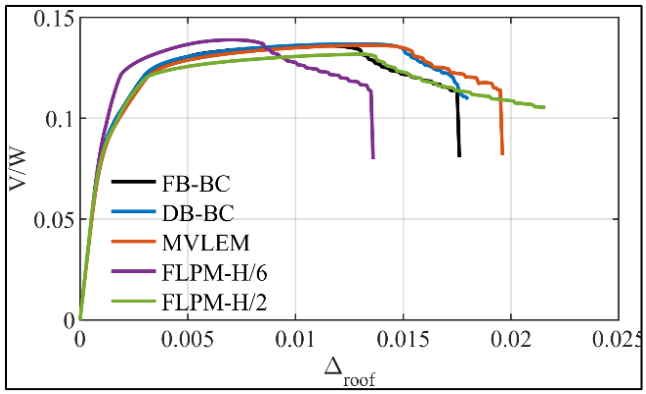

Figure 5.11: Pushover curves of the 8-story building.

5.6 Variability in Performance Assessment Parameters

The model-to-model variability in the performance assessment parameters described in the previous section is quantified in Figure 5.12 as boxplots that show normalized results. The maximum values of the average results of each parameter were normalized by the mean value from the four considered models. Since the boxplots were normalized by the mean value from the four models, the mean value of each boxplot is 1.0, thus allowing more consistent comparisons between the different response parameters. The

number presented under each boxplot indicates the coefficient of variation (COV) for that boxplot.

Overall, the global assessment parameters (i.e., IDR and Δ_{roof} in plots a-c and g-i, respectively) presented considerably less variation between the different numerical models than the local assessment parameters (i.e., θ_p and ϕ_{cr} in plots d-f and j-l, respectively). For example, the COV for the interstory drift ratio was less than or equal to 4.0%, while the COV for the plastic hinge rotation was in general greater than 10%. Furthermore, the boxplot sizes for the global parameters were similar regardless of the hazard level, suggesting that similar levels of model-to-model variability may be expected in these parameters at different hazard levels. These results show that global parameters are more appropriate for performance assessment of buildings since different modeling approaches are more likely to yield similar results, and consequently similar performance classification of a given building.

The largest variability among the considered parameters was for the curvature at the critical length, ϕ_{cr}, even though the same critical length and material constitutive relationships were used in the four models. This shows that performance assessment based on material strains obtained from curvature predictions is highly dependent on the modeling approach, and may result in different performance outcomes of a building when using different models. The results for ϕ_{cr} were also more sensitive to the hazard level (i.e., increasing boxplot size with increased hazard level), when compared to the other assessment parameters. In comparison, the variability and sensitivity to the hazard level were reduced when using the plastic hinge rotation, θ_p (Figure 5.12d-f).

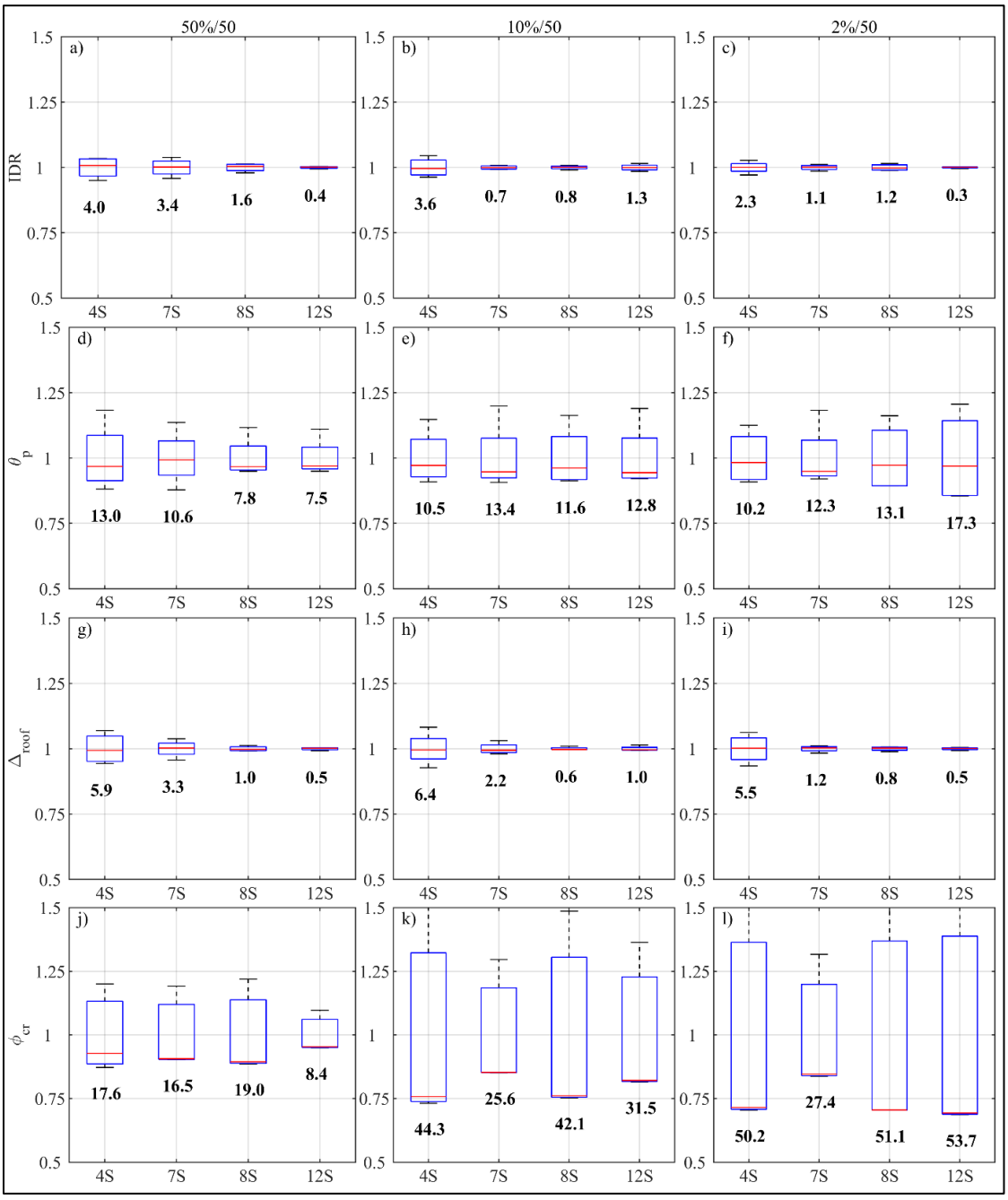

Figure 5.12: Normalized variability in performance assessment parameters. a-c) Maximum interstory drift ratio; d-f) maximum plastic hinge rotation; g-i) maximum roof drift ratio; and j-l) maximum curvature at L_{cr}. COV values are presented in bold.

5.7 Variability in Damage Fragility Curves

The previous two sections investigated the model-to-model variability in the performance parameters of the four buildings at three hazard levels. The current section further investigates this variability based on predicted damage fragility curves of the 4-, 7-, 8-, and 12-story buildings. Specifically, incremental dynamic analyses, IDA (Vamvatsikos & Allin Cornell, 2002) were conducted to obtain damage fragility curves using the twenty-two far-field pairs of records from the FEMA P695 (2009) methodology.

To demonstrate the process, Figure 5.13a shows the IDA results of the 8-story building obtained with the DB-BC model. The red markers represent the ground motion intensities based on spectral acceleration, S_a, at $C_u T_a$ (i.e., approximate value for the fundamental period of the structure according ASCE 7 (2010), as required by FEMA P695) corresponding to assumed collapse due to failure of the slab-column gravity system at an IDR limit of 5% as described in the previous section. However, experimental evidence (Matzke et al., 2015) has shown that failure of the slab-column system can develop at interstory drift ratios between 2% to 8%, thus presenting a range of IDR at which collapse can be expected. As such, it is important to evaluate fragility curves over a range of performance parameter values, rather than at a single value. For example, the black and blue markers in Figure 13a show the ground motion intensities at IDR limits of 3% and 7%, respectively.

As is typical in fragility analysis, lognormal fragility curves [Eq. (5-1)] were fitted to the collapse S_a values for each IDR limit (Figure 5.13b). The fragility curves of the 8-story building obtained with the four modeling approaches are compared in Figure 5.13c

for IDR=3%, 5% and 7%. These results show that the differences between the fragility curves predicted by the models increased as the IDR limit was increased. This difference was expected since greater IDR corresponds to greater amounts of nonlinear behavior in the models, thus leading to greater differences in the predicted response.

$$PE = \Phi\left(\frac{\ln S_a - \mu_{\ln S_a}}{\sigma_{\ln S_a}}\right) = \Phi\left(\frac{\ln(S_a/\theta)}{\beta}\right) \tag{5-1}$$

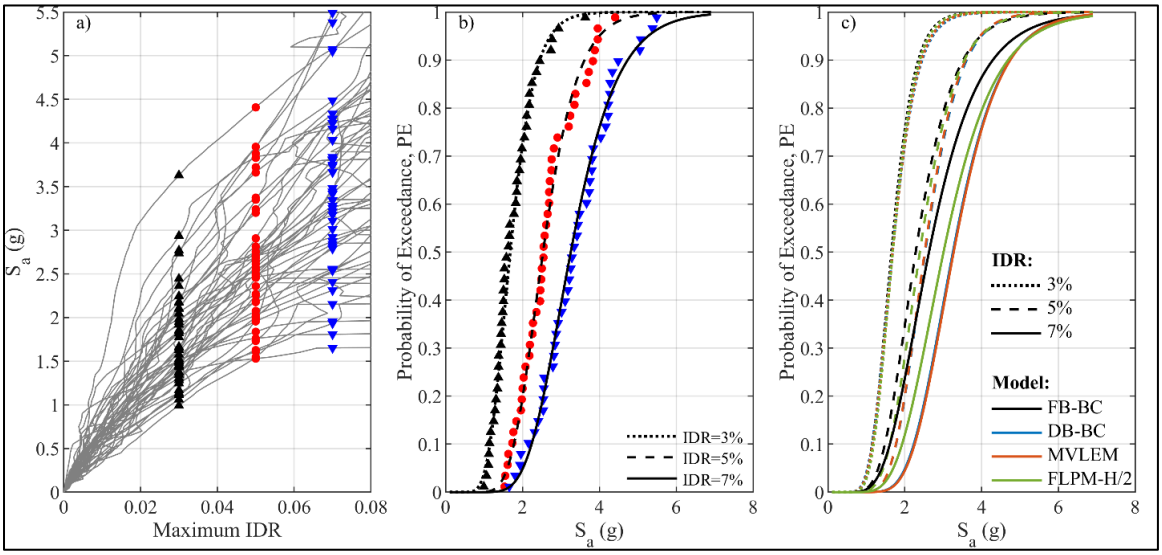

Figure 5.13: Variability in collapse fragility curves of the 8-story building. a) IDA results for the DB-BC model; b) collapse fragility curves for the DB-BC model at IDR=3%, 5%, and 7%; c) collapse fragility curves for the four models at IDR=3%, 5%, and 7%.

Considering that the selected IDR values of 3%, 5%, and 7% in Figure 5.13 are rather arbitrary, comparisons of fragility curves from the four models were made over a range of values for the four performance parameters (IDR, θ_p, Δ_{roof}, and ϕ_{cr}). Each lognormal fragility curve was defined using the median, θ, and the logarithmic standard deviation, β [i.e., the standard deviation of $\ln(S_a)$]. The median represents the value of

ground motion intensity (i.e., S_a at $C_u T_a$) that corresponds to a 50% probability of exceeding a certain damage state. This is an important metric for comparing fragility curves because larger median values correspond to views of lower vulnerability (i.e., relatively less conservative) whereas smaller median values correspond to views of higher vulnerability (i.e., relatively more conservative). For example, it can be seen in Figure 5.13b that the median S_a increased as the IDR limit assumed for collapse was increased, indicating reduced vulnerability of reaching IDR=7% as compared to 5% or 3% (i.e., IDR limit of 7% is the least conservative value for predicting collapse).

The variation in θ between the four models for each of the four buildings and for varying values of the global response parameters (IDR and Δ_{roof}) and local response parameters (θ_p and ϕ_{cr}) are presented in Figure 5.14. The most conservative results for θ (i.e., smaller θ values) were obtained using models with a force-based formulation (i.e., FB-BC and FLPM-H/2), while models with a displacement-based formulation (i.e., DB-BC and MVLEM) presented less conservative results. For performance assessment based on global parameters (i.e., IDR in Figure 5.14a-d and Δ_{roof} in Figure 5.14i-l), the FB-BC model consistently provided the lowest value of θ among the models, especially at larger IDR and Δ_{roof}. In terms of local parameters (i.e., θ_p in Figure 5.14e-h and ϕ_{cr} in Figure 5.14m-p), the θ values from the DB-BC and MVLEM models were essentially the same (showing small differences at larger values of θ_p and ϕ_{cr}), since both models used a displacement-based approach with the same critical length. Contrarily, larger differences in θ were obtained for the local parameters from the FB-BC and FLPM-H/2 models,

because these models used different critical lengths even though they both utilized a force-based formulation.

Similarly, the variation in β is presented in Figure 5.15, where the DB-BC and MVLEM models were comparable, while the FB-BC and FLPM-H/2 models presented larger differences. Additionally, the results show that the largest values of β were generally obtained for close to zero values of the damage response parameters IDR, θ_p, Δ_{roof}, and ϕ_{cr}, where the model-to-model differences were small. This may have been because the wall responses for these cases were still in the linear-elastic range, and thus the record-to-record variability was high (i.e., large in β) while the model-to-model variability was small.

The variability in the damage fragility curves predicted with the four numerical models is further quantified in Figure 5.16 in terms of the coefficient of variation, COV in θ and β over the range of each response parameter. The results again show that, in general, the models presented less variability when considering global parameters (Figure 5.16a-d and Figure 5.16i-l) rather than local parameters (Figure 5.16e-h and Figure 5.16m-p). Moreover, the COV of β was less than the COV of θ, presenting values mostly less than 0.15 in the considered range of the response parameters. The COV of θ generally increased for larger values of IDR, θ_p, and Δ_{roof} (Figure 5.16a-d, Figure 5.16e-h, and Figure 5.16i-l, respectively), with the largest COV values less than or equal to 0.2, except for the 12-story building (see Figure 5.16d,h,l). In contrast, the COV of θ did not show a clear tendency for ϕ_{cr} (Figure 5.16m-p), and presented values mostly greater than 0.2 in the considered range. Therefore, significant variations in fragility curves may be expected from

different models when using ϕ_{cr}, and consequently material strains, as assessment response parameters.

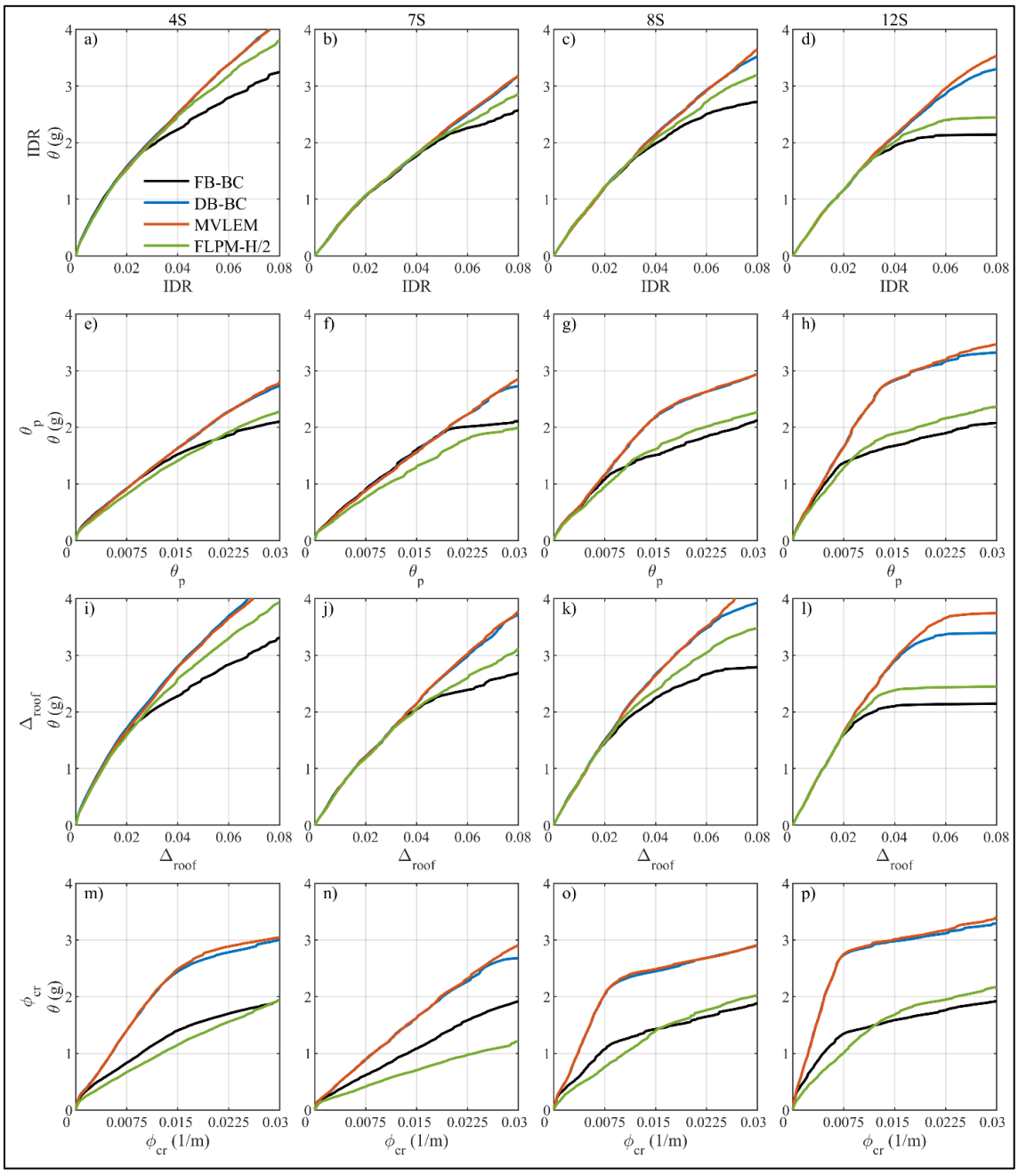

Figure 5.14: Variation in fragility curve parameter θ. a-d) Maximum interstory drift ratio; e-h) maximum plastic hinge rotation; i-l) maximum roof drift ratio; and m-p) maximum curvature at L_{cr}.

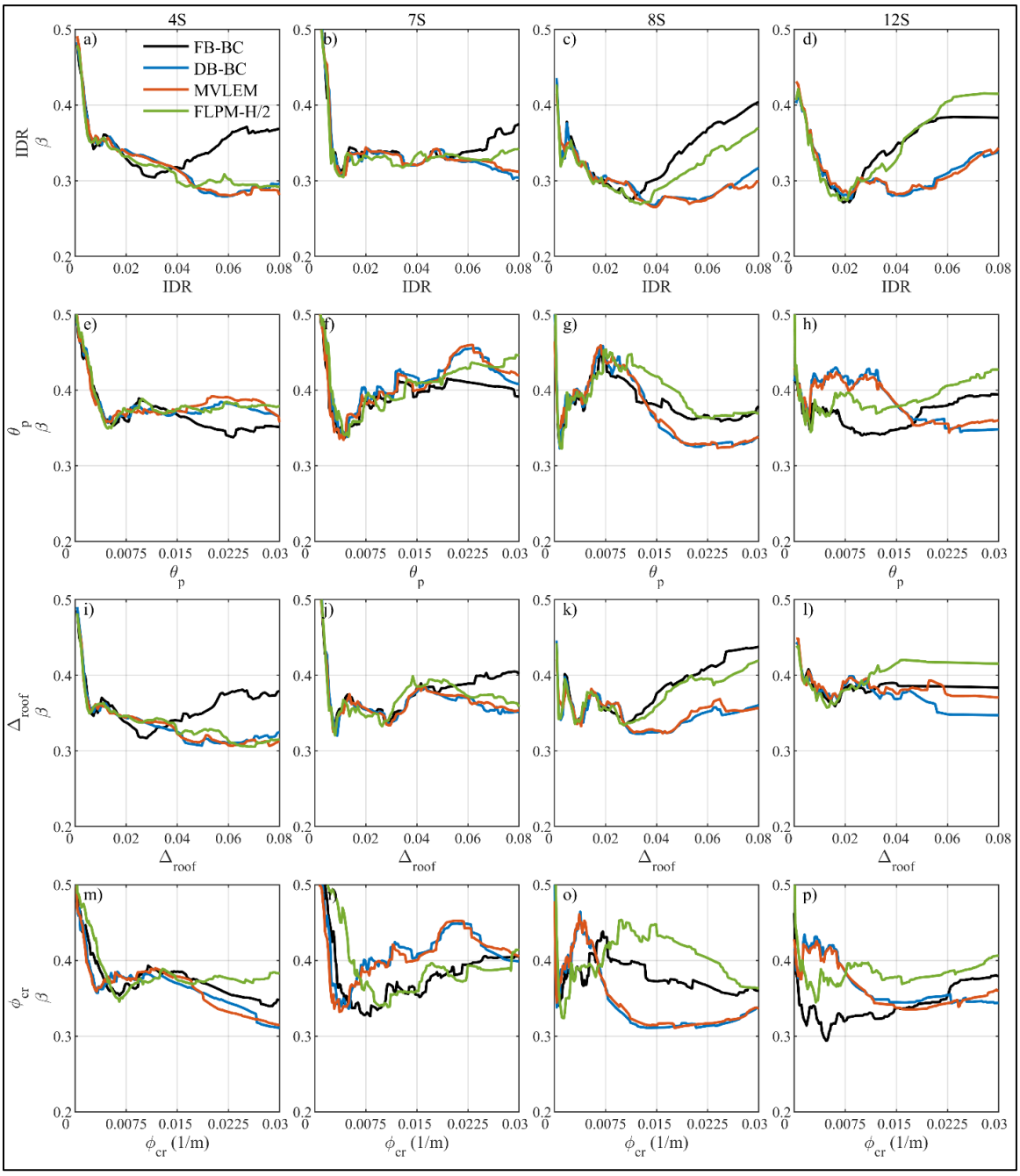

Figure 5.15: Variation in fragility curve parameter β. a-d) Maximum interstory drift ratio; e-h) maximum plastic hinge rotation; i-l) maximum roof drift ratio; and m-p) maximum curvature at L_{cr}.

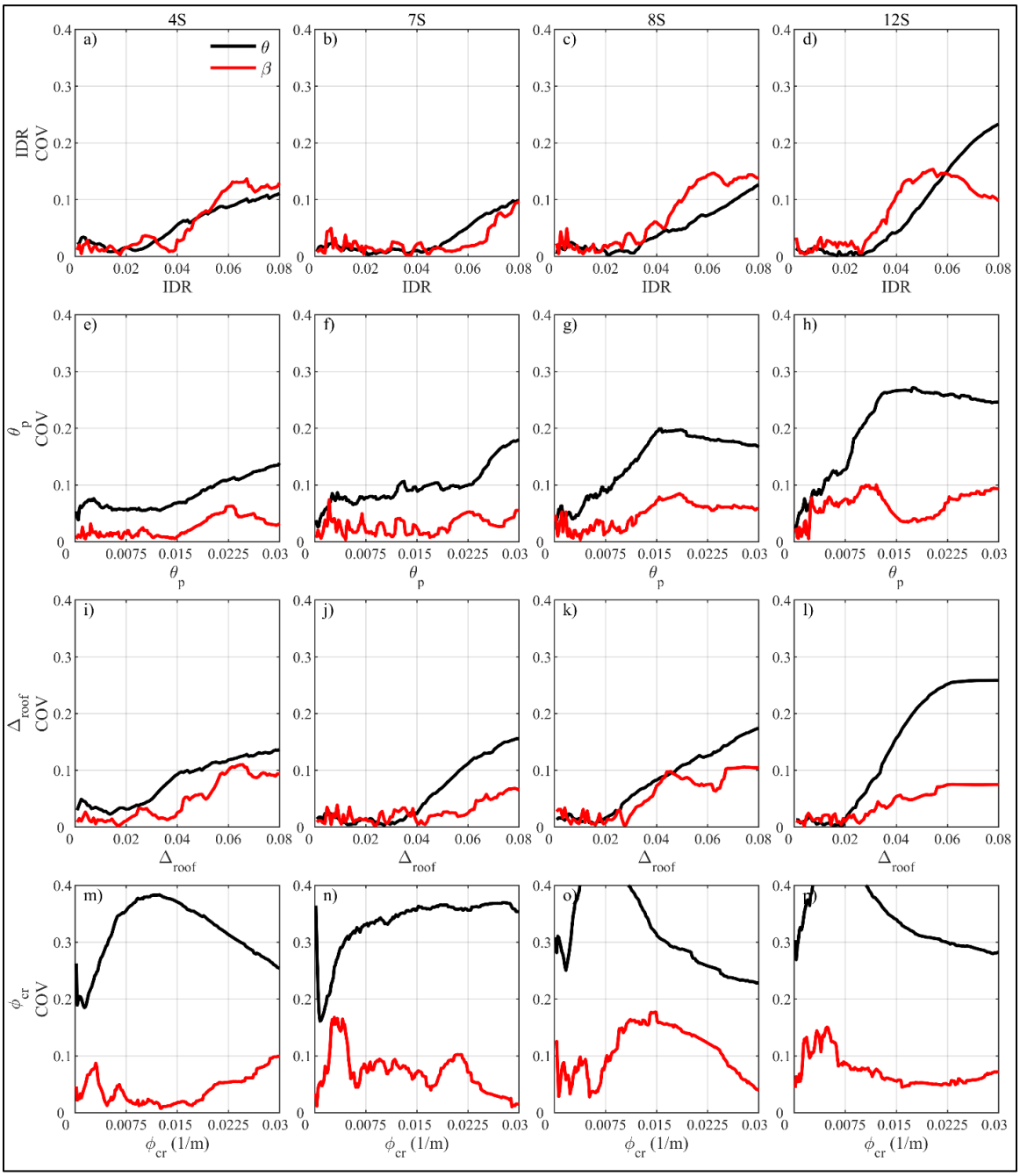

Figure 5.16: Coefficient of variation in fragility curve parameters. a-d) Maximum interstory drift ratio; e-h) maximum plastic hinge rotation; i-l) maximum roof drift ratio; and m-p) maximum curvature at L_{cr}.

5.8 Summary and Conclusions

This study investigated the variability in the simulated seismic response of slender RC wall buildings to the nonlinear numerical modeling approach. First, five different nonlinear modeling approaches (i.e., FB-BC, DB-BC, MVLEM, FLPM-H/6, and FLPM-H/2) were validated against experimental results of a 7-story wall building shake-table test. Then, four of these modeling approaches (i.e., FB-BC, DB-BC, MVLEM, FLPM-H/2) were used to conduct nonlinear dynamic response analyses of the 7-story test specimen and three additional wall building designs (4-, 8-, and 12-story buildings) to investigate the variability in selected global response parameters (interstory drift ratio, IDR, and roof drift ratio, Δ_{roof}) and local response parameters (plastic hinge rotation, θ_p, and curvature at the critical length, ϕ_{cr}), including damage fragility curves. The models used the same material constitutive relationships and other analysis inputs (e.g., damping) so that the quantified differences in the building performance were caused by the numerical modeling approach rather than other user-selected parameters. The most important findings of this study are summarized below:

1. Reasonable error magnitudes within 30% were obtained for the simulated dynamic response of the shake-table test specimen, except for the maximum interstory drift ratio and base shear using the FLPM-H/6 model. In general, it is recommended that FLPM models be used with caution when significant nonlinearity is expected.
2. Overall, the global response parameters (IDR and Δ_{roof}) presented considerably less variation between the different numerical models than the local parameters (θ_p and ϕ_{cr}). For example, the coefficient of variation, COV for the interstory drift ratio was

less than or equal to 4.0%, while the COV for the plastic hinge rotation was in general greater than 10%.

3. The variability for the global response parameters was similar regardless of the hazard level (i.e., using (50%/50, 10%/50, and 2%/50 ground motion sets), suggesting that similar levels of model-to-model variability may be expected in these parameters at different hazard levels.
4. The curvature at the critical length, which has been previously recommended to calculate maximum material strains in performance based seismic design, was the response parameter that varied the most between the numerical models. Therefore, evaluating the performance of a wall building using the curvature at the critical length can provide significantly different outcomes when using different models.
5. The most conservative fragility curves (i.e., resulting in the lowest ground motion intensity corresponding to a certain damage state) were obtained with models using a force-based approach (i.e., FB-BC and FLPM-H/2), while models with a displacement-based formulation (i.e., DB-BC and MVLEM) presented less conservative results.
6. For the fragility curves based on global parameters (IDR and Δ_{roof}), the FB-BC model consistently provided the lowest median, θ (i.e., 50% probability of exceeding a damage state) among the models, especially at larger IDR and Δ_{roof}.
7. In terms of local parameters (θ_p and ϕ_{cr}), the θ values of the fragility curves from the DB-BC and MVLEM models were essentially the same (showing small differences at larger values of θ_p and ϕ_{cr}), since both models used a displacement-based approach with the same critical length. Contrarily, larger differences in θ were obtained for the

local parameters from the FB-BC and FLPM-H/2 models, because these models used different critical lengths even though they both utilized a force-based formulation.

8. The COV of θ from the different numerical models generally increased for larger values of IDR, θ_p, and Δ_{roof}, with largest values less than or equal to 0.2, except for the 12-story building. In contrast, the COV of θ did not show a clear tendency for ϕ_{cr}, and presented values mostly greater than 0.2, showing that significant variations in fragility curves may be expected from different models when ϕ_{cr}, and consequently material strains, are considered as response parameters.

It is strongly recommended that the performance assessment of slender RC wall buildings be done based on global response parameters and not local response parameters since the simulated results from different nonlinear modeling approaches are expected to vary considerably less when using global response parameters.

CHAPTER 6:

SUMMARY, CONCLUSIONS, AND FUTURE WORK

This chapter presents: 1) a summary of this dissertation, including its objectives and principal contributions; 2) important conclusions from the research; and 3) identified areas for related future work.

6.1 Summary

The focus of this research was to evaluate and provide guidelines for the nonlinear seismic analysis of axial-flexural RC elements using distributed plasticity models. Different models were used to simulate the cyclic behavior of slender (flexure-dominant) RC walls and columns. Four planar shear-dominant walls were also studied in Chapter 2. Greater emphasis was placed on structures with softening post-peak behavior due to concrete crushing with or without bar buckling because: 1) this type of behavior has been commonly observed to dominate axial-flexural failure of slender RC walls and columns during experimental tests and after earthquakes; and 2) the prediction of this behavior can be highly sensitive to the mesh size used in numerical modeling. The accomplished specific objectives of this research are:

1. Evaluate existing nonlinear modeling approaches for isolated planar RC walls and provide modeling recommendations to accurately predict their global cyclic lateral force-displacement behavior based on previously tested wall specimens.
2. Develop a regularized plastic hinge modeling approach to simulate both the global and local cyclic behaviors of slender isolated RC walls and columns.
3. Evaluate wall modeling approaches based on comparisons with previous shake-table test measurements of a 7-story wall building subassembly.
4. Quantify the variability in the predicted dynamic seismic performance of RC wall buildings obtained by different nonlinear models.

The principal contributions of this dissertation include: 1) detailed modeling recommendations to accurately simulate the global cyclic behavior of slender and squat RC walls; 2) a new metric to quantitatively evaluate numerical simulations of hysteretic behavior; 3) combination of plastic hinge integration and material regularization to accurately simulate the nonlinear behavior of slender RC walls and columns through axial-flexural failure; 4) a new confined concrete crushing energy equation for regularized concrete post-peak stress-strain relationships of RC columns; and 5) quantification of variability in the predicted seismic performance of RC wall buildings considering important local and local response parameters.

6.2 Conclusions

The following important observations and conclusions were made from this research. These observations and conclusions are also listed at the end of each chapter and are repeated herein as a complete list for convenience to the reader. Note that the conclusions may be limited

to the numerical models, material relationships, and modeling assumptions used in the investigation.

6.2.1 Conclusions from Specific Objective 1

- The modeling parameters presented in this study for the PERFORM 3D and MVLEM models were adequate to simulate the global cyclic behavior of slender RC walls. In addition, the modeling parameters for the SFI-MVLEM and BTM models were found suitable to simulate the global cyclic behavior of both slender and squat walls. Therefore, the proposed parameters may be used in PBSD to estimate the cyclic lateral force-displacement behavior of planar RC walls.
- Simulations from PERFORM 3D, MVLEM, and SFI-MVLEM presented small variations in RK_e, RV_{max}, and NSE_m when varying the discretization of the walls. Consequently, the responses from these models did not substantially improve when using finer meshes, and a coarse mesh can be used to simulate the global cyclic behavior of RC walls with these three models. In comparison, wall discretization had a large effect on the BTM simulations, and thus, the number of elements in length and height should be carefully selected when using this model. Values of m and n that result in a diagonal angle, θ_d close to the value calculated with Eq. (2-7) are needed to adequately simulate the hysteretic behavior of the walls.
- The effective stiffness from the numerical simulations presented large variations and inaccuracy when compared with the experimental test results. The effective stiffness was in general highly overestimated by the MVLEM and SFI-MVLEM simulations, while it was mostly underestimated by PERFORM 3D and BTM. The large variability

in effective stiffness was also observed from the experimental results of two identical RC walls, corroborating the comparatively large unpredictability of this evaluation metric.

- The proposed Modified Nash-Sutcliffe Efficiency (NSE_m) was shown to be an appropriate metric to quantify the ability of the models to simulate the hysteretic behavior of RC walls, as it was able to accurately evaluate complex cyclic behaviors including strength and stiffness deterioration, and pinching. Additionally, limit values of NSE_m were defined to classify the hysteretic simulations, which agreed with qualitative evaluations of the predicted force-displacement curves. Based on these classifications, shear-uncoupled PERFORM 3D and MVLEM models provided good and satisfactory simulations of the hysteretic behavior for the studied slender walls, but provided poor simulations of the hysteretic behavior for the squat walls, because of the lack of shear-flexure interaction. In comparison, shear-coupled models SFI-MVLEM and BTM resulted in NSE_m factors of more than 0.90 (classified as satisfactory) for seven of the eight walls investigated.
- The ultimate displacements predicted by the shear-coupled SFI-MVLEM and BTM models were within 8.6% error, showing the ability of these models to capture the reduction in lateral strength of three walls with different shear span-to-depth ratios.
- Significant differences in computing time were found between the shear-coupled and shear-uncoupled models, where the latter ones were faster. Although the computing times required to simulate the considered rectangular RC walls were short (with the

longest time over 2 minutes), the comparisons presented in the chapter are helpful in evaluating the numerical efficiency of the RC wall models.

- Comparisons of the local behavior (i.e., base curvatures and strains) for the flexure-dominated wall RW2 simulated by MVLEM showed that the horizontal discretization parameter, m has a negligible effect on the results. However, the local results were significantly influenced by the vertical discretization of the wall (parameter n), with larger numerical curvatures resulting from finer vertical discretizations. Significant improvements in curvature and tension strain accuracy and reduced sensitivity to the vertical discretization of the wall were obtained when using curvatures postprocessed according Section 2.6.5.

6.2.2 Conclusions from Specific Objective 2 for RC Walls

- The use of material regularization with the Gauss-Lobatto integration method results in mesh-objective predictions of the global behavior of slender RC walls. However, the local section curvature and material strains from these models are still extremely sensitive to the mesh size. Normalization of the curvatures based on an assumed plastic hinge length has been proposed in the literature, showing significant reductions of this sensitivity. As an important limitation, the equations needed for curvature normalization have not been generalized. Furthermore, the need to normalize the curvatures in a second step after the nonlinear analysis has been lost or not emphasized in some of the recent literature on nonlinear RC wall modeling.
- In comparison, the use of unregularized materials with the Gauss-Lobatto integration method results in objective section curvatures and material strains. However, the

predicted ultimate displacement at failure is extremely sensitive to the length of the critical integration point.

- The modified Gauss-Radau plastic hinge integration method allows the user to match the critical length to an assumed plastic hinge length. As a major benefit demonstrated in this chapter, the sensitivity of the model results to the assumed plastic hinge length is significantly reduced when regularized rather than unregularized materials are used.
- As an additional benefit, curvature and strain predictions using the modified Gauss-Radau plastic hinge integration method with regularized materials do not require an additional normalization step. As such, this approach is suitable for a wider range of nonlinear modeling applications.
- Regularization of the concrete stress-strain relationship has a more significant effect on the analysis results than regularization of the steel stress-strain relationship.

6.2.3 Conclusions from Specific Objective 2 for RC Columns

- The proposed regularization equation for the confined concrete crushing energy provided reasonably accurate simulations of the ultimate (i.e., failure) lateral displacement of the 28 column specimens, including the 11 validation columns that were not used in the calibration of the equation. The confined concrete crushing energy is given in Eq. (4-8) and is based on the unconfined concrete crushing energy using Eq. (4-7) from Nakamura and Higai (2001). Unlike available regularization procedures for slender RC walls, the proposed model for RC columns does not require regularization of the reinforcing steel stress-strain relationship.

- The full reversed-cyclic hysteretic behaviors up to the ultimate displacement of the 28 column specimens were also generally well captured by the proposed regularized plastic hinge model, simulating cyclic strength and stiffness degradation.
- The accuracy and variability of the effective stiffness and maximum strength from the simulation of the 28 columns were similar among the three unregularized and two regularized sets of material parameters. The effective stiffness was generally overpredicted (as is common for the numerical modeling of RC components), while the maximum strength was predicted within $\pm$20% error.
- The ultimate (failure) lateral displacement of the columns presented much larger variability than effective stiffness and maximum strength. The best unregularized model results were obtained using the concrete material parameters from Priestley et al. (1996). The model using the available regularization equations for slender RC walls was not adequate to consistently simulate the ultimate displacement of the column specimens with high accuracy. In comparison, the model using the proposed regularization equation presented significant improvements of accuracy in the prediction of ultimate displacement.
- In terms of local column responses, unregularized (with concrete material parameters from Priestley et al. (1996)) and regularized (using the proposed regularization equation) plastic hinge models presented similar curvature predictions, which generally underestimated the measured values at the critical sections of two column specimens, with better predictions at greater lateral displacements.

- The simulation results from the unregularized (with concrete material parameters from Priestley et al. (1996)) and regularized (using the proposed regularization equation) plastic hinge models mostly underestimated the available measured extreme confined concrete compression strains for seven columns. This underestimation was because the plastic hinge lengths used in these models were larger than the potentiometer lengths used for the measurements, thus modeling average strains over greater lengths. At large column displacements, the strains from the proposed regularized plastic hinge model were better than the simulations from the unregularized model.
- The predicted ultimate displacement was very sensitive to the assumed plastic hinge length, L_p when using unregularized models. This sensitivity was significantly reduced when using regularized models, and further improved when using the proposed regularization equation. This presents a major advantage of the proposed regularized plastic hinge model over unregularized plastic hinge models.
- The predictions of local behavior (curvatures and strains) were very sensitive to the assumed plastic hinge length, L_p for both the unregularized and regularized models. As such, regularization of the material stress-strain relationships did not reduce the sensitivity of the simulated local behaviors to the assumed L_p, unlike the effectiveness of regularization in reducing the sensitivity of the simulated global behavior to L_p.
- The simulations of local behavior would not have provided accurate results even if the assumed L_p values exactly matched the gauge lengths of the potentiometers used in the experimental measurements of column curvatures and concrete strains. Further, different $L_p/L_{p,mean}$ ratios would be needed to obtain accurate simulations of local

behavior for the different column specimens. Since the sensitivity of global column response to the assumed L_p is significantly reduced by using the proposed regularized plastic hinge model, future development of new L_p equations calibrated based on measured local (rather than global) column behavior can ultimately result in accurate predictions of both global and local behaviors.

6.2.4 Conclusions from Specific Objectives 3 and 4

- Reasonable error magnitudes within 30% were obtained for the simulated dynamic response of the shake-table test specimen, except for the maximum interstory drift ratio and base shear using the FLPM-H/6 model. In general, it is recommended that FLPM models be used with caution when significant nonlinearity is expected.
- Overall, the global response parameters (IDR and Δ_{roof}) presented considerably less variation between the different numerical models than the local parameters (θ_p and ϕ_{cr}). For example, the coefficient of variation, COV for the interstory drift ratio was less than or equal to 4.0%, while the COV for the plastic hinge rotation was in general greater than 10%.
- The variability for the global response parameters was similar regardless of the hazard level (i.e., using (50%/50, 10%/50, and 2%/50 ground motion sets), suggesting that similar levels of model-to-model variability may be expected in these parameters at different hazard levels.
- The curvature at the critical length, which has been previously recommended to calculate maximum material strains in performance based seismic design, was the response parameter that varied the most between the numerical models. Therefore,

evaluating the performance of a wall building using the curvature at the critical length can provide significantly different outcomes when using different models.

- The most conservative fragility curves (i.e., resulting in the lowest ground motion intensity corresponding to a certain damage state) were obtained with models using a force-based approach (i.e., FB-BC and FLPM-H/2), while models with a displacement-based formulation (i.e., DB-BC and MVLEM) presented less conservative results.
- For the fragility curves based on global parameters (IDR and Δ_{roof}), the FB-BC model consistently provided the lowest median, θ (i.e., 50% probability of exceeding a damage state) among the models, especially at larger IDR and Δ_{roof}.
- In terms of local parameters (θ_p and ϕ_{cr}), the θ values of the fragility curves from the DB-BC and MVLEM models were essentially the same (showing small differences at larger values of θ_p and ϕ_{cr}), since both models used a displacement-based approach with the same critical length. Contrarily, larger differences in θ were obtained for the local parameters from the FB-BC and FLPM-H/2 models, because these models used different critical lengths even though they both utilized a force-based formulation.
- The COV of θ from the different numerical models generally increased for larger values of IDR, θ_p, and Δ_{roof}, with largest values less than or equal to 0.2, except for the 12-story building. In contrast, the COV of θ did not show a clear tendency for ϕ_{cr}, and presented values mostly greater than 0.2, showing that significant variations in fragility curves may be expected from different models when ϕ_{cr}, and consequently material strains, are considered as response parameters.

6.3 Future Work

The primary focus of this Ph.D. research was to develop numerical modeling guidelines for the nonlinear seismic analysis of axial-flexural RC elements within the scope described in Section 1.3. Future research is needed on nonplanar RC walls (e.g., C-, U-, and T-shaped walls), coupled walls, non-square/rectangular columns, as well as shear-dominant structures to increase the robustness and accuracy of their global and local behavior predictions for performance-based seismic design and analysis. Finally, an investigation of different concrete crushing energy equations is needed for use with other concrete constitutive material models (i.e., different than the *Concrete02* material used in Chapter 3 and Chapter 4).

BIBLIOGRAPHY

Abdullah, S. (2019). *Reinforced Concrete Structural Walls: Test Database and Modeling Parameters*. PhD dissertation. University of California, Los Angeles.

ACHISINA. (2017). *Diseño Sísmico Basado en Desempeño*. *Noviembre*, 23. http://www.achisina.cl/index.php/publicaciones/manuales-guias

ACI 318. (2014). *Building code requirements for structural concrete (ACI 318-14) and commentary (ACI 318R-14)*. American Concrete Institute, Committe 318.

ACI 318. (2019). *Building code requirements for structural concrete (ACI 318-19) and commentary (ACI 318R-19)*. American Concrete Institute, Committe 318.

Alarcon, C., Hube, M. A., & de la Llera, J. C. (2014). Effect of axial loads in the seismic behavior of reinforced concrete walls with unconfined wall boundaries. *Engineering Structures*, *73*, 13–23. https://doi.org/10.1016/j.engstruct.2014.04.047

Almeida, J. P., Tarquini, D., & Beyer, K. (2016). Modelling approaches for inelastic behaviour of RC walls: multi-level assessment and dependability of results. *Archives of Computational Methods in Engineering*, *23*(1), 69–100. https://doi.org/10.1007/s11831-014-9131-y

Amón, J. (2018). *Experimental study of seismic behaviour and residual capacity of slender reinforced concrete walls*. M.S. thesis (in Spanish). Pontificia Universidad Católica de Chile.

Ang, B. (1981). *Ductility of reinforced concrete bridge piers under seismic loading*. University of Canterbury, Christchurch, New Zealand.

Arteta, C. A., To, D. V., & Moehle, J. P. (2014). Experimental response of boundary elements of code-compliant reinforced concrete shear walls. *NCEE 2014 - 10th U.S. National Conference on Earthquake Engineering: Frontiers of Earthquake Engineering*, *February*. https://doi.org/10.4231/D37H1DN29

ASCE 41. (2017). *Seismic evaluation and retrofit of existing buildings. ASCE/SEI 41-17*. American Society of Civil Engineers. https://doi.org/10.1061/9780784414859

ASCE 7. (2010). *Minimum Design Loads for Buildings and Other Structures*. American

Society of Civil Engineers.

ASCE 7. (2017). *Minimum design loads and associated criteria for buildings and other structures*. American Society of Civil Engineers. https://doi.org/10.1061/9780784414248

ASCE Task Committee. (1993). Criteria for evaluation of watershed models. *Journal of Irrigation and Drainage Engineering*, *119*(3), 429–442. https://doi.org/10.1061/(ASCE)0733-9437(1993)119:3(429)

Atalay, M., & Penzien, J. (1975). The seismic behavior of critical regions of reinforced concrete components as infuenced by moment, shear and axial force. In *Eartquake Engineering Reserach Center, University of California, Berkeley*.

Bae, S., & Bayrak, O. (2008). Plastic hinge length of reinforced concrete columns. *ACI Structural Journal*, 290–300.

Belarbi, A., & Hsu, T. T. C. (1994). Constitutive laws of concrete in tension and reinforcing bars stiffened by concrete. *ACI Structural Journal*, *91*(4), 465–474. https://doi.org/10.14359/4154

Berry, M. P., Lehman, D. E., & Lowes, L. N. (2008). Lumped-plasticity models for performance simulation of bridge columns. *ACI Structural Journal*, *105*, 270–279.

Berry, M., Parrish, M., & Eberhard, M. (2004). PEER Structural Performance Database User ’s Manual. In *Pacific Earthquake Engineering Research Center*.

Birely, A. C. (2012). *Seismic performance of slender reinforced concrete structural walls*. PhD dissertation. University of Washington. https://digital.lib.washington.edu/researchworks/handle/1773/22577

Blandon, C. A., Arteta, C. A., Bonett, R. L., Carrillo, J., Beyer, K., & Almeida, J. P. (2018). Response of thin lightly-reinforced concrete walls under cyclic loading. *Engineering Structures*, *176*(March), 175–187. https://doi.org/10.1016/j.engstruct.2018.08.089

Bohl, A., & Adebar, P. (2011). Plastic hinge length in high-rise concrete shear walls. *ACI Structural Journal*, *108*(2), 148–157.

Bournonville, M., Dahnke, J., & Darwin, D. (2004). *Statistical analysis of the mechanical properties and weight of reinforcing bars*. University of Kansas Report 04-1.

Bozorgnia, Y., & Bertero, V. V. (2004). *Earthquake engineering: From engineering seismology to performance-based engineering*. CRC press.

Chacón, M. F., de la Llera, J. C., Hube, M. A., Marques, J., & Lemnitzer, A. (2017). Epistemic uncertainty in the seismic response of RC free-plan buildings. *Engineering*

Structures, *141*(June), 687–702. https://doi.org/10.1016/j.engstruct.2017.03.015

Chang, G. A., & Mander, J. B. (1994). *Seismic energy based fatigue damage analysis of bridge columns: Part I - evaluation of seismic capacity*. NCEER Technical Report No. NCEER-94-0006. State University of New York at Buffalo.

Chopra, A. K., & McKenna, F. (2016). Modeling viscous damping in nonlinear response history analysis of buildings for earthquake excitaion. *Earthquake Engineering & Structural Dynamics*, *45*(2), 193–211. https://doi.org/10.1002/eqe.2622

Coleman, J., & Spacone, E. (2001). Localization Issues in Force-Based Frame Elements. *Journal of Structural Engineering*, *127*(11), 1257–1265. https://doi.org/10.1061/(asce)0733-9445(2001)127:11(1257)

Corley, W. G. (1966). Rotational capacity of reinforced concrete beams. *Journal of the Structural Division*, *92*(5), 121–146.

CSI. (2018). *Perform-3D. Nonlinear analysis and performance assessment for 3D structures. Version 7*. Computers and Structures, Inc. http://www.csiamerica.com/

Dazio, A., Beyer, K., & Bachmann, H. (2009). Quasi-static cyclic tests and plastic hinge analysis of RC structural walls. *Engineering Structures*, *31*(7), 1556–1571. https://doi.org/10.1016/j.engstruct.2009.02.018

Deger, Z. T., & Wallace, J. W. (2015). Collapse assessment of the Alto Rio building in the 2010 Chile earthquake. *Earthquake Spectra*, *31*(3), 1397–1425. https://doi.org/10.1193/060812EQS209M

Deng, M., Liang, X., & Yang, K. (2008). Experimental study on seismic behavior of high performance concrete shear wall with new strategy of transverse confining stirrups. *14th World Conference on Earthquake Engineering*, 1–8.

Dhakal, R. P., & Maekawa, K. (2002). Modeling for Postyield Buckling of Reinforcement. *Journal of Structural Engineering*, *128*(9), 1139–1147. https://doi.org/10.1061/(asce)0733-9445(2002)128:9(1139)

FEMA. (2018). Seismic Performance Assessment of Buildings (FEMA P-58-1). In *Fema P-58-1* (2nd ed., Vol. 1, Issue December). https://www.fema.gov/media-library-data/1396495019848-0c9252aac91dd1854dc378feb9e69216/FEMAP-58_Volume1_508.pdf

FEMA 356. (2000). *Prestandard and Commentary for the Seismic Rehabilitation of Buildings*. Federal Emergency Management Agency.

FEMA P695. (2009). *Quantification of Building Seismic Performance Factors*. Federal Emergency Management Agency.

Feng, D., Ren, X.-D., & Li, J. (2018). Cyclic behavior modeling of reinforced concrete shear walls based on softened damage-plasticity model. *Engineering Structures*, *166*(August 2017), 363–375. https://doi.org/10.1016/j.engstruct.2018.03.085

Filippou, F. C., Popov, E. P., & Bertero, V. V. (1983). Effects of bond deterioration on hysteretic behaviour of reinforced concrete joints. Report No. UCB/EERC-83/19. In *EERC Report No. UCB/EERC-83/19. Earthquake Engineering Research Center. University of California. Berkeley, California.* University of California. http://www.ce.berkeley.edu/~filippou/Research/Publications/Reports/EERC-83-19.pdf

Fischinger, M., Rejec, K., & Isaković, T. (2012). Modeling inelastic shear response of RC walls. *Proceedings of 15th World Conference on Earhquake Engineering*.

Ghannoum, W. M., & Matamoros, A. B. (2014). Nonlinear modeling parameters and acceptance criteria for concrete columns. *ACI Special Publication*, *297*, 1–24.

Gogus, A., & Wallace, J. W. (2015). Seismic Safety Evaluation of Reinforced Concrete Walls through FEMA P695 Methodology. *Journal of Structural Engineering*, *141*(10), 1–17. https://doi.org/10.1061/(ASCE)ST.1943-541X.0001221

Grange, S., Kotronis, P., & Mazars, J. (2009). Numerical modelling of the seismic behaviour of a 7-story building: NEES benchmark. *Materials and Structures*, *42*, 1433–1442. https://doi.org/10.1617/s11527-008-9462-y

Haselton, C. B., Liel, A. B., Taylor-Lange, S. C., & Deierlein, G. G. (2016). Calibration of model to simulate response of reinforced concrete beam-columns to collapse. *ACI Structural Journal*, *113*(6), 1141–1152. https://doi.org/10.14359/51689245

Hellesland, J., & Scordelis, A. (1981). Analysis of RC bridge columns under imposed deformations. *IABSE Colloquium*.

Hoult, R. D., Goldsworthy, H. M., & Lumantarna, E. (2018). Plastic hinge analysis for lightly reinforced and unconfined concrete structural walls. *Bulletin of Earthquake Engineering*, *16*(10), 4825–4860. https://doi.org/10.1007/s10518-018-0369-x

Hube, M. A., Marihuén, A., de la Llera, J. C., & Stojadinovic, B. (2014). Seismic behavior of slender reinforced concrete walls. *Engineering Structures*, *80*, 377–388. https://doi.org/10.1016/j.engstruct.2014.09.014

Hube, M. A., Santa María, H., & López, M. (2017). Experimental campaign of thin reinforced concrete shear walls for low-rise constructions. *16th World Conference on Earthquake, January*.

Hueste, M. B. D., Kang, T. H. K., & Robertson, I. N. (2009). Lateral drift limits for structural concrete slab-column connections, including shear reinforcement effects.

Proceedings of the 2009 Structures Congress - Don't Mess with Structural Engineers: Expanding Our Role, 1515–1524. https://doi.org/10.1061/41031(341)165

Huy, N. X. (2008). Seven-Story Building Subjected To Seismic Loading: Experimentation and Modeling. *Asian Journal of Civil Engineering*, *9*(2), 131–139.

Jalali, A., & Dashti, F. (2010). Nonlinear behavior of reinforced concrete shear walls using macroscopic and microscopic models. *Engineering Structures*, *32*(9), 2959–2968. https://doi.org/10.1016/j.engstruct.2010.05.015

Jansen, D. C., & Shah, S. P. (2002). Effect of Length on Compressive Strain Softening of Concrete. *Journal of Engineering Mechanics*, *123*(1), 25–35. https://doi.org/10.1061/(asce)0733-9399(1997)123:1(25)

Jara, J. M., Hernández, E. J., Olmos, B. A., & Martínez, G. (2020). Building damages during the September 19, 2017 earthquake in Mexico City and seismic retrofitting of existing first soft-story buildings. *Engineering Structures*, *209*. https://doi.org/10.1016/j.engstruct.2019.109977

Jiang, H., & Kurama, Y. C. (2010). Analytical modeling of medium-rise reinforced concrete shear walls. *ACI Structural Journal*, *107*(4), 400–410.

Jünemann, R., de la Llera, J. C., Hube, M. A., Cifuentes, L. A., & Kausel, E. (2015). A statistical analysis of reinforced concrete wall buildings damaged during the 2010, Chile earthquake. *Engineering Structures*, *82*, 168–185. https://doi.org/10.1016/j.engstruct.2014.10.014

Jünemann, Rosita, De la Llera, J. C., Hube, M. A., Vásquez, J. A., & Chacón, M. F. (2016). Study of the damage of reinforced concrete shear walls during the 2010 Chile earthquake. *Earthquake Engineering & Structural Dynamics*, *45*(10), 1621–1641. https://doi.org/10.1002/eqe.2750

Kam, W. Y., Pampanin, S., & Elwood, K. (2011). Seismic performance of reinforced concrete buildings in the 22 February Christchurch (Lyttelton) earthquake. *Bulletin of the New Zealand Society for Earthquake Engineering*, *44*(4), 239–278.

Karthik, M. M., & Mander, J. B. (2011). Stress-block parameters for unconfined and confined concrete based on a unified stress-strain model. *Journal of Structural Engineering*, *137*(2), 270–273. https://doi.org/10.1061/(ASCE)ST.1943-541X.0000294

Kazaz, İ. (2013). Analytical study on plastic hinge length of structural walls. *Journal of Structural Engineering*, *139*(11), 1938–1950. https://doi.org/10.1061/(asce)st.1943-541x.0000770

Kelly, T. (2007). A blind prediction test of nonlinear analysis procedures for reinforced

concrete shear walls. *Bulletin of the New Zealand Society for Earthquake Engineering*, *40*(3), 142–159. https://doi.org/10.5459/bnzsee.40.3.142-159

Kim, S. H., & Koutromanos, I. (2016). Constitutive Model for Reinforcing Steel under Cyclic Loading. *Journal of Structural Engineering*, *142*(12), 04016133. https://doi.org/10.1061/(asce)st.1943-541x.0001593

Kolozvari, K., Arteta, C., Fischinger, M., Gavridou, S., Hube, M., Isaković, T., Lowes, L., Orakcal, K., Vásquez, J., & Wallace, J. (2018). Comparative study of state-of-the-art macroscopic models for planar reinforced concrete walls. *ACI Structural Journal*, *115*(6), 1637–1657. https://doi.org/10.14359/51710835

Kolozvari, K, Piatos, G., & Beyer, K. (2017). Practical nonlinear modeling of U-shaped reinforced concrete walls under bi-directional loading. *16th World Conference on Earthquake Engineering*.

Kolozvari, Kristijan. (2013). *Analytical modeling of cyclic shear - flexure interaction in reinforced concrete structural walls*. PhD dissertation. University of California, Los Angeles.

Kolozvari, Kristijan, Biscombe, L., Dashti, F., Dhakal, R. P., Gogus, A., Gullu, M. F., Henry, R. S., Massone, L. M., Orakcal, K., Rojas, F., Shegay, A., & Wallace, J. (2019). State-of-the-art in nonlinear finite element modeling of isolated planar reinforced concrete walls. *Engineering Structures*, *194*(April), 46–65. https://doi.org/10.1016/j.engstruct.2019.04.097

Kolozvari, Kristijan, Orakcal, K., & Wallace, J. W. (2015a). Modeling of cyclic shear-flexure interaction in reinforced concrete structural walls. I: Theory. *Journal of Structural Engineering*, *141*(5), 04014135. https://doi.org/10.1061/(ASCE)ST.1943-541X.0001059

Kolozvari, Kristijan, Orakcal, K., & Wallace, J. W. (2015b). Shear-flexure interaction modeling for reinforced concrete structural walls and columns under reversed cyclic loading. *Pacific Earthquake Engineering Research Center, College of Engineering, University of California, Berkeley*, *PEER 2015/12*. http://peer.berkeley.edu/publications/peer_reports/reports_2015/webPEER-2015-12-kolozvari.pdf

Kolozvari, Kristijan, Orakcal, K., & Wallace, J. W. (2018). New opensees models for simulating nonlinear flexural and coupled shear-flexural behavior of RC walls and columns. *Computers and Structures*, *196*(November), 246–262. https://doi.org/10.1016/j.compstruc.2017.10.010

Kolozvari, Kristijan, Tran, T. A., Orakcal, K., & Wallace, J. W. (2015). Modeling of cyclic shear-flexure interaction in reinforced concrete structural walls. II: experimental validation. *Journal of Structural Engineering*, *141*(5), 04014136.

https://doi.org/10.1061/(ASCE)ST.1943-541X.0001083

Kolozvari, Kristijan, & Wallace, J. W. (2016). Practical nonlinear modeling of reinforced concrete structural walls. *American Society of Civil Engineers*, *142*(12). https://doi.org/10.1061/(ASCE)ST.1943-541X.0001492.

LATBSDC. (2017). *An alternative procedure for seismic analysis and design of tall buildings located in the Los Angeles region*. Los Angeles Tall Buildings Structural Design Council.

Lowes, L., Lehman, D., & Baker, C. (2016). Recommendations for modeling the nonlinear response of slender reinforced concrete walls using PERFORM-3D. *SEAOC 2016 Convention Proceedings*, 1–18.

Lowes, L. N., Lehman, D. E., & Whitman, Z. (2019). Investigation of failure mechanisms and development of design recommendations for flexural reinforced concrete walls. *Engineering Structures*, *186*(5), 323–335. https://doi.org/10.1016/j.engstruct.2019.01.122

Lu, X., Xie, L., Guan, H., Huang, Y., & Lu, X. (2015). A shear wall element for nonlinear seismic analysis of super-tall buildings using OpenSees. *Finite Elements in Analysis and Design*, *98*, 14–25. https://doi.org/10.1016/j.finel.2015.01.006

Lu, Yiqiu, & Henry, R. S. (2017). Numerical modelling of reinforced concrete walls with minimum vertical reinforcement. *Engineering Structures*, *143*, 330–345. https://doi.org/10.1016/j.engstruct.2017.02.043

Lu, Yiqiu, & Henry, R. S. (2018). Comparison of minimum vertical reinforcement requirements for reinforced concrete walls. *ACI Structural Journal*, *115*(3), 673–687. https://doi.org/10.14359/51701146

Lu, Yiqiu, Henry, R. S., Gultom, R., & Ma, Q. T. (2017). Cyclic Testing of Reinforced Concrete Walls with Distributed Minimum Vertical Reinforcement. *Journal of Structural Engineering (United States)*, *143*(5), 1–17. https://doi.org/10.1061/(ASCE)ST.1943-541X.0001723

Lu, Yuan, & Panagiotou, M. (2014). Three-dimensional cyclic beam-truss model for nonplanar reinforced concrete walls. *Journal of Structural Engineering*, *140*(3), 04013071. https://doi.org/10.1061/(ASCE)ST.1943-541X.0000852

Lu, Yuan, Panagiotou, M., & Koutromanos, I. (2016). Three-dimensional beam-truss model for reinforced concrete walls and slabs - part 1: modeling approach, validation, and parametric study for individual reinforced concrete walls. *Earthquake Engineering & Structural Dynamics*, *45*(9), 1495–1513. https://doi.org/10.1002/eqe.2719

Maffei, J., Bonelli, P., Kelly, D., Lehman, D. E., Lowes, L., Moehle, J., Telleen, K., Wallace, J., & Willford, M. (2014). *Recommendations for Seismic Design of Reinforced Concrete Wall Buildings Based on Studies of the 2010 Maule, Chile Earthquake*. National Institute of Standards and Technology. https://www.nist.gov/publications/recommendations-seismic-design-reinforced-concrete-wall-buildings-based-studies-2010

Mander, J. B., Priestley, N., & Park, R. (1988). Theoretical stress-strain model for confined concrete. *ASCE Journal of Structural Engineering*, *114*(8), 1804–1826.

Mansour, M., & Hsu, T. T. C. (2005). Behavior of reinforced concrete elements under cyclic shear. II: Theoretical model. *Journal of Structural Engineering*, *131*(1), 54–65. https://doi.org/10.1061/(ASCE)0733-9445(2005)131:1(54)

Marafi, N. A., Ahmed, K. A., Lehman, D. E., & Lowes, L. N. (2019). Variability in Seismic Collapse Probabilities of Solid- and Coupled-Wall Buildings. *Journal of Structural Engineering*, *145*(6), 1–17. https://doi.org/10.1061/(ASCE)ST.1943-541X.0002311

Marini, A., & Spacone, E. (2006). Analysis of reinforced concrete elements including shear effects. *ACI Structural Journal*, *103*(5), 645–655. https://doi.org/10.14359/16916

Martinelli, P., & Filippou, F. C. (2009). Simulation of the shaking table test of a seven-story shear wall building. *Earthquake Engineering & Structural Dynamics*, *38*, 587–607. https://doi.org/10.1002/eqe

Massone, L. M., & Alfaro, J. I. (2016). Displacement and curvature estimation for the design of reinforced concrete slender walls. *The Structural Design of Tall and Special Buildings*, *25*(16), 823–841. https://doi.org/10.1002/tal.1285

Massone, L. M., & Moroder, D. (2009). Buckling modeling of reinforcing bars with imperfections. *Engineering Structures*, *31*(3), 758–767. https://doi.org/10.1016/j.engstruct.2008.11.019

Massone, L. M., Orakcal, K., & Wallace, J. W. (2009). Modeling of squat structural walls controlled by shear. *ACI Structural Journal*, *106*, 646–655.

Massone, L. M., & Wallace, J. W. (2004). Load-deformation responses of slender reinforced concrete walls. *ACI Structural Journal*, *101*(1), 103–113.

Mattock, A. H. (1967). Discussion of "Rotational Capacity of Hinging Regions in Reinforced Concrete Beams" by W.G. Corley. *Journal of the Structural Division*, 519–522. https://doi.org/10.14359/16716

Matzke, E. M., Lequesne, R. D., Parra-Montesinos, G. J., & Shield, C. K. (2015). Behavior of biaxially loaded slab-column connections with shear studs. *ACI Structural Journal*, *112*(3), 335–346. https://doi.org/10.14359/51687408

McKenna, F., Fenves, G., Scott, M., & Jeremic, B. (2000). *Open system for earthquake engineering simulation (OpenSees)*. Pacific Earhquake Engineering Research Center, University of California.

Menegotto, M., & Pinto, P. E. (1973). Method of analysis for cyclically loaded R.C. plane frames including changes in geometry and non-elastic behavior of elements under combined normal force and bending. *Proceedings, IABSE Symposium*, 15–22. https://doi.org/10.5169/seals-13741

Moharrami, M., Koutromanos, I., Panagiotou, M., & Girgin, S. C. (2014). Analysis of shear-dominated RC columns using the nonlinear truss analogy. *Earthquake Engineering & Structural Dynamics*, *44*(5), 677–694. https://doi.org/10.1002/eqe.2480

Moriasi, D. N., Arnold, J. G., Liew, M. W. Van, Bingner, R. L., Harmel, R. D., & Veith, T. L. (2007). Model evaluation guidelines for systematic quantification of accuracy in watershed simulations. *Transactions of the ASABE*, *50*(3), 885–900.

Nakamura, H., & Higai, T. (2001). *Compressive frature energy and fracture zone length of concrete*. Modeling of Inelastic Behavior of RC Structures under Seismic Loads. American Society of Civil Engineers.

Nash, J. E., & Sutcliffe, J. V. (1970). River flow forecasting through conceptual models. Part I-a discussion of principles. *Journal of Hydrology*, *10*(3), 282–290. https://doi.org/10.1016/0022-1694(70)90255-6

NIST. (2017a). *Guidelines for Nonlinear Structural Analysis for Design of Buildings. Part IIb – Reinforced Concrete Moment Frames. NIST GCR 17-917-46v3*. National Institute of Standards and Technology. https://doi.org/10.6028/NIST.GCR.17-917-46v3

NIST. (2017b). Guidelines for Nonlinear Structural Analysis for Design of Buildings Part I - General. In *NIST GCR 17-917-46v1*. National Institute of Standards and Technology. https://doi.org/10.6028/NIST.GCR.17-917-46v1

NIST. (2017c). *Recommended modeling parameters and acceptance criteria for nonlinear analysis in support of seismic evaluation, retrofit, and design. NIST GCR 17-917-45*. National Institute of Standards and Technology. https://doi.org/10.6028/NIST.GCR.17-917-45

Oh, Y. H., Han, S. W., & Lee, L. H. (2002). Effect of boundary element details on the seismic deformation capacity of structural walls. *Earthquake Engineering and Structural Dynamics*, *31*(8), 1583–1602. https://doi.org/10.1002/eqe.177

Ohno, T., & Nishioka, T. (1984). An experimental study on energy absorption capacity of columns in reinforced concrete structures. *Doboku Gakkai Ronbunshu*, *350*, 23–33.

https://doi.org/10.2208/jscej.1984.350_23

Orakcal, K. (2004). *Nonlinear modeling analysis of slender reinforced concrete walls*. PhD dissertation. University of California, Los Angeles. https://doi.org/10.1016/B978-012397720-5.50034-7

Orakcal, K., Massone, L. M., & Wallace, J. W. (2006). *Analytical modeling of reinforced concrete walls for predicting flexural and coupled-shear-flexural responses*. Pacific Earhquake Engineering Research Center, University of California, Los Angeles.

Orakcal, K., & Wallace, J. W. (2006). Flexural modeling of reinforced concrete walls - experimental verification. *ACI Structural Journal*, *103*(2), 196–206.

Orakcal, K., Wallace, J. W., & Conte, J. P. (2004). Flexural modeling of reinforced concrete walls - model attributes. *ACI Structural Journal*, *101*(5), 688–698.

Panagiotou, M. (2008). *Seismic design, testing and analysis of reinforced concrete wall buildings*. PhD dissertation. University of California, San Diego. https://escholarship.org/uc/item/0xp4r2hb

Panagiotou, M., Restrepo, J. I., & Conte, J. P. (2011). Shake-Table Test of a Full-Scale 7-Story Building Slice. Phase I: Rectangular Wall. *Journal of Structural Engineering*, *137*(6), 691–704. https://doi.org/10.1061/(ASCE)ST.1943-541X.0000332.

Panagiotou, M., Restrepo, J. I., Schoettler, M., & Kim, G. (2012). Nonlinear cyclic truss model for reinforced concrete walls. *ACI Structural Journal*, *109*(2), 205–214.

Pang, W. C., Rosowsky, D. V., Pei, S., & van de Lindt, J. W. (2007). Evolutionary parameter hysteretic model for wood shear walls. *Journal of Structural Engineering*, *133*(8), 1118–1129. http://ascelibrary.org/doi/10.1061/%28ASCE%290733-9445%282007%29133%3A8%281118%29

Parra, P. F., Arteta, C. A., & Moehle, J. P. (2019). Modeling criteria of older non-ductile concrete frame–wall buildings. *Bulletin of Earthquake Engineering*, *17*(12), 6591–6620. https://doi.org/10.1007/s10518-019-00697-y

Paulay, T., & Priestley, M. J. N. (1992). Seismic Design of Reinforced Concrete and Masonry Buildings. In *John Wiley & Sons Inc.: New York*. https://doi.org/10.1002/9780470172841.fmatter

Paulay, T., & Priestley, M. J. N. (1993). Stability of ductile structural walls. *ACI Structural Journal*, 385–392.

PEER/ATC. (2010). *Modeling and acceptance criteria for seismic design and analysis of tall buildings, PEER/ATC 72-1*. Pacific Earthquake Engineering Research Center, Applied Technology Council.

Pozo, J. D., Hube, M. A., & Kurama, Y. C. (2020). Quantitative assessment of nonlinear macro-models for global behavior and design of planar RC walls. *Engineering Structures*, *224*(12). https://doi.org/10.1016/j.engstruct.2020.111190

Priestley, M. J. N., & Park, R. (1987). Strength and ductility of concrete bridge columns under seismic loading. *Structural Journal ACI*, *84*(1), 285–336.

Priestley, M. J. N., Seible, F., & Calvi, G. M. (1996). *Seismic design and retrofit of bridges*. John Wiley & Sons.

Pugh, J. S., Lowes, L. N., & Lehman, D. E. (2015). Nonlinear line-element modeling of flexural reinforced concrete walls. *Engineering Structures*, *104*(12), 174–192. https://doi.org/10.1016/j.engstruct.2015.08.037

Rojas, F., Anderson, J. C., & Massone, L. M. (2016). A nonlinear quadrilateral layered membrane element with drilling degrees of freedom for the modeling of reinforced concrete walls. *Engineering Structures*, *124*, 521–538. https://doi.org/10.1016/j.engstruct.2016.06.024

Saatcioglu, M., & Grira, M. (1999). Confinement of reinforced concrete columns with welded reinforcement grids. *ACI Structural Journal*, *96*(1), 29–39. https://doi.org/10.14359/593

Saatcioglu, M., & Ozcebe, G. (1989). Response of reinforced concrete columns to simulated seismic loading. *ACI Structural Journal*, *86*(1), 3–12. https://doi.org/10.14359/2607

Saatcioglu, M., & Razvi, S. R. (1992). Strength and ductility of confined concrete. *Journal of Structural Engineering*, *118*(6), 1590–1607. https://doi.org/10.1061/(asce)0733-9445(1992)118:6(1590)

Salonikios, T. N., Kappos, A. J., Tegos, I. a, & Penelis, G. G. (1999). Cyclic load behavior of low-slenderness reinforced concrete walls: design basis and test results. *ACI Structural Journal*, *96*(4), 649–660. https://doi.org/10.14359/703

Scott, B. D., Park, R., & Priestley, M. J. N. (1982). Stress-strain behavior of concrete confined by overlapping hoops at low and high strain rates. *ACI Journal Proceedings*, *79*(2), 13–27. https://doi.org/10.14359/10875

Scott, M. H., & Hamutçuoğlu, O. M. (2008). Numerically consistent regularization of force-based frame elements. *International Journal for Numerical Methods in Engineering*, *76*(10), 1612–1631. https://doi.org/10.1002/nme.2386

Scott, Michael H., & Fenves, G. L. (2006). Plastic Hinge Integration Methods for Force-Based Beam–Column Elements. *Journal of Structural Engineering*, *132*(2), 244–252. https://doi.org/10.1061/(asce)0733-9445(2006)132:2(244)

Scott, Michael H., & Ryan, K. L. (2013). Moment-rotation behavior of force-based plastic hinge elements. *Earthquake Spectra*, *29*(2), 597–607. https://doi.org/10.1193/1.4000136

Segura, C. L. (2017). *Seismic performance limitations of slender reinforced concrete structural walls*. PhD dissertation. University of California, Los Angeles.

Segura, C. L., & Wallace, J. W. (2018a). Impact of geometry and detailing on drift capacity of slender walls. *ACI Structural Journal*, *115*(3), 885–895. https://doi.org/10.14359/51702046

Segura, C. L., & Wallace, J. W. (2018b). Seismic performance limitations and detailing of slender reinforced concrete walls. *ACI Structural Journal*, *115*(3), 849–859. https://doi.org/10.14359/51701918

Sideris, P., & Salehi, M. (2016). A gradient inelastic flexibility-based frame element formulation. *Journal of Engineering Mechanics*, *142*(7), 1–14. https://doi.org/10.1061/(ASCE)EM.1943-7889.0001083

Soesianawati, M. T. (1986). Limited ductility design of reinforced concrete Columns. In *MEng Thesis, University of Canterbury, Christchurch, New Zealand*. MEng thesis. University of Canterbury, Christchurch, New Zealand.

Somerville, P., Smith, N., Punyamurthula, S., & Sun, J. (1997). *Development of Ground Motion Time History for Phase 2 of the FEMA/SAC Steel Project. Report No. SAC/BD-97/04*. SAC Joint Venture, Sacramento, CA.

Spacone, E., Filippou, F. C., & Taucer, F. F. (1996). Fibre beam-column model for non-linear analysis of R/C frames: Part I. Formulation. *Earthquake Engineering and Structural Dynamics*, *25*(7), 711–726.

Sritharan, S., Beyer, K., Henry, R. S., Chai, Y. H., Kowalsky, M., & Bull, D. (2014). Understanding poor seismic performance of concrete walls and design implications. *Earthquake Spectra*, *30*(1), 307–334. https://doi.org/10.1193/021713EQS036M

Stevens, S. J., Uzumeri, S. M., Collins, M. P., & Will, G. T. (1991). Constitutive model for reinforced concrete Finite Element Analysis. *ACI Structural Journal*, *88*(1), 49–59.

Takahashi, S., Yoshida, K., Ichinose, T., Sanada, Y., Matsumoto, K., Fukuyama, H., & Suwada, H. (2013). Flexural drift capacity of reinforced concrete wall with limited confinement. *ACI Structural Journal*, *110*(1), 95–104. https://doi.org/10.14359/51684333

Tanaka, H. (1990). *Effect of lateral confining reinforcement on the ductile behaviour of reinforced concrete columns*. PhD dissertation. University of Canterbury, Christchurch, New Zealand.

TBI. (2017). Guidelines for performance-based seismic design of tall buildings. In *PEER Report 2017/06* (Issue May). Pacific Earthquake Engineering Research Center.

Thomsen, J., & Wallace, J. (2004). Displacement-based design of slender reinforced concrete structural walls—experimental verification. *Journal of Structural Engineering*, *130*(4), 618–630. https://doi.org/10.1061/(ASCE)0733-9445(2004)130:4(618)

Thomsen, J., & Wallace, J. W. (1995). *Displacement-based design of reinforced concrete structural walls: an experimental investigation of walls with rectangular ans T-shaped cross-sections*. Department of Civil Engineering, Clarkson University. Tech. Rep. No. CU/CEE-95/06.

Tran, T. A., & Wallace, J. W. (2012). Experimental study of nonlinear flexural and shear deformations of reinforced concrete structural walls. *Proceedings of 15th World Conference on Earhquake Engineering*.

Ulegtekin, D. (2010). *Analytical modeling of reinforced concrete panel elements under reversed cyclic loadings*. M.S. thesis, Bogazici University.

Vamvatsikos, D., & Allin Cornell, C. (2002). Incremental dynamic analysis. *Earthquake Engineering and Structural Dynamics*, *31*(3), 491–514. https://doi.org/10.1002/eqe.141

Vásquez, J. A., Jünemann, R., de la Llera, J. C., Hube, M. A., & Chacón, M. (2020). Three-dimensional nonlinear response history analyses for earthquake damage assessment: An reinforced concrete wall building case study. *Earthquake Spectra*, *1*(27). https://doi.org/10.1177/8755293020944180

Vásquez, Jorge A., De la Llera, J. C., & Hube, M. A. (2016). A regularized fiber element model for reinforced concrete shear walls. *Earthqueake Engineering & Structural Dynamics*, *45*(13), 2063–2083. https://doi.org/10.1002/eqe.2731

Vecchio, F. J., & Collins, M. P. (1986). The modified compression-field theory for reinforced concrete elements subjected to shear. *ACI Structural Journal*, *83*(2), 219–231.

Vulcano, A., Bertero, V. V, & Colotti, V. (1988). Analytical modeling of R/C structural walls. *Proceedings of 9th World Conference on Earhquake Engineering*, 41–46.

Wallace, J. W., Massone, L. M., Bonelli, P., Dragovich, J., Lagos, R., Lüders, C., & Moehle, J. (2012). Damage and implications for seismic design of RC structural wall buildings. *Earthquake Spectra*, *28*(S1), S281–S299. https://doi.org/10.1193/1.4000047

Wallace, J. W., & Orakcal, K. (2002). ACI 318-99 provisions for seismic design of

structural walls. *ACI Structural Journal*, *99*(4), 499–508. https://doi.org/10.14359/12119

Waugh, J., Aaleti, S., Sritharan, S., & Zhao, J. (2008). *Nonlinear analysis of rectangular and T-shaped concrete walls* (Issue December). ISU-ERI-Ames Report ERI-09327, Department of Civil, Construction, and Environmental Engineering, Iowa State University. http://scholar.google.com/scholar?hl=en&btnG=Search&q=intitle:Nonlinear+Analysis+of+Rectangular+and+T-Shaped+Concrete+Walls#0

Wu, Y.-T., Lan, T.-Q., Xiao, Y., & Yang, Y.-B. (2017). Macro-modeling of reinforced concrete structural walls: state-of-the-art. *Journal of Earthquake Engineering*, *21*(4), 652–678. https://doi.org/10.1080/13632469.2016.1174754

Yassin, M. (1994). *Nonlinear Analysis of Prestressed Concrete Structures under Monotonic and Cycling Loads*. PhD dissertation. University of California, Berkeley.

Zendaoui, A., Kadid, A., & Yahiaoui, D. (2016). Comparison of Different Numerical Models of RC Elements for Predicting the Seismic Performance of Structures. *International Journal of Concrete Structures and Materials*, *10*(4), 461–478. https://doi.org/10.1007/s40069-016-0170-7

Zhang, P., Restrepo, J. I., Conte, J. P., & Ou, J. (2017). Nonlinear finite element modeling and response analysis of the collapsed Alto Rio building in the 2010 Chile Maule earthquake. *Structural Design of Tall and Special Buildings*, *26*(16). https://doi.org/10.1002/tal.1364

APPENDIX A: OPENSEES MODEL EXAMPLES

This section presents examples of the OpenSees models used in the dissertation. The analysis file (Appendix A.1) was used to run all the models presented in the following subsections (A.2 to A.6). The MVLEM (A.2), SFI-MVLEM (A.3), and BTM (A.4) files were used to simulate the RC walls in Chapter 2. The OpenSees code for defining the regularized plastic hinge model (RPHM) for walls (Chapter 3) is presented in Appendix A.5. Finally, the code for defining the RPHM for columns (Chapter 4) is presented in Appendix A.6. The sample files presented in Appendices A.2 to A.5 are for wall WSH6, while the file presented in Appendix A.6 is for column ID 6.

A.1 Analysis File

```
exec >&@stdout $::env(COMSPEC) /c cls;
wipe all;
model basic -ndm 2 -ndf 3

#Models defined in kip-in units
set in 1.;
set kip 1.;
set sec 1.;
set kN [expr 0.2248089431*$kip];
set ksi [expr $kip/pow($in,2)];
set psi [expr $ksi/1000.];
set mm [expr $in/25.4];
set mm2 [expr $mm*$mm];
set mm4 [expr $mm2*$mm2];
set MPa [expr 145.*$psi];
set GPa [expr 1000.*$MPa];
```

```
#Load model
source MVLEM_WSH6.tcl; # or another model name

#Lateral Analysis
set Nsteps 1
set Tol 1.0e-5;
set Nmax 1000;
test EnergyIncr   $Tol $Nmax
system BandGeneral
numberer Plain
constraints Plain
algorithm KrylovNewton -maxDim 10 -increment initial

#Cyclic pushover: Displacement protocol from file
set d1 0.;
while {[gets $file temp] > 0} {
   foreach d2 $temp {
      set DLoad [expr {($d2 - $d1)/$Nsteps}];
      integrator DisplacementControl $IDctrlNode $IDctrlDOF $DLoad
      analysis Static
      set ok [analyze $Nsteps]
      if {$ok != 0} {
                              if {$ok != 0} {
         puts "Trying Newton"
         algorithm Newton -initial
         set ok [analyze 1 ]
         algorithm KrylovNewton -maxDim 10 -increment initial
        };
                              if {$ok != 0} {
         puts "Trying Newton Line Search"
         algorithm NewtonLineSearch -maxIter $Nmax
         set ok [analyze 1 ]
         algorithm KrylovNewton -maxDim 10 -increment initial
        };
        if {$ok != 0} {
                                       puts "ANALYSIS NOT FINISHED"
         return -1
        };
      };
      set d1 $d2;
   };
};
if {$ok != 0 } {
```

```
   puts "ANALYSIS NOT FINISHED"
} else {
   puts "DONE!! :)"
};
```

A.2 MVLEM

```
##-----------------------------------------------------------
## GEOMETRY

set H 177.9528;          #Height (in)
set L 78.7402;           #Length (in)
set t 5.9055;            #Thickness (in)

#Nodes
node 1 0 [expr 0*$H];
node 2 0 [expr 0.090909*$H];
node 3 0 [expr 0.18182*$H];
node 4 0 [expr 0.27273*$H];
node 5 0 [expr 0.36364*$H];
node 6 0 [expr 0.45455*$H];
node 7 0 [expr 0.54545*$H];
node 8 0 [expr 0.63636*$H];
node 9 0 [expr 0.72727*$H];
node 10 0 [expr 0.81818*$H];
node 11 0 [expr 0.90909*$H];
node 12 0 [expr 1*$H];

fix 1 1 1 1;              #fix the base
set IDctrlNode 12;       #Control node
set IDctrlDOF 1;         #Control DOF


##-----------------------------------------------------------
## MATERIALS

#Reinforcing steel
uniaxialMaterial SteelMPF 1 [expr 576.0*$MPa] [expr 576.0*$MPa] [expr 200000.*$MPa] 0.02 0.02 20. 0.925 0.15; #For boundary regions
uniaxialMaterial SteelMPF 2 [expr 583.7*$MPa] [expr 583.7*$MPa] [expr 200000.*$MPa] 0.02 0.02 20. 0.925 0.15; #For web regions
#Concrete
```

```
uniaxialMaterial ConcreteCM 3 -[expr 58.1*$MPa] -0.00536 [expr 34350.*$MPa] 9.28 1.106 [expr 2.09*$MPa] 0.00008 1.20 10000. -GapClose 1; #Confined
uniaxialMaterial ConcreteCM 4 -[expr 45.6*$MPa] -0.00226 [expr 34350.*$MPa] 6.87 1.065 [expr 2.09*$MPa] 0.00008 1.20 10000. -GapClose 1; #Unconfined
# Shear
set Ec [expr 34350.*$MPa]; # Concrete Young's Modulus
set G [expr 0.4*$Ec];
set GA [expr 0.1*$G*$L*$t];
uniaxialMaterial Elastic 5 $GA;


##-------------------------------------------------------
## ELEMENTS

set Dens 0.0;                 #Wall density (to get mass for dynamic analyses)
set c 0.4;                    #Element rotation center (from node i)
set pb 0.0174;                #Boundary region steel ratio
set pw 0.0049813;             #Web region steel ratio
set w1 [expr 260*$mm];        #Boundary region width
set w2 [expr 740*$mm];        #Web region width
set m 4;                      #Number of macro fibers

element MVLEM 1 $Dens 1 2 4 $c -thick $t $t $t $t -width $w1 $w2 $w2 $w1 -rho $pb $pw $pw $pb -matConcrete 3 4 4 3 -matSteel 1 2 2 1 -matShear 5;
element MVLEM 2 $Dens 2 3 4 $c -thick $t $t $t $t -width $w1 $w2 $w2 $w1 -rho $pb $pw $pw $pb -matConcrete 3 4 4 3 -matSteel 1 2 2 1 -matShear 5;
element MVLEM 3 $Dens 3 4 4 $c -thick $t $t $t $t -width $w1 $w2 $w2 $w1 -rho $pb $pw $pw $pb -matConcrete 3 4 4 3 -matSteel 1 2 2 1 -matShear 5;
element MVLEM 4 $Dens 4 5 4 $c -thick $t $t $t $t -width $w1 $w2 $w2 $w1 -rho $pb $pw $pw $pb -matConcrete 3 4 4 3 -matSteel 1 2 2 1 -matShear 5;
element MVLEM 5 $Dens 5 6 4 $c -thick $t $t $t $t -width $w1 $w2 $w2 $w1 -rho $pb $pw $pw $pb -matConcrete 3 4 4 3 -matSteel 1 2 2 1 -matShear 5;
element MVLEM 6 $Dens 6 7 4 $c -thick $t $t $t $t -width $w1 $w2 $w2 $w1 -rho $pb $pw $pw $pb -matConcrete 3 4 4 3 -matSteel 1 2 2 1 -matShear 5;
element MVLEM 7 $Dens 7 8 4 $c -thick $t $t $t $t -width $w1 $w2 $w2 $w1 -rho $pb $pw $pw $pb -matConcrete 3 4 4 3 -matSteel 1 2 2 1 -matShear 5;
element MVLEM 8 $Dens 8 9 4 $c -thick $t $t $t $t -width $w1 $w2 $w2 $w1 -rho $pb $pw $pw $pb -matConcrete 3 4 4 3 -matSteel 1 2 2 1 -matShear 5;
element MVLEM 9 $Dens 9 10 4 $c -thick $t $t $t $t -width $w1 $w2 $w2 $w1 -rho $pb $pw $pw $pb -matConcrete 3 4 4 3 -matSteel 1 2 2 1 -matShear 5;
element MVLEM 10 $Dens 10 11 4 $c -thick $t $t $t $t -width $w1 $w2 $w2 $w1 -rho $pb $pw $pw $pb -matConcrete 3 4 4 3 -matSteel 1 2 2 1 -matShear 5;
```

```
element MVLEM 11 $Dens 11 12 4 $c -thick $t $t $t $t -width $w1 $w2 $w2 $w1 -rho $pb $pw $pw $pb -matConcrete 3 4 4 3 -matSteel 1 2 2 1 -matShear 5;


##------------------------------------------------------------
## LOADS

#Gravity Load
set P [expr 1476*$kN];
pattern Plain 1 "Linear" {
   load $IDctrlNode  0.0 [expr  -$P]  0.0
};
set Tol 1.0e-5;
integrator LoadControl 0.1
system BandGeneral
test NormDispIncr $Tol  100 0
numberer RCM
constraints Transformation
algorithm Newton
analysis Static
analyze 10
loadConst -time 0.0; #Keep axial load constant

#Lateral Load
set Plateral 1.0;
pattern Plain 2 "Linear" {
        load $IDctrlNode $Plateral 0.0 0.0
};
set file [open "Protocolo.dat" r]; #File with disp protocol in in


##------------------------------------------------------------
## RECORDERS

set WallName WSH6;#Wall name
file mkdir Results;      #Save results in "Results" folder
recorder Node -file Results.out -time -node $IDctrlNode -dof $IDctrlDOF disp
recorder Node -file Results/FD$WallName.out -time -node $IDctrlNode -dof $IDctrlDOF disp
recorder Node -file Results/NodeDisplacements$WallName.out -time -nodeRange 1 10000000 -dof 1 2 3 disp;
recorder Element -file Results/FiberStrain$WallName.out -time -eleRange 1 11 fiber_strain;
```

```
recorder Element -file Results/FiberStressC$WallName.out -time -eleRange 1 11 fiber_stress_concrete
recorder Element -file Results/FiberStressS$WallName.out -time -eleRange 1 11 fiber_stress_steel
```

A.3 SFI-MVLEM

```
##------------------------------------------------------------
## GEOMETRY

set H 177.9528;                 #Height (in)
set L 78.7402;          #Length (in)
set t 5.9055;           #Thickness (in)

#Nodes
node 1 0 [expr 0*$H];
node 2 0 [expr 0.16667*$H];
node 3 0 [expr 0.33333*$H];
node 4 0 [expr 0.5*$H];
node 5 0 [expr 0.66667*$H];
node 6 0 [expr 0.83333*$H];
node 7 0 [expr 1*$H];

fix 1 1 1 1;       #fix the base
set IDctrlNode 7;   #Control node
set IDctrlDOF 1;    #Control DOF
##------------------------------------------------------------
## MATERIALS

#Reinforcing steel
uniaxialMaterial SteelMPF 1 [expr 576.0*$MPa] [expr 576.0*$MPa] [expr 200000.*$MPa] 0.02 0.02 20. 0.925 0.15; #For boundary regions
uniaxialMaterial SteelMPF 2 [expr 583.7*$MPa] [expr 583.7*$MPa] [expr 200000.*$MPa] 0.02 0.02 20. 0.925 0.15; #For web regions
uniaxialMaterial SteelMPF 3 [expr 518.9*$MPa] [expr 518.9*$MPa] [expr 200000.*$MPa] 0.02 0.02 20. 0.925 0.15; #Horizontal steel
#Concrete
uniaxialMaterial ConcreteCM 4 -[expr 58.1*$MPa] -0.00535 [expr 34350.*$MPa] 9.28 1.2157 [expr 2.09*$MPa] 0.00008 1.20 10000. -GapClose 1; #Confined
uniaxialMaterial ConcreteCM 5 -[expr 45.6*$MPa] -0.00226 [expr 34350.*$MPa] 6.87 1.1428 [expr 2.09*$MPa] 0.00008 1.20 10000. -GapClose 1; #Unconfined


##------------------------------------------------------------
## ELEMENTS

set Dens 0.0;                   #Wall density (to get mass for dynamic analyses)
```

```
set c 0.4;                  #Element rotation center (from node i)
set w1 [expr 260*$mm];      #Boundary region width
set w2 [expr 740*$mm];      #Web region width
set m 4;                    #Number of macro fibers
#Longitudinal steel
set pbY 0.0174;             #Boundary region steel ratio
set pwY 0.0049813;          #Web region steel ratio
#Horizontal steel
set pbX 0.0025133;          #Boundary region steel ratio
set pwX 0.0025133;          #Web region steel ratio

#Shear parameters
set nu 1;                   #Concrete friction coefficient
set alfadow 0.002;          #Dowel action coefficient

#FSAM materials
nDMaterial FSAM     6    $Dens  3   1    4   $pbX   $pbY   $nu  $alfadow; #Boundary region
nDMaterial FSAM     7    $Dens  3   2    5   $pwX   $pwY   $nu  $alfadow; #Web region

element SFI_MVLEM 1 1 2 4 $c -thick $t $t $t $t -width $w1 $w2 $w2 $w1 -mat 6 7 7 6;
element SFI_MVLEM 2 2 3 4 $c -thick $t $t $t $t -width $w1 $w2 $w2 $w1 -mat 6 7 7 6;
element SFI_MVLEM 3 3 4 4 $c -thick $t $t $t $t -width $w1 $w2 $w2 $w1 -mat 6 7 7 6;
element SFI_MVLEM 4 4 5 4 $c -thick $t $t $t $t -width $w1 $w2 $w2 $w1 -mat 6 7 7 6;
element SFI_MVLEM 5 5 6 4 $c -thick $t $t $t $t -width $w1 $w2 $w2 $w1 -mat 6 7 7 6;
element SFI_MVLEM 6 6 7 4 $c -thick $t $t $t $t -width $w1 $w2 $w2 $w1 -mat 6 7 7 6;


##-----------------------------------------------------------
## LOADS

#Gravity Load
set P [expr 1476*$kN];
pattern Plain 1 "Linear" {
   load $IDctrlNode  0.0 [expr  -$P]  0.0
};
set Tol 1.0e-5;
integrator LoadControl 0.1
system BandGeneral
test NormDispIncr $Tol  100 0
numberer RCM
constraints Transformation
algorithm Newton
```

```
analysis Static
analyze 10
loadConst -time 0.0; #Keep axial load constant

#Lateral Load
set Plateral 1.0;
pattern Plain 2 "Linear" {
        load $IDctrlNode $Plateral 0.0 0.0
};
set file [open "Protocolo.dat" r]; #File with disp protocol in in


##------------------------------------------------------
## RECORDERS

set WallName WSH6;#Wall name
file mkdir Results;     #Save results in "Results" folder
recorder Node -file Results.out -time -node $IDctrlNode -dof $IDctrlDOF disp
recorder Node -file Results/FD$WallName.out -time -node $IDctrlNode -dof $IDctrlDOF
disp
recorder Node -file Results/NodeDisplacements$WallName.out -time -nodeRange 1
10000000 -dof 1 2 3 disp
recorder Element -file Results/SX1$WallName.out -time -eleRange 1 6 RCPanel 1
strain_stress_steelX;
recorder Element -file Results/SY1$WallName.out -time -eleRange 1 6 RCPanel 1
strain_stress_steelY;
recorder Element -file Results/C11$WallName.out -time -eleRange 1 6 RCPanel 1
strain_stress_concrete1;
recorder Element -file Results/C21$WallName.out -time -eleRange 1 6 RCPanel 1
strain_stress_concrete2;
recorder Element -file Results/CrackAngles1$WallName.out -time -eleRange 1 6
RCPanel 1 cracking_angles;
recorder Element -file Results/SX2$WallName.out -time -eleRange 1 6 RCPanel 2
strain_stress_steelX;
recorder Element -file Results/SY2$WallName.out -time -eleRange 1 6 RCPanel 2
strain_stress_steelY;
recorder Element -file Results/C12$WallName.out -time -eleRange 1 6 RCPanel 2
strain_stress_concrete1;
recorder Element -file Results/C22$WallName.out -time -eleRange 1 6 RCPanel 2
strain_stress_concrete2;
recorder Element -file Results/CrackAngles2$WallName.out -time -eleRange 1 6
RCPanel 2 cracking_angles;
recorder Element -file Results/SX3$WallName.out -time -eleRange 1 6 RCPanel 3
strain_stress_steelX;
```

```
recorder Element -file Results/SY3$WallName.out -time -eleRange 1 6 RCPanel 3 strain_stress_steelY;
recorder Element -file Results/C13$WallName.out -time -eleRange 1 6 RCPanel 3 strain_stress_concrete1;
recorder Element -file Results/C23$WallName.out -time -eleRange 1 6 RCPanel 3 strain_stress_concrete2;
recorder Element -file Results/CrackAngles3$WallName.out -time -eleRange 1 6 RCPanel 3 cracking_angles;
recorder Element -file Results/SX4$WallName.out -time -eleRange 1 6 RCPanel 4 strain_stress_steelX;
recorder Element -file Results/SY4$WallName.out -time -eleRange 1 6 RCPanel 4 strain_stress_steelY;
recorder Element -file Results/C14$WallName.out -time -eleRange 1 6 RCPanel 4 strain_stress_concrete1;
recorder Element -file Results/C24$WallName.out -time -eleRange 1 6 RCPanel 4 strain_stress_concrete2;
recorder Element -file Results/CrackAngles4$WallName.out -time -eleRange 1 6 RCPanel 4 cracking_angles;
recorder Element -file Results/GlobalForce$WallName.out -time -eleRange 1 6 globalForce;
recorder Element -file Results/ShearDef$WallName.out -time -eleRange 1 6 ShearDef;
```

A.4 BTM

```
##-------------------------------------------------------
## GEOMETRY

set H 177.9528;         #Height (in)
set L 78.7402;          #Length (in)
set t 5.9055;           #Thickness (in)
set  Ld  480.2437;      #Diagonal element length (mm)
set  Lv  410.9091;      #Vertical element length (mm)
set  Lh  248.5714;      #Horizontal element length (mm)
set  wd  8.3734;        #Diagonal element width (in)
set  wv  9.7113;        #Vertical web element width (in)
set  wh  16.1775;       #Horizontal element width (in)
set  wb  10.2362;       #Vertical boundary element width (in)

#Nodes
node  1   5.1181   0.0000
node  2   14.9044  0.0000
node  3   24.6907  0.0000
node  4   34.4769  0.0000
node  5   44.2632  0.0000
node  6   54.0495  0.0000
node  7   63.8358  0.0000
node  8   73.6220  0.0000
node  9   5.1181   16.1775
node  10  14.9044  16.1775
node  11  24.6907  16.1775
node  12  34.4769  16.1775
node  13  44.2632  16.1775
node  14  54.0495  16.1775
node  15  63.8358  16.1775
node  16  73.6220  16.1775
node  17  5.1181   32.3550
node  18  14.9044  32.3550
node  19  24.6907  32.3550
node  20  34.4769  32.3550
node  21  44.2632  32.3550
node  22  54.0495  32.3550
node  23  63.8358  32.3550
node  24  73.6220  32.3550
node  25  5.1181   48.5326
node  26  14.9044  48.5326
node  27  24.6907  48.5326
```

node 28 34.4769 48.5326
node 29 44.2632 48.5326
node 30 54.0495 48.5326
node 31 63.8358 48.5326
node 32 73.6220 48.5326
node 33 5.1181 64.7101
node 34 14.9044 64.7101
node 35 24.6907 64.7101
node 36 34.4769 64.7101
node 37 44.2632 64.7101
node 38 54.0495 64.7101
node 39 63.8358 64.7101
node 40 73.6220 64.7101
node 41 5.1181 80.8876
node 42 14.9044 80.8876
node 43 24.6907 80.8876
node 44 34.4769 80.8876
node 45 44.2632 80.8876
node 46 54.0495 80.8876
node 47 63.8358 80.8876
node 48 73.6220 80.8876
node 49 5.1181 97.0651
node 50 14.9044 97.0651
node 51 24.6907 97.0651
node 52 34.4769 97.0651
node 53 44.2632 97.0651
node 54 54.0495 97.0651
node 55 63.8358 97.0651
node 56 73.6220 97.0651
node 57 5.1181 113.2427
node 58 14.9044 113.2427
node 59 24.6907 113.2427
node 60 34.4769 113.2427
node 61 44.2632 113.2427
node 62 54.0495 113.2427
node 63 63.8358 113.2427
node 64 73.6220 113.2427
node 65 5.1181 129.4202
node 66 14.9044 129.4202
node 67 24.6907 129.4202
node 68 34.4769 129.4202
node 69 44.2632 129.4202
node 70 54.0495 129.4202
node 71 63.8358 129.4202

```
node  72  73.6220  129.4202
node  73  5.1181   145.5977
node  74  14.9044  145.5977
node  75  24.6907  145.5977
node  76  34.4769  145.5977
node  77  44.2632  145.5977
node  78  54.0495  145.5977
node  79  63.8358  145.5977
node  80  73.6220  145.5977
node  81  5.1181   161.7752
node  82  14.9044  161.7752
node  83  24.6907  161.7752
node  84  34.4769  161.7752
node  85  44.2632  161.7752
node  86  54.0495  161.7752
node  87  63.8358  161.7752
node  88  73.6220  161.7752
node  89  5.1181   177.9528
node  90  14.9044  177.9528
node  91  24.6907  177.9528
node  92  34.4769  177.9528
node  93  44.2632  177.9528
node  94  54.0495  177.9528
node  95  63.8358  177.9528
node  96  73.6220  177.9528

#Restrictions
fix  1   1  1  1
fix  2   1  1  1
fix  3   1  1  1
fix  4   1  1  1
fix  5   1  1  1
fix  6   1  1  1
fix  7   1  1  1
fix  8   1  1  1
fix  9   0  0  0
fix  10  0  0  1
fix  11  0  0  1
fix  12  0  0  1
fix  13  0  0  1
fix  14  0  0  1
fix  15  0  0  1
fix  16  0  0  0
fix  17  0  0  0
```

```
fix  18  0  0  1
fix  19  0  0  1
fix  20  0  0  1
fix  21  0  0  1
fix  22  0  0  1
fix  23  0  0  1
fix  24  0  0  0
fix  25  0  0  0
fix  26  0  0  1
fix  27  0  0  1
fix  28  0  0  1
fix  29  0  0  1
fix  30  0  0  1
fix  31  0  0  1
fix  32  0  0  0
fix  33  0  0  0
fix  34  0  0  1
fix  35  0  0  1
fix  36  0  0  1
fix  37  0  0  1
fix  38  0  0  1
fix  39  0  0  1
fix  40  0  0  0
fix  41  0  0  0
fix  42  0  0  1
fix  43  0  0  1
fix  44  0  0  1
fix  45  0  0  1
fix  46  0  0  1
fix  47  0  0  1
fix  48  0  0  0
fix  49  0  0  0
fix  50  0  0  1
fix  51  0  0  1
fix  52  0  0  1
fix  53  0  0  1
fix  54  0  0  1
fix  55  0  0  1
fix  56  0  0  0
fix  57  0  0  0
fix  58  0  0  1
fix  59  0  0  1
fix  60  0  0  1
fix  61  0  0  1
```

```
fix  62  0  0  1
fix  63  0  0  1
fix  64  0  0  0
fix  65  0  0  0
fix  66  0  0  1
fix  67  0  0  1
fix  68  0  0  1
fix  69  0  0  1
fix  70  0  0  1
fix  71  0  0  1
fix  72  0  0  0
fix  73  0  0  0
fix  74  0  0  1
fix  75  0  0  1
fix  76  0  0  1
fix  77  0  0  1
fix  78  0  0  1
fix  79  0  0  1
fix  80  0  0  0
fix  81  0  0  0
fix  82  0  0  1
fix  83  0  0  1
fix  84  0  0  1
fix  85  0  0  1
fix  86  0  0  1
fix  87  0  0  1
fix  88  0  0  0
fix  89  0  0  0
fix  90  0  0  0
fix  91  0  0  0
fix  92  0  0  0
fix  93  0  0  0
fix  94  0  0  0
fix  95  0  0  0
fix  96  0  0  0

#Top beam Equal DOF
equalDOF  89  90  1
equalDOF  89  91  1
equalDOF  89  92  1
equalDOF  89  93  1
equalDOF  89  94  1
equalDOF  89  95  1
equalDOF  89  96  1
```

```
set IDctrlNode 89;  #Control node
set IDctrlDOF 1;    #Control DOF


##------------------------------------------------------------
## MATERIALS

set SteelB       1;
set SteelW       2;
set SteelX       3;
set ConVertW 4;
set ConVertB  5;
set ConHor      6;
set ConDiag    7;

#Reinforcing steel
uniaxialMaterial Steel02 $SteelB [expr 576.0*$MPa] [expr 200000.*$MPa] 0.02 20. 0.925 0.15; #For boundary regions
uniaxialMaterial Steel02 $SteelW [expr 583.7*$MPa] [expr 200000.*$MPa] 0.02 20. 0.925 0.15; #For web regions
uniaxialMaterial Steel02 $SteelX [expr 518.9*$MPa] [expr 200000.*$MPa] 0.02 20. 0.925 0.15; #Horizontal steel
#Concrete for vertical web elements
uniaxialMaterial ConcretewBeta $ConVertW -[expr 45.6*$MPa] -0.002 -[expr 22.8*$MPa] -0.00383 -0.001 -0.00566 [expr 2.23*$MPa] 0.001 0.0004 0.001 0.0008 -E [expr 33764.*$MPa] -alpha 0.5 -M 0.0467;
#Concrete for vertical boundary elements
uniaxialMaterial ConcretewBeta $ConVertB -[expr 45.6*$MPa] -0.002 -[expr 29.1*$MPa] -0.00949 -0.001 -0.01423 [expr 2.23*$MPa] 0.001 0.0004 0.001 0.0008 -E [expr 33764.*$MPa] -alpha 0.5 -M 0.10875 -conf -[expr 58.1*$MPa] -0.00475
#Concrete for horizontal elements
uniaxialMaterial ConcretewBeta $ConHor -[expr 45.6*$MPa] -0.002 -[expr 22.8*$MPa] -0.00555 -0.001 -0.00911 0.001 0.001 0.0004 0.001 0.0008 -E [expr 33764.*$MPa] -alpha 161.4;
#Concrete for diagonal elements
uniaxialMaterial ConcretewBeta $ConDiag -[expr 45.6*$MPa] -0.002 -[expr 22.8*$MPa] -0.00439 -0.001 -0.00677 0.001 0.001 0.0004 0.001 0.0008 -E [expr 33764.*$MPa] -alpha 161.4 -beta 0.4 0.01767 0.1 0.07068
#Concrete Young's Modulus for transfer beam
set Ec [expr 33764.*$MPa]


##------------------------------------------------------------
```

```
## SECTIONS

#Vertical boundary
set Boundary 1
set dY   [expr $wb/2.0];
set dZ   [expr $t/2.0];
set Ny   6;
set Nz   1;
section fiberSec $Boundary {
   patch rect $ConVertB $Ny $Nz -$dY -$dZ $dY $dZ
   fiber  [expr  100*$mm] 0.0 [expr 226.1947*$mm2] $SteelB;
   fiber  [expr    0*$mm] 0.0 [expr 226.1947*$mm2] $SteelB;
   fiber  [expr -100*$mm] 0.0 [expr 226.1947*$mm2] $SteelB;
};

#Vertical web
set pv 0.0049813;       #Vertical web steel ratio
set Hw [expr $t*$wv];
set Aw [expr $pv*$Hw];

#Horizontal
set ph 0.0025133;       #Horizontal steel ratio
set Hh [expr $t*$wh];
set Ah [expr $ph*$Hh];

#Diagonal
set Hd [expr $t*$wd];

#Transfer beam
set Avc [expr 400.*1000.*$mm2];
set Ivc [expr 400.*pow(1000.,3)/12.*$mm4];


##-----------------------------------------------------------
## ELEMENTS

#Vertical boundary elements
set NIP 2
set FBETol 1.e-5;
set FBEiter 1000;
geomTransf Linear 1;
element forceBeamColumn 1 1 9 $NIP $Boundary 1 -integration Lobatto -iter
$FBEiter $FBETol;
```

```
element forceBeamColumn 2 9 17 $NIP $Boundary 1 -integration Lobatto -iter $FBEiter $FBETol;
element forceBeamColumn 3 17 25 $NIP $Boundary 1 -integration Lobatto -iter $FBEiter $FBETol;
element forceBeamColumn 4 25 33 $NIP $Boundary 1 -integration Lobatto -iter $FBEiter $FBETol;
element forceBeamColumn 5 33 41 $NIP $Boundary 1 -integration Lobatto -iter $FBEiter $FBETol;
element forceBeamColumn 6 41 49 $NIP $Boundary 1 -integration Lobatto -iter $FBEiter $FBETol;
element forceBeamColumn 7 49 57 $NIP $Boundary 1 -integration Lobatto -iter $FBEiter $FBETol;
element forceBeamColumn 8 57 65 $NIP $Boundary 1 -integration Lobatto -iter $FBEiter $FBETol;
element forceBeamColumn 9 65 73 $NIP $Boundary 1 -integration Lobatto -iter $FBEiter $FBETol;
element forceBeamColumn 10 73 81 $NIP $Boundary 1 -integration Lobatto -iter $FBEiter $FBETol;
element forceBeamColumn 11 81 89 $NIP $Boundary 1 -integration Lobatto -iter $FBEiter $FBETol;
element forceBeamColumn 12 8 16 $NIP $Boundary 1 -integration Lobatto -iter $FBEiter $FBETol;
element forceBeamColumn 13 16 24 $NIP $Boundary 1 -integration Lobatto -iter $FBEiter $FBETol;
element forceBeamColumn 14 24 32 $NIP $Boundary 1 -integration Lobatto -iter $FBEiter $FBETol;
element forceBeamColumn 15 32 40 $NIP $Boundary 1 -integration Lobatto -iter $FBEiter $FBETol;
element forceBeamColumn 16 40 48 $NIP $Boundary 1 -integration Lobatto -iter $FBEiter $FBETol;
element forceBeamColumn 17 48 56 $NIP $Boundary 1 -integration Lobatto -iter $FBEiter $FBETol;
element forceBeamColumn 18 56 64 $NIP $Boundary 1 -integration Lobatto -iter $FBEiter $FBETol;
element forceBeamColumn 19 64 72 $NIP $Boundary 1 -integration Lobatto -iter $FBEiter $FBETol;
element forceBeamColumn 20 72 80 $NIP $Boundary 1 -integration Lobatto -iter $FBEiter $FBETol;
element forceBeamColumn 21 80 88 $NIP $Boundary 1 -integration Lobatto -iter $FBEiter $FBETol;
element forceBeamColumn 22 88 96 $NIP $Boundary 1 -integration Lobatto -iter $FBEiter $FBETol;

#Vertical web elements
```

```
element truss  23  2   10  $Hw  $ConVertW;    element truss  1023  2  10   $Aw  $SteelW;
element truss  24  10  18  $Hw  $ConVertW;    element truss  1024  10 18   $Aw  $SteelW;
element truss  25  18  26  $Hw  $ConVertW;    element truss  1025  18 26   $Aw  $SteelW;
element truss  26  26  34  $Hw  $ConVertW;    element truss  1026  26 34   $Aw  $SteelW;
element truss  27  34  42  $Hw  $ConVertW;    element truss  1027  34 42   $Aw  $SteelW;
element truss  28  42  50  $Hw  $ConVertW;    element truss  1028  42 50   $Aw  $SteelW;
element truss  29  50  58  $Hw  $ConVertW;    element truss  1029  50 58   $Aw  $SteelW;
element truss  30  58  66  $Hw  $ConVertW;    element truss  1030  58 66   $Aw  $SteelW;
element truss  31  66  74  $Hw  $ConVertW;    element truss  1031  66 74   $Aw  $SteelW;
element truss  32  74  82  $Hw  $ConVertW;    element truss  1032  74 82   $Aw  $SteelW;
element truss  33  82  90  $Hw  $ConVertW;    element truss  1033  82 90   $Aw  $SteelW;
element truss  34  3   11  $Hw  $ConVertW;    element truss  1034  3  11   $Aw  $SteelW;
element truss  35  11  19  $Hw  $ConVertW;    element truss  1035  11 19   $Aw  $SteelW;
element truss  36  19  27  $Hw  $ConVertW;    element truss  1036  19 27   $Aw  $SteelW;
element truss  37  27  35  $Hw  $ConVertW;    element truss  1037  27 35   $Aw  $SteelW;
element truss  38  35  43  $Hw  $ConVertW;    element truss  1038  35 43   $Aw  $SteelW;
element truss  39  43  51  $Hw  $ConVertW;    element truss  1039  43 51   $Aw  $SteelW;
element truss  40  51  59  $Hw  $ConVertW;    element truss  1040  51 59   $Aw  $SteelW;
element truss  41  59  67  $Hw  $ConVertW;    element truss  1041  59 67   $Aw  $SteelW;
element truss  42  67  75  $Hw  $ConVertW;    element truss  1042  67 75   $Aw  $SteelW;
element truss  43  75  83  $Hw  $ConVertW;    element truss  1043  75 83   $Aw  $SteelW;
element truss  44  83  91  $Hw  $ConVertW;    element truss  1044  83 91   $Aw  $SteelW;
element truss  45  4   12  $Hw  $ConVertW;    element truss  1045  4  12   $Aw  $SteelW;
element truss  46  12  20  $Hw  $ConVertW;    element truss  1046  12 20   $Aw  $SteelW;
element truss  47  20  28  $Hw  $ConVertW;    element truss  1047  20 28   $Aw  $SteelW;
element truss  48  28  36  $Hw  $ConVertW;    element truss  1048  28 36   $Aw  $SteelW;
element truss  49  36  44  $Hw  $ConVertW;    element truss  1049  36 44   $Aw  $SteelW;
element truss  50  44  52  $Hw  $ConVertW;    element truss  1050  44 52   $Aw  $SteelW;
element truss  51  52  60  $Hw  $ConVertW;    element truss  1051  52 60   $Aw  $SteelW;
element truss  52  60  68  $Hw  $ConVertW;    element truss  1052  60 68   $Aw  $SteelW;
element truss  53  68  76  $Hw  $ConVertW;    element truss  1053  68 76   $Aw  $SteelW;
element truss  54  76  84  $Hw  $ConVertW;    element truss  1054  76 84   $Aw  $SteelW;
element truss  55  84  92  $Hw  $ConVertW;    element truss  1055  84 92   $Aw  $SteelW;
element truss  56  5   13  $Hw  $ConVertW;    element truss  1056  5  13   $Aw  $SteelW;
element truss  57  13  21  $Hw  $ConVertW;    element truss  1057  13 21   $Aw  $SteelW;
element truss  58  21  29  $Hw  $ConVertW;    element truss  1058  21 29   $Aw  $SteelW;
element truss  59  29  37  $Hw  $ConVertW;    element truss  1059  29 37   $Aw  $SteelW;
element truss  60  37  45  $Hw  $ConVertW;    element truss  1060  37 45   $Aw  $SteelW;
element truss  61  45  53  $Hw  $ConVertW;    element truss  1061  45 53   $Aw  $SteelW;
element truss  62  53  61  $Hw  $ConVertW;    element truss  1062  53 61   $Aw  $SteelW;
element truss  63  61  69  $Hw  $ConVertW;    element truss  1063  61 69   $Aw  $SteelW;
element truss  64  69  77  $Hw  $ConVertW;    element truss  1064  69 77   $Aw  $SteelW;
element truss  65  77  85  $Hw  $ConVertW;    element truss  1065  77 85   $Aw  $SteelW;
element truss  66  85  93  $Hw  $ConVertW;    element truss  1066  85 93   $Aw  $SteelW;
```

```
element truss  67  6   14  $Hw  $ConVertW;    element truss  1067  6  14   $Aw  $SteelW;
element truss  68  14  22  $Hw  $ConVertW;    element truss  1068  14 22  $Aw  $SteelW;
element truss  69  22  30  $Hw  $ConVertW;    element truss  1069  22 30  $Aw  $SteelW;
element truss  70  30  38  $Hw  $ConVertW;    element truss  1070  30 38  $Aw  $SteelW;
element truss  71  38  46  $Hw  $ConVertW;    element truss  1071  38 46  $Aw  $SteelW;
element truss  72  46  54  $Hw  $ConVertW;    element truss  1072  46 54  $Aw  $SteelW;
element truss  73  54  62  $Hw  $ConVertW;    element truss  1073  54 62  $Aw  $SteelW;
element truss  74  62  70  $Hw  $ConVertW;    element truss  1074  62 70  $Aw  $SteelW;
element truss  75  70  78  $Hw  $ConVertW;    element truss  1075  70 78  $Aw  $SteelW;
element truss  76  78  86  $Hw  $ConVertW;    element truss  1076  78 86  $Aw  $SteelW;
element truss  77  86  94  $Hw  $ConVertW;    element truss  1077  86 94  $Aw  $SteelW;
element truss  78  7   15  $Hw  $ConVertW;    element truss  1078  7  15   $Aw  $SteelW;
element truss  79  15  23  $Hw  $ConVertW;    element truss  1079  15 23  $Aw  $SteelW;
element truss  80  23  31  $Hw  $ConVertW;    element truss  1080  23 31  $Aw  $SteelW;
element truss  81  31  39  $Hw  $ConVertW;    element truss  1081  31 39  $Aw  $SteelW;
element truss  82  39  47  $Hw  $ConVertW;    element truss  1082  39 47  $Aw  $SteelW;
element truss  83  47  55  $Hw  $ConVertW;    element truss  1083  47 55  $Aw  $SteelW;
element truss  84  55  63  $Hw  $ConVertW;    element truss  1084  55 63  $Aw  $SteelW;
element truss  85  63  71  $Hw  $ConVertW;    element truss  1085  63 71  $Aw  $SteelW;
element truss  86  71  79  $Hw  $ConVertW;    element truss  1086  71 79  $Aw  $SteelW;
element truss  87  79  87  $Hw  $ConVertW;    element truss  1087  79 87  $Aw  $SteelW;
element truss  88  87  95  $Hw  $ConVertW;    element truss  1088  87 95  $Aw  $SteelW;

#Horizontal elements
element truss  89   9   10  $Hh  $ConHor;     element truss  1089  9   10  $Ah  $SteelX;
element truss  90   10  11  $Hh  $ConHor;     element truss  1090  10  11  $Ah  $SteelX;
element truss  91   11  12  $Hh  $ConHor;     element truss  1091  11  12  $Ah  $SteelX;
element truss  92   12  13  $Hh  $ConHor;     element truss  1092  12  13  $Ah  $SteelX;
element truss  93   13  14  $Hh  $ConHor;     element truss  1093  13  14  $Ah  $SteelX;
element truss  94   14  15  $Hh  $ConHor;     element truss  1094  14  15  $Ah  $SteelX;
element truss  95   15  16  $Hh  $ConHor;     element truss  1095  15  16  $Ah  $SteelX;
element truss  96   17  18  $Hh  $ConHor;     element truss  1096  17  18  $Ah  $SteelX;
element truss  97   18  19  $Hh  $ConHor;     element truss  1097  18  19  $Ah  $SteelX;
element truss  98   19  20  $Hh  $ConHor;     element truss  1098  19  20  $Ah  $SteelX;
element truss  99   20  21  $Hh  $ConHor;     element truss  1099  20  21  $Ah  $SteelX;
element truss  100  21  22  $Hh  $ConHor;     element truss  1100  21  22  $Ah  $SteelX;
element truss  101  22  23  $Hh  $ConHor;     element truss  1101  22  23  $Ah  $SteelX;
element truss  102  23  24  $Hh  $ConHor;     element truss  1102  23  24  $Ah  $SteelX;
element truss  103  25  26  $Hh  $ConHor;     element truss  1103  25  26  $Ah  $SteelX;
element truss  104  26  27  $Hh  $ConHor;     element truss  1104  26  27  $Ah  $SteelX;
element truss  105  27  28  $Hh  $ConHor;     element truss  1105  27  28  $Ah  $SteelX;
element truss  106  28  29  $Hh  $ConHor;     element truss  1106  28  29  $Ah  $SteelX;
element truss  107  29  30  $Hh  $ConHor;     element truss  1107  29  30  $Ah  $SteelX;
element truss  108  30  31  $Hh  $ConHor;     element truss  1108  30  31  $Ah  $SteelX;
```

```
element truss 109 31 32 $Hh $ConHor;    element truss 1109 31 32 $Ah $SteelX;
element truss 110 33 34 $Hh $ConHor;    element truss 1110 33 34 $Ah $SteelX;
element truss 111 34 35 $Hh $ConHor;    element truss 1111 34 35 $Ah $SteelX;
element truss 112 35 36 $Hh $ConHor;    element truss 1112 35 36 $Ah $SteelX;
element truss 113 36 37 $Hh $ConHor;    element truss 1113 36 37 $Ah $SteelX;
element truss 114 37 38 $Hh $ConHor;    element truss 1114 37 38 $Ah $SteelX;
element truss 115 38 39 $Hh $ConHor;    element truss 1115 38 39 $Ah $SteelX;
element truss 116 39 40 $Hh $ConHor;    element truss 1116 39 40 $Ah $SteelX;
element truss 117 41 42 $Hh $ConHor;    element truss 1117 41 42 $Ah $SteelX;
element truss 118 42 43 $Hh $ConHor;    element truss 1118 42 43 $Ah $SteelX;
element truss 119 43 44 $Hh $ConHor;    element truss 1119 43 44 $Ah $SteelX;
element truss 120 44 45 $Hh $ConHor;    element truss 1120 44 45 $Ah $SteelX;
element truss 121 45 46 $Hh $ConHor;    element truss 1121 45 46 $Ah $SteelX;
element truss 122 46 47 $Hh $ConHor;    element truss 1122 46 47 $Ah $SteelX;
element truss 123 47 48 $Hh $ConHor;    element truss 1123 47 48 $Ah $SteelX;
element truss 124 49 50 $Hh $ConHor;    element truss 1124 49 50 $Ah $SteelX;
element truss 125 50 51 $Hh $ConHor;    element truss 1125 50 51 $Ah $SteelX;
element truss 126 51 52 $Hh $ConHor;    element truss 1126 51 52 $Ah $SteelX;
element truss 127 52 53 $Hh $ConHor;    element truss 1127 52 53 $Ah $SteelX;
element truss 128 53 54 $Hh $ConHor;    element truss 1128 53 54 $Ah $SteelX;
element truss 129 54 55 $Hh $ConHor;    element truss 1129 54 55 $Ah $SteelX;
element truss 130 55 56 $Hh $ConHor;    element truss 1130 55 56 $Ah $SteelX;
element truss 131 57 58 $Hh $ConHor;    element truss 1131 57 58 $Ah $SteelX;
element truss 132 58 59 $Hh $ConHor;    element truss 1132 58 59 $Ah $SteelX;
element truss 133 59 60 $Hh $ConHor;    element truss 1133 59 60 $Ah $SteelX;
element truss 134 60 61 $Hh $ConHor;    element truss 1134 60 61 $Ah $SteelX;
element truss 135 61 62 $Hh $ConHor;    element truss 1135 61 62 $Ah $SteelX;
element truss 136 62 63 $Hh $ConHor;    element truss 1136 62 63 $Ah $SteelX;
element truss 137 63 64 $Hh $ConHor;    element truss 1137 63 64 $Ah $SteelX;
element truss 138 65 66 $Hh $ConHor;    element truss 1138 65 66 $Ah $SteelX;
element truss 139 66 67 $Hh $ConHor;    element truss 1139 66 67 $Ah $SteelX;
element truss 140 67 68 $Hh $ConHor;    element truss 1140 67 68 $Ah $SteelX;
element truss 141 68 69 $Hh $ConHor;    element truss 1141 68 69 $Ah $SteelX;
element truss 142 69 70 $Hh $ConHor;    element truss 1142 69 70 $Ah $SteelX;
element truss 143 70 71 $Hh $ConHor;    element truss 1143 70 71 $Ah $SteelX;
element truss 144 71 72 $Hh $ConHor;    element truss 1144 71 72 $Ah $SteelX;
element truss 145 73 74 $Hh $ConHor;    element truss 1145 73 74 $Ah $SteelX;
element truss 146 74 75 $Hh $ConHor;    element truss 1146 74 75 $Ah $SteelX;
element truss 147 75 76 $Hh $ConHor;    element truss 1147 75 76 $Ah $SteelX;
element truss 148 76 77 $Hh $ConHor;    element truss 1148 76 77 $Ah $SteelX;
element truss 149 77 78 $Hh $ConHor;    element truss 1149 77 78 $Ah $SteelX;
element truss 150 78 79 $Hh $ConHor;    element truss 1150 78 79 $Ah $SteelX;
element truss 151 79 80 $Hh $ConHor;    element truss 1151 79 80 $Ah $SteelX;
element truss 152 81 82 $Hh $ConHor;    element truss 1152 81 82 $Ah $SteelX;
```

```
element truss  153  82  83  $Hh  $ConHor;     element truss  1153  82  83  $Ah  $SteelX;
element truss  154  83  84  $Hh  $ConHor;     element truss  1154  83  84  $Ah  $SteelX;
element truss  155  84  85  $Hh  $ConHor;     element truss  1155  84  85  $Ah  $SteelX;
element truss  156  85  86  $Hh  $ConHor;     element truss  1156  85  86  $Ah  $SteelX;
element truss  157  86  87  $Hh  $ConHor;     element truss  1157  86  87  $Ah  $SteelX;
element truss  158  87  88  $Hh  $ConHor;     element truss  1158  87  88  $Ah  $SteelX;

#Diagonal elements
element Truss2  159  1   10  9   2   $Hd  $ConDiag;     element Truss2  160  9  2   1   10
$Hd  $ConDiag;
element Truss2  161  2   11  10  3   $Hd  $ConDiag;     element Truss2  162  10  3  2   11
$Hd  $ConDiag;
element Truss2  163  3   12  11  4   $Hd  $ConDiag;     element Truss2  164  11  4  3   12
$Hd  $ConDiag;
element Truss2  165  4   13  12  5   $Hd  $ConDiag;     element Truss2  166  12  5  4   13
$Hd  $ConDiag;
element Truss2  167  5   14  13  6   $Hd  $ConDiag;     element Truss2  168  13  6  5   14
$Hd  $ConDiag;
element Truss2  169  6   15  14  7   $Hd  $ConDiag;     element Truss2  170  14  7  6   15
$Hd  $ConDiag;
element Truss2  171  7   16  15  8   $Hd  $ConDiag;     element Truss2  172  15  8  7   16
$Hd  $ConDiag;
element Truss2  173  9   18  17  10  $Hd  $ConDiag;     element Truss2  174  17  10  9  18
$Hd  $ConDiag;
element Truss2  175  10  19  18  11  $Hd  $ConDiag;     element Truss2  176  18  11  10
19  $Hd  $ConDiag;
element Truss2  177  11  20  19  12  $Hd  $ConDiag;     element Truss2  178  19  12  11
20  $Hd  $ConDiag;
element Truss2  179  12  21  20  13  $Hd  $ConDiag;     element Truss2  180  20  13  12
21  $Hd  $ConDiag;
element Truss2  181  13  22  21  14  $Hd  $ConDiag;     element Truss2  182  21  14  13
22  $Hd  $ConDiag;
element Truss2  183  14  23  22  15  $Hd  $ConDiag;     element Truss2  184  22  15  14
23  $Hd  $ConDiag;
element Truss2  185  15  24  23  16  $Hd  $ConDiag;     element Truss2  186  23  16  15
24  $Hd  $ConDiag;
element Truss2  187  17  26  25  18  $Hd  $ConDiag;     element Truss2  188  25  18  17
26  $Hd  $ConDiag;
element Truss2  189  18  27  26  19  $Hd  $ConDiag;     element Truss2  190  26  19  18
27  $Hd  $ConDiag;
element Truss2  191  19  28  27  20  $Hd  $ConDiag;     element Truss2  192  27  20  19
28  $Hd  $ConDiag;
element Truss2  193  20  29  28  21  $Hd  $ConDiag;     element Truss2  194  28  21  20
29  $Hd  $ConDiag;
```

```
element Truss2 195 21 30 29 22 $Hd $ConDiag;    element Truss2 196 29 22 21 30 $Hd $ConDiag;
element Truss2 197 22 31 30 23 $Hd $ConDiag;    element Truss2 198 30 23 22 31 $Hd $ConDiag;
element Truss2 199 23 32 31 24 $Hd $ConDiag;    element Truss2 200 31 24 23 32 $Hd $ConDiag;
element Truss2 201 25 34 33 26 $Hd $ConDiag;    element Truss2 202 33 26 25 34 $Hd $ConDiag;
element Truss2 203 26 35 34 27 $Hd $ConDiag;    element Truss2 204 34 27 26 35 $Hd $ConDiag;
element Truss2 205 27 36 35 28 $Hd $ConDiag;    element Truss2 206 35 28 27 36 $Hd $ConDiag;
element Truss2 207 28 37 36 29 $Hd $ConDiag;    element Truss2 208 36 29 28 37 $Hd $ConDiag;
element Truss2 209 29 38 37 30 $Hd $ConDiag;    element Truss2 210 37 30 29 38 $Hd $ConDiag;
element Truss2 211 30 39 38 31 $Hd $ConDiag;    element Truss2 212 38 31 30 39 $Hd $ConDiag;
element Truss2 213 31 40 39 32 $Hd $ConDiag;    element Truss2 214 39 32 31 40 $Hd $ConDiag;
element Truss2 215 33 42 41 34 $Hd $ConDiag;    element Truss2 216 41 34 33 42 $Hd $ConDiag;
element Truss2 217 34 43 42 35 $Hd $ConDiag;    element Truss2 218 42 35 34 43 $Hd $ConDiag;
element Truss2 219 35 44 43 36 $Hd $ConDiag;    element Truss2 220 43 36 35 44 $Hd $ConDiag;
element Truss2 221 36 45 44 37 $Hd $ConDiag;    element Truss2 222 44 37 36 45 $Hd $ConDiag;
element Truss2 223 37 46 45 38 $Hd $ConDiag;    element Truss2 224 45 38 37 46 $Hd $ConDiag;
element Truss2 225 38 47 46 39 $Hd $ConDiag;    element Truss2 226 46 39 38 47 $Hd $ConDiag;
element Truss2 227 39 48 47 40 $Hd $ConDiag;    element Truss2 228 47 40 39 48 $Hd $ConDiag;
element Truss2 229 41 50 49 42 $Hd $ConDiag;    element Truss2 230 49 42 41 50 $Hd $ConDiag;
element Truss2 231 42 51 50 43 $Hd $ConDiag;    element Truss2 232 50 43 42 51 $Hd $ConDiag;
element Truss2 233 43 52 51 44 $Hd $ConDiag;    element Truss2 234 51 44 43 52 $Hd $ConDiag;
element Truss2 235 44 53 52 45 $Hd $ConDiag;    element Truss2 236 52 45 44 53 $Hd $ConDiag;
element Truss2 237 45 54 53 46 $Hd $ConDiag;    element Truss2 238 53 46 45 54 $Hd $ConDiag;
```

```
element Truss2 239 46 55 54 47 $Hd $ConDiag;    element Truss2 240 54 47 46 55 $Hd $ConDiag;
element Truss2 241 47 56 55 48 $Hd $ConDiag;    element Truss2 242 55 48 47 56 $Hd $ConDiag;
element Truss2 243 49 58 57 50 $Hd $ConDiag;    element Truss2 244 57 50 49 58 $Hd $ConDiag;
element Truss2 245 50 59 58 51 $Hd $ConDiag;    element Truss2 246 58 51 50 59 $Hd $ConDiag;
element Truss2 247 51 60 59 52 $Hd $ConDiag;    element Truss2 248 59 52 51 60 $Hd $ConDiag;
element Truss2 249 52 61 60 53 $Hd $ConDiag;    element Truss2 250 60 53 52 61 $Hd $ConDiag;
element Truss2 251 53 62 61 54 $Hd $ConDiag;    element Truss2 252 61 54 53 62 $Hd $ConDiag;
element Truss2 253 54 63 62 55 $Hd $ConDiag;    element Truss2 254 62 55 54 63 $Hd $ConDiag;
element Truss2 255 55 64 63 56 $Hd $ConDiag;    element Truss2 256 63 56 55 64 $Hd $ConDiag;
element Truss2 257 57 66 65 58 $Hd $ConDiag;    element Truss2 258 65 58 57 66 $Hd $ConDiag;
element Truss2 259 58 67 66 59 $Hd $ConDiag;    element Truss2 260 66 59 58 67 $Hd $ConDiag;
element Truss2 261 59 68 67 60 $Hd $ConDiag;    element Truss2 262 67 60 59 68 $Hd $ConDiag;
element Truss2 263 60 69 68 61 $Hd $ConDiag;    element Truss2 264 68 61 60 69 $Hd $ConDiag;
element Truss2 265 61 70 69 62 $Hd $ConDiag;    element Truss2 266 69 62 61 70 $Hd $ConDiag;
element Truss2 267 62 71 70 63 $Hd $ConDiag;    element Truss2 268 70 63 62 71 $Hd $ConDiag;
element Truss2 269 63 72 71 64 $Hd $ConDiag;    element Truss2 270 71 64 63 72 $Hd $ConDiag;
element Truss2 271 65 74 73 66 $Hd $ConDiag;    element Truss2 272 73 66 65 74 $Hd $ConDiag;
element Truss2 273 66 75 74 67 $Hd $ConDiag;    element Truss2 274 74 67 66 75 $Hd $ConDiag;
element Truss2 275 67 76 75 68 $Hd $ConDiag;    element Truss2 276 75 68 67 76 $Hd $ConDiag;
element Truss2 277 68 77 76 69 $Hd $ConDiag;    element Truss2 278 76 69 68 77 $Hd $ConDiag;
element Truss2 279 69 78 77 70 $Hd $ConDiag;    element Truss2 280 77 70 69 78 $Hd $ConDiag;
element Truss2 281 70 79 78 71 $Hd $ConDiag;    element Truss2 282 78 71 70 79 $Hd $ConDiag;
```

```
element Truss2 283 71 80 79 72 $Hd $ConDiag;    element Truss2 284 79 72 71 80 $Hd $ConDiag;
element Truss2 285 73 82 81 74 $Hd $ConDiag;    element Truss2 286 81 74 73 82 $Hd $ConDiag;
element Truss2 287 74 83 82 75 $Hd $ConDiag;    element Truss2 288 82 75 74 83 $Hd $ConDiag;
element Truss2 289 75 84 83 76 $Hd $ConDiag;    element Truss2 290 83 76 75 84 $Hd $ConDiag;
element Truss2 291 76 85 84 77 $Hd $ConDiag;    element Truss2 292 84 77 76 85 $Hd $ConDiag;
element Truss2 293 77 86 85 78 $Hd $ConDiag;    element Truss2 294 85 78 77 86 $Hd $ConDiag;
element Truss2 295 78 87 86 79 $Hd $ConDiag;    element Truss2 296 86 79 78 87 $Hd $ConDiag;
element Truss2 297 79 88 87 80 $Hd $ConDiag;    element Truss2 298 87 80 79 88 $Hd $ConDiag;
element Truss2 299 81 90 89 82 $Hd $ConDiag;    element Truss2 300 89 82 81 90 $Hd $ConDiag;
element Truss2 301 82 91 90 83 $Hd $ConDiag;    element Truss2 302 90 83 82 91 $Hd $ConDiag;
element Truss2 303 83 92 91 84 $Hd $ConDiag;    element Truss2 304 91 84 83 92 $Hd $ConDiag;
element Truss2 305 84 93 92 85 $Hd $ConDiag;    element Truss2 306 92 85 84 93 $Hd $ConDiag;
element Truss2 307 85 94 93 86 $Hd $ConDiag;    element Truss2 308 93 86 85 94 $Hd $ConDiag;
element Truss2 309 86 95 94 87 $Hd $ConDiag;    element Truss2 310 94 87 86 95 $Hd $ConDiag;
element Truss2 311 87 96 95 88 $Hd $ConDiag;    element Truss2 312 95 88 87 96 $Hd $ConDiag;

#Transfer beam
element elasticBeamColumn 313 89 90 $Avc $Ec $Ivc 1;
element elasticBeamColumn 314 90 91 $Avc $Ec $Ivc 1;
element elasticBeamColumn 315 91 92 $Avc $Ec $Ivc 1;
element elasticBeamColumn 316 92 93 $Avc $Ec $Ivc 1;
element elasticBeamColumn 317 93 94 $Avc $Ec $Ivc 1;
element elasticBeamColumn 318 94 95 $Avc $Ec $Ivc 1;
element elasticBeamColumn 319 95 96 $Avc $Ec $Ivc 1;


##------------------------------------------------------------
## LOADS
```

```
#Gravity Load
set P [expr 1476*$kN];
pattern Plain 1 "Linear" {
   load 89 0.0 [expr -$P/8] 0.0;
   load 90 0.0 [expr -$P/8] 0.0;
   load 91 0.0 [expr -$P/8] 0.0;
   load 92 0.0 [expr -$P/8] 0.0;
   load 93 0.0 [expr -$P/8] 0.0;
   load 94 0.0 [expr -$P/8] 0.0;
   load 95 0.0 [expr -$P/8] 0.0;
   load 96 0.0 [expr -$P/8] 0.0;
};
set Tol 1.0e-5;
integrator LoadControl 0.1
system BandGeneral
test NormDispIncr $Tol  100 0
numberer RCM
constraints Transformation
algorithm Newton
analysis Static
analyze 10
loadConst -time 0.0; #Keep axial load constant

#Lateral Load
set Plateral 1.0;
pattern Plain 2 "Linear" {
        load $IDctrlNode $Plateral 0.0 0.0
};
set file [open "Protocolo.dat" r]; #File with disp protocol in in

##------------------------------------------------------------
## RECORDERS

set WallName WSH6;#Wall name
file mkdir Results;      #Save results in "Results" folder
recorder Node -file Results.out -time -node $IDctrlNode -dof $IDctrlDOF disp
recorder Node -file Results/FD$WallName.out -time -node $IDctrlNode -dof $IDctrlDOF
disp
recorder Node -file Results/NodeDisplacements$WallName.out -time -nodeRange 1
10000000 -dof 1 2 3 disp
recorder Element -file Results/StressStrainConcrete$WallName.out -time -eleRange 23
312 -material stressStrain
recorder Element -file Results/StressStrainSteel$WallName.out -time -eleRange 1023
1158 -material stressStrain
```

```
recorder Element -file Results/StressStrainFiberCLeft$WallName.out -time -eleRange 1 11 section 1 fiber [expr  100*$mm] 0 $ConVertB stressStrain
recorder Element -file Results/StressStrainFiberSLeft$WallName.out -time -eleRange 1 11 section 1 fiber [expr  100*$mm] 0 $SteelB stressStrain
recorder Element -file Results/StressStrainFiberCRight$WallName.out -time -eleRange 12 22 section 1 fiber [expr  -100*$mm] 0 $ConVertB stressStrain
recorder Element -file Results/StressStrainFiberSRight$WallName.out -time -eleRange 12 22 section 1 fiber [expr  -100*$mm] 0 $SteelB stressStrain
```

A.5 RPHM for RC Walls

```
##-------------------------------------------------------
## GEOMETRY

set H 177.9528;              #Height (in)
set L 78.7402;               #Length (in)
set t 5.9055;                #Thickness (in)
set Lb 10.2362;              #Confined length (in)
set rech 0.0709;             #Horizontal clear cover (in)
set recv 0.0709;             #Vertical clear cover (in)
set Lp 21.3223;              #Plastic hinge length (in)

#Nodes
node 1 0 0;
node 2 0 $H;

fix 1 1 1 1;             #fix the base
set IDctrlNode 2;        #Control node
set IDctrlDOF 1;          #Control DOF


##-------------------------------------------------------
## MATERIALS

#Reinforcing steel
uniaxialMaterial Steel02 10 [expr 576.0*$MPa] [expr 200000.*$MPa] 0.01904 20. 0.925 0.15; #For boundary regions
uniaxialMaterial Steel02 20 [expr 583.7*$MPa] [expr 200000.*$MPa] 0.02331 20. 0.925 0.15; #For web regions
uniaxialMaterial MinMax 1 10 -min -0.007905;
uniaxialMaterial MinMax 2 20 -min -0.012409;
#Concrete
uniaxialMaterial Concrete02 3 -[expr 58.1*$MPa] -0.00365 -1.679 -0.012409 0.1 0.323 230.1; #Confined
uniaxialMaterial Concrete02 4 -[expr 45.6*$MPa] -0.00287 -1.322 -0.007905 0.1 0.323 230.1; #Unconfined
# Shear
set Ec [expr 31738.*$MPa]; # Concrete Young's Modulus
set G [expr (5./6.)*0.4*$Ec];
set GA [expr 0.1*$G*$L*$t];
uniaxialMaterial Elastic 5 $GA;
```

```
##-------------------------------------------------------
## SECTIONS

set nfibersb 40;        #Number of fibers for boundary regions
set nfibersw 200;       #Number of fibers for web regions
set A1 0.3506;          #Area of 12 mm bar x2 (for boundary regions)
set A2 0.1558;          #Area of 8 mm bar x2 (for web regions)
section fiberSec 10 {
patch rect 3  $nfibersb 1  [expr ($L/2.)-$Lb+$rech]  -[expr $t/2.-$recv]  [expr $L/2.-$rech]
[expr $t/2.-$recv]
patch rect 4  $nfibersw 1 -[expr ($L/2.)-$Lb+$rech]  -[expr $t/2.]  [expr ($L/2.)-
$Lb+$rech]  [expr $t/2.]
patch rect 3  $nfibersb 1 -[expr $L/2.-$rech]  -[expr $t/2.-$recv] -[expr ($L/2.)-
$Lb+$rech]  [expr $t/2.-$recv]
patch rect 4  $nfibersb 1  [expr ($L/2.)-$Lb+$rech]  -[expr $t/2.]  [expr ($L/2.)-$rech]
-[expr $t/2.-$recv]
patch rect 4  $nfibersb 1  [expr ($L/2.)-$Lb+$rech]  [expr $t/2.-$recv]  [expr ($L/2.)-$rech]
[expr $t/2.]
patch rect 4  3  1  [expr ($L/2.)-$rech]  -[expr $t/2.]  [expr ($L/2.)]  [expr
$t/2.]
patch rect 4  $nfibersb 1 -[expr ($L/2.)-$rech]  -[expr $t/2.]  -[expr ($L/2.)-$Lb+$rech]
-[expr $t/2.-$recv]
patch rect 4  $nfibersb 1 -[expr ($L/2.)-$rech]  [expr $t/2.-$recv] -[expr ($L/2.)-
$Lb+$rech]  [expr $t/2.]
patch rect 4  3  1 -[expr ($L/2.)]  -[expr $t/2.]  -[expr ($L/2.)-$rech]  [expr
$t/2.]
fiber  38.1890 0.0 $A1 1
fiber  34.2520 0.0 $A1 1
fiber  30.3150 0.0 $A1 1
fiber  25.3937 0.0 $A2 2
fiber  20.4724 0.0 $A2 2
fiber  15.5512 0.0 $A2 2
fiber  10.6299 0.0 $A2 2
fiber  5.7087  0.0 $A2 2
fiber  0.0000  0.0 $A2 2
fiber -5.7087  0.0 $A2 2
fiber -10.6299 0.0 $A2 2
fiber -15.5512 0.0 $A2 2
fiber -20.4724 0.0 $A2 2
fiber -25.3937 0.0 $A2 2
fiber -30.3150 0.0 $A1 1
fiber -34.2520 0.0 $A1 1
fiber -38.1890 0.0 $A1 1
};
```

```
section Aggregator      1  5  Vy -section 10


##------------------------------------------------------------
## ELEMENTS

set gT 1
set FBETol 1.e-8;
set FBEiter 1000;
geomTransf Linear   $gT;
set integration "HingeEndpoint 1 $Lp 1 [expr 0.*$Lp] 1"
element forceBeamColumn  1  1  2  $gT $integration;


##------------------------------------------------------------
## LOADS

#Gravity Load
set P [expr 1476*$kN];
pattern Plain 1 "Linear" {
   load $IDctrlNode  0.0 [expr  -$P]  0.0
};
set Tol 1.0e-5;
integrator LoadControl 0.1
system BandGeneral
test NormDispIncr $Tol  100 0
numberer RCM
constraints Transformation
algorithm Newton
analysis Static
analyze 10
loadConst -time 0.0; #Keep axial load constant

#Lateral Load
set Plateral 1.0;
pattern Plain 2 "Linear" {
        load $IDctrlNode $Plateral 0.0 0.0
};
set file [open "Protocolo.dat" r]; #File with disp protocol in in


##------------------------------------------------------------
## RECORDERS
```

```
set WallName WSH6;#Wall name
file mkdir Results;      #Save results in "Results" folder
recorder Node -file Results.out -time -node $IDctrlNode -dof $IDctrlDOF disp
recorder Node -file Results/FD$WallName.out -time -node $IDctrlNode -dof $IDctrlDOF
disp
recorder Element -file Results/Concrete1$WallName.out -time -ele 1 section 1 fiber [expr
-$L/2.0] 0.0 3 stressStrain
recorder Element -file Results/Concrete2$WallName.out -time -ele 1 section 1 fiber [expr
$L/2.0] 0.0 3 stressStrain
recorder Element -file Results/Steel1$WallName.out    -time -ele 1 section 1 fiber [expr -
$L/2.]  0.0 1 stressStrain
recorder Element -file Results/Steel2$WallName.out    -time -ele 1 section 1 fiber [expr
$L/2.]  0.0 1 stressStrain
```

A.6 RPHM for RC Columns

```
##-------------------------------------------------------
## GEOMETRY

set H 21.653;          #Column cross section height (in)
set W 21.653;          #Column cross section width (in)
set L 64.96;           #Column length (in)
set cover 1.57;        #Column cross section cover (in)
set Lp 10.5;           #Plastic hinge length (in)

#Nodes
node 1 0 0;
node 2 0 $L;

fix 1 1 1 1;           #fix the base
set IDctrlNode 2;      #Control node
set IDctrlDOF 1;       #Control DOF


##-------------------------------------------------------
## MATERIALS

#Reinforcing steel
uniaxialMaterial Steel02 10 74.095 29000. 0.0094 20. 0.925 0.15; #Longitudinal steel
uniaxialMaterial MinMax 1 10 -min -0.02392;
#Concrete
uniaxialMaterial Concrete02 2 -6.40  -0.00332  -1.281   -0.02392  0.1  0.27 192.75;
#Confined
uniaxialMaterial Concrete02 3 -4.64  -0.00241  -0.928   -0.01117  0.1  0.27 192.75;
#Unconfined
# Shear
set Ec [expr 26587.2*$MPa]; # Concrete Young's Modulus
set G [expr (5./6.)*0.4*$Ec];
set GA [expr 0.1*$G*$H*$W];
uniaxialMaterial Elastic 4 $GA;


##-------------------------------------------------------
## SECTIONS

set nh 4
set nv 4
set dl 0.787;                  #Diameter of longitudinal bar (in)
```

```
set As 0.486;                           #Area of longitudinal bar (in²)
set dt 0.472;                           #Diameter of transverse bars (in)
set rec [expr $cover+$dt/2.];           #Bar cover
set dx [expr $cover+$dt+$dl/2.];        #Distance from the edge to the bar
set sx [expr ($H-2.*$dx)/($nh-1)];      #Distance between bar layers
set nfibers 200;                        #Number of fibers for confined region
section fiberSec 10 {
        patch rect 3  30          1  -[expr ($H/2.)]     -[expr ($W/2.)]     -[expr ($H/2.-$rec)]
        [expr ($W/2.)]
        patch rect 3  $nfibers    1  -[expr ($H/2.-$rec)]  [expr ($W/2.-$rec)]  [expr ($H/2.-
$rec)]  [expr ($W/2.)]
        patch rect 3  $nfibers   1        -[expr ($H/2.-$rec)] -[expr ($W/2.)]     [expr ($H/2.-
$rec)] -[expr ($W/2.-$rec)]
        patch rect 3  30          1    [expr ($H/2.-$rec)] -[expr ($W/2.)]        [expr ($H/2.)]
[expr ($W/2.)]
        patch rect 2  $nfibers    1  -[expr ($H/2.-$rec)] -[expr ($W/2.-$rec)]  [expr ($H/2.-
$rec)]  [expr ($W/2.-$rec)]
        fiber [expr (-$H/2.+$dx+0.*$sx)]                0.0  [expr $nv*$As]  1
        for {set i 1} {$i<=[expr $nh-2]} {incr i 1} {
                        fiber [expr (-$H/2.+$dx+$i*$sx)]  0.0  [expr 2.*$As]   1
        };
        fiber [expr (-$H/2.+$dx+($nh-1)*$sx)]     0.0  [expr $nv*$As]  1
};
section Aggregator     1  4  Vy -section 10


##------------------------------------------------------------
## ELEMENTS

set gT 1
set FBETol 1.e-8;
set FBEiter 1000;
geomTransf Linear   $gT;
set integration "HingeEndpoint 1 $Lp 1 $Lp 1"
element forceBeamColumn  1  1  2  $gT $integration;


##------------------------------------------------------------
## LOADS

#Gravity Load
set P [expr 968.0*$kN];
pattern Plain 1 "Linear" {
   load $IDctrlNode  0.0 [expr  -$P]  0.0
```

```
};
set Tol 1.0e-5;
integrator LoadControl 0.1
system BandGeneral
test NormDispIncr $Tol  100 0
numberer RCM
constraints Transformation
algorithm Newton
analysis Static
analyze 10
loadConst -time 0.0; #Keep axial load constant

#Lateral Load
set Plateral 1.0;
pattern Plain 2 "Linear" {
        load $IDctrlNode $Plateral 0.0 0.0
};
set file [open "Protocolo.dat" r]; #File with disp protocol in in


##------------------------------------------------------------
## RECORDERS

set ColumnID 6;                 #Column ID
file mkdir Results;     #Save results in "Results" folder
recorder Node -file Results.out -time -node $IDctrlNode -dof $IDctrlDOF disp
recorder Node -file Results/FD$ColumnID.out -time -node $IDctrlNode -dof $IDctrlDOF
disp
recorder Element -file Results/Concrete1$ColumnID.out -time -ele 1 section 1 fiber [expr
-$L/2.0] 0.0 2 stressStrain
recorder Element -file Results/Concrete2$ColumnID.out -time -ele 1 section 1 fiber [expr
$L/2.0] 0.0 2 stressStrain
recorder Element -file Results/Steel1$ColumnID.out    -time -ele 1 section 1 fiber [expr -
$L/2.]  0.0 1 stressStrain
recorder Element -file Results/Steel2$ColumnID.out    -time -ele 1 section 1 fiber [expr
$L/2.]  0.0 1 stressStrain
```